GEORG-AUGUST-UNIVERSITÄT GÖTTINGEN IN PUBLICA COMMODA SEIT 1737

UNIVERSITÄTSMEDIZIN GÖTTINGEN UMG

Differentiation-Induced Rearrangement of the Mitochondrial Calcium Uniporter Complex Regulates T-Cell-Mediated Immunity

Dissertation

for the award of the degree

"Doctor rerum naturalium" (Dr. rer. nat.)

of the Georg-August-Universität Göttingen

within the doctoral program *Cardiovascular Science*

of the Georg-August University School of Science

submitted by

Magdalena Shumanska

born in Berovo, North Macedonia

Göttingen, October 2022

Thesis Committee Members

Prof. Dr. Ivan Bogeski (supervisor, first reviewer)

Department of Molecular Physiology

Institute of Cardiovascular Physiology

University Medical Center Göttingen

Prof. Dr. mult. Thomas Meyer (second reviewer)

Department of Molecular Psycho-Cardiology

Clinic of Psychosomatic Medicine

University Medical Center Göttingen

Prof. Dr. Jürgen Wienands

Institute for Cellular and Molecular Immunology

University Medical Center Göttingen

Examination Committee Members

Prof. Dr. Ralph Kehlenbach

Department of Molecular Biology

Institute for Biochemistry and Molecular Cell Biology

University Medical Center Göttingen

Prof. Dr. Alexander Flügel

Department of Molecular and Cellular Neuroimmunology

Institute for Neuroimmunology and Multiple Sclerosis Research

University Medical Center Göttingen

Prof. Dr. Stefan Jakobs

Mitochondrial Structure and Dynamics

Department of NanoBiophotonics

Max Planck Institute for Multidisciplinary Sciences, Göttingen

Date of oral examination: *16 December 2022*

Supervised by:

Prof. Dr. Ivan Bogeski

To all who supported me

endlessly and without doubt

Table of Contents

List of Common Abbreviations

$^1O_2$	Singlet oxygen	**Ab**	Antibody
AFG3L2	AFG3-like protein 2	**ADP**	Adenosine diphosphate
AP1	Activator protein 1	**ANOVA**	Analysis of variance
APC	Antigen-presenting cell	**ATP**	Adenosine triphosphate
CCR	Chemokine receptor	**BS**	Beam splitter
CD	Cluster of differentiation	**$_c[Ca^{2+}]$**	Cytosolic calcium concentration
cDNA	Complementary DNA	**CaV**	Voltage-activated Ca^{2+} channel
CXCR4	C-X-C chemokine receptor type 4	**CCCP**	Carbonylcyanide-3-chlorophenyl-hydrazone
DC	Dendritic cell	**CFP**	Cyan fluorescent protein
DEG	Differentially expressed gene	**CRAC**	Ca^{2+} release-activated Ca^{2+} channel
EMRE	Essential MCU regulator	**DAG**	Diacylglycerol
E-value	Efficiency value	**DNA**	Deoxyribonucleic acid
FC	Fold change	**DTT**	Dithiothreitol
GECI	Genetically-encoded Ca^{2+} indicator	**EAE**	Experimental autoimmune encephalomyelitis
gly	Glycerine	**ECAR**	Extracellular acidification rate
GSK3	Glycogen-synthase kinase 3	**E_{GSH}**	Glutathione redox potential
H_2O_2	Hydrogen peroxide	**ELISA**	Enzyme-linked immunosorbent assay
H3	Histone H3	**Em**	Emission
HF	Heart failure	**ER**	Endoplasmic reticulum
HK gene	Housekeeping gene	**Exc**	Excitation
IFNγ	Interferon γ	**FACS**	Fluorescence activated cell sorting
IK	Inward-rectifying K^+ channel	**FADH**	Flavin adenine dinucleotide (reduced)
IL	Interleukin	**FCS**	Fetal calf serum
ITAM	Immunoreceptor tyrosine-based activation motif	**Fe-S**	Iron-sulphur
JNK	JUN N-terminal kinase	**FMN**	Flavin mononucleotide
KD	Knockdown	**FRET**	Förster resonance energy transfer
K_d	Dissociation constant	**GADS**	GRB2-related adapter protein
KO	Knockout	**GFP**	Green fluorescent protein
Lck	Lymphocyte-specific protein tyrosine kinase	**GTPase**	Guanosine triphosphatase
m-AAA protease	Mitochondrial ATP-dependent protease	**IMM**	Inner mitochondrial membrane
max	Maximal	**IP3**	Inositol-1,4,5-trisphosphate
MCU	Mitochondrial calcium uniporter	**JC-1**	5,5,6,6'-tetrachloro-1,1',3,3'tetraethylbenzimi-dazoylcarbocyanine iodide
MCUR1	Mitochondrial calcium uniporter regulator 1	**LAT**	linker for activation of T-cells
MEF	Myocyte enhancer factor-2	**$_m[Ca^{2+}]$**	Mitochondrial calcium concentration
MHC	Major histocompatibility complex	**MBP**	Myelin basic protein

MI	Myocardial infarction
Micu	Mitochondrial calcium uptake protein
min	Minimal
mPTP	Mitochondrial permeability transition pore
mRNA	Messenger RNA
NFAT	Nuclear factor of activated T-cells
NFκB	Nuclear factor κB
NK cell	Natural killer cell
NOX	NADPH oxidase
P2RX	Purinergic receptor channel 2
PBMC	Peripheral blood mononuclear cell
PI3	Phosphatidylinositol 3
PMCA	Plasma membrane Ca^{2+} ATPase
RNAi	RNA interference
RNAseq	RNA sequencing
RNS	Reactive nitrogen species
RORγt	Retinoic acid receptor-related orphan receptor gamma-T
ROS	Reactive oxygen species
rpm	Rounds per minute
RT	Room temperature
RT-qPCR	Real-time quantitative PCR
Ru	Ruthenium
RyR	Ryanodine receptor
S Figure	Supplementary figure
S Table	Supplementary table
SCID	Severe combined immunodeficiency
SDS-PAGE	Sodium dodecyl sulphate polyacrylamide gel electrophoresis
SERCA	Sarco/endoplasmic reticulum Ca^{2+}-ATPase
siRNA	Small interference RNA
SOCE	Store-operated Ca^{2+} entry
SOD	Superoxide dismutase
STAT	Signal transducer and activator of transcription
STIM	Stromal interaction molecule
Tbet	T box transcription factor
TBP	TATA-binding protein
TCR	T-cell receptor
MICOS	Mitochondrial contact site and cristae organizing system
MS	Multiple sclerosis
N. A	Numerical aperture
NADH	Nicotinamide adenine dinucleotide (reduced)
NCLX	Mitochondrial $Na^{+}/Ca^{2+}/Li^{+}$ exchanger
OCR	Oxygen consumption rate
OH^{-}	Hydroxyl radical
OMM	Outer mitochondrial membrane
OPA1	Optic atrophy type 1
PIP2	Phosphatidylinositol-3,4-bisphosphate
PLCγ1	Phospholipase Cγ1
PM	Plasma membrane
ps	Protospacer
***p*-value**	Significance value
RNA	Ribonucleic acid
roGFP	Redox-sensitive GFP
SD	Standard deviation
SEM	Standard error of means
sgRNA	Short guide RNA
SLP76	SH2-domain containing leukocyte protein of 76 kDa
TCA	Tricarboxylic acid cycle
TCGF	T-cell growth factor
TMRE	Tetramethylrhodamine ethyl ester
TRP	Transient receptor potential channel
WB	Western blot
WT	Wild type
YFP	Yellow fluorescent protein
Zap70	ζ chain-associated protein of 70 kDa
ΔΨm	Mitochondrial membrane potential

Tfh	Follicular helper T-cell
Tg	Thapsigargin
TGFβ	Transforming growth factor β
Th cell	T-helper cell
TM	Transmembrane domain
TMBIM5	Transmembrane BAX Inhibitor-1 Motif Containing Protein 5
T_o	Observed optimal primer annealing temperature
Treg	Regulatory T-cell
VDAC	Voltage-dependent anion channels

Abstract

$CD4^+$ T-cells are an important cell type involved in proper mediation of the human adaptive immune system. Activation of $CD4^+$ T-cells is a regulated process which includes a tightly controlled cytosolic calcium (Ca^{2+}) increase. Multiple fundamental T-cell processes are governed by Ca^{2+} ions, including cell subtype differentiation, energy production, proliferation, migration, and effector molecule secretion. Mitochondria are the main Ca^{2+} buffering system in T-cells, allowing proper regulation and support of cellular metabolic demands. The mitochondrial calcium uniporter (MCU) complex is the main regulator of mitochondrial Ca^{2+} influx in the inner mitochondrial membrane of T-cells; thus, MCU alterations could be associated with mediation of T-cell immune responses. However, the exact role of MCU in T-cells is poorly understood. This Doctoral Thesis aimed to explore the role of MCU in isolated primary human $CD4^+$ T-cells by generating a model of transient MCUa downregulation and investigating its effect on $CD4^+$ T-cell mitochondrial metabolism and function. We show that activation of T-cells causes a rearrangement of the MCU complex, leading to elevated mitochondrial Ca^{2+} uptake and increased mitochondrial bioenergetics. Downregulation of MCU diminishes this effect and suppresses mitochondrial respiration, ATP generation and proinflammatory T-cell function. Additionally, our results show that an elevation of the mitochondrial-AAA protease AFG3L2 acts as a compensatory mechanism upon MCUa downregulation, controlling MCU complex stability via EMRE proteolysis. Finally, downregulation of MCUa in primary rat effector T-cells not only validated the results obtained in human T-cells but also caused a delay in disease onset in an experimental model of multiple sclerosis *in vivo*. In conclusion, mitochondrial Ca^{2+} influx through the MCU complex is essential for proper T-cell function and metabolism, and is involved in mediating autoimmunity. Targeting MCU in T-cells could prove beneficial for suppression of progressive autoimmune disease.

1. Introduction

1.1 The fundamentals of the human immune system

A desire to uncover the enigma of the immune system, and to develop immunology as a science, has fueled scientists as early as the 18th century when the main focus was to simply prevent the spread of disease and treat the sick (McComb, 2019). Early work of microbiologists in that time addressed the neutralisation of microbial toxins, today known as the vaccination process, setting the basis for modern medicine. Edward Jenner (1749-1823), known for his research and development of the smallpox vaccine, Louis Pasteur (1822-1895), for his pasteurisation method and development of the rabies vaccine, Robert Koch (1843-1910), for his "Koch's postulates", and Paul Ehrlich (1854–1915), for his theory of antibody formation, are some of the famous milestone founders in the early history of immunology, setting the foundations of *humoral* (or *acquired*) *immunity* (Silverstein, 2009). As bacterial properties were being discovered, the work of Elias Metchnikoff (1845–1916) on the identification of phagocytosis (Greek for "*phagein*"-to eat, and "*cyte*"-cell) laid the basis for the evolutionarily-older arm of the immune system – *innate immunity* (Gordon, 2008). Scientists had a dichotomous view of the two immunity types, leading to many debates throughout the years. Today, it is well established that innate and acquired immunity are highly interconnected, with overlapping and mutually beneficial pathways.

In biology, immunity (derived from the Latin word "*immunis*"-to be exempt) is defined as "the ability of the body to protect itself from disease-causing entities" (Delves et al., 2011). It serves three main functions: 1) to recognise and get rid of abnormal "self-cells", 2) to remove damaged and dead cells, and 3) to protect the body from pathogens. When these functions fail, severe infections, tumors, autoimmune diseases, overreactive responses, or immunodeficiencies, among others, can develop (Silverthorn, 2016). The human immune system is divided into three levels of defense: 1) A physical barrier provided by the skin, as well as mucous secretions covering the respiratory, digestive and reproductive tracts; 2) Innate immunity-a non-specific, but highly-effective defense system; and 3) Acquired (or adaptive) immunity-a sophisticated and specific response system (Delves et al., 2011).

Upon entry of a pathogen, innate immunity occurs shortly after (up to 96 hrs after infection). Evolutionary conserved pathogen-associated and danger-associated molecular patterns are detected by the innate immune system and killed by phagocytosis, secretion of destructive enzymes, production of reactive oxygen (ROS) or nitrogen species (RNS), and

defensins. Main players in innate immunity include macrophages, mast cells, basophils, neutrophils, natural killer (NK) cells (although it has been shown that they can form immunological memory and can be considered a part of acquired immunity as well (Parkin & Cohen, 2001)), eosinophils, soluble proteins of the complement system, and lysozymes. Like all species, pathogens can quickly evolve and adapt (such as the influenza virus or the novel SARS-CoV-2 virus), therefore innate immune responses are not always sufficient.

Acquired immune responses take longer to be functionally active (between 4 and 7 days after the innate immune response), but are specifically designed against the nature of the pathogen of interest. The innate system 'gives information' to the acquired system and allows time to achieve the required specificity against the pathogen. Thus, acquired immunity is highly dependent on the innate one. The hallmarks of acquired immunity include: 1) antigen-specific responses, mediated by clonal expansion of lymphocytes, and 2) the generation of immunological memory. There are two types of acquired immunity: active and passive. Active acquired immunity occurs when the body produces its own antibodies against the pathogen it has been exposed to. Conversely, passive acquired immunity occurs when the body later acquires antibodies that have been produced in another organism (e.g. transfer from mother to fetus). The two types of lymphocytes mediating the acquired immune responses include B- and T-lymphocytes (Delves et al., 2011).

B-cells develop in the bone marrow. Upon antigen encounter, these cells develop into plasma cells which are able to secrete antigen-specific antibodies at very high rates. Memory B-cells form after the initial encounter with the antigen, making the secondary immune responses considerably faster and more efficient. These responses form the basis of effective disease protection with vaccinations (Cano & Lopera, 2013).

T-cells carry out cell-mediated immunity and are discussed in more detail in the following chapter.

1.2 T-cell-mediated immunity

1.2.1 T-cell development

T-cells are derived from bone-marrow hematopoietic precursor stem cells which migrate to the thymus. The critical role that the thymus plays in the developmental process of T-cells has been demonstrated in cases of genetic defects or after thymectomy in mice, both leading to severe immunodeficiencies (Mohtashami et al., 2016). Thus, *in vitro* development of T-cells with the use of stem cells has been shown to be quite complex (Mohtashami et al., 2016). T-cells (called thymocytes at the beginning of their developmental process) undergo several differentiation steps based on the expression of surface markers, outlined in Figure 1 below.

Thymocytes in the outer thymic cortical region initially develop into double-negative $CD4^-$ $CD8^-$ cells. The double-negative population can be further divided into cells which express CD44 (cell surface glycoprotein) and cells which express CD25 (interleukin-2 receptor α-chain). Cells which express CD25 but lack expression of CD44 undergo a process known as β-selection – a critical checkpoint in T-cell development when proper T-cell receptor (TCR) gene rearrangement occurs. Thymocytes are required to signal through a pre-TCR, consisting of a properly-rearranged TCRβ gene, a pre-Tα, and CD3 molecules, via CXCR4 (receptor for stromal-derived factor-1) and Notch1 (activator of phosphoinositide 3 kinase and the Akt-pathway). Thymocytes which successfully "pass" β-selection develop into double-positive $CD4^+$ $CD8^+$, expressing proper TCRαβ complexes. Cells that do not "pass" β-selection undergo apoptosis. Double-positive cells undergo further positive selection by interacting with self-antigens in the context of major histocompatibility complex (MHC) class I or class II molecules. The cells that interact with MHCs with an appropriate affinity survive, whereas a weaker affinity leads to apoptosis. Selected cells migrate to the thymic medulla and undergo negative selection by reacting with self-antigens presented by antigen-presenting cells (APCs). Most of the cells would react strongly to self-antigens and would further undergo apoptosis. Finally, downregulation of either one of the co-receptors produces naive $CD4^+$ or naive $CD8^+$ T-cells which leave the thymus and migrate to the periphery (Delves et al., 2011; Germain, 2002; Silverthorn, 2016).

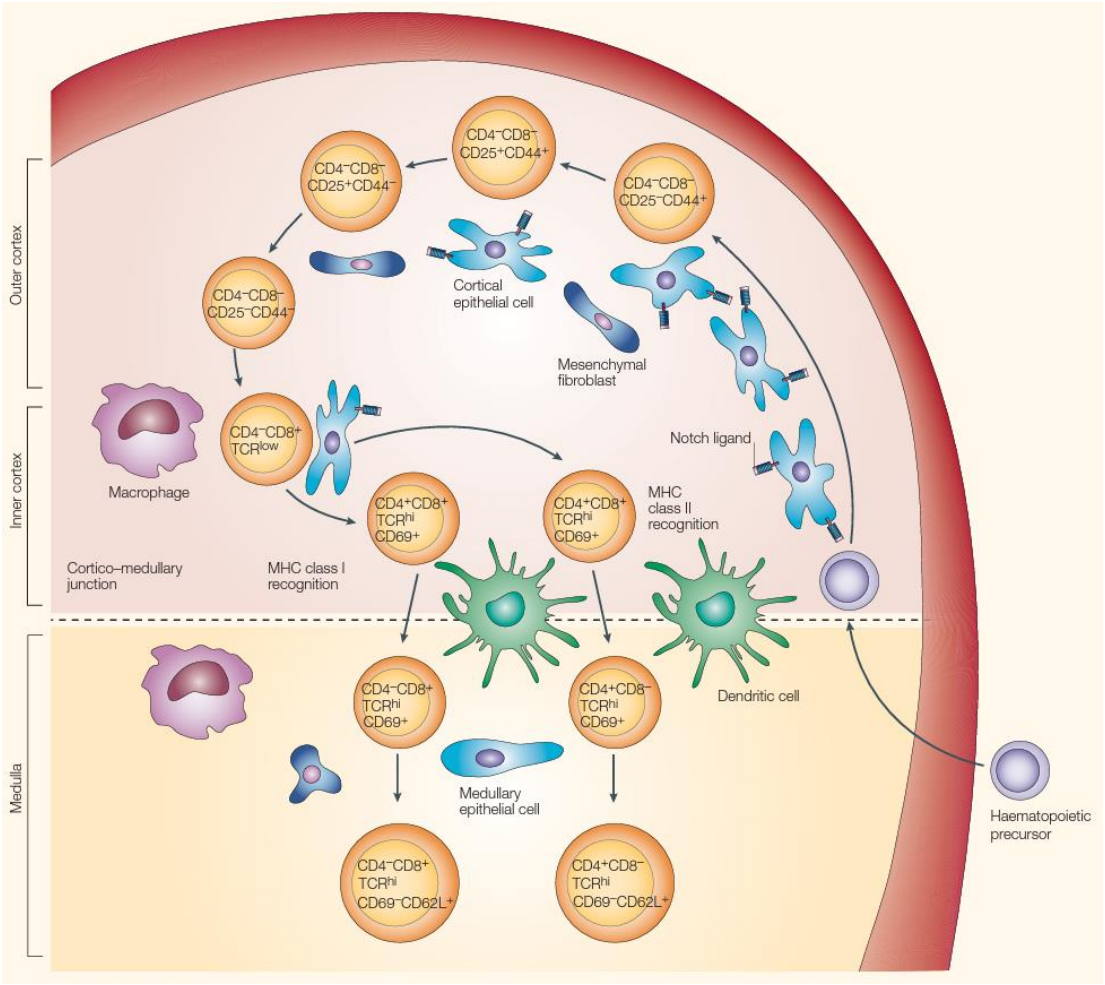

Figure 1. T-cell development in the thymus. The thymus is structured into cortical and medullary areas, each characterized by the presence of thymocyte precursors at defined maturation stages. Thymocyte differentiation is characterized by the expression of cell-surface markers, including CD4 and CD8, as well as by the status of the T-cell receptor (TCR). Immature thymocytes localized in the cortical region do not express CD4 or CD8 and are known as double negative (DN) cells. As they progress in differentiation, they begin to express TCRs, as well as CD4 and CD8, becoming double positive (DP) thymocytes. These cells are then submitted to selection, moving toward the medulla and becoming single positive (SP) cells for either CD4 or CD8. Image taken from Zúñiga-Pflücker, 2004.

T-cells can be found in virtually every organ and tissue in the body, mainly within the bone marrow, spleen, tonsils and lymph nodes, but also in lungs, intestines, skin and blood (normal range in blood between 500 and 1,600 T-cells per mm^3) (Kumar et al., 2018). Thymopoiesis is highest at birth, and age-related changes have been observed through a decrease in thymic volume and its gradual replacement by fat tissue. Human naive T-cells can have a life span of up to 10 years, accounting for their persistence in old age. TCR functionality analyses have shown that naive T-cells maintain their function and are able to respond to diverse antigens for longer periods of time. The role of T-cells is different in distinct life stages.

At an early age, encounters with new antigens for the first time are high, therefore pathogen responses and memory formation are crucial. After childhood, T-cell homeostasis is achieved by constant immunoregulation and tumor surveillance. At an advanced age, T-cell function declines and the susceptibility to infections, cancer and autoimmunity is increased (Salam et al., 2013).

The two types of T-cells, $CD4^+$ and $CD8^+$, are distinct not only by their expression of co-receptors but also by their effector function in the body. $CD8^+$ T-cells, also known as cytotoxic T-cells, are MHC class I-restricted and are involved in anti-viral and anti-tumor immunity. Upon recognition of an infected or cancer target cell, cytotoxic T-cells are able to kill via the Fas/Fas ligand pathway and the perforin/granzyme pathway, both leading to activation of caspases which rapidly initiate apoptosis (Delves et al., 2011).

$CD4^+$ T-cells are the main focus of this thesis, therefore their differentiation, function and signalling pathways are extensively covered in the following chapters.

1.3 $CD4^+$ T-cells

As technology developed, so did the area of immunology investigating $CD4^+$ T-cells (also known as helper-T-cells; Th). Tim Mossman and Robert Coffman developed the first hypothesis on the existence of different $CD4^+$ T-cell types in 1986: T-helper 1 (Th1) and T-helper 2 (Th2) cells. They explained that: "two very different subsets of helper-T-cells exist, distinguished by different sets of cytokines secreted after activation and, as a consequence, mediating very different regulatory and effector functions" (Coffman, 2006; Zhu & Paul, 2008). Since then, many scientists have worked on Th cell differentiation, activation and cytokine secretion, and have attempted to link these cells to several pathologies.

The initial step of naive $CD4^+$ T-cell differentiation is antigenic stimulation which occurs as an interaction between a TCR and an antigen-MHC class II complex presented by an APC. Among APCs, dendritic cells (DCs) are considered the most important due to their enhanced ability to activate naive T-cells (Delves et al., 2011).

The TCR (Figure 2) is a membrane-bound molecule composed of two disulphide-linked chains which fold into two domains, one with an unchanged structure and the other with a highly-variable structure. The variable region is important for MHC contacts. There are two classes of TCRs: TCR1 and TCR2, also known as γδTCR and αβTCR, respectively. γδTCR-cells are common in epithelial tissues and the lungs. These cells are intriguing because they do not require antigen presentation in the context of MHC. αβTCR-cells are more common (70% presence in circulation) and are known for undergoing somatic recombination during development, resulting in a diverse repertoire of αβTCRs. CD3 is an integral part of the TCR, noncovalently-bound to it. CD3 contains multiple immunoreceptor tyrosine-based activation motifs (ITAMs) which, upon encounter with an antigen, become phosphorylated and act as a platform for further intracellular signalling pathways. CD4 is an important co-receptor for MHC II molecules and is considered a part of the entire TCR complex. CD4 is a single polypeptide chain containing four immunoglobulin-like domains which project from the cell surface. The cytosolic tail of CD4 is crucial for signalling since it is bound to the protein tyrosine kinase Lck which initiates signal transduction cascades upon antigen stimulation. Moreover, CD28 is another important co-receptor expressed in all naive T-cells. CD28 binds to CD80 and CD86 on the surface of DCs and is involved in the prevention of apoptosis (Delves et al., 2011; Shah et al., 2021).

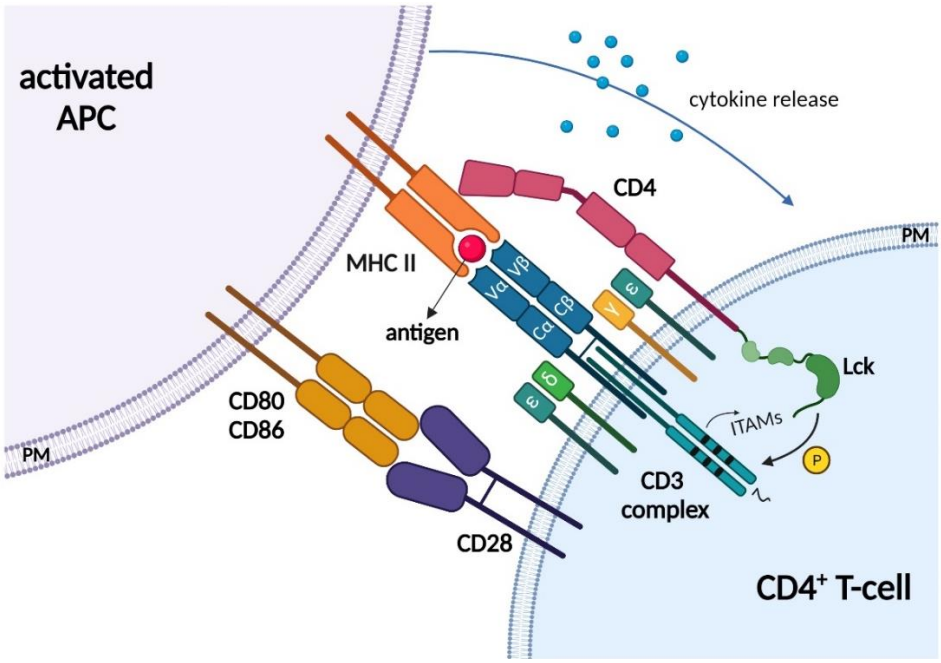

Figure 2. CD4⁺ T-cell receptor structure. Two co-stimulatory signals are required for CD4⁺ T-cell activation. The first signal is via the T-cell receptor (TCR), consisting of variable (V) and constant (C) α and β chains, a polypeptide CD4 receptor bound to Lck kinase, and a CD3 complex containing multiple chains (ε, δ, γ and ζ) with several tyrosine-based activation motifs (ITAMs) required for subsequent signalling. The TCR complex binds to MHC class II molecules on antigen presenting cells (APCs). The second signal is through CD28 which binds CD80 and CD86 on the surface of APCs. Cytokine release from APCs is also crucial for proper T-cell activation. Image created with BioRender.

TCR stimulation leads to downstream signalling pathways which initiate naive T-cell proliferation and differentiation into specific effector types. Table 1 lists the CD4⁺ T-cell subtypes, their respective 'master-regulator' cytokines and transcription factors, inhibitory signals, and the main secreted cytokines.

1.3.1 Th1 cells

Cytokine production by activated T-cells and APCs, as well as the cytokine milieu surrounding the cells, have a high impact on CD4⁺ T-cell differentiation. Interleukin 12 (IL-12) and Interferon γ (IFNγ) are crucial for Th1 differentiation. IL-12 is secreted mainly by APCs, which induces IFNγ secretion by NK cells. IFNγ secretion induces activation of the transcription factor signal transducer and activator of transcription 1 (STAT1), which further activates the "master-regulator" of Th1 differentiation – T box transcription factor (Tbet). Tbet enhances IFNγ production, suppresses the development of Th2 and Th17 cells and upregulates IL-12 receptor expression. IL-12 is important for activation of STAT4 which further induces IFNγ production, creating a positive feedback loop for T-bet and IL-12 receptor expression

(Luckheeram et al., 2012).

Th1 cells mediate intracellular pathogen immune responses. They play a particular role in resistance to mycobacterial infections and have been shown to be responsible for the induction of autoimmune diseases (Luckheeram et al., 2012; Zhu & Paul, 2008).

1.3.2 Th2 cells

Important cytokines for Th2 differentiation include IL-4 and IL-2. IL-4 induces the activation of STAT6, which in turn activates the major transcription factor involved in the lineage-GATA binding protein 3 (GATA3). GATA3 enhances Th2 cytokine production and proliferation, and inhibits Th1 differentiation by interacting with Tbet. STAT5, activated by IL-2, is also important for Th2 differentiation by coordinating with GATA3 and further inducing IL-4 production. IL-6, produced by APCs, has a role in enhancing IL-4 production and upregulation of nuclear factor of activated T-cells (NFAT) proteins (Luckheeram et al., 2012).

Th2 cells mediate immunity against extracellular pathogens and parasites. They also have a role in inducing asthma and other allergies. Other important cytokines produced by Th2 cells include IL-5, IL-9, IL-10, IL-13 and IL-25 (Zhu & Paul, 2008).

1.3.3 Th17 cells

Signalling cytokines involved in Th17 differentiation include IL-6, IL-21, IL-23 and transforming growth factor (TGF) β. At low concentrations and in the presence of IL-6, TGF-β can induce Th17 differentiation, production of IL-21 and expression of IL-23 receptors. It also leads to the activation of retinoic acid receptor-related orphan receptor gamma-T (RORγt)- the main regulator of Th17 differentiation. RORγt induces secretion of IL-17. STAT3 also plays a role in this process by further increasing RORγt expression. IL-21 and IL-23 are required for the expansion and maintenance of the Th17 cell population (Luckheeram et al., 2012).

Th17 cells are important for mediating immune responses against extracellular bacteria and fungi (Zhu & Paul, 2008).

1.3.4 Th9 cells

Th9 cells were initially considered a subset of Th2 cells. TGF-β was found to be the main player in Th9 differentiation, in combination with IL-4. The main transcription factor involved in Th9 differentiation is PU.1 Th9 cells have been associated with roles in tumorigenesis and

allergies via IL-9 secretion (J. Chen et al., 2019).

1.3.5 Treg cells

Regulatory (Treg) cells (further classified in induced and natural Tregs) are forkhead transcription factor (FoxP3)+, $CD4^+$ and $CD25^+$ cells. High concentrations of TGF-β are the critical signal responsible for the initiation of the Treg cell lineage. Smad2, Smad3 and STAT5 are also important factors involved in the differentiation process (Luckheeram et al., 2012).

Treg cells play a critical role in self-tolerance and in regulating immune responses. Tregs exert their suppressive functions mainly through the production of cytokines, including TGF-β, IL-10, and IL-35 (Zhu & Paul, 2008).

1.3.6 Tfh cells

Follicular helper T-cells (Tfh) are C-X-C motif receptor 5 (CXCR5)-expressing cells located in follicular areas of lymphoid tissues. They are involved in the development of antigen-specific B-cell immunity. IL-6 and IL-21 are the main cytokines involved in the differentiation of Tfh cells, and STAT3 and Bcl6 are important transcription factors (Crotty, 2014).

1.3.7 Th22 cells

Despite the fact that Th1 and Th17 cells were known as the main cell types associated with IL-22 expression, a new cell subtype, Th22, was described due to its significantly higher secretion of IL-22 and no secretion of other Th1 and Th17-related cytokines. Th22 cells can differentiate into Th1 or Th2 cells under appropriate conditions, demonstrating their high plasticity. Th22 cells can be identified by cell surface markers (CCR4, CCR6 and CCR10), transcription factors (AhR and STAT3), and IL-22 secretion. A combination of several transcription factors and cytokines is required for Th22 differentiation (Jiang et al., 2021).

Th22 cells play important roles in epidermal wound healing (Jiang et al., 2021).

Table 1. Characteristics of the regulation of different $CD4^+$ T-cell subtypes (Luckheeram et al., 2012).

$CD4^+$ T-cell subtype	Regulating cytokines	Main transcription factors	Inhibitory transcription factors	Cytokines secreted	Surface marker profile
Th1	IFNγ, IL-12	Tbet	GATA3	IFNγ, TNF-α, IL-2	CD4, CD94, CD119, CXCR3
Th2	IL-4, IL-2	GATA3	Tbet	IL-4, IL-5, IL-13	CD4, CD119, CCR3
Th17	IL-6, IL-21, IL-23, TGF-β	RORγt	Tbet, FoxP3	IL-17A, IL-17F, IL-21, IL-22	CD4, CD161, CCR4, CCR6
Th9	TGF-β, IL-4	PU.1	Exact combination not known	IL-9	CD4, CCR6
Treg	TGF-β, IL-2	FoxP3	Exact combination not known	TGF-β, IL-10, IL-35	CD4, CD25
Tfh	IL-6, IL-21	STAT3, Bcl6	Exact combination not known	IL-21	CD4, CXCR5, CD69
Th22	IL-6, TNF-α, IL-23, IL-1	AhR, RORγt, STAT3	Tbet	IL-22, IL-13, IL-26, TNF-α, granzyme B	CD4, CCR4, CCR6, CCR10

1.3.8 Early events in $CD4^+$ T-cell signalling

Interaction between the TCR, its co-receptors and the MHC II-antigen complex initially leads to phosphorylation of the TCR chain by protein kinase Lck. This creates binding sites for the recruitment of ζ chain-associated protein of 70 kDa (Zap70) which phosphorylates two key proteins: linker for activation of T-cells (LAT) and SH2-domain containing leukocyte protein of 76 kDa (SLP76). Activation of LAT results in recruitment of GRB2-related adapter protein (GADS) which has been associated with changes in T-cell shape. Furthermore, phosphorylated LAT initiates two main signalling cascades: the Ras/MAPK pathway, mostly involved in proliferation, and the phosphatidylinositol pathway, involved in calcium (Ca^{2+}) signalling and *IL-2* transcription (Delves et al., 2011).

1.4 Calcium signalling in T-cell activation

Calcium (Ca^{2+}) is a universal secondary messenger in all cell types, including T-cells. Cells invest a great amount of energy in order to maintain cytosolic Ca^{2+} concentrations ($_c[Ca^{2+}]$) and to alter those concentrations when necessary. A constant Ca^{2+} transport between the plasma membrane (PM) and the cytosol is mainly governed by a Ca^{2+} concentration gradient, favoring a strong driving force towards the cytosol (Clapham, 2007), where the resting T-cell $_c[Ca^{2+}]$ is 50-100 nM compared with 1-2 mM in the PM (Cahalan & Chandy, 2009). The electrical gradient (or membrane potential) is another important parameter influencing Ca^{2+} influx or efflux, determined by voltage-activated Ca^{2+} channels (CaVs) and ion channels conducting sodium (Na^+), potassium (K^+) and chloride (Cl^-). The PM resting potential is maintained around –80 mV, also favoring cytosolic Ca^{2+} influx (Cahalan & Chandy, 2009). An increase in $_c[Ca^{2+}]$ can also come from the endoplasmic reticulum (ER), where the $[Ca^{2+}]$ is 300 μM – 1 mM (Parker & Smith, 2010). Mitochondria serve as important Ca^{2+} buffering systems, taking up Ca^{2+} ions from Ca^{2+} microdomains formed upon sustained $_c[Ca^{2+}]$ increases in the range of 1-10 μM. Ca^{2+} efflux from mitochondria occurs mainly via mitochondrial $Na^+/Ca^{2+}/Li^+$ exchanger (NCLX) (L. Boyman et al., 2013). Ca^{2+} release from endosomes, exosomes and lysosomes was also proven essential for T-cells and T-cell activation. Some functions include endosomal recycling of exhausted signalling molecules involved in T-cell activation (Benzing et al., 2013) and guided cytokine release at the immune synapse by exosomes and lysosomes (Davis et al., 2012), both governed by Ca^{2+} fluxes.

Binging of Ca^{2+} ions to proteins alters their conformation, thereby their protein-protein interaction and function (Clapham, 2007). The ability of Ca^{2+} to affect local electrostatic fields and protein conformations is the main tool of signal transduction. Many cellular proteins have adapted to bind Ca^{2+} (mainly via EF-hand domains) in a vast range of affinities (from nM to mM) to buffer or lower Ca^{2+} levels or to trigger cellular processes and cell-to-cell signalling (Nakayama & Kretsinger, 1994).

1.4.1 Store-operated Ca^{2+} entry

As stated previously, antigen binding to the TCR initiates a cascade of signalling pathways in $CD4^+$ T-cells. One of the main pathways (and best-described in T-cells, stemming from 1986) is store-operated Ca^{2+} entry (SOCE), mediated by Ca^{2+} release-activated Ca^{2+} channels (CRAC) (Feske et al., 2001; Putney, 1986). Upon TCR engagement, phosphorylation events lead to activation of LAT which further activates phospholipase Cγ1 (PLCγ1) (Lewis,

2003). Activation of PLCγ1 results in hydrolysis of phosphatidylinositol-3,4-bisphosphate (PIP2) to diacylglycerol (DAG) and inositol-1,4,5-trisphosphate (IP3). IP3 binds to its IP3 receptor in the ER membrane, which itself is a Ca^{2+}-conducting channel, causing ER Ca^{2+} store depletion (Hughes & Putney, 1990). ER Ca^{2+} release causes a transient $_{c}[Ca^{2+}]$ increase, but more importantly, it causes the activation of the SOCE pathway (Trebak & Kinet, 2019).

Stromal interaction molecules 1 and 2 (STIM 1/2) are the main sensors of ER $[Ca^{2+}]$, containing a Ca^{2+}-binding EF-hand motif localised in the N-terminal facing the ER lumen. In the cytosolic domain, STIM1 and -2 form a CRAC-activating domain which can directly interact with CRAC channels (Stathopulos et al., 2008). Under resting conditions, STIM1 and 2 are distributed throughout the ER in a dimeric form. Upon ER store depletion, the dimers can undergo rapid oligomerisation and move into PM junctions, interacting with CRAC channels-Orai 1, 2 and 3 via coiled-coil domains (Soboloff et al., 2012). Orai channel activation causes a rapid and sustained T-cell $_{c}[Ca^{2+}]$ increase, essential for the immune synapse, activation of NFAT pathways, and subsequent cytokine production, proliferation and proper immune function (Feske, 2007).

- Orai1:

Orai1 was first identified as a gene regulating CRAC channels via a genome-wide RNA interference (RNAi) screen in *Drosophila* (Vig et al., 2006). In this screen, two CRAC modulators – CRACM1 and CRACM2, were investigated, both showing abolished currents upon pharmacological inhibition. Moreover, the human ortholog of CRACM1, i.e. Orai1 (a 38 kD protein), was confirmed to be a key modulator of CRAC channels in HEK293 and Jurkat T-cells (Prakriya et al., 2006; Vig et al., 2006; Zhang et al., 2011).

Orai1 is a four-transmembrane cell-surface protein with both its N- and C-termini located in the cytosol. In Jurkat T-cells, it has been shown that Orai1 is a pore subunit of CRAC channels, with its two conserved glutamate residues located in transmembrane helices, E221 and E245, which have an important role in SOCE and interaction with STIMs (Feske et al., 2006).

The highly essential role of Orai1, and in general SOCE, in T-cells has been described by Feske et al. (2006), who showed that cells from patients with hereditary severe combined immunodeficiency (SCID) are defective in SOCE and Orai function. Genomic DNA sequencing of 23 SCID patients showed an association of SCID with a missense mutation in exon 1 of human Orai1 (a C-to-T transition at position 271), leading

to the replacement of a highly conserved arginine residue by tryptophan. All disease carriers were genotypically heterozygous for the mutation, compared with healthy controls and unaffected family members. Expression of WT Orai1 in isolated T-cells from SCID patients restored CRAC currents, further corroborating its importance.

- Orai2:

  A sequence database research for homologous Orai proteins identified Orai2, which is structurally related to Orai1 (Fahrner et al., 2018; Mercer et al., 2006). Orai2 has been proposed as a negative regulator of Orai1 by Vaeth et al. (2017). Deletion of Orai2 in $CD4^+$ T-cells enhanced SOCE in naive cells, with no impact on effector cells. Furthermore, the study showed that effector T-cells highly downregulate Orai2 and upregulate Orai1, allowing for a robust T-cell activation by SOCE (Vaeth et al., 2017).

- Orai3:

  Orai3 is the second homolog of Orai, showing a high percentage of homology with the other two members: 63% with Orai1 and 66% with Orai2 (Sanchez-Collado et al., 2021). Orai3 lacks a cysteine residue C195 found in the other two proteins, which is involved in H_2O_2-dependent inactivation of the channel, thereby making it resistant to oxidative stress (Bogeski et al., 2010). The protein region between the amino acids 42 and 62 has been reported as essential for Ca^{2+}-dependent activation of Orai3 (Lis et al., 2010). It has also been shown that Orai3 can be selectively activated by arachidonic acid (Thompson et al., 2010), which is one of the most abundant fatty acids in the brain, explaining the high protein expression score of Orai3 in the cerebral cortex (Uhlén et al., 2015) [Human Protein Atlas]. Overexpression of Orai3 has been reported in breast, prostate and lung cancer, among others. The role of Orai3 in T-cells is not entirely understood, but it has been reported that effector T-cells overexpress it, which may help explain why these cells can proliferate, secrete cytokines and survive well in an oxidant-rich environment (Bogeski et al., 2010; Saul et al., 2016).

Figure 3 below details the SOCE pathway and its main players involved in $CD4^+$ T-cell activation.

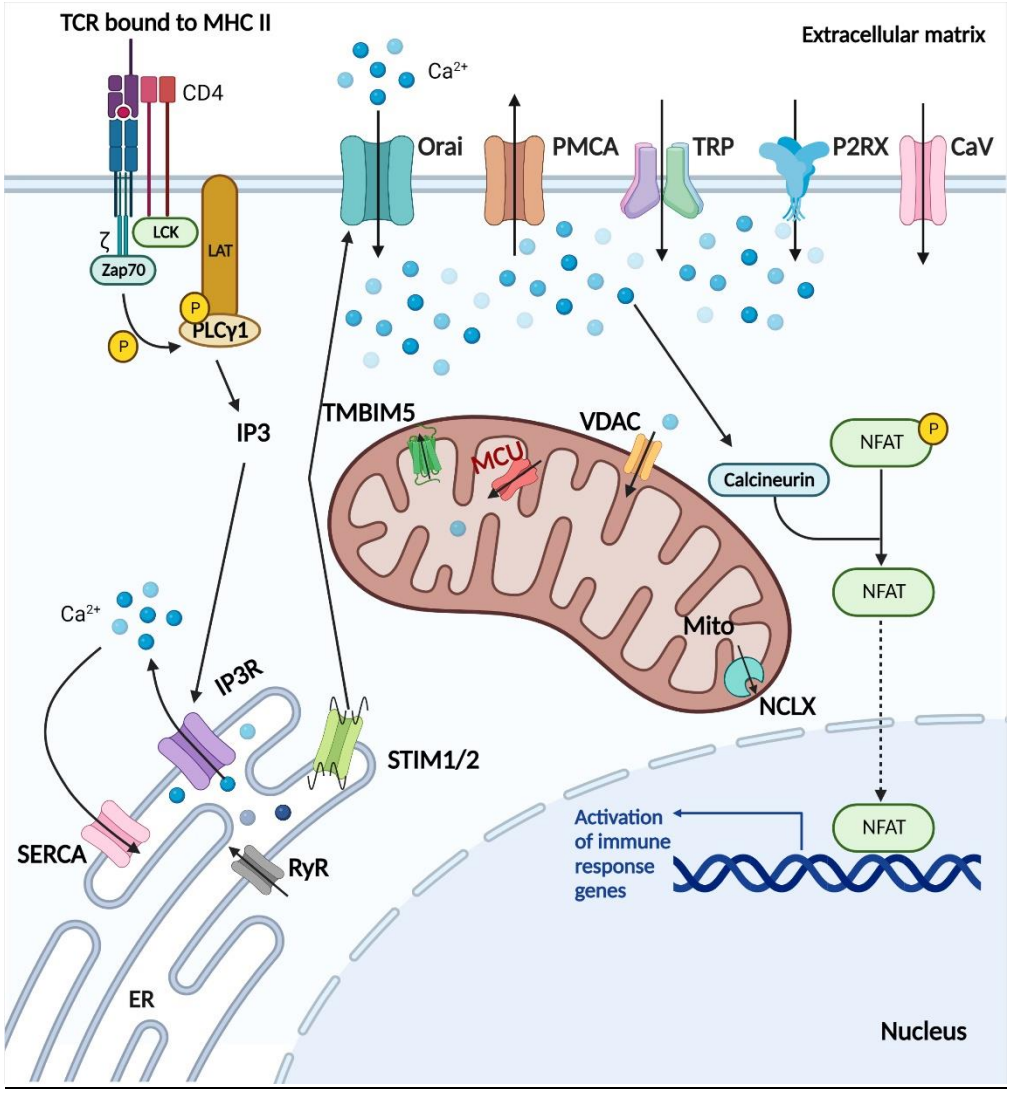

Figure 3. Store-operated Ca^{2+} entry (SOCE) signalling pathway. Stimulation of the T-cell receptor (TCR) activates kinases which phosphorylate the adaptor protein linker for activation of T-cells (LAT). LAT activates phospholipase C γ1 (PLCγ1). PLCγ1 induces inositol-3-phosphate (IP3) formation, which binds to IP3 receptors in the ER membrane, resulting in the release of Ca^{2+} from stores. A decrease in the Ca^{2+} content of the ER is 'sensed' by stromal interaction molecules 1 and 2 (STIM1/2), which bind to CRAC (Orai) channels in the plasma membrane. Ca^{2+} influx though Orai channels activates calcineurin and nuclear factor of activated T-cells (NFAT), finally leading to expression of target genes and T-cell differentiation. Mitochondria are able to buffer $_{c}Ca^{2+}$ via uptake through voltage-dependent anion channels (VDAC) and mitochondrial calcium uniporter (MCU) channels. Other abbreviations: PMCA- plasma membrane Ca^{2+} ATPase; TRP- transient receptor potential channel; P2RX-purinergic receptor channel 2; CaV-voltage-gated Ca^{2+} channel; NCLX-mitochondrial Na^{+}/Ca^{2+} exchanger; RyR-ryanodine receptor; SERCA- sarco/endoplasmic reticulum Ca^{2+}-ATPase; TMBIM5-transmembrane BAX inhibitor motif containing protein 5. Image created in BioRender.

1.4.2 Other mechanisms regulating [Ca^{2+}] in T-cells

In addition to the mechanisms described above, T-cells have multiple other means to regulate $_c[Ca^{2+}]$.

Transient receptor potential cation (TRP) channels are highly expressed in T-cells and their altered expression can cause dysregulation of TCR engagement. Several TRP channels are known: 1) TRP4, which is a Ca^{2+}-activated-Na^+-selective channel and a potent regulator of Ca^{2+} entry through Orai (Launay et al., 2002); 2) TRP7, which regulates Orai1 signalling and coordinates TCR signalling termination through phosphorylation of PLCγ isoforms and is therefore critical for T-cell development (Krishnamoorthy et al., 2018); 3) TRP2, which supports Ca^{2+} signalling in a high-oxidant environment due to its activation by H_2O_2 (Guse et al., 1999); and 4) TRP1, which has been reported to have a role in TCR engagement and proinflammatory T-cell function (Bertin et al., 2014); however, the exact mechanism of TRP1 regulation is still unclear.

Purinergic ionotropic receptors (P2RX) are directly activated by extracellular ATP and represent channels which conduct Na^+ and Ca^{2+}. Seven such channels exist; however, their electrophysiological characterisation in T-cells is lacking. P2RX1, P2RX4, or P2RX7 knockout displayed normal T-cell development, whereas double P2RX2/P2RX3 knockout mice exhibited splenomegaly (Coutinho-Silva et al., 2005). One study has shown a connection between P2RX1, P2RX4, and P2RX7 and T-cell IL-2 production and proliferation (Di Virgilio et al., 2017). Little is known about P2RX5 and P2RX6.

All four members of L-type Ca^{2+} channels (CaV) are expressed in T-cells, and that expression increases upon TCR stimulation (Badou et al., 2013). However, their regulation and function in T-cells have been debated and studies investigating CaV channels are sparse. Some experimental data on CaV1.1 in T-cells exists, which showed that an alternatively spliced variant of CaV1.1 could be involved in coupling with ryanodine receptors (RyR) at ER–PM junctions in order to induce higher ER Ca^{2+} release (Matza et al., 2016). In a recent study, CaVβ1 was reported as a regulator of T-cell function (Erdogmus et al., 2022). Deletion of CaVβ1 in $CD4^+$ T-cells caused a significant decrease in cell survival, but was dispensable for Ca^{2+} influx into the cytosol upon cell activation and for cytokine production (Erdogmus et al., 2022). However, the mechanism by which CaVβ1 governs T-cell survival remains unclear.

T-type (transient) Ca^{2+} channel currents have also been measured in T-cells, mainly through CaV3.1, using whole-cell voltage-clamp. Ca^{2+} entry through CaV3.1 was independent of SOCE, and deletion of CaV3.1 in Th17 cells led to a decrease in IL-17A, IL-17F and IL-21 secretion. Even though L- and T-type Ca^{2+} transients are low in T-cells, they likely contribute

to Ca^{2+} microdomains important for TCR signalling pathways (H. Wang et al., 2016).

K^+ channels influence Ca^{2+} influx in T-cells via the generation of a negative membrane potential. Opening of voltage-gated Kv1.3 and inward-rectifying K^+ (IK1) channels maintains the sustained $_c[Ca^{2+}]$ increases (Conforti, 2017).

Cl^- currents have also been investigated in T-cells, working in line with Kv1.3 currents to regulate cellular volume through anion and osmolyte influx and efflux (Cahalan & Lewis, 1988). Further studies on Cl^- channels in T-cells are lacking.

Ion pumps, such as PM Ca^{2+} ATPases (PMCA) (Calì et al., 2017) and sarcoplasmic/ER Ca^{2+} ATPases (SERCA) (Chemaly et al., 2018), transport Ca^{2+} against the electrochemical gradient, thereby using ATP as an energy resource.

1.4.3 Transcription factor regulation

A key-step in T-cell activation is the induction of gene expression which orchestrates T-cell differentiation and function. The roles of nuclear factor of activated T-cells (NFAT) proteins have been recognised since the late 1980s when NFAT1 was coupled with activation of the IL-2 gene (Shaw et al., 1988). Five such NFAT proteins have been identified, NFAT1 through 5, and all except NFAT5 are Ca^{2+}-calcineurin-activated. Stimulation of the TCR without CD28 co-stimulation induces T-cell anergy through NFAT signalling, illustrating the importance of these transcription factors. All NFAT proteins have a highly conserved DNA-binding sequence important for their function (Macian, 2005).

Increased levels of $_c[Ca^{2+}]$ cause Ca^{2+} binding to calmodulin, which activates calcineurin (a calmodulin-dependent phosphatase). Calcineurin binds to the N-terminus of NFATs and dephosphorylates them, which leads to their nuclear translocation and induction of gene transcription. Kinases, including JUN N-terminal kinase (JNK) and glycogen-synthase kinase 3 (GSK3), can phosphorylate NFATs and thus control their nuclear import. Studies have also shown that NFAT activity can be mediated via cytokine receptor signalling (e.g. IL-2, IL-15 and IL-6) (Barlic et al., 2004; Macian, 2005).

NFAT proteins can interact with other transcription factors in the nuclei, including activator protein 1 (AP1). NFAT-AP1 interplay integrates two important signalling pathways induced during T-cells activation: Ca^{2+} signalling and Ras/MAPK signalling (crucial for functional differentiation and determination of T-cell function) (Macián et al., 2001). Other NFAT cofactors include myocyte enhancer factor-2 (MEF), members of the GATA transcription factor family and signal transducer and activator of transcription (STAT) factors (Quintana et al., 2005).

NFAT proteins have crucial roles in T-cell development (specifically the transition of double-negative thymocytes to single-positive T-cells), in $CD4^+$ T-cell differentiation to Th1 or Th2 lineages (via STAT proteins), in T-cell activation through the regulation of IL-2, in regulation of cell cycle through downregulation of cyclin-dependent kinase 4, and in T-cell anergy (as shortly mentioned previously) (Macian, 2005).

Nuclear factor κB (NFκB) proteins are a family of inducible transcription factors crucial for pathways involved in immune and inflammatory responses. NFκB factors translocate to the nucleus upon increase in $_c[Ca^{2+}]$ and dissociation with the inhibitory IκB proteins. Canonical NF-κB family members have a central role in mediating TCR signaling and T-cell differentiation (T. Liu et al., 2017). Aberrant NFκB activity has been associated with impaired T-cell proliferation, activation and cytokine secretion (Barnabei et al., 2021; Quintana et al., 2005).

1.4.4 Experimental measurements of cytosolic Ca^{2+} dynamics

Considering the great importance of Ca^{2+} in T-cells, as outlined in the previous chapters, it is relevant to precisely quantify $_c[Ca^{2+}]$, on *in vitro*, *in vivo*, and *ex vivo* levels.

Some of the first $_c[Ca^{2+}]$ measurements were carried out in murine thymocytes by using the fluorescent dye Quin2 (excited at ~340 nm) (Tsien et al., 1982). The same dye was also used later in Jurkat T-cells to assess antibody stimulation (Weiss et al., 1984). However, not long after the establishment of these measurements did dyes such as Fura2 replace non-ratiometric readouts. Fura2 (excitation peaks at 340 and 380 nm) is the most commonly used dye for T-cell measurements characterised by a higher affinity for Ca^{2+} and a better selectivity against other ions, as well as its ability to provide more precise ratiometric quantifications of $_c[Ca^{2+}]$. Indo1 is another dye often used for the same purpose, characterised by its ratiometric emission (~475 nm in Ca^{2+}-free solution to ~430 nm upon Ca^{2+} saturation). Many other $_cCa^{2+}$ indicators have been developed throughout the years (some are mentioned in Table 2) and can be classified based on whether they are ratiometric or not, their excitation-emission spectra, their chemical form (salt or ester conjugates) and their Ca^{2+}-binding affinity (reflected by the dissociation constant-K_d) (Takahashi et al., 1999).

Table 2. List of commonly known fluorescent $_cCa^{2+}$ indicators (information taken from Takahashi et al. (1999) and thermofisher.com).

Name of dye	Readout	Exc/Emi (Ca^{2+}-free)	Exc/Emi (+ Ca^{2+})	Ca^{2+} K_d
Fura2-AM	Change in ratiometric excitation	363/512 nm	335/505 nm	224 nM
Fura Red-AM	Change in ratiometric excitation	472/657 nm	436/637	140 nM
Indo1-AM	Change in ratiometric emission	346/475 nm	330/401 nm	230 nM
Quin2	Fluorescence intensity increase upon binding Ca^{2+}	353/495 nm	333/495 nm	60 nM
Oregon Green 488 BAPTA-1	14-fold fluorescence intensity increase upon binding Ca^{2+}	494/523 nm	494/523 nm	170 nM
Oregon Green 488 BAPTA-6F	14-fold fluorescence intensity increase upon binding Ca^{2+}	494/523 nm	494/523 nm	580 nM
Oregon Green 488 BAPTA-5N	14-fold fluorescence intensity increase upon binding Ca^{2+}	492/517 nm	492/517 nm	20 µM
Fluo3	Fluorescence intensity increases upon binding Ca^{2+}	503/526 nm	506/526 nm	335 nM
Fluo4-AM	>100-fold in fluorescence intensity increase upon binding Ca^{2+}	494/- nm	494/506 nm	345 nM
Fluo5F-AM	>100-fold in fluorescence intensity increase upon binding Ca^{2+}	494/- nm	494/516 nm	2.3 µM
Fluo4FF-AM	>100-fold in fluorescence intensity increase upon binding Ca^{2+}	494/- nm	494/516 nm	9.7 µM
X-Rhod1-AM	Large fluorescence intensity increases upon binding Ca^{2+}	576/- nm	580/602 nm	700 nM
X-Rhod5F-AM	Large fluorescence intensity increases upon binding Ca^{2+}	576/- nm	580/603 nm	350 µM
Calcium green-1	14-fold fluorescence intensity increase upon binding Ca^{2+}	506/531 nm	506/531 nm	190 nM
Calcium green-5N	14-fold fluorescence intensity increase upon binding Ca^{2+}	506/532 nm	506/532 nm	14 µM
Calcium orange	14-fold fluorescence intensity increase upon binding Ca^{2+}	549/575 nm	549/575 nm	185 nM
Calcium orange-5N	14-fold fluorescence intensity increase upon binding Ca^{2+}	549/582 nm	549/582 nm	20µM
Calcium crimson	14-fold fluorescence intensity increase upon binding Ca^{2+}	590/615 nm	590/615 nm	185 nM

Many studies have analysed intracellular Ca^{2+} using fluorescent indicators in primary murine T-cells stimulated through an immunological synapse. One way of stimulating these cells is by activating the TCR with antibodies (anti-CD3+CD28) or with antibody-coated beads. A more physiological way is to use APCs; however, this method is quite challenging. Studies have reported immediate rises in $_c[Ca^{2+}]$ upon stimulation by using Fura2-loaded cells. These could be mimicked by "artificial" stimulation with thapsigargin (SERCA inhibitor, leading to the emptying of ER Ca^{2+} stores) (Kim et al., 2018). Few such measurements of this kind have been performed in primary human T-cells; nevertheless, antibody-coated bead stimulation has led to high intracellular Ca^{2+} increases. One study determined a resting T-cell $_c[Ca^{2+}]$ of 50 nM that increased to 150-300 nM, which was sufficient to initiate cell proliferation (Zitt et al., 2004). Another study also showed that different subtypes of $CD4^+$ T-cells had variable $_c[Ca^{2+}]$, directly linking the importance of Ca^{2+} to T-cell phenotype generation (Kircher et al., 2018).

Although fluorescent dyes have been extremely useful and fairly easy to utilise and detect Ca^{2+} fluctuations, they are limited by their retention in the cell and the use of an optimal cell-to-dye ratio which can affect the final intensity. In addition, some dyes are toxic and thus, cannot be used for long-term measurements. Photobleaching is also quite common, as well as the pH-sensitivity of some of the dyes. Finally, using these dyes for *in vivo* Ca^{2+} monitoring is technically very challenging (Jensen, 2012; Whitaker, 2010).

To overcome these limitations, genetically-encoded Ca^{2+} indicators (GECIs) have been developed which can be expressed inside the cell via transfection or transduction. The first such indicator was developed in 1997 by Tsien and Persecchini (Persechini et al., 1997) and was based on a link between green fluorescent protein (GFP, originally found in the jellyfish *Aequoria victoria*) and a recombinant calcium binding domain. This led to the rapid development of a family of GFP-based sensors (also called cameleons). Different colored variants with altered excitation and emission spectra were also developed, such as cyan and yellow fluorescent proteins (CFP and YFP). GECIs can be divided into two big groups: Förster resonance energy transfer (FRET)-based and single fluorescent protein (FP)-based sensors.

FRET-based sensors rely on the overlapping emission and excitation spectra of two closely-located fluorophores and the transfer of energy between them. The transfer of energy leads to a reduction in the fluorescence intensity of a donor fluorophore (e.g. CFP), and an increase in the emission intensity of an acceptor fluorophore (e.g. YFP) (Jares-Erijman & Jovin, 2003). In the case of Ca^{2+} FRET-based GECIs, the binding of calmodulin to the sensor decreases the distance between both FPs, thereby increasing the FRET signal. These sensors

are ratiometric and less susceptible to imaging artefacts caused by bleaching or sensor expression differences in various cell compartments (Zhang et al., 2021).

Single FP-based sensors usually consist of one fluorescent protein fused to a Ca^{2+}-sensing calmodulin domain and the calmodulin-binding M13 peptide and are able to exhibit increases in fluorescence intensity upon binding to Ca^{2+}. Such sensors include, for example, pericams (YFP-based) (Nagai et al., 2001) and GCaMPs (GFP-based) (Nakai et al., 2001).

Not so many studies have reported using GECIs to measure Ca^{2+} dynamics in human T-cells, most probably due to technical limitations related to sensor expression. The CFP-YFP-FRET cameleon has been used to investigate physiologically-relevant changes in $_{c}[Ca^{2+}]$ in murine T-cells by using retroviral transduction of the sensor (Borgne et al., 2016). The expression of the sensor did not affect cell proliferation or development. *In vivo* T-cell activation in mice has been measured using the FRET-based Twitch sensor (Thestrup et al., 2014), and in rats using GFP, YFP and Cherry-based sensors, via two-photon microscopy (Lodygin et al., 2019; Lodygin & Flügel, 2017). A transgenic mouse model expressing the CFP-YFP-FRET cameleon has also been generated and used for Ca^{2+} flux investigations (Borgne et al., 2016). A model of experimental autoimmune encephalomyelitis (EAE) has been vastly used to analyse T-cells *in vivo* in the context of the nervous system. EAE is the most commonly used model for multiple sclerosis (MS), an inflammatory demyelinating disease of the central nervous system (Constantinescu et al., 2011) affecting up to 2.8 million people worldwide and up to 252,000 in Germany alone (according to the 2020 statistics in the Atlas of MS, 3rd edition). Autoreactive T-cells are key players in this complex disease. Two-photon microscopy, as the name suggests, is based on two-photon excitation of fluorescent molecules – a process related to the simultaneous absorption of two photons whose combined energy is sufficient to produce a transition to an excited electronic state (Diaspro et al., 2006), therefore thick samples and isolated cells in *in vivo* samples can be easily imaged.

The main advantage of GECIs is that they can be targeted to specific cellular compartments, not only the cytosol. $_{c}Ca^{2+}$ release from CRAC channels and ER stores was vastly examined and many methods to study this have been established in T-cells. However, the fluctuations of $[Ca^{2+}]$ coming from different cellular compartments are also important and need careful investigation.

1.5 Mitochondria

Mitochondria are found in almost all eukaryotic cells and have crucial roles in multiple aspects of cellular life, the most important being energy production. According to the endosymbiotic theory, initially proposed by the botanist Konstantin Mereschkowski in 1905, then further supported by Lynn Mergulis in his book *Origin of Eukaryotic Cells* published in the 1970s, mitochondria evolved from bacteria via symbiosis within a eukaryotic host cell (Chinnery & Hudson, 2013; Gray, 2012; Mergulis, 1970). This theory was also supported by the discovery of mitochondrial DNA (containing 37 genes: 11 messenger RNAs translated to 13 proteins, 2 ribosomal RNAs, and 22 transfer RNAs) and the independent mitochondrial protein translation system (Chinnery & Hudson, 2013). Mitochondria have been linked to many pathologies, including cancer, aging, cardiovascular diseases, neurodegenerative diseases, myopathies, as well as immune system-related pathologies (Nunnari & Suomalainen, 2012). In addition, mitochondrial DNA is particularly susceptible to damage and has a mutation rate 10-20 times higher than that of nuclear DNA. Mutations are maternally inherited and clinical manifestations can be highly variable, occur in childhood or adulthood, and affect one or multiple organs. Classic syndromes associated with mitochondrial DNA mutations include ophthalmoplegia, Pearson syndrome, Leigh syndrome and rhabdomyolysis (Lax et al., 2011; Taylor & Turnbull, 2005).

1.5.1 Mitochondrial structure and dynamics

Mitochondria are bound by two phospholipid membranes: the outer mitochondrial membrane (OMM) and the inner mitochondrial membrane (IMM). The two membranes divide mitochondria into two distinct sub-compartments: the mitochondrial matrix and the intermembrane space (IMS) (Figure 4) (Kühlbrandt, 2015). The OMM is structurally similar to other eukaryotic cell membranes, whereas the IMM is more similar to bacterial membranes, characterised by a higher protein-to-lipid ratio. The IMM forms highly dense invaginations in the mitochondrial matrix, called cristae, where the oxidative phosphorylation machinery is located to allow for efficient energy production (Protasoni & Zeviani, 2021). Maintenance of cristae structure and dynamics requires the help of several proteins, including the mitochondrial contact site and cristae organizing system (MICOS) and the fusion protein Optic atrophy type 1 (OPA1) (Cogliati et al., 2016). The OMM and IMM also differ in their permeability. The OMM allows the passage of ions and small molecules through voltage-dependent anion channels (VDACs), whereas only H_2O, O_2 and CO_2 can pass freely through the IMM. This

selectivity allows for the formation of the electrochemical gradient necessary for ATP production and Ca^{2+} signalling regulation (Protasoni & Zeviani, 2021).

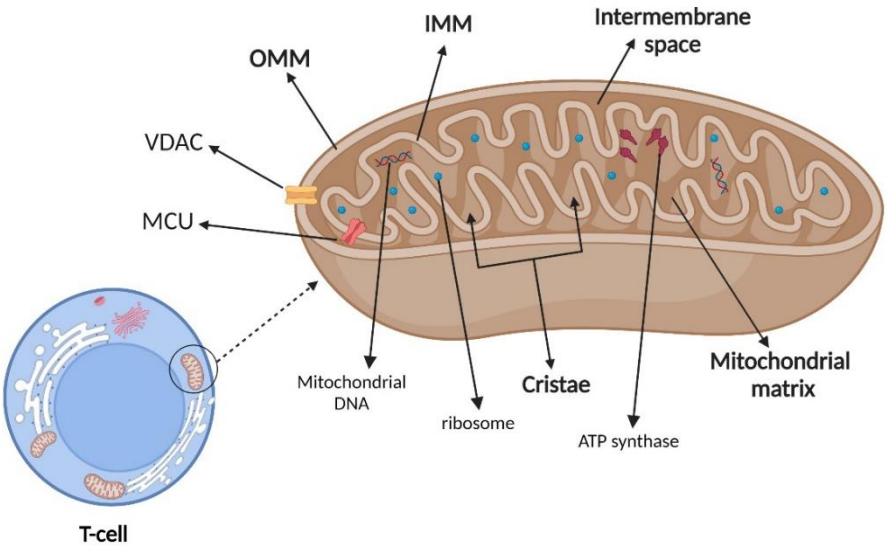

Figure 4. Mitochondrial structure. Mitochondria have a double membrane which separates the organelle into four distinct compartments - the outer mitochondrial membrane (OMM), the intermembrane space, the inner mitochondrial membrane (IMM), and the matrix. Image created in BioRender.

Mitochondria are dynamic organelles; they undergo fusion and fission events in order to maintain a specific morphology network based on the energy requirements of the cell. Mitochondrial fusion allows for cell sharing of metabolites, proteins and mitochondrial DNA, which promotes cell survival. Mitochondrial dynamics are usually controlled by guanosine triphosphatases (GTPases) (Tilokani et al., 2018). Mitochondrial motility within the cell is also important, especially during cell division, governed by myosins, kinesins and dyneins (Protasoni & Zeviani, 2021).

1.5.2 Mitochondrial function in energy production and oxidative phosphorylation

The main cellular energy source derives from the dephosphorylation of adenosine triphosphate (ATP) to adenosine diphosphate (ADP). ATP is generated via two pathways: anaerobic glycolysis taking place in the cytosol, which produces two molecules of ATP, and the aerobic tricarboxylic acid cycle (TCA; also known as Krebs cycle) taking place in mitochondria, which produces 34 molecules of ATP from a single molecule of glucose (Bartolák-Suki et al., 2017). The TCA cycle, illustrated in Figure 5, consists of nine enzymatic reactions occurring throughout the electron transport chain (ETC).

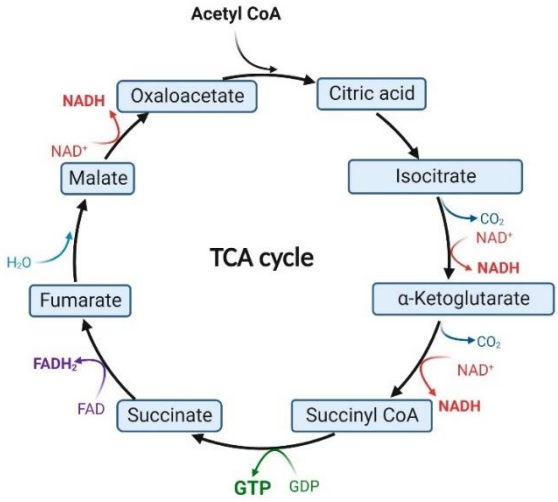

Figure 5. The tricarboxylic acid (TCA) cycle. The TCA cycle is the main source of ATP in the cell. Initially, acetyl CoA associates with oxaloacetate to form citric acid which is further converted to isocitrate. Isocitrate is then oxidised to α-ketoglutarate (via isocitrate dehydrogenase), leading to the release of CO_2 and NADH. α-ketoglutarate is further oxidised to succinyl CoA, releasing a second molecule of both CO_2 and NADH. Conversion of succinyl CoA to succinate produces one molecule of GTP. Succinate is later converted into fumarate, producing one molecule of $FADH_2$. Fumarate is then converted into malate, which in the final step is converted to oxaloacetate and the final molecule of NADH is produced. Each glucose molecule produces two molecules of pyruvate which in turn produce two molecules of acetyl CoA (Eniafe & Jiang, 2021). Image created in BioRender.

The ETC is a collection of proteins bound to the IMM, consisting of complex I, complex II, coenzyme-Q, complex III, cytochrome c, complex IV, and complex V (Figure 6).

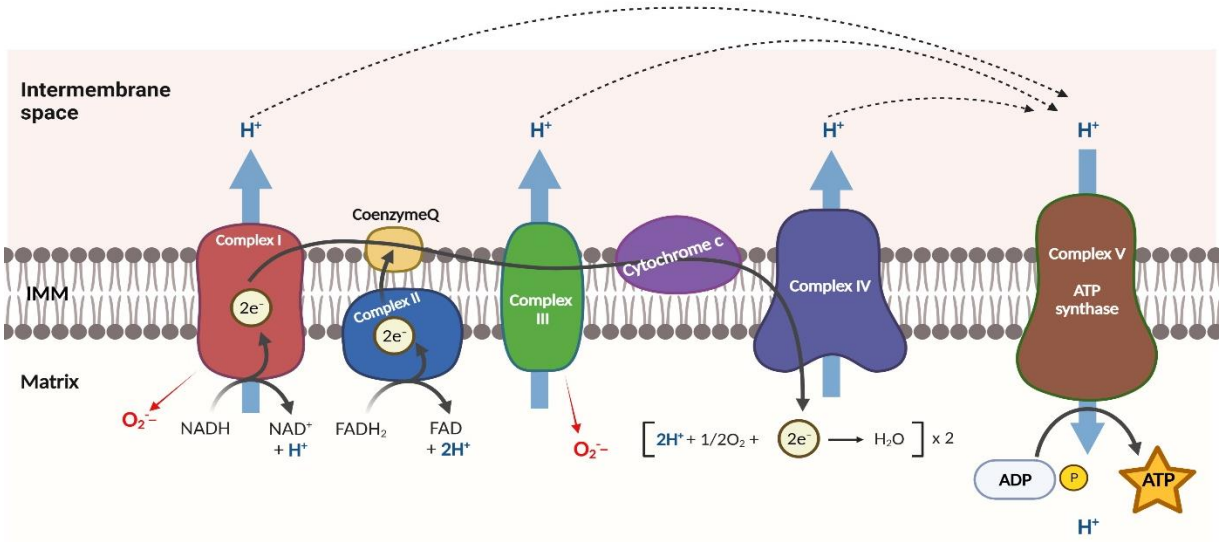

Figure 6. The electron transport chain. Electrons are transported through the ETC through five large complexes. Complex I utilises the electron carrier NADH coming from the TCA cycle. It pumps protons into the intermembrane space and transfers energetic electrons to coenzyme Q which transfers them to Complex III. Complex II uses the electron carrier $FADH_2$ and provides more electrons to coenzyme Q. Complex III pumps protons to the intermembrane space and delivers electrons to cytochrome-C. Complex IV performs the final delivery of electrons to O_2 in the mitochondrial matrix, forming H_2O. Complex V uses the generated proton gradient to form ATP. Image created in BioRender.

Complex I, known as ubiquinone oxidoreductase, consists of NADH dehydrogenase, flavin mononucleotide (FMN), and eight iron-sulphur (Fe-S) clusters. Two electrons are transferred from NADH (coming from glycolysis) to FMN (oxidizing it to NAD^+), then to Fe-S clusters, and finally from Fe-S clusters to coenzyme-Q. Throughout this process, four H^+ ions pass from the mitochondrial matrix to the intermembrane space, contributing to the electrochemical gradient (Ahmad et al., 2022).

Complex II, or succinate dehydrogenase, is the second entry point which accepts electrons from succinate. When succinate oxidizes to fumarate, two electrons are accepted by flavin adenine dinucleotide (FAD) found within complex II, which passes them to Fe-S clusters and then to coenzyme-Q (Ahmad et al., 2022).

Complex III, or cytochrome c reductase, consists of cytochrome b, Rieske subunits (with two Fe-S clusters), and cytochrome c proteins. The oxidation states of the heme groups contained within the cytochrome proteins are important for electron transfer, which occurs in two steps. In step one, oxidized coenzyme-Q (also known as ubiquinone) and reduced coenzyme-Q (known as ubiquinol) bind to separate sites on Complex III and transfer electrons: one to cytochrome c, and one to cytochrome b and then to coenzyme-Q bound on the other side. This process releases two H^+ in the intermembrane space. Ubiquinol is now oxidized to ubiquinone and dissociates from the complex. In the second step, ubiquinol transfers other two electrons, and this time one is used to produce another molecule of ubiquinol which can be recycled and used for another cycle. This process releases two additional H^+. Cytochrome c then transfers the accepted electrons to Complex IV (Ahmad et al., 2022).

Complex IV is known as cytochrome c oxidase and has a role in cytochrome c oxidation and electrons transfer to O_2, forming H_2O. The free energy from the electron transfer causes four H^+ to pass into the intermembrane space, contributing to the proton gradient (Ahmad et al., 2022).

Complex V, or ATP synthase, uses the generated proton gradient to form ATP molecules. It consists of F0 and F1 subunits which act as a rotational motor system. Conformational changes in F1 subunits catalyse the formation of ATP from ADP and phosphate ions. For every four H^+, one ATP molecule is produced (Ahmad et al., 2022).

1.5.3 Mitochondrial function in reactive oxygen species generation

Reactive oxygen species (ROS) are highly-reactive products of O_2 and comprise free and non-free radical oxygen intermediates, such as superoxide radicals ($O_2^{-\bullet}$), hydrogen peroxide (H_2O_2), hydroxyl radicals ($OH^\bullet$), and singlet oxygen ($^1O_2$). Although initially

considered toxic by-products promoting disease and cell death, it is now generally accepted that ROS molecules are important signalling messengers regulating cell proliferation, differentiation and inflammation. Indeed, an imbalance of ROS levels can lead to oxidative stress and irreversible cell damage through the oxidation of DNA, lipid peroxidation, or protein modifications. Oxidative stress can generate proinflammatory molecules which play a role in major diseases, including, but not limited to, autoimmune-, neurodegenerative, respiratory and vascular diseases (Checa & Aran, 2020; Pizzino et al., 2017; Sies, 2015).

Mitochondria are considered a major source of ROS due to oxidative phosphorylation. Even though most of the O_2 gets reduced to H_2O at Complex IV, partial reduction accompanied by ROS generation can also occur (Lambert & Brand, 2009). The most commonly produced ROS molecule is $O_2^{-\bullet}$, which is converted by mitochondrial superoxide dismutase (SOD; a metalloenzyme) into H_2O_2 via the Fenton reaction (Murphy, 2009):

$$Fe^{2+} + H_2O_2 \rightarrow Fe^{3+} + \bullet OH + OH^-$$
$$Fe^{3+} + H_2O_2 \rightarrow Fe^{2+} + HOO\bullet + H^+$$
$$2H_2O_2 \rightarrow \bullet OH + HOO\bullet + H_2O$$

Mitochondrial ROS production is tightly coupled with Ca^{2+} signalling. Other endogenous sources of ROS include membrane-bound NADPH oxidases (NOX and DUOX) which transfer electrons from NADPH to O_2 to produce $O_2^{-\bullet}$, and metabolic enzymes such as monoamine oxidases, cytochrome b5 reductases and glycerol-3-phosphate dehydrogenases. Cell organelles including peroxisomes and the ER can also contribute to cellular ROS levels (Checa & Aran, 2020). Some of the main exogenous sources of ROS include cigarette smoke, traffic exhausts and industrial pollution, solar radiation, nutrition and radiotherapy. These are almost always associated with disease (Samet & Wages, 2018).

It has been shown that upon TCR stimulation, T-cells produce high amounts of ROS which play a role in T-cell regulation (Siemoni & Bogeski, 2015). Mitochondrial ROS production is delayed compared to NOX-mediated ROS production (peaks 1–2 hrs after T-cell activation) (Kamiński et al., 2012). Studies have shown that ROS molecules affect IL-2, IL-6 and IL-4 production, as well as activation of NF-κB and AP-1.

1.5.4 Mitochondrial function in calcium homeostasis

The observation that mitochondria can take up Ca^{2+} dates back to the 1960s when Selwyn et al. measured mitochondrial Ca^{2+} uptake in isolated mitochondria from rat liver cells (Selwyn et al., 1970). Since then, theories about mitochondrial Ca^{2+} influx and efflux have

been called into question, and the mechanisms involved in the regulation of mitochondrial Ca^{2+} homeostasis have been characterised only throughout the past 12 years.

Upon SOCE activation and cytosolic [Ca^{2+}] increase, mitochondria are able to sequester and release Ca^{2+} ions, buffering the cellular concentration. Ca^{2+} traverses the OMM via VDAC, characterised by its high conductance, and the IMM via the mitochondrial calcium uniporter (MCU) channel into the matrix. In the mitochondrial matrix, Ca^{2+} regulates various enzymes involved in the ETC, modulates mitochondrial metabolism and respiration, and induces the mitochondrial permeability transition pore (mPTP) (Pozzan & Rizzuto, 2000). The accumulation of mitochondrial Ca^{2+} ($_mCa^{2+}$) stimulates ATP production by modulating the activity of ketoglutarate dehydrogenase, isocitrate dehydrogenase and pyruvate dehydrogenase. Mitochondrial ROS production also increases, hence the cooperation and homeostasis between $_mCa^{2+}$ and ROS are important for proper cellular function and survival (Figure 7) (Zhou & Tian, 2018).

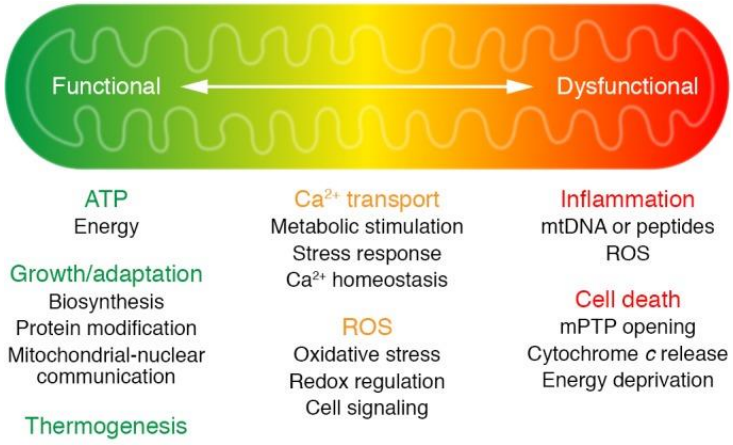

Figure 7. Mitochondrial function in homeostasis and oxidative stress. In normal conditions, mitochondria produce cellular energy in the form of ATP and allow for protein biosynthesis, modifications and thermogenesis. Moderate ROS increase is important for metabolic stimulation, cell signalling and Ca^{2+} homeostasis; however, under pathological conditions and high oxidative stress, Ca^{2+} and ROS overload lead to mPTP opening, energy deprivation and cell death. Image taken from Zhou & Tian, 2018.

1.5.5 Experimental measurements of mitochondrial Ca^{2+} dynamics

The very first measurements of $_m[Ca^{2+}]$ have been performed in the 1960s in isolated mitochondria (Pozzan & Rudolf, 2009). Since then, several methods for measuring $_m[Ca^{2+}]$ have been developed using a principle similar to $_cCa^{2+}$ detection.

A frequently used chemical probe for $_m[Ca^{2+}]$ measurements, both *in vitro* and *in vivo*, is Rhod2 (K_d for Ca^{2+}=570 nM). Rhod-2 is mainly used in its cell-permeant acetoxymethyl (AM) ester form. The positive charge of the dye allows its accumulation within the

mitochondrial matrix, where it is hydrolysed and trapped. In comparison to other Ca^{2+} sensors, upon increased [Ca^{2+}], Rhod-2 increases its fluorescence emission (intensiometric) which is a disadvantage. Another issue is the uneven distribution of the dye within mitochondria, and often in other organelles, which could lead to over- or under-estimation of the Ca^{2+} levels. Finally, the potential toxicity of this dye has not been thoroughly assessed (Kosmach et al., 2021; Pozzan & Rudolf, 2009).

GECIs specifically designed to target mitochondria have been commonly used in recent years. The concept of mitochondrial GECIs is similar to cytosolic GECIs explained in section 1.4.4. FRET-based cameleons and pericams are the most commonly used probes, designed to contain a mitochondrial-targeting sequence derived from human cytochrome c oxidase subunit VIII or cytochrome c oxidase subunit IV. Ca^{2+} affinity is an important parameter for mitochondrial GECIs because $_{m}[Ca^{2+}]$ can reach up to 100 µM, therefore low-Ca^{2+} affinity GECIs have been generated by modifying their Ca^{2+}-responsive elements. pH sensitivity is another important parameter that needs to be considered since abrupt pH changes in mitochondria are common. Both IMM and OMM-targeted GECIs exist (Table 3) (Suzuki et al., 2016; Li et al., 2020).

In vivo genetically-altered mouse models expressing mitochondrial GECIs, such as 2mtYC2 (yellow cameleon) have also been used for monitoring $_{m}Ca^{2+}$ uptake in skeletal muscle cells (Rudolf et al., 2004).

Table 3. Mitochondria-targeted GECIs (information taken from Suzuki et al., 2016; Li et al., 2020).

Name	Type of sensor	Ca^{2+} K_d
YC2mt, YC2.1mt, YC3.1mt, YC4.1mt	FRET-based	1.24 µM
2mt8YC2	FRET-based	1.24 µM
2mtD1cpv	FRET-based	-
2mtD2cpv	FRET-based	7.67 µM
2mtD3cpv	FRET-based	760 nM
2mtD4cpv	FRET-based	49.7 µM
4mtD1cpv	FRET-based	-
4mtD3cpv	FRET-based	760 nM
GCaMP2-mt	Intensiometric	124 nM
mito-GCaMP6s	Intensiometric	144 nM
mito-R-GECO1	Intensiometric	482 nM
Ratiometric-Pericam-mt	Ratiometric	1.7 µM
N33D1cpv	FRET-based	-
OMM-pcm-ER	Ratiometric	460 nM
mt-riG6m	Ratiometric	245 nM
Cepia2mt	Intensiometric	160 nM

1.6 Mitochondrial Calcium Uniporter complex

The first identification of proteins responsible for $_{m}Ca^{2+}$ uptake came through *in silico* screening techniques applied on the MitoCarta Database – a database of 1,136 human and 1,140 mouse genes which encode for proteins with a mitochondrial localisation. Through this screening, the first protein associated with $_{m}Ca^{2+}$ uptake, Mitochondrial Calcium Uptake 1-Micu1, was discovered (Perocci et al., 2010). The following year, the Mitochondrial Calcium Uniporter (MCU) was identified by De Stefani et al. (2011) and Baughman et al. (2011) using the same database. Tissue expression profiling showed the ubiquitous presence of MCU in various tissues, including from the heart, skeletal muscle, kidneys, brain, spleen and liver. Silencing MCU in HeLa cells showed strong inhibition of $_{m}Ca^{2+}$ uptake in isolated mitochondria, whereas MCU overexpression led to increased uptake (De Stefani et al., 2011). The structure of the MCU macrocomplex is outlined in Figure 8.

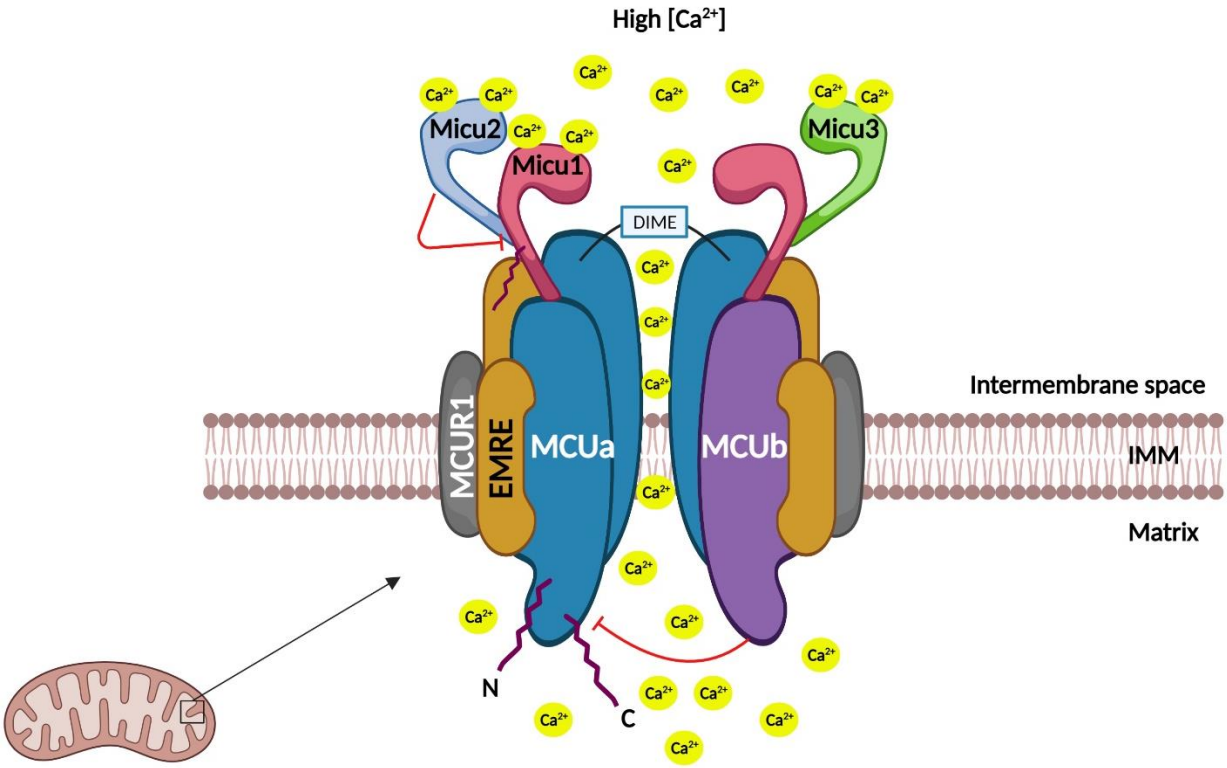

Figure 8. The MCU macrocomplex. Upon high [Ca^{2+}] increases in the intermembrane space, the MCU complex opens the pore up to allow flow of Ca^{2+} ions in the matrix. The 450 kD macrocomplex consists of the pore-forming units MCUa and MCUb, gate-keeping units Micu1 and Micu2 (also Micu3 which is specific for brain tissues), essential MCU regulator (EMRE), and MCU regulator 1 (MCUR1). Image created in Biorender.

1.6.1 MCUa

The *MCUa* gene (original name *CCDC109a*) is well-conserved among all organisms except yeasts. MCUa (also known as simply MCU; a ~35 kD-protein) consists of two coiled-coil domains and two transmembrane domains (TM1 and TM2) separated by a loop exposed to the intermembrane space. This loop contains the highly-conserved "DIME-motif" characterised by its negatively-charged amino acids which are required for Ca^{2+} uptake. The N- and C-termini face the mitochondrial matrix (De Stefani et al., 2011). MCUa is arranged as a tetrameric oligomer, forming a narrow, electronegative, Ca^{2+}-sensitive channel (Feno et al., 2021). It has been shown that MCUa oligomerisation depends on S-glutathionylation of cysteine 97 in conditions of oxidative stress (O-Uchi et al., 2014).

1.6.2 MCUb

MCUb is another part of the pore-forming unit of the MCU complex, sharing 50% homology with MCUa. Its structure is similar to the one of MCUa, with a crucial amino acid substitution in the loop region (E256V) which highly decreases the conductivity of the channel (Raffaello et al., 2013). Accordingly, MCUb is a negative regulator of MCUa, leading to a decreased $_{m}Ca^{2+}$ uptake when over-expressed in cell types (Feno et al., 2021). Indeed, studies have shown that tissues with low $_{m}Ca^{2+}$ transients, such as the heart, have a higher MCUb/MCUa ratio, compared to tissues which require fast $_{m}Ca^{2+}$ transients, such as skeletal muscle (Fieni et al., 2012).

1.6.3 EMRE

The Essential MCU Regulator (EMRE) is a 10 kD-protein located in the IMM. It consists of a transmembrane domain, a highly-conserved C-terminus involved in the interaction with Micu1 and Micu2, and a short N-terminus. It has been suggested that EMRE modulates the interaction between the pore-forming unit (MCUa+MCUb) and the regulatory Micu units. Furthermore, it is needed to form a functional MCU channel (Sancak et al., 2013). Isolated mitochondria from $EMRE^{-/-}$ KO mice showed no $_{m}Ca^{2+}$ uptake (Liu et al., 2020).

1.6.4 Micu1

Mitochondrial Calcium Uptake protein 1 (Micu1) was the first identified component of the MCU complex, as mentioned previously (Feno et al., 2021). Micu1 is a regulatory subunit, that functions as one of the "gate-keepers" of the MCU pore. The *Micu1* gene is highly-conserved among species, except in fungi, and codes for a 54 kD-protein consisting of an N-

terminal mitochondrial targeting sequence and two classical EF-hand Ca^{2+} binding domains. Micu1 keeps the MCU channel closed when $_{c}[Ca^{2+}]$ levels are below a certain threshold (<500 nM), and opens the channel up when those levels increase (Csordias et al., 2013). Most $Micu1^{-/-}$ KO mice die prenatally, and the ones which survive are severely affected by ataxia. Micu1 is a frequent target of post-translational modifications, especially phosphorylation which can affect $_{m}Ca^{2+}$ uptake and ROS production (Marchi et al., 2019; Petrungaro et al., 2015).

1.6.5. Micu2

Mitochondrial Calcium Uptake protein 2 (Micu2) is a paralog of Micu1 and shares 42% similarity with it. Furthermore, it has a similar tissue expression pattern to Micu1. Sequence alignment of Micu1 and Micu2 showed that the N-terminus of Micu2 is drastically different when compared with Micu1, probably affecting the 3-dimensional structure of the protein and its functional role in regulating $_{m}Ca^{2+}$ uptake (Xing et al., 2019). Although different models have been proposed, Micu2 acts as a proper "gate-keeper", negatively regulating the function of Micu1 and preventing Ca^{2+} overload by increasing the $_{c}[Ca^{2+}]$ threshold. Micu1 and Micu2 can form heterodimers, stabilised by a disulphide bond between two conserved cysteine residues. These heterodimers interact with MCU in a Ca^{2+}-dependent manner. Increasing $_{c}[Ca^{2+}]$ induces a conformational change in the heterodimer and its release from MCU. The stoichiometry of Micu1/Micu2 and MCU has been shown to control tissue-specific $_{m}Ca^{2+}$ transients. Absence of Micu1 causes destabilisation of Micu2 (Park et al., 2020).

1.6.6. Micu3

Mitochondrial Calcium Uptake protein 3 (Micu3) is another paralogue of Micu1; a 55 kD-protein that shares 34% and 47% similarity to Micu1 and Micu2 respectively. Micu3 is a brain-specific protein. Studies have shown that Micu3 can form heterodimers with Micu1 and act as a stimulator of MCU activity, with no obvious "gate-keeping" function. Silencing Micu3 significantly decreases Ca^{2+} signalling and synaptic activity in neurons (Patron et al., 2019).

1.6.7. MCUR1

Mitochondrial Calcium Uniporter Regulator 1 (MCUR1) was identified in 2012 as an integral membrane protein required for MCU-dependent $_{m}Ca^{2+}$ uptake in HEK293T cells. In the absence of MCUR1, $_{m}Ca^{2+}$ uptake is significantly blunted (Mallilankaraman et al., 2012). In addition, it was shown that MCUR1 also plays a crucial role in Complex V assembly and its downregulation decreases the mitochondrial membrane potential (Paupe et al., 2015). Therefore, whether MCUR1 has a direct or more indirect modulation of MCU activity is under debate.

1.7 Experimental *in vivo* models of the MCU complex

1.7.1 MCUa

The crucial role of MCU in $_{m}Ca^{2+}$ uptake has been supported by many animal models in which MCU was disrupted or knocked out. The first total-MCU KO mouse model was designed in 2013 by Pan et al. They showed that isolated mitochondria from several cell types ablated $_{m}Ca^{2+}$ uptake; however, the mice were developing normally, and there were only minor alterations in mitochondrial bioenergetics. In addition, they hypothesised that *in vivo* effects of changed $_{m}Ca^{2+}$ uptake are probably more relevant under stress conditions (for example after treadmill running) (Pan et al., 2013).

In a follow-up study from 2015, a mouse model of myocardial-targeted transgenic dominant-negative MCU expression was developed by Rasmussen and colleagues. The study showed that inhibition of MCU in the heart increased $_{c}[Ca^{2+}]$, consistent with a loss of mitochondrial buffering capacity. However, total ATP production was reduced, whereas mitochondrial respiration was increased in these mice, giving inconclusive results and pointing to the probability that other mechanisms are involved in this pathway and further models are needed to study MCU function in more detail (Rasmussen et al., 2015).

Mammucari et al. have also reported an MCU knockdown model in mouse skeletal muscle (Mammucari et al., 2015), generated by using viral transduction and *in vivo* electroporation in living animals, thereby bypassing embryonic development. The results from this study showed that MCU-dependent $_{m}Ca^{2+}$ uptake is important for skeletal muscle since MCU ablation showed an increase in muscle atrophy, probably by affecting Pparg coactivator 1α4 (PGC-1α4) and insulin-like growth factor 1 (IGF1)-PI3K-Akt signalling. Nevertheless, full deletion of *MCU* in mouse skeletal muscle affected neither muscle size, nor Akt signalling (Kwong et al., 2018).

Inducible MCU mouse models with targeted *MCU* deletion in cardiomyocytes, skeletal muscle and adipose tissue were also published, in order to check if those tissues could show more pronounced effects upon MCU ablation. In a cardiomyocyte mouse model developed by Kwong et al., *MCU* deletion was induced in 8-week-old $Mcu^{fl/fl}$ x αMHC-MCM adult mice by administrating tamoxifen. MCU protein expression was reduced up to 80%. $_{m}[Ca^{2+}]$ was measured in permeabilised isolated cardiomyocytes with the mitochondrial-targeted dye Rhod2, and uptake was significantly blunted upon external addition of Ca^{2+}. Despite the Ca^{2+} changes, no effects were observed in cellular morphology and structure, mitochondrial

structure, or cardiac performance. These results showed that MCU is not essential for cardiomyocyte function (Kwong et al., 2015).

MCU silencing has been performed in a *Drosophila* model as well, both global and neuron-specific. MCU mutant flies were resistant to oxidative stress and had impaired memory when MCU was deleted during the pupal phase (Drago & Davis, 2016).

Taken together, the data from these models showed that MCU is required for rapid $_{m}Ca^{2+}$ uptake, probably most relevant in situations which require a high cell energetic demand rather than for basal function. Furthermore, additional $_{m}Ca^{2+}$ entry routes probably exist, which can explain the discrepancies, as well as the lack of significant functional and bioenergetics phenotypes in the abovementioned models. It is also possible that adaptive mechanisms exist in models where *MCU* is constitutively deleted.

1.7.2 EMRE

The effects of EMRE deletion in a mouse model were examined recently by Liu and colleagues by using CRISPR Cas9 gene editing. Isolated mitochondria from several tissues were not able to take up Ca^{2+}, similarly to MCU KO mitochondria. There was no effect on the basal mitochondrial metabolism measured *in vivo* and *in vitro* in *EMRE*$^{-/-}$ KO mice. Furthermore, the mice did not have significant impairments at rest or during exercise. The absence of phenotypic changes upon EMRE KO again points to compensatory pathways for lack of $_{m}Ca^{2+}$ uptake (Liu et al., 2020).

1.7.3 Micu1

Multiple models and several genetic strategies have been used to investigate the role of Micu1 *in vivo*. Homozygous *Micu1* KO has been shown to be lethal because it interferes with brain stem function (Antony et al., 2016). Using CRISPR Cas9, some *Micu1*$^{-/-}$ pups survive but develop severe ataxia and loss of skeletal muscle strength. These animals also have reduced numbers of B-cells, indicating that Micu1 might also affect the immune system. *In vitro*, *Micu1*$^{-/-}$ fibroblasts have excessive $_{m}Ca^{2+}$ uptake and mPTP overload (Liu et al., 2016).

Micu1 deletion specifically in skeletal muscle results in muscle atrophy via a reduced $_{m}Ca^{2+}$ uptake during muscle contraction and diminished efficiency of repair after muscle fiber injury during exercise (Debattisti et al., 2019).

In an interesting study by Xue and colleagues, the role of Micu1 in reperfusion injury was investigated by siRNA delivery against *Micu1* via intramyocardial injections in mice. They showed that Micu1 knockdown (of up to 50%) significantly worsened reperfusion injury

evidenced by enlarged infarct size, reduced cardiac function and increased apoptosis. Furthermore, there was a significant $_{m}[Ca^{2+}]$ overload, decreased mitochondrial function and disrupted structure (Xue et al., 2017).

According to the aforementioned studies, Micu1 is functionally more important for baseline and "un-stressed" conditions, whereas MCU kicks in when the energy demand is significantly increased.

1.7.4 MCUb

Genetic mouse models investigating MCUb have mainly looked at cardiac function. It has been shown that MCUb expression is upregulated upon myocardial infarction or reperfusion injury, and generally upon hypoxia. A study by Huo et al. used mice with MCUb overexpression in cardiomyocytes and showed that overexpression did not change baseline cardiac function, but the heart was protected from mPTP opening and reperfusion injury. In the same study, they showed that cardiomyocytes with *MCUb*$^{-/-}$ did not have alterations in $_{m}Ca^{2+}$ uptake, respiration or cardiac functions (Huo et al., 2020).

1.8 The MCU complex in disease

Genetic diseases caused by mutations in the MCU complex and disruption of $_{m}Ca^{2+}$ flux mainly include Micu1 and Micu2. Loss-of-function mutations in *Micu1* have been linked to proximal myopathy, learning defects, fatigue and muscle weakness and rarely to encephalopathy and developmental defects. A homozygous mutation in *Micu2* causing protein truncation has been associated with severe cognitive impairment and muscle stiffness (Garbincius & Elrod, 2022).

Several non-genetic pathologies, including cardiac, neurodegenerative diseases and cancer, have been associated with alterations in $_{m}Ca^{2+}$, with nearly all MCU complex components involved. The mentioned diseases have been heavily investigated and discussed in scientific literature, and are covered below.

1.8.1 Myocardial ischemia, heart failure and stroke

Mitochondrial Ca^{2+} overload is a major cause of cardiomyocyte death. Excessive $_{m}Ca^{2+}$ uptake causes increased mitochondrial ROS production in the context of myocardial infarction (MI), further exacerbating the decline in contractile function in the weeks following MI (Rasmussen et al., 2015). Therefore, careful and short pharmacological inhibition of $_{m}Ca^{2+}$ uptake might be beneficial during reperfusion and the cardiac decompensation that follows afterwards.

In the context of end-stage heart failure (HF), the situation is the opposite. It has been hypothesised that insufficient $_{m}Ca^{2+}$ uptake exacerbates HF, caused by increased Na^{+} concentrations in the cytosol. The NCLX increases Na^{+} uptake in mitochondria and limits the accumulation of Ca^{2+}. This impairs the TCA cycle and ATP production, restricting cardiac contractility (Liu et al., 2021). Therefore, promoting $_{m}Ca^{2+}$ uptake in end-stage HF patients might be a potential therapeutic goal.

As in MI, excessive $_{m}Ca^{2+}$ uptake is a critical factor causing damage to the brain tissue after stroke. Impairment of the TCA cycle, the mitochondrial membrane potential and increased ROS production all lead to progressive neuronal damage and apoptosis. Pharmacological MCU inhibition prior to ischemia has been shown to reduce brain infarct size in mice (Zhang et al., 2018).

1.8.2 Neurodegenerative diseases

Alzheimer's disease is characterised by neuronal dysfunction and death, the main hallmark being the accumulation of β-amyloid plaques (Soria Lopez et al., 2019). It has been shown that there is increased communication between mitochondria and ER in cell models of Alzheimer's; therefore, the probability that more Ca^{2+} is transferred from ER to mitochondria via IP3Rs is high, causing $_{m}[Ca^{2+}]$ overload. β-amyloid plaques have also been shown to stimulate ER Ca^{2+} release and block NCLX function (Venugopal et al., 2020). However, the complexity of Alzheimer's disease requires further detailed investigation on the role of MCU and its potential as a therapeutic target.

Parkinson's disease is caused by death of dopaminergic neurons and is characterised by bradykinesia, tremors and gait impairments (Dey et al., 2020). In models of Parkinson's, it has been shown that $_{m}[Ca^{2+}]$ overload leads to neuronal death via impaired ATP production. Mutations associated with Parkinson's have in addition been associated with increases in $_{m}[Ca^{2+}]$ (Soman et al., 2019). Based on this, MCU inhibition or genetic disruption has shown a reduction in neuronal death in zebrafish and mouse models (Dey et al., 2020; Soman et al., 2019).

Multiple Sclerosis (MS) is an autoimmune-mediated neurodegenerative disease characterised by destruction of the myelin sheath surrounding axons in the central nervous system (CNS). The cause of MS is multifactorial, involving both environmental factors and genetic predisposition (Ghasemi et al., 2017). Nevertheless, the primary cause of myelin destruction is the infiltration of macrophages and autoreactive T-cells which lead to formation of CNS lesions that manifest into sensorimotor defects, ataxia, visual disturbance, and fatigue, among other symptoms (Loma & Heyman, 2011). Studies have implicated deficits in $_{m}Ca^{2+}$ buffering as a mark of MS progression (Campbell & Mahad, 2012; Licht-Mayer et al., 2020). A study by Holman et al. (2020) examined the effects of MCU deletion in neurons of mice subjected to EAE. Their findings suggested that suppressed $_{m}Ca^{2+}$ buffering and ATP production contributes to axonal damage and disrupts remyelination. There was also evidence of excessive autophagy and increased inflammation in these mice upon EAE induction (Holman et al., 2020). However, compensatory pathways occurring after MCU deletion in neurons were not assessed in this study. Furthermore, there are no known studies investigating the specific role of MCU in $CD4^{+}$ T-cells which contribute to MS.

1.8.3 Cancer

Cancer cells are characterised by their metabolic shift to aerobic glycolysis, unrestricted cell proliferation, metastasis, and therapeutic resistance (Liberti & Locasale, 2016). Since mitochondria have a critical role in cellular metabolism, their role in cancer is certainly of great importance.

Multiple cancer types have shown an increased expression profile of MCU, the highest upregulation observed in ovarian and colorectal cancer (discussed below). Multiple other cancers have shown differences in expression patterns in almost all MCU complex components, including breast, pancreatic, liver cancer, myeloma, osteosarcoma and melanoma (Vultur et al., 2018). The role of MCU varies in different cancer types; therefore, one treatment method would not be beneficial for all, thus it is crucial to understand why MCU patterns differ among cancer types and, in addition, among disease stages (Stejerean-Todoran et al., 2022).

- Ovarian cancer and MCU:

A recent study by Wang et al. looked at the role of MCU in the human ovarian adenocarcinoma cell line SK-OV-3 by using lentiviral *MCU* silencing with siRNA. They showed that MCU downregulation decreased cell proliferation and migration. Furthermore, ROS production was decreased and expression of Micu1 was reduced (Wang et al., 2022). Not many other studies on the role of MCU in ovarian cancer exist, despite its high expression in this context.

- Colorectal cancer and MCU:

A study by Liu et al. examined the expression of MCU in colorectal cancer tissue and its clinical significance. Upregulation of MCU was associated with poor patient prognosis and, not surprisingly, with enhanced $_{m}Ca^{2+}$ uptake. $_{m}Ca^{2+}$ uptake promoted mitochondrial biogenesis and colorectal cancer cell growth by activation of NF-κB signalling via increased ROS production (Liu et al., 2020).

1.8.4 Pharmacological regulation of MCU

All pharmacological treatments under development have to meet certain prerequisites before moving onto clinical trials, one of which is the specific targeting of a drug to a certain signalling pathway in order to halt side effects as much as possible. Most of the existing MCU inhibitors are non-specific and can therefore induce multiple side effects (Woods & Wilson, 2020).

Mitoxantrone hydrochloride, an immunosuppressive drug approved for treatment of acute myeloid leukemia and progressive forms of multiple sclerosis, has been characterised as a direct MCU inhibitor, without affecting respiration. However, mitoxantrone intercalates with DNA and interacts with topoisomerase 2, causing DNA fragmentation and cell death; therefore, it cannot be used for long-term specific targeting and treatment (Arduino et al., 2017).

DS16570511 was identified as a potent, cell-permeable MCU inhibitor based on a drug-screening library of 120,000 small-molecule compounds (Kon et al., 2017). It was shown to inhibit $_{m}Ca^{2+}$ uptake driven by either MCU or Micu1; however, studies have also shown that it highly depolarises mitochondria and induces mPTP opening (Payne et al., 2019).

The most widely used MCU inhibitor is the inorganic trinuclear oxo-bridged complex Ruthenium Red (RuRed), named after its intense red color which was initially used as a cytological stain. Despite its potential to inhibit MCU, RuRed is usually synthesised with poor purity and therefore, has poor selectivity for MCU channels. A derivative of RuRed – Ru360, has been synthesised, representing a more selective and potent MCU inhibitor (Woods & Wilson, 2020). It has been shown that it prevents reperfusion injury upon ischemia, as well as neuronal apoptosis (Jesús García-Rivas et al., 2005). Ru360 inhibits $_{m}Ca^{2+}$ uptake through interactions with the DIME-motif of the loop of MCU. A disadvantage of Ru360 is its low cell permeability which has led to variable results (Matlib et al., 1998).

A cell-permeable selective MCU inhibitor, called Ru265, is the most recently synthesised and reported inhibitor by Woods et al. (2019). Ru265 is taken up by cells twice as effectively as Ru360, is relatively non-toxic, has no effects on mitochondrial membrane potential and mPTP opening, and does not affect NCLX function. An MCU cysteine residue at position 97 is important for the mechanism of action of Ru265, indicating that redox activation of MCU is crucial for the inhibitory action of Ru265 (Woods et al., 2020).

An interesting recent study by De Mario and colleagues (De Mario et al., 2021) identified molecules which have the ability to modulate $_{m}Ca^{2+}$ uptake by performing a high-throughput screening on a USA Food and Drug Administration (FDA)-approved drug library consisting of over 1,600 compounds. They were able to identify two compounds: Amorolfine

(an antifungal drug that inhibits the sterol synthesis pathway) and Benzethonium (an antiseptic), acting as an activator and an inhibitor of $_{m}Ca^{2+}$ uptake, respectively. Amorolfine had a hypertrophic effect *in vivo*, mimicking results in studies where MCU was overexpressed. Benzethonium had negative effects on cancer cell growth and migration, mimicking studies which silenced *MCU* (De Mario et al., 2021). Even though these compounds are promising, their cell permeability and unspecific effects have yet to be determined.

1.9 MCU in T-cell (patho)physiology

Mitochondria can shape TCR-activated signalling pathways by re-organising and moving towards the immunological synapse (Quintana et al., 2007). It has been shown that upon stimulation, the distance between the immunological synapse and mitochondria in human Th1-cells and Jurkat T-cells decreases to values lower than 200 nm (Quintana et al., 2007). Inevitably, $_{m}Ca^{2+}$ uptake via MCU is important for proper T-cell function. Nonetheless, discrepancies between studies investigating the role of MCU in T-cells exist. Therefore, whether MCU is a crucial regulator of T-cell function has not been fully investigated and is under debate.

Based on existing data, MCU downregulation in T-cells is expected to impair mitochondrial function, such as oxidative phosphorylation and ROS production, with potentially the strongest effects seen on T-cell subsets which heavily increase their mitochondrial metabolism in a short time (Tregs and blast-effector $CD4^+$ and $CD8^+$ T cells) (Wang et al., 2020). Downregulation of proteins involved in the Ca^{2+} signalling machinery in T-cells, including Orai1, STIM1, IP3R and RyR, leads to compensatory downregulation of the MCU complex and alterations in mitochondrial metabolism, as shown in a study by Shanmughapriya et al. (2015). Furthermore, another study showed that reduction of the mitochondrial membrane potential, a driving force for MCU function, causes CRAC channel inactivation and decreased nuclear import of NFATs (Sena et al., 2013). It is now clear that the intensity of the TCR-signalling, the T-cell polarization processes, and the metabolic reprogramming in the T-cell itself trigger different Ca^{2+} signalling dynamics which have to be taken into consideration when examining T-cell $_{m}Ca^{2+}$ uptake (Uzhachenko et al., 2016).

A study by Yoast and colleagues investigated the role of MCU activity by using CRISPR Cas9 *MCU* KO in several mammalian cell lines, including Jurkat T-cells and primary mouse $CD4^+$ T-cells. Interestingly, they showed that MCU KO enhanced cytosolic Ca^{2+} signalling and activation of NFAT, contradictory to previous studies and discussions. They propose that abolished MCU-mediated Ca^{2+} uptake prevents the transfer of Ca^{2+} from the cytosol to mitochondria, causing $_{c}[Ca^{2+}]$ overaccumulation (Yoast et al., 2021). However, other compensatory pathways and alterations of other NFAT regulatory mechanisms cannot be excluded. In another study by Wu et al., MCU-dependent $_{m}Ca^{2+}$ uptake was investigated in a $CD4^+$-T-cell-specific $Mcu^{fl/fl}CD4^{Cre}$ mouse model. The study showed that “chronic” MCU ablation had no obvious effects on T-cell metabolism and effector function (Wu et al., 2021). It is a possibility that compensations in mitochondria, as well as the presence of other, so far

unidentified $_{m}Ca^{2+}$ channels, may exist. Therefore, further research requires careful evaluation of MCU modeles, particularly in immune cells.

1.10 Objectives

Based on the current understanding of $CD4^+$ T-cells, cytosolic and mitochondrial Ca^{2+} signalling, and existing MCU models, this Doctoral Thesis aimed to investigate the role of MCU in $CD4^+$ T-cell metabolism and effector function by developing an experimental model of MCUa downregulation in primary human $CD4^+$ T-cells, and validating the findings *in vivo* in an EAE rat model of multiple sclerosis.

The main objectives of this thesis can be categorised as follows:

1. Generating and characterising a transient MCUa knockdown model in primary human $CD4^+$ T-cells;
2. Providing insights into the role of MCU-mediated $_mCa^{2+}$ uptake in human $CD4^+$ T-cell metabolism and function;
3. Investigating the mechanism of MCU regulation in $CD4^+$ T-cells;
4. Examining the role of MCU *in vivo* using a rat EAE model of multiple sclerosis.

2. Materials and Methods

2.1 MATERIALS

2.1.1 Chemicals

Table 1. List of chemicals often used throughout the study (not mentioned in other tables below) (continues on next page).

Chemical name	Company	Catalogue number	Used for
Thapsigargin	Sigma	T9033-1 MG	SERCA inhibitor; $_{c}[Ca^{2+}]$ increase
Ionomycin	ThermoFisher	I2422	Ca^{2+} ionophore; $_{c}[Ca^{2+}]$ and $_{m}[Ca^{2+}]$ increase
Oligomycin	Sigma	O4876-5 MG	ATP synthase inhibitor
Antimycin A	Sigma	A8674	Complex III inhibitor
Rotenone	MP Biomedicals	215015401	Complex I inhibitor
CCCP	Sigma	C2759-100 MG	Mitochondrial uncoupling agent
Mg-ATP	Sigma	A-9062	External ATP addition
Ruthenium 265	Sigma	SML2991	MCU inhibitor
Mitoxantrone dihydrochloride	Sigma	M6545-10 mg	MCU inhibitor
DMSO	Roth	4720.1	Organosulfur compound used for dilutions and as an experimental control
Digitonin	Sigma	D141-100 mg	Non-ionic detergent; $_{c}[Ca^{2+}]$ and $_{m}[Ca^{2+}]$ increase
Histamine	Sigma	H7125-1G	Ca^{2+} stimulant used on HeLa cells
DTT	Sigma	D.0632	Small-molecule reducing reagent
CM4620	Selleckchem	S6834For	SOCE (Orai1/STIM1) inhibitor
BSA	AppliChem	A 6588	Protein concentration standard (WB)
Lipofectamine™ 2000	Thermo Fisher	11668019	Transfection reagent (HeLa cells)
P3 Primary Cell 4D-Nucleofector Solution (+supplement)	Lonza	V4XP-3024	Primary human T-cell transfection reagent
HBSS	Biozym	882010 (BE10-527F)	Cell culture solution with Ca^{2+}, Mg^{2+}, w/o phenol red
OptiMEM	Thermo Fisher	31985070	Reduced serum medium for lipid transfection purposes
Trypsin	Life Technologies	R002100	HeLa cell digestion
H_2O_2 (30%)	Sigma	H1009-100 ML	Oxidation reagent
FCS	Sigma	F7524-500 ML	Serum for media
Trypan Blue	Sigma	T8154-20 ml	Cell impermeant dye used to stain dead cells (for cell counting purposes)
Agarose standard	Roth	3810.4	Agarose gel preparation

Chemical name	Company	Catalogue number	Used for
Poly-L-ornithine hydrobromide	Sigma	P3655	Coating of coverslips for live cell imaging
peqGreen DNA/RNA dye	Bioswisstec	37-5000	Fluorescent dye for the detection of nucleic acids and agarose gel staining
Poly-D-lysine hydrobromide	Sigma	P7886	Seahorse 96-well plate coating
H_2SO_4	Merck	100731	Sulfuric acid; used for ELISA stop solution
GeneRuler 100 bp DNA ladder ready-to-use	Thermo Fisher	SM0241	DNA ladder
Matrigel	Corning	354234	Basement membrane for coating

2.1.2 Solutions

Table 2. Protein lysis-DDM-buffer composition.

Chemical (stock concentration)	Working concentration	Company	Catalogue number
Tris/HCl (1 M)	20 mM	Thermo Fisher	15568025
NaCl (3 M)	150 mM	AppliChem	A2942
EDTA (0,5 M)	1 mM	AppliChem	A2937, 0500
Glycerol	10%		
N-dodecyl-β-d-maltopyranoside (DDM) (10%)	0.5%	Thermo Fisher	BN2005
Protease Inhibitor (PI) (10x) (added fresh on day of use)	1x	cOmplete™, Mini, EDTA-free Protease Inhibitor Cocktail, Roche	183617001
ddH_2O	-	-	-

Table 3. Bradford reagent composition.

Chemical (stock concentration)	Working concentration	Company	Catalogue number
COOMASSIE® Brilliant Blue G-250	339 µM	Serva	35050
Ethanol (96%)	19.2%	Carl Roth	P075.4
H_3PO_4 (85%)	34%	Carl Roth	9079.1
ddH_2O	-	-	-

Table 4. 1x Gel running buffer composition.

Chemical	Working concentration	Company	Catalogue number
Tris	25 mM	Carl Roth	5429.3
Glycine	192 mM	AppliChem	A1067
SDS	0.1%	Sigma	L-4509
ddH_2O	-	-	-

pH 8.3

Table 5. 1x Gel transfer buffer composition.

Chemical (stock concentration)	Working concentration	Company	Catalogue number
5x Transfer buffer*	1x	Bio-Rad	1704270
Ethanol (96%)	20%	Carl Roth	P075.4
ddH_2O	-	-	-

*Provided by Trans-Blot® Turbo™ RTA mini nitrocellulose transfer kit.

Table 6. 10x Tris-buffered saline (TBS) composition.

Chemical	Working concentration	Company	Catalogue number
Tris	50 mM	Carl Roth	5429.3
NaCl	150 mM	AppliChem	A2942
ddH_2O	-	-	-

pH 7.6, adjusted with NaOH (2 M) and HCl (1 M)

Table 7. 1x Tris-buffered saline (TBS)-T composition.

Chemical	Working concentration	Company	Catalogue number
10x TBS	1x in ddH_2O	-	-
Tween® 20	0.1%	Carl Roth	9127.1

Table 8. Stacking gel (SG) buffer composition.

Chemical	Working concentration	Company	Catalogue number
Tris	0.5 M	Carl Roth	5429.3
SDS	0.4%	Sigma	L-4509
ddH_2O	-	-	-

pH 6.8, adjusted with NaOH (2 M) and HCl (1 M)

Table 9. Separation gel (TG) buffer composition.

Chemical	Working concentration	Company	Catalogue number
Tris	1.5 M	Carl Roth	5429.3
SDS	0.4%	Sigma	L-4509
ddH_2O	-	-	-

pH 8.8, adjusted with NaOH (2 M) and HCl (1 M)

Table 10. Stacking gel composition (5%).

Chemical (stock concentration)	Volume used for 5 mL	Company	Catalogue number
SG-buffer (4x)	1.25 mL	-	-
Acrylamide (40%)	0.63 mL	Carl Roth	248272357
APS (10%)	37.5 µL	Sigma	A3678
TEMED	7.5 µL	Sigma	T7024
ddH_2O	3.08 mL	-	-

Table 11. Separation gel composition (10%).

Chemical (stock concentration)	Volume used for 10 mL	Company	Catalogue number
TG-buffer (4x)	2.5 mL	-	-
Acrylamide (40%)	3 mL	Carl Roth	248272357
APS (10%)	75 µL	Sigma	A3678
TEMED	15 µL	Sigma	T7024
ddH_2O	4.41 mL	-	-

Table 12. Membrane blocking buffer composition.

Chemical	Amount used for 50 mL	Company	Catalogue number
DPBS 1x (ready-to-use)	50 mL	Sigma	4190-094
Skim milk powder	5% (2.5 g)	AppliChem	A-0830,1000

Table 13. 4x Laemli Buffer composition.

Chemical	Company	Catalogue number
4x Laemli buffer	Bio-Rad	1610747
β-mercaptoethanol (mixed 1:10)	Gibco	1985-023

Table 14. Protein size standard used.

Name	Company	Catalogue number
Precision Plus Protein™ Dual Color Standard	Bio-Rad	161-0374

Table 15. Ringer solution composition (without Ca^{2+} *).

Component (stock concentration)	Working concentration	Company	Catalogue number
NaCl (3 M)	145 mM	AppliChem	A2942
KCl (1 M)	4 mM	Roth	6781.1
Hepes (pH 7.4, 1 M)	10 mM	Roth	HN78.3
Glucose (1 M)	10 mM	AppliChem	A-1422
$MgCl_2$ (1 M)	2 mM	AppliChem	A.1036
EGTA (500 mM)	1 mM	Sigma	E3889-25 G

*[$CaCl_2$] variable according to cell type used; 0, 0.5 mM or 1 mM. pH 7.4, adjusted with NaOH (2 M) and HCl (1 M)

Table 16. Erythrocyte lysis buffer composition.

Component	Concentration	Company	Catalogue number
NH_4Cl	155 mM	AppliChem	A3661, 0500
$KHCO_3$	10 mM	Sigma	60339-500 G
EDTA	0.1 mM	AppliChem	A2937, 0500

pH 7.3, adjusted with NaOH (2 M) and HCl (1 M)

Table 17. 10x Gel Tris/Borate/EDTA (TBE) buffer composition.

Component	Concentration	Company	Catalogue number
Tris pufferan	108 g/L	Roth	5429.3
Boric acid	55 g/L	Roth	6943.1
EDTA	9.3 g/L	AppliChem	A2937, 0500

pH 8.3, adjusted with NaOH (2 M) and HCl (1 M)

Table 18. List of cell culture media formulations used throughout the study.

Name	Composition	Company	Catalogue number	Used for
AIM V 10%	+ L-Glutamine, 50 µg/mL Streptomycin Sulfate, 10 µg/mL Gentamicin Sulfate, phenol red, 10% Fetal calf serum (FCS)	Thermo Fisher	12055091	Culture of non-transfected primary human $CD4^+$ T-cells
RPMI 1640 10%	+ High glucose, GlutaMAX™, HEPES, phenol red, 100 mg/L calcium nitrate, 10% Fetal calf serum (FCS)	Thermo Fisher	72400021	Culture of transfected primary human $CD4^+$ T-cells
Dulbecco's Modified Eagle Medium (DMEM) 10%	+High glucose, sodium pyruvate, L-glutamine, phenol red, 10% Fetal calf serum (FCS)	Thermo Fisher	41966029	Culture of HeLa cells
Seahorse XF DMEM medium, pH 7.4	+Hepes 5 mM	Agilent	103575-100	Seahorse Assay
T-cell growth factor (TCGF) medium	DMEM-based medium containing 1% non-essential amino acids, 1% sodium pyruvate, 1% Pen-strep, Glutamine, Asparagine, 4 µL/L β-mercaptoethanol, 5% ConA supernatant, and 10% horse serum	-	-	Rat $CD4^+$ T-cell culture
Re-stimulation medium	T-cell medium + 1% serum	-	-	GP+E86 cell culture and maintenance

2.1.3 Oligonucleotides

Table 19. List of human primer pairs used for RT-qPCR analyses (sequences 5'-3').

Name of gene	Forward sequence	Reverse sequence	T_o	E value
HK *TBP*	CGGAGAGTTCTGGGATTGT	GGTTCGTGGCTCTCTTATC	58°C	1.912
ORAI1	ATGAGCCTCAACGAGCACT	GTGGGTAGTCGTGGTCAG	58°C	1.828
ORAI2	TGGAACTGGTCACCTCTAAC	GGGTACTGGTACTGCGTCT	58°C	1.529
ORAI3	GTACCGGGAGTTCGTGCA	GGTACTCGTGGTCACTCT	58°C	1.462
STIM1	CAGAGTCTGCATGACCTTCA	GCTTCCTGCTTAGCAAGGTT	58°C	1.899
STIM2	GTCTCCATTCCACCCTATCC	GGCTAATGATCCAGGAGGTT	58°C	1.829
NFAT1	AAACTCGGCTCCAGAATCCA	TGGACTCTGGGATGTGAACT	58°C	1.860
NFAT4	ACCCTTTACCTGGAGCAAAC	CTTGCAGTAGCGACTGTCTT	58°C	1.901
MCUa	CACACAGTTTGGCATTTTGG	TGTCTGTCTCTGGCTTCTGG	58°C	2.003
MCUb	TTTTGCGTGTGAAGCTGTGT	TACCAAGGGAAGGCCATGT	58°C	1.925
EMRE	CTTGAGGAAAGATGGCGATG	CGACATAGAGAAAGGGGATCA	58°C	1.914
Micu1	GTGTTCAGCCCTCACAACCT	CCACCAAACTGCCTCTCAGT	58°C	2.042
Micu2	AGCGCTTCATGCAGTTTTCT	CAGCTGTTTGGATCCCTGAC	58°C	1.933
Micu3	CCAGTTTGGAAAGGCTCATC	ATTCTGAACCCTGCATGTGG	58°C	1.929
MCUR1	GCCCTTCCCCAGTACCAC	AGAGTTTCCTGCTCCCAGAA	58°C	1.917
NCLX	ATGGTGGCTGTGTTCCTGACCT	GGTGCAGAGAATCACAGTGACC	58°C	2.074
IL-2	TGTCACAAACAGTGCACCTA	TCAGTTCTGTGGCCTTCTTG	58°C	1.859
IFNγ	GCTGTTACTGCCAGGACCC	TTTTCTGTCACTCTCCTCTTTCC	58°C	1.867
IL-6	ACCCCCAGGAGAAGATTCCA	CACCAGGCAAGTCTCCTCATT	62°C	1.927
IL-4	CTTTGCTGCCTCCAAGAACAC	CCAACGTACTCTGGTTGGCT	62°C	1.908
IL-17	AGACCTCATTGGTGTCACTGC	CAGTCCGGGGGAAGTTCTTG	60°C	1.958
IL-21	TGCCAGCTCCAGAAGATGTAG	CACATGAAGGGCATGTTAGTCT	58°C	1.792
IL-22	GCCCTATATCACCAACCGCA	AGCGCTCACTCATACTGACTC	60°C	1.855
IL-9	TTGGGCATTCCCTCTGACAA	GTGGTTTGGTTGCATGGCTG	58°C	1.819
IL-7	GCATCGATCAATTATTGGACAGCA	GCGAGCAGCACGGAATAAAA	60°C	1.847
IL-10	CCAGACATCAAGGCGCATGT	TAGATGCCTTTCTCTTGGAGCTTA	60°C	1.858
TNFα	TAGCCCATGTTGTAGCAAACC	ATGAGGTACAGGCCCTCTGAT	60°C	1.688
TGFβ	ATTCCTGGCGATACCTCAGC	CGGTAGTGAACCCGTTGATG	60°C	1.873
FoxP3	CAGCACATTCCCAGAGTTCCT	AGGCAAACATGCGTGTGAAC	58°C	1.845
GATA3	CCCTCATTAAGCCCAAGCGA	AGTCAGGGGTCTGTTAATATTGTG	58°C	1.964
Tbet	TGATCATCACCAAGCAGGGAC	GTACAGGCGGTTTCCTGGCA	60°C	1.623
RORγ-t	GCAGCGCTCCAACATCTTCT	ACGTACTGAATGGCCTCGGT	58°C	1.825
CD25	AATGCACAAGCTCTGCCACT	TGCCCCACCACGAAATGATA	58°C	1.416
CXCR3	AGCTTTGACCGCTACCTGAA	CGGAACTTGACCCCTACAAA	58°C	1.422
AFG3L2	ACGAGTGATTGGTGGCTTAGAG	GCCACGTGGGATGATGGAT	60°C	1.920

HK = housekeeping gene, T_o = observed optimal annealing temperature, E-value = primer efficiency value.

Table 20. List of human primer pairs used for RT-qPCR analyses-mitochondrial-encoded genes (sequences 5'-3').

Name of gene	Forward sequence	Reverse sequence	T_o
ATP6	GGACTCCTGCCTCACTCATTTAC	AATCACTGTGCCCGCTCATAAG	58°C
COX1	ATACCAAACGCCCCTCTTCG	TGTTGAGGTTGCGGTCTGTT	58°C
COX2	GAACTATCCTGCCCGCCATC	AGGGATCGTTGACCTCGTCT	58°C
COX3	AGGCATCACCCCGCTAAATC	GTACTCTGAGGCTTGTAGGAGG	58°C
ND1	ATGACGCACTCTCCCCTGAAC	AGTTGGTCGTAGCGGAATCG	58°C
ND2	ATCCCCACCATCATAGCCAC	AGGAGTAGCGTGGTAAGGGC	58°C
ND3	ATCCACCCCTTACGAGTGCG	AGTTGTTTGTAGGGCTCATGGT	58°C
ND4	ACACAATGGGGCTCACTCAC	GGAGGAGAATGGGGGATAGG	58°C
ND4L	CCCACTCCCTCTTAGCCAAT	ACGTAGTCTAGGCCATATGTGTTG	58°C
ND5	CACACCGCACAATCCCCTAT	TGGAGGTGGAGATTTGGTGCT	58°C
ND6	GATTGTTAGCGGTGTGGTCG	CCCCATGCCTCAGGATACTC	58°C
ATP8	ACCTACCTCCCTCACCAAAGC	GGCAATGAATGAAGCGAACAG	58°C
CytB	AGGCGTCCTTGCCCTATTAC	GCTTACTGGTTGTCCTCCGATTC	58°C

Table 21. List of rat primer pairs used for RT-qPCR analyses (sequences 5'-3').

Name of gene	Forward sequence	Reverse sequence	T_o
HK *β-actin*	GTACAACCTCCTTGCAGCTCCT	TTGTCGACGACGAGCGC	58°C
IL-2	CCTGAGAGGGATCGATAATTACA	TCCGAGTTCATTTTCCAGGCA	58°C
IFNγ	AACAGTAAAGCAAAAAAGGATGCATT	TTCATTGACAGCTTTGTGCTGG	58°C

HK = housekeeping gene.

Table 22. Master mix used for one RT-qPCR reaction (human primer sets).

Reagent name	Volume used
2x GoTaq® qPCR Master Mix (Promega, Cat# A6001)	25 µL
Forward primer (10 µM)	1.5 µL
Reverse primer (10 µM)	1.5 µL
ddH_2O	12 µL

Table 23. Master mix used for one RT-qPCR reaction (rat primer sets).

Reagent name	Volume used
TaqMan® polymerase master mix (Eurogentech)	7.5 µL
Rat primers mix	3 µL

Table 24. RT-qPCR cycling conditions.

	Temp (°C)	Time	Number of cycles
Initial activation	95	10 min	1
Denaturation	94	15 sec	
Annealing	*	30 sec	x 45
Elongation	72	30 sec	
Dissociation	95	1 min	
	*	30 sec	1
	95	30 sec	

*Depending on T_o (refer to Table 19).

2.1.4 Small interfering RNAs

Table 25. List of small interfering (si) RNAs used throughout the study.

Name	Targeted protein	Sense strand sequence (5'-3')	Overhang 3'	Company
siMS_Control	Non-targeted control	AGGUAGUGUAAUCGCCUUG	dTdT	Microsynth
siMCU_1	MCUa	CAGGUGCCUUGCAAAGGUUGATT	dTdT	Microsynth
siAFG3L2_1	AFG3L2	GAACUUUGCUGCUCUACUUTT	dTdT	Microsynth

2.1.5 Plasmids

Table 26. List of commonly used plasmids throughout the study.

Name of plasmid	Provider	Used for
Ratiometric MT3.1 Pericam	Nagai et al. (2001)	Mitochondrial calcium measurements
GCaMP6s	Addgene, plasmid#40753	Mitochondrial calcium measurements
HyPer3	Addgene, plasmid#42131	Cytosolic H_2O_2 measurements
HyPer-dMito	Evrogen, #FP942	Mitochondrial H_2O_2 measurements
Grx1-roGFP2	Addgene, plasmid#64975	Cytosolic glutathione redox potential measurements
mitoGrx1-roGFP2	Addgene, plasmid#64977	Mitochondrial glutathione redox potential measurements

2.1.6 Dyes

Table 27. List of dyes used throughout the study.

Name of dye	Company	Catalogue number	Purpose
Fura2-AM	ThermoFisher	F1221	Cytosolic calcium indicator (ratiometric)
TMRE	ThermoFisher	T669	Mitochondrial membrane potential
Cell Titer Glo®	Promega	G7571	Global ATP levels
Cell Titer Blue®	Promega	G8081	Cellular proliferation/Metabolism
JC-1	ThermoFisher	T3168	Mitochondrial membrane potential
Mito-ATP-Red	Merck	SCT045	Mitochondrial ATP levels
CellMask Green	ThermoFisher	C37608	Plasma membrane stain
MitoTracker Deep red	ThermoFisher	M22426	Mitochondrial stain
H_2DCFDA	ThermoFisher	D399	Detection of ROS and RNS

2.1.7 Antibodies

Table 28. List of primary antibodies used for Western Blotting.

Name	Species	Clonality	Protein size (kD)	Company	Catalogue number	Working dilution
Histone H3	Rabbit	Monoclonal	18	Cell Signaling Technology	4499S	1:1000
Calnexin	Rabbit	Polyclonal	98	Enzo	ADI-SPA-860-F	1:1000
β-actin	Mouse	Monoclonal	45	Sigma	A5441	1:2500
MCU	Rabbit	Monoclonal	30	Cell Signaling Technology	14997S	1:1000
Micu1	Rabbit	Polyclonal	50	Sigma	HPA37479	1:500
NDUFA9	Rabbit	Polyclonal	38	Custom-made*	-	1:1000
SDHA	Mouse	Monoclonal	60	Invitrogen	459200	1:2000
COX1	Rabbit	Polyclonal	40	Custom-made	-	1:1000
COX6A	Rabbit	Polyclonal	9	Custom-made	-	1:2000
TACO1	Rabbit	Polyclonal	30	Custom-made	-	1:1000
MITRAC12	Rabbit	Polyclonal	12	Custom-made	-	1:500
ATP5B	Rabbit	Polyclonal	51	Custom-made	-	1:10000
AFG3L2	Rabbit	Polyclonal	80	Custom-made	-	1:1000
uL1m	Rabbit	Polyclonal	36	Custom-made	-	1:1000
uL10m	Rabbit	Polyclonal	28	Custom-made	-	1:1000
uS14m	Rabbit	Polyclonal	15	Proteintech	16301-1-AP	1:500

*Custom-made antibodies were a kind gift from Dr. Sven Dennerlein, AG Rehling, Institute of Biochemistry, Göttingen.

Table 29. List of secondary antibodies used for Western Blot.

Name	Company	Catalogue number	Working dilution
IRDye 800CW Donkey anti-Rabbit	Li-Cor	926-32213	1:10000
IRDye 680LT Donkey anti-Mouse	Li-Cor	926-68022	1:10000

Table 30. List of anti-human antibodies used for FACS.

Name	Fluorochrome	Company	Catalogue number	Working dilution
anti-human CD3	VioBlue	Miltenyi Biotech	130-114-710	1:40
anti-human CD4	PE	Miltenyi Biotech	5190304074	1:40
anti-human CD8	PE	Miltenyi Biotech	130-104-168	1:40

2.1.8 Cytokines and Chemokines

Table 31. List of cytokines and chemokines used throughout the study.

Name	Company	Catalogue number	Lot number	Working concentration
Recombinant human CCL19	Peprotech	300-29B	510105	50 ng/mL
Recombinant human CXCL12	Peprotech	300-28A	31992	50 ng/mL

2.1.9 Kits

Table 32. List of commonly used kits throughout the study.

Name	Company	Catalogue number
CellTiter-Blue® Cell Viability Assay	Promega	G8081
CellTiter-Glo® Luminescent Assay	Promega	G7571
Nucleospin™ RNA Plus Kit	Macherey-Nagel	740984.250
NucleoSpin™ RNA Mini	Macherey-Nagel	740955.50
Superscript™ IV Reverse Transcriptase Kit	Invitrogen	18090050
GoTaq® qPCR Master Mix	Promega	A6002
Lumit human IL-2 Immunoassay	Promega	CS2032B01
Lumit human IL-6 Immunoassay	Promega	W6030
IFN gamma Human Uncoated ELISA Kit with Plates	Thermo Fisher	88-7316-86
QIAquick Gel Extraction kit	Qiagen	28704

2.1.10 Consumables and Devices

Table 33. Materials and consumables specifically used for PBMC and CD4$^+$ T-cell isolation and activation.

Type of material/consumable	Company	Catalogue number
Leukoreduction system (LRS) chambers	Trima Accel® (Gambro BCT)	
Leucosep tubes	Greiner	227290
20 mL Syringes	Braun, Omnifix	8508750N
Combifix Adapters	Braun	4090306
Lymphocyte separation medium	Promocell	C44010
Isolation buffer (1xDPBS+5% FCS)	-	-
Countess™ II and 3 Automated Cell Counters	ThermoFisher	AMQAX1000; AMQAX2000
Centrifuge	Heraeus™ Labofuge™ 400R, Thermo Fisher	
CD4$^+$ T Cell Isolation Kit, human	Miltenyi Biotec	130-096-533
QuadroMACS™ (LS) Separator	Miltenyi Biotec	130-090-976
LS Columns	Miltenyi Biotec	130-042-401
Pre-separation filters (30 µm)	Miltenyi Biotec	130-041-407
MACS® MultiStand	Miltenyi Biotec	130-042-303
DynaMag-15™ magnet	Invitrogen	12301D
Dynabeads® Human T-Activator CD3/CD28	Gibco	11132D
ImmunoCult™ Human CD3/CD28 T-cell Activator	StemCell Technologies	10991

Table 34. Commonly used consumables.

Name	Company	Catalogue number
Falcon tubes (15 mL)	Sarstedt	62.554.002
Falcon tubes (50 mL)	Sarstedt	62.547.004
Serological pipettes (5 mL)	Sarstedt	86.1253.001
Serological pipettes (10 mL)	Sarstedt	86.1254.001
24-well plates	Sarstedt	83.3922.005
6-well plates	Sarstedt	833920
96-well plates	Sarstedt	83.3924
Black, clear bottom 96-well plates	BD	353219
Eppendorf® tubes (1.5 mL)	Sigma	T9661-1000EA
Eppendorf® tubes (2 mL)	Sigma	72695500
96-well RT-qPCR plates	Agilent Technologies	401333
Glass coverslips (25 mm, #1.5)	VWR®	631-0172
Glass coverslips (12 mm, #1.5)	TH. GEYER	6080181
FACS tubes	StemCell Technologies	352058
T75 cell culture flasks	Sarstedt	833910002
Filter tips (10 µL)	Starlab	S1121-3810
Filter tips 20 µL	Starlab	S1120-1810
Filter Tips 200 µL	Starlab	I1011-0830
Filter tips 1000 µL	Starlab	S1126-7810
Transwell 6.5 mm inserts with 5.0 µm pore membranes	Costar	3421
Seahorse XF96 V3 PS Culture Microplates	Agilent	101085-004

Table 35. Commonly used devices (continues on next page).

Name	Manufacturer	Used for
Microscopes	Carl Zeiss Axiovert S100TV (equipped with a Visitron CMOS camera)	Fura2-AM ($_c[Ca^{2+}]$ single cell measurements)
	Cell D1 Observer microscope (Zeiss) equipped with a Colibri LED fluorescence lamp (Zeiss), and a fluorescence camera (Axiocam 702 mono, Zeiss)	Single cell fluorescence measurements
	LSM800/Duolink Confocal (Zeiss)	Confocal microscopy
Microplate Readers	CLARIOstar, BMG LABTECH	IL-2 Lumit assay, ELISA, Cell Titer Glo® assay
	Berthold, Mithras LB 940	Protein determination, Cell Titer Blue® assay

Name	Manufacturer	Used for
Western blot membrane Imaging system	Odyssey® CLx, Li-Cor Biosciences	Membrane imaging
PCR cycler	C1000TM Thermal Cycler, Bio-Rad	cDNA synthesis, Gradient PCR
RT-qPCR cycler	Stratagene MX3000 pro, Agilent	RT-qPCR
Spectrophotometer	NanoDrop 2000c, Thermo Fisher	Determination of RNA/DNA concentration
4D Nucleofector® Core and X Unit	Lonza	Primary T-cell transfection
FACS Canto II	BD Biosciences	FACS experiment and analyses
Gel electrophoresis system	GibcoBRL, Life Technologies, ST 606 T	Electrophoresis system
Dual Intensity Ultraviolet Transilluminator with camera	Geneo Labstore, 4550-105-01	Agarose gel imaging under UV
Seahorse XFe Analyzer	Agilent	Mitochondrial respiration and ATP production rate

2.1.11 Software

Table 36. Software commonly used for data processing, analysis and figure design.

Name	Device
GraphPad Prism 9	PC
Microsoft Office Package 2019	PC
MARS Data Analysis software	CLARIOstar microplate reader
MikroWin 2000	Berthold microplate reader
MxPro qPCR 4.10	Stratagene MX3000 pro
Nanodrop 2000c	Nanodrop™ 2000c
VisiView 2.1.2®	Carl Zeiss Axiovert S100TV
Zen 2.6	Cell D1 Observer microscope (Zeiss)
Zen 3.5	LSM800/Duolink Confocal microscope (Zeiss)
FACS Diva	FACS Canto II
FlowJo_v10.8.0	PC
Image Studio Lite Ver 5.2	PC
ImageJ-Fiji	PC
Seahorse Wave Desktop Software	Seahorse XFe Analyzer
BioRender	PC
Python (v3.8)	PC

2.2 METHODS

Unless specified otherwise, details regarding the particular materials used are given in Tables **1** through **36** in Materials section (2.1).

2.2.1 Peripheral Blood Mononuclear Cell (PBMC) isolation

Leukoreduction system (LRS) chambers were obtained from the blood bank in the Department of Transfusion Medicine in the University Medical Center Göttingen (Ethical approval 2/3/18). The LRS chambers use a specific filtration technology in order to remove white blood cells from platelets during routine thrombocyte donations from healthy human donors and are a valuable source of PBMCs. The isolation procedure was performed at room temperature (RT).

Initially, a leucosep tube (50 mL) was filled with 17 mL of lymphocyte separation medium, followed by a centrifugation step (2500 rpm, 1 min) (Table 33). This was performed under low-light conditions since the separation medium is light-sensitive. Afterwards, the LRS chamber was adjusted so that a continuous blood flow is achieved in the leucosep tube by using a metal stand and cutting the chamber tubes with sterilized scissors. To increase the acquired cell number, the chamber was flushed once with HBSS buffer using a 20 mL syringe attached to a Combifix adapter and a pipette tip. A final volume of 50 mL was obtained, followed by density gradient centrifugation for 30 min at 1600 rpm, without centrifugation brake. Gradient centrifugation separates the blood components based on their density into three layers: plasma on top, followed by a yellow-white layer of leukocytes, and erythrocytes on the bottom of the tube. The leukocyte ring was transferred to a new 50 mL falcon tube which was filled with HBSS buffer up to 50 mL. After mixing the cells by inverting the tube several times, a centrifugation step followed at 1300 rpm for 15 min (with brake). The cell pellet obtained was resuspended with 2 mL of erythrocyte lysis buffer (Table 16 for composition) and incubated for 2 min. Erythrocyte lysis was stopped by addition of up to 50 mL of HBSS buffer. After another centrifugation step (1100 rpm, 10 min), the PBMC pellet was resuspended in 20 mL ice-cold isolation buffer consisting of 1xDPBS supplemented with 5% FCS. A small volume of cell suspension was diluted 1:10 in isolation buffer and used for cell counting with the Countess™ II or 3 Automatic Cell Counters, (a 1:1 staining with Trypan blue was performed to label dead cells). Isolated PBMCs were stored at 4°C or on ice until further use.

2.2.2 Primary human naive $CD4^+$ T-cell isolation

Primary human naive $CD4^+$ T-cells were isolated from $40x10^6$ PBMCs per donor by using a human $CD4^+$ T-cell isolation microbeads kit (Miltenyi Biotec) with negative isolation. The kit consists of a $CD4^+$ T-cell human biotin antibody cocktail (antibodies against CD8a, CD14, CD15, CD16, CD19, CD36, CD56, CD123, TcRγ/δ, and CD235a) and a MicroBead cocktail conjugated to monoclonal anti-biotin antibody (isotype mouse-IgG1) and monoclonal anti-CD61 antibody (isotype mouse IgG1). 10 mL of PBMC suspension were filtered through a 30 µm pre-separation filter to remove cell clumps. The required volume of filtered PBMCs was transferred to a 15 mL falcon tube and a centrifugation step followed (1800 rpm, 8 min, 4°C). The obtained cell pellet was resuspended with 160 µL ice-cold isolation buffer and mixed with 40 µL of T-cell biotin antibody cocktail by pipetting up and down. After incubating for 5 min at 4°C, the cells were mixed with 120 µL isolation buffer and 80 µL of T-cell microbeads by pipetting up and down. An incubation step of 10 min at 4°C followed. In the meantime, the Quadro MACS™ magnetic separator was placed onto the multistand and LS separating columns were prepared by placing them tightly in the gap of the magnet and washing once with 3 mL ice-cold isolation buffer (Table 33). The effluent was collected in a 15 mL falcon tube and discarded. The mixed cells and microbeads solution were washed with 600 µL of ice-cold isolation buffer and loaded into the column slowly, without forming bubbles. Unlabelled naive $CD4^+$ T-cells were collected in a 15 mL falcon tube. The empty column reservoir was washed once with 3 mL ice-cold isolation buffer to ensure maximal T-cell collection. The collected cells were spun down at 1600 rpm, 8 min, RT. The cell pellet was resuspended with 2 mL AIM V 10% cell culture medium (Table 18) and cells were counted by using the Countess™ II or 3 Automatic Cell Counters, and staining 1:1 with Trypan blue. $2x10^6$ cells/mL were seeded in a 24-well plate (1 mL/well) and cultured under standard incubator culture conditions (37ºC, 5% CO_2). Usually, cells from 2 or 3 donors were isolated simultaneously.

2.2.3 Naive $CD4^+$ T-cell activation and effector $CD4^+$ T-cell re-stimulation

Activation of naive $CD4^+$ T-cells was achieved in two ways: 1) by using Dynabeads™ Human T-Activator CD3/CD28, or 2) by using ImmunoCult™ Human CD3/CD28 T-cell Activator (Table 33). The naive T-cells were activated by either adding 50 µL of washed beads (1:1 cell-to-bead ratio), or by adding 50 µL of ImmunoCult™ antibody solution onto $2x10^6$ cells (according to manufacturer's instructions). Effector T-cells were obtained 48-72 hrs after initial activation. Effector $CD4^+$ T-cells were cultured in AIM V 10% medium under standard culture conditions (37ºC, 5% CO_2).

Effector $CD4^+$ T-cell re-stimulation was performed by either adding 30 µL of washed beads, or by adding 30 µL of ImmunoCult™ antibody solution onto $2x10^6$ cells for 8 hrs. ImmunoCult antibody concentration was titrated according to the type of experiment performed afterwards (0.5 to 25 µL/mL).

2.2.4 Culture of HeLa cells

HeLa is an immortal adherent cell line derived from cervical cancer, used often for scientific research. HeLa cells were cultured in T75 cell culture flasks and regularly split in 1:10 ratios twice a week. To digest the cells, 1 mL of Trypsin was used, after washing the cells twice with warm 1x DPBS. After 3 min, digestion was stopped by adding 4 mL of warm DMEM 10% cell culture medium (Table 18). The cell suspension was mixed well to ensure maximal detachment and 4.5 mL were transferred to a 15 mL falcon tube and used for further experiments. The leftover cells (0.5 mL) were mixed with DMEM 10% medium up to 10 mL. $2x10^5$ cells were used per well for seeding in 6-well plates. $4\text{-}6x10^4$ cells were used for seeding onto glass coverslips (25 mm). The cells were cultured under standard incubator culture conditions (37ºC, 5% CO_2).

2.2.5 Transient cell transfection

2.2.5.1 $CD4^+$ T-cell plasmid DNA transfection.

Introduction of plasmid DNA in both naive and effector $CD4^+$ T-cells was performed by an electroporation method using the 4D Nucleofector® technology by Lonza. The technology uses a combination of optimized electrical parameters and solutions, enabling a direct transfer of a small molecule into the cell nucleus. Since it acts independently from cell proliferation, it allows for efficient transfection of non-dividing primary cells (lonza.com). Plasmid DNAs used for transient transfection in this study are given in Table 26. The P3 Primary Cell 4D Nucleofector™ X Kit was used and the protocol was followed accordingly.

Firstly, the entire supplement provided by the kit was added to the P3 solution. A transfection mix was prepared for each plasmid by mixing 1 µg/mL plasmid DNA with 95 µL of supplemented P3 solution, keeping it at RT. If cells had been activated by using beads, the beads were removed by magnetic separation using the DynaMag-15™ magnet. $2x10^6$ cells (naive or effector) per donor were aliquoted for transfection after counting. After a centrifugation step (1000 rpm, 5 min, RT), the cell pellet was resuspended with the prepared transfection mix (avoiding bubble formation) and quickly transferred to Nucleocuvette™

vessels (100 µL format, provided in the kit). The cuvettes were gently tapped and electroporation was performed in the 4D Nucleofector™ Core and X Unit using different pulse protocols depending on the cell type (Table 37).

Table 37. Contents of one transfected sample and electroporation settings.

T-cell type	**Naive/Unstimulated human $CD4^+$ T-cells**	**Effector/Stimulated human $CD4^+$ T-cells**
Cell number	$2x10^6$	$2x10^6$
Plasmid DNA	1 µg/µL	1 µg/µL
P3 solution	100 µL final volume	100 µL final volume
Electroporation pulse program	EH-100	E0-115

After electroporation, the cells were left to settle at RT for 15 min before adding 900 µL of warm RPMI 10% directly into the cuvette. Using plastic sterile pipettes (provided by Lonza kit), the cell suspension was transferred into a 1.5 mL Eppendorf tube. $2x10^6$ naive $CD4^+$ T-cells and/or $1x10^6$ effector $CD4^+$ T-cells were seeded per well in a 24-well plate and maintained at standard culture conditions (37ºC, 5% CO_2). The cells were incubated for 48 hrs prior to live cell fluorescence imaging.

2.2.5.2 $CD4^+$ T-cell siRNA transfection (generation of MCU knockdown models)

Transient knockdown in primary human $CD4^+$ T-cells was achieved by introduction of small interfering (si) RNAs (listed in Table 25) targeting MCU and a non-targeted control sequence (to control for non-specific effects related to siRNA delivery).

The mechanism of siRNA action is based on RNA interference by which double-stranded RNA induces gene silencing by targeting complementary mRNA for degradation. siRNAs introduced in the cell are usually bound by a complex known as RNA-induced silencing complex (RISC). In this complex, the two siRNA strands are separated, and the more stable strand is integrated to the active RISC complex and it then guides and aligns the complex on the target mRNA. mRNA cleavage finally occurs through a catalytic reaction, and thus no translation into amino acids and protein occurs (Dana et al., 2017).

siRNA delivery in 5-$6x10^6$ primary T-cells was done by using the 4D Nucleofector® technology and the P3 Primary Cell 4D Nucleofector™ X Kit. Electroporation was performed as depicted in Table 38:

Table 38. Electroporation settings of siRNA delivery in CD4$^+$ T-cells.

T-cell type	Naive/Unstimulated human CD4$^+$ T-cells	Effector/Stimulated human CD4$^+$ T-cells
Cell number	5-6x10^6	5-6x10^6
siRNA	2 µM	1.2 µM
P3 solution	100 µL final volume	100 µL final volume
Electroporation pulse program	EH-100	E0-115

- "Late-stage" MCU knockdown model

The "late-stage" MCU knockdown model refers to MCU knockdown achieved at the effector-T-cell-stage (72 hrs after TCR stimulation with beads). Beads were removed from the T-cells using magnetic separation and the cells were counted using the Countess™ II or 3 Automatic Cell Counters. 5 to 6x10^6 cells were aliquoted and pelleted (1000 rpm, 5 min, RT). After resuspending the pellet with 100 µL of P3 + siRNA transfection mix (siMCU_1 or siMS_Control), the cells were added to the cuvettes and electroporation was performed. Further transfection with plasmid DNA was performed 24 hrs after siRNA delivery, when required. Experiments were performed 48 hrs after siRNA delivery. Knockdown efficiency was confirmed via RT-qPCR and WB. Cells were kept under standard culture conditions (37ºC, 5% CO_2).

- "Early-stage" MCU knockdown model

The "early-stage" MCU knockdown model refers to MCU knockdown achieved at the naive-T-cell-stage, followed by cell activation with beads 24 hrs after siRNA delivery. 5 to 6x10^6 naive CD4$^+$ T-cells were pelleted and resuspended in 100 µL of P3 + siRNA transfection mix (siMCU_1 or siMS_Control). Electroporation was performed as described in Table 38. Cells were activated by using beads 24 hrs after siRNA delivery, and further transfected with plasmid DNA 24 hrs later, when necessary. Experiments were performed 72 hrs after siRNA delivery and 48 hrs after cell activation. Knockdown efficiency was confirmed via RT-qPCR. Cells were kept under standard culture conditions (37ºC, 5% CO_2).

2.2.5.3 HeLa cell plasmid DNA and siRNA transfection

Plasmid DNA and siRNA transfection in HeLa cells was performed by using lipid-based transfection with the Lipofectamine™ 2000 transfection reagent (Table 1). Lipofection technology works by using vesicles called liposomes that have the same composition as the cell membrane. A liposome complex is formed around the DNA or RNA sequence that is being

transfected and depending on the cell type, the liposome can be endocytosed or fused with the cell membrane to release the construct (Dalby et al., 2004). Initially, the siRNA transfection solution was set up by mixing 1.2 µM of siRNA stock (refer to Table 25) diluted in 50 µL of OptiMEM with 2.5 µL of Lipofectamine™ 2000 reagent diluted in 50 µL OptiMEM (1:1 ratio, vortexing to mix). The solution was incubated for 15 min at RT under low-light conditions. Then, 1 µg/µL of plasmid DNA (Table 26) was diluted in 50 µL OptiMEM and mixed with 2.5 µL of Lipofectamine™ 2000 reagent diluted in 50 µL OptiMEM (1:1 ratio, vortexing to mix). The same incubation step followed (15 min at RT under low-light conditions). After incubation was complete, 100 µL of siRNA mix and 100 µL of plasmid DNA mix were pipetted dropwise on top of the previously seeded HeLa cells (into 6-well plates, with or without 25 mm coverslips). The plates were swirled to ensure that the mix is properly distributed. Medium change with fresh and warm DMEM 10% was performed 4 hrs after transfection to ensure adequate cell growth. Measurements were performed 48 hrs later.

2.2.6 Determination of $CD4^+$ T-cell volume

$CD4^+$ T-cells (both naive and effector) were counted by using the Countess™ 3 Automatic Cell Counter and staining 1:1 with Trypan blue. The countess is able to give precise information regarding average cell size (diameter in µm), which was used to determine T-cell volume by using the formula for volume of a sphere:

$$V(\mu m^3) = \frac{4}{3}\pi r^3$$

$CD4^+$ T-cell volume was used for normalization purposes in further experiments.

2.2.7 Cell Titer Blue® Cell Viability Assay

In order to estimate the number of viable proliferating and metabolically active cells, the Cell Titer Blue® Cell Viability assay from Promega (Table 32) was used. This assay is a fluorometric method based on the indicator dye resazurin. Metabolically active and viable cells have the ability to reduce resazurin into a fluorescent compound resorufin which can be easily detected (excitation: 579 nm; emission: 584 nm) (promega.com).

For performing the assay, $5x10^4$ $CD4^+$ T-cells (naive, siRNA-treated, or inhibitor-treated) or $1x10^4$ HeLa cells (siRNA-treated) were seeded per well (in triplicates) in a 96-well plate (100 µl/well), in their respective cell culture medium. Cell culture medium alone was used as a background fluorescence control. For obtaining effector $CD4^+$ T-cells, the seeded naive cells were stimulated with beads or antibody solution (1.5 µL/well), depending on the

experiment being performed. The seeded cells were left to settle in standard culture conditions (37ºC, 5% CO_2) for 2, 24, 48 and 72 hrs before adding 20 µL of warm Cell Titer Blue® reagent per well. The plates were incubated in standard culture conditions for 3 hrs after reagent addition before measuring resorufin fluorescence levels. For this purpose, the Berthold, Mithras LB 940 microplate reader (Table 35) was used. Background fluorescence was subtracted from the overall fluorescence signal. Absolute fluorescence signal was plotted against the time of measurement and different cell lines or conditions were compared.

2.2.8 Cell Titer Glo® Luminescent Cell Viability Assay

For estimation of global ATP levels in the different cell types, the Cell Titer Glo® Luminescent Cell Viability Assay (Table 32) was used. This assay determines the number of viable cells in culture, based on the quantification of the ATP present. Addition of the Cell Titer Glo® reagent results in cell lysis and generation of a luminescent signal which is proportional to the amount of ATP present (promega.com).

When using T-cells, the cell seeding and assay were performed on the same day. Firstly, $2x10^5$ $CD4^+$ T-cells (naive, effector, or siRNA-treated) (murine or human) were seeded (at least in triplicates) per well in an opaque, clear bottom 96-well plate (100 µL/well) in their respective cell culture medium. The cells were left to equilibrate and settle for 30 min at standard culture conditions (37ºC, 5% CO_2). In the meantime, an ATP standard (Mg-ATP stock=100 mM) was prepared in 1.5 mL Eppendorf tubes in the range from 10 nM to 500 µM. The standards were later added to the plate (100 µL/well in triplicates), as well as a blank background control (only cell culture medium). Immediately after, 100 µL of warm Cell Titer Glo® reagent was added per well and the plate was incubated for 15 min under low-light conditions at RT. Luminescence levels (RLU) were measured by using the CLARIOstar microplate reader (Table 35), according to the following protocol:

Table 39. Cell Titer Glo® Luminescent Cell Viability Assay microplate reader protocol.

Type of reading	Top
Focal height	9.0 mm
Gain*	3,600

*Gain was set according to the optimal dynamic range of the analyte.

When using HeLa cells, the seeding was performed one day before measurement. $1x10^4$ cells (siRNA-treated) were seeded per well (at least in triplicates) in an opaque, clear bottom 96-well plate (100 µL/well) in DMEM 10%. The cells were allowed to attach overnight and

the assay was performed as described for the $CD4^+$ T-cells the following day.

ATP levels were calculated by subtracting the background signal and using the standard curve average values (standard form of equation of a line: y=ax+b).

2.2.9 Determination of gene expression

2.2.9.1 Primer design and validation

All human-primer sets used to determine gene expression were designed by using the National Center for Biotechnology Information (NCBI) database. The mRNA sequence of the gene of interest was used to generate a primer pair using the Primer-BLAST function. Important selected primer parameters included: 1) a PCR product size of maximum 200 base pairs, 2) a maximum melting temperature difference of 3 degrees between the single primers, 3) an exon-exon junction span, and 4) an intron separation on the corresponding genomic DNA. These parameters were modified only when a primer pair was unable to be generated as such. The designed sequences were ordered from Sigma, Germany. Lyophilized primers were diluted to 100 µM with RNase-free sterile H_2O. For subsequent reactions, the primers were further diluted to 10 µM.

To evaluate the optimal primer annealing temperature (T_o), a gradient PCR was performed for each primer pair using a thermo cycler. A template cDNA known to highly express the gene of interest (usually effector $CD4^+$ T-cells) was used. The PCR mix for one reaction (25 µL) is given in Table 40:

Table 40. Reaction mix used for one reaction of gradient PCR.

Name	Volume used
OneTaq 2x Master Mix with Standard Buffer (New England BioLabs, Cat# M0482)	12.5 µL
Forward primer (10 µM)	0.5 µL
Revers primer (10 µM)	0.5 µL
Template cDNA (<1000 ng)	1 µL
ddH_2O	10.5 µL

The cycling conditions used for the gradient PCR are shown in Table 41. The temperature gradient range included temperatures between (and including) 54°C and 68°C, with a 2-degree increment.

Table 41. Gradient PCR cycling conditions.

Stage	Temperature (°C)	Time	Cycle number
Initial denaturation	95	30 sec	1
Step 1	95	15 sec	40
Step 2	54-68 (gradient)	20 sec	
Step 3	68	60 sec	
Final extension	68	300 sec	1
Hold	4	Forever	-

The amplified DNA samples were cooled down to 4°C and 5 µL of each sample were loaded on a 1% agarose gel stained with a DNA dye (Table 1). The gel was run for 45 min at 100 V in an electrophoresis chamber. Gel visualization was performed under UV light. The thickest band with the correct size was matched with the temperature used. This temperature was determined as the T_o for that primer set. The remaining 20 µL of the sample at the optimal annealing temperature were loaded on a 1% agarose gel (45 min, 100 V). The obtained band was visualized under UV light and cut out using a clean scalpel. Gel clean-up and DNA purification were performed by using a kit (QIAquick Gel Extraction kit by Qiagen), according to manufacturer's instructions. DNA concentration was measured by using the Nanodrop 2000c. The starting DNA volume for generating a standard curve (amount corresponding to 10^9 copy numbers) was calculated and a 1:10 serial dilution was used to generate a standard curve for each primer set. The standard curve was analysed by quantitative real-time PCR using the Stratagene Mx3000P qPCR System. The master mix and cycling conditions used are shown in Tables 22 and 24. A standard curve was generated automatically through the software, including information such as equation of the line, R-squared, slope, and primer efficiency (E) values, based on the T_o. The E-values (given in Table 19) were used for normalization purposes when estimating gene expression.

All rat-primer sets were kindly provided by Dr. Dmitri Lodygin (group member in the Institute of Neuroimmunology and Multiple Sclerosis Research, Göttingen). Primer sets for mitochondrial-encoded genes were kindly provided by Dr. Sven Dennerlein and PhD student Angela Boshnakovska (group members in the Department of Cellular Biochemistry, Göttingen).

2.2.9.2 RNA isolation

Total RNA from $CD4^+$ T-cells was isolated using the NucleoSpin™ RNA Plus kit, and from HeLa cells by using the NucleoSpin™ RNA Mini (both from Macherey-Nagel), according to manufacturer's instructions. Cells were collected and washed once with 1xDPBS.

The collected cell pellet was lysed and homogenized with 350 µL of lysis buffer (addition of 3.5 µL of β-mercaptoethanol when lysing T-cells). The lysates were filtered through a removal column (provided by the kits) with centrifugation (11,000 rpm, 1 min, RT). The flowthrough was mixed with 350 µL of 70% ethanol and filtered through a NucleoSpin^{TM} RNA column (centrifugation at 11,000 rpm, 1 min, RT). 350 µL of membrane desalting buffer (provided by the kit) were used for salt removal, followed by a 15 min incubation with rDNase digest mix. Three subsequent washing steps were performed (with centrifugation steps at 11,000 rpm, 1 min, RT) and finally RNA was eluted with 40-60 µL of RNase-free H_2O. RNA concentration was measured using the Nanodrop 2000c, keeping the samples on ice. Isolated RNA was immediately used for complementary DNA (cDNA) synthesis, or stored at -80°C until further use.

RNA lysates from rat $CD4^+$ T-cells were kindly prepared by Simon Mole (group member and technical assistant in the Institute of Neuroimmunology and Multiple Sclerosis Research, Göttingen).

2.2.9.3 Reverse transcription and complementary DNA synthesis

Isolated RNA was used as a template for cDNA synthesis with reverse transcription which was utilised to quantify mRNA expression. For this purpose, 200-800 ng of isolated RNA per sample (depending on the obtained concentration) were mixed with 1 µL of Oligo $d(T)_{20}$ (50 µM) (Invitrogen, Cat# 18418-020) and 1 µL of dNTP (10 mM) (Invitrogen, Cat# 18427-013). Denaturation was performed for 5 min at 65°C in a thermo cycler. This was followed by addition of 7 µL of reverse transcription master mix (components per sample given in Table 42). Reverse transcription was performed for 10 min at 50°C, followed by 10 min at 80°C. Synthesized cDNA was diluted 1:10 and used for quantitative real-time PCR or stored at -20°C until further use.

Table 42. Reverse transcription master mix.

Name	Volume used	Company	Catalogue number
5x SSIV buffer	4 µL	Invitrogen	18090200
DTT	1 µL	Invitrogen	D1532
Ribonuclease inhibitor	1 µL	Invitrogen	10777-019
SuperScript IV Reverse Transcriptase	1 µL	Invitrogen	18090200

2.2.9.4 Quantitative real-time polymerase chain reaction (primary human $CD4^+$ T-cells and HeLa cells)

To quantify gene expression in the different human cell types, several primer pairs were used (Tables 19 and 20). 40 µL of master mix (Table 22) were added per well in a RT-qPCR 96-well plate, subsequently adding 10 µL of either pre-diluted cDNA template, or a water (non-template, NT) control. Amplification and detection were analysed by using the Stratagene Mx3000P system. The Ct values were analysed in the MxPro 4.10 software. These values represent the number of PCR cycles after the detection of a fluorescent signal from the sample (above the given threshold).

To calculate the relative expression of the gene of interest, the $2^{-\Delta Ct}$ analysis method was used, where ΔCt represents: $Ct_{\text{gene of interest}} - Ct_{\text{housekeeping gene}}$. The Ct values were normalized to the housekeeping (HK) gene TATA-binding protein (*TBP*) and by primer E-values.

2.2.9.5 Quantitative real-time PCR (rat $CD4^+$ T-cells)

To quantify gene expression in rat $CD4^+$ T-cells, several primer pairs were used (Table 21). 7.5 µL of polymerase master mix (Table 23) were mixed with 3 µL of primer mix (10 µM). 10.5 µL of this mix were added per well in a RT-qPCR 96-well plate, subsequently adding 4.5 µL of either 1:10 pre-diluted cDNA template, or a water (non-template, NT) control.

Amplification and detection were analysed by using the StepOnePlus™ Real-Time PCR system (Thermo Fisher, Cat# 4376600). The Ct values were analysed in the StepOne Software v2.3. To calculate the relative expression of the gene of interest, the $2^{-\Delta Ct}$ analysis method was used, as previously explained. The Ct values were normalized to the HK gene *β actin*.

2.2.9.6 mRNA sequencing

Sample preparation for mRNA sequencing was performed using the same RNA isolation protocol as explained in section 2.2.9.2. Naive, 72-hrs effector, si-MCU-treated, and siMS_Control-treated human $CD4^+$ T-cells from 2 biological repeats were used for this purpose (in duplicate). Samples containing 1500 ng RNA were sent to the NGS Integrative Genomic Core Unit in the Institute of Human Genetics in Göttingen. The HiSeq 4000 sequencing system (Illumina) was used to perform detailed mRNA sequencing.

Analysis of RNAseq data obtained from the Institute of Human Genetics was performed by Christian Ickes (group member in AG Bogeski). Briefly, processed RNAseq data was filtered to identify differentially-expressed genes (DEGs). Candidates for the 'siControl-

siMCU' dataset were selected using a *p*-value cut-off of 0.05. Candidates for the 'naive-effector' dataset were obtained using a false discovery rate (FDR) cut-off of 0.05. Both datasets were further filtered by an absolute logarithmical fold change (log2 FC) of 0.5 and sorted as up- or down-regulated depending on the fold change (up – FC>0; down – FC<0). Significant DEGs were illustrated using volcano plots. Proteomaps were generated by using Bionic Visualisations based on the DEGs in each dataset. Functional annotation of gene ontology of all obtained DEGs was done using PANTHER (Mi et al., 2019). KEGG Pathways were obtained using DAVID Tools (Sherman et al., 2022). Annotated terms and pathways were filtered by an FDR cut-off of 0.05. In order to better interpret gene ontology terms, specific denominations, such as Metabolic Processes (GO:0008152), Immune System Processes (GO:0002376), Mitochondria (GO:0005739), Cell Migration (GO:0016477) and Cell Adhesion (GO:0007155) were selected using QuickGO. For a deeper understanding of the DEGs, sets of human transcription factors and families of integrins and chemokines were shown separately (Bachelerie et al., 2020; Farndale & Jarvis, 2019; Lambert et al., 2018).

2.2.10 Determination of protein expression

To determine expression levels of different proteins in the cell lines used in this study, the Western blot (WB) technique was used. Using this technique, specific proteins of interest can be identified from a mixture of proteins isolated from cells through separation by size and labelling with appropriate antibodies (Mahmood & Yang, 2012).

2.2.10.1 Protein isolation

- $CD4^+$ T-cells:

At least $5x10^6$ $CD4^+$ T-cells per condition (naive, effector, siRNA-treated) were cultured and used for protein extraction. Cells were pelleted and washed once with ice-cold 1xDPBS in order to remove traces of serum, followed by cell lysis with 40 µL of ice-cold protein lysis-DDM buffer (Table 2) (fresh addition of 10x PI). The cells were incubated for 20 min on ice, vortexing once after 10 min to ensure full lysis, and a centrifugation step (max speed, 10 min, 4°C) followed. The supernatant containing isolated proteins was collected in a clean 1.5 mL Eppendorf tube and kept on ice or stored at -80°C until further use.

- HeLa cells:

HeLa cells were grown in 6-well plates up to 70-80% confluence. Prior to lysis, the cells were washed twice with 1xDPBS to remove serum residues and then digested with 300 µL of Trypsin (per well) for 3-5 min. Cells were then collected with 2 mL DMEM 10% culture medium in 15 mL falcon tubes, pelleted and washed once with ice-cold 1xDPBS to remove serum residues. Cell lysis was performed by addition of 50-80 µL of ice-cold protein lysis-DDM buffer (Table 2) (fresh addition of 10x PI), depending on cell confluence. After vortexing and an incubation step of 20 min on ice, the lysates were centrifuged at max speed for 10 min, at 4°C. Supernatants containing isolated proteins were collected in Eppendorf tubes and kept on ice or stored at -80°C until further use.

2.2.10.2 Determination of protein concentration and sample preparation

Protein concentrations were determined by using the Bradford colorimetric assay based on COOMASSIE® Brilliant Blue G-250 (Table 3). Upon binding to proteins, this reagent displays a shift in absorbance from 470 to 595 nm (Bradford, 1976). 1 µL of each isolated protein sample was mixed with 799 µL of ddH_2O and 200 µL of prepared Bradford reagent. 200 µL were loaded per well in a 96-well plate (in triplicate). A BSA standard curve was also generated, in concentrations ranging from 0.5 to 20 µg/mL. Absorbance was measured immediately after plate preparation by using the Berthold Mithras LB 940. Protein concentration of unknown samples was calculated based on the standard curve obtained (standard form of equation of a line: y=ax+b). The absorption measured was directly proportional to the protein present in the sample. All samples were adjusted to the same concentration (25 to 100 µg), mixed with 4x Laemli buffer (+ β-mercaptoethanol) and denatured for 5 min at 95°C before being resolved on SDS-polyacrylamide gels.

2.2.10.3 SDS-PAGE

Sodium dodecyl sulfate polyacrylamide gel electrophoresis (SDS-PAGE) was used for protein separation by molecular weight. The recipes for gel buffers and gel preparations are given in Tables 8-11. Proteins with small molecular weight are able to migrate faster, whereas proteins with high molecular weight migrate slower through the gel. Upon applying a constant electrical field, the proteins migrate towards the anode (positive charge), each with a different speed (Matsumoto et al., 2019).

Denatured samples were loaded onto the prepared polyacrylamide gels (sandwiched between two glass plates) which were placed in an electrophoresis chamber containing running

buffer (Table 4). The Precision Plus Protein™ Dual Color Standard was used as a marker to determine protein size. A constant voltage of 85 V was applied (~2.5 hrs) (refer to Table 35 for device information).

2.2.10.4 Immunoblotting

Following SDS-PAGE, separated proteins were transferred onto a 0.2 µm nitrocellulose membrane using the Trans-Blot® TurboTM Transfer System (Bio Rad). The membrane and transfer stacks (provided by Bio Rad) were pre-equilibrated in ice-cold transfer buffer (Table 5) for 2-3 min. The transfer was assembled as depicted in Figure 9 below:

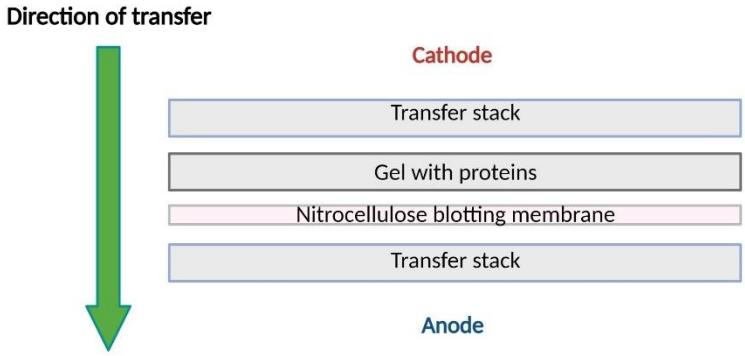

Figure 9. Transfer assembly. The membrane transfer was assembled in the following order (from anode to cathode): transfer paper stack, nitrocellulose membrane, gel, transfer paper stack. Image created in BioRender.

The transfer was performed at 1.3 A and 25 V for 10 min.

After transfer, the membranes were blocked for at least 1 hr with blocking buffer (Table 12). Primary antibody incubation was performed overnight at 4°C (in a 50 mL falcon tube, under rotation). Primary antibodies used and their working dilutions are given in Table 28. Membranes were washed 3 times with 1x TBS-T (Tables 6-7), for 5 min each, and incubated in secondary antibodies (based on species) for 1 hr at RT under low-light conditions, while shaking. Afterwards, the membranes were washed again 3 times with 1x TBS-T, for 10 min each.

Imaging was performed using the Odyssey® CLx system. Bands were quantified using Image Studio™ Lite (normalization with background, and loading or sample controls).

Part of the membranes were incubated in primary antibodies (components of the oxidative phosphorylation chain) and imaged by Dr. Sven Dennerlein (group member in the Department of Cellular Biochemistry, Göttingen).

2.2.11 Fluorescence activated cell sorting (FACS)

To ensure that a pure $CD4^+$ T-cell population has been isolated, FACS analysis was performed. This technique allows for the examination of different cell parameters, including size, granularity and surface protein expression. The used fluorochrome-conjugated antibodies are shown in Table 30.

Initially, $1x10^6$ naive $CD4^+$ T-cells were centrifuged (1000 rpm, 5 min, RT) and washed once with 1xDPBBS. The obtained pellets were resuspended with 100 µL 1xDPBS supplemented with 5% FCS. Subsequently, 2.5 µL of each antibody (Table 30) were added and the cells were incubated under low-light conditions for 25 min at 4°C. The staining scheme was as follows: Single staining with α-CD3, α-CD4 and α-CD8, double staining with α-CD3+α-CD4 and α-CD3+α-CD8, and no staining as a negative control. To remove unbound antibody after incubation, the cells were washed with 1 mL of 1xDPBS supplemented with 5% FCS. Afterwards, the cells were resuspended with 200 µL of 1xDPBS with 5% FCS and stored under low-light conditions (on ice or at 4°C to ensure fluorochrome stability, in FACS tubes). FACS analysis was performed on the FACS Canto II analyser (Table 35). Analysis and gating were done using the FACS Diva software and FlowJo v10.8.0.

2.2.12 Quantification of secreted Interleukin 2 and Interleukin 6

Secreted levels of interleukin 2 (IL-2) and interleukin 6 (IL-6) by $CD4^+$ T-cells were measured using the novel Lumit™ Immunoassay technology by Promega. These assays are based on the NanoLuc® Binary Technology. Antibodies are chemically labelled with small and large subunits of the NanoLuc® luciferase which, when coming into close proximity, are able to form an active luciferase enzyme and generate a bright luminescence signal (Figure 10) proportional to the concentration of the cytokine in question (promega.com). This technology is a good alternative to traditional immunoassays, such as ELISA, since it is much faster, sensitive, and does not require washing steps.

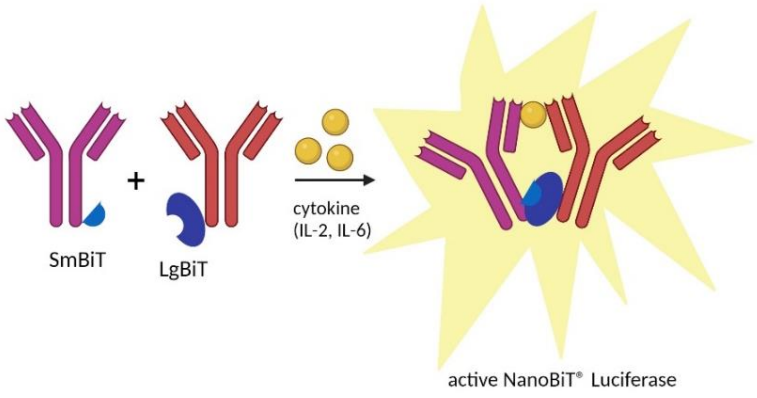

Figure 10. Principle of Lumit Immunoassays. Antibodies labelled with small and large subunits of the luciferase come into close proximity and generate a luminescence signal. Image created in BioRender.

The components included in the assay kits are given in Table 43 below.

Table 43. Components used for Lumit™ Immunoassays.

Name of component
Human IL-2 or IL-6 standard
Lumit™ anti-hIL-2 or anti-hIL-6 mAb-LgBiT
Lumit™ anti-hIL-2 or anti-hIL-6 mAb-SmBiT
Lumit™ Detection substrate B
Lumit™ Detection buffer B

Supernatants collected from $2x10^6$ naive, effector (8 hrs-restimulated), or siRNA-treated (and further 8 hrs-restimulated) $CD4^+$ T-cells were used as templates for the assays. Initially, frozen supernatant samples were diluted 1:100 (except naive cell samples which were not diluted, since low cytokine levels were expected) in the respective cell culture medium (AIM V 10% or RPMI 10%). 50 µL of sample per well were pipetted in triplicates in a black, clear bottom 96-well plate. Afterwards, human-IL-2 or IL-6 standard was prepared in 3.5-fold serial dilutions in cell culture medium (range between 25,000 and 13.6 pg/mL), using the provided standard stock (10 µg/mL). 50 µL per well of each standard, as well as a zero-background control, were pipetted in the same 96-well plate, in duplicate. An antibody mixture of 1:240 diluted mAb-LgBiT and 1:333 diluted mAb-SmBiT was prepared into a single volume of cell culture medium and 50 µL of this mixture were added per sample in the assay plate. The plate was briefly mixed with a plate shaker (300 rpm, 1 min) and was incubated at RT for 70 min under low-light conditions. After the incubation step, the detection reagent was prepared as a 1:20 dilution of Lumit™ Detection substrate B in RT-warmed Lumit™ Detection buffer B. 25 µL of detection reagent were pipetted per well in the assay plate. The plate was mixed with a plate shaker (300 rpm, 2 min) under low-light conditions. Luminescence values were immediately evaluated using the CLARIOstar microplate reader (Table 35), according to the following protocol:

Table 44. Lumit™ Immunoassay microplate reader protocol.

Type of reading	Top
Focal height	11.0 mm
Gain	3,500

*Gain was set according to the optimal dynamic range of the analyte.

Average luminescence readings (RLU) for replicate wells were calculated and the average zero-background control was subtracted from each sample and standard. A standard curve was generated from the known standard concentrations and was used to calculate the cytokine concentration of unknown samples (standard form of equation of a line: y=ax+b). Microsoft Excel 2019 and GraphPad Prism 9 were used for calculation and plotting purposes.

2.2.13 Interferon gamma enzyme-linked immunosorbent assay (ELISA)

Secretion of IFNγ by $CD4^+$ T-cells was measured with the sandwich ELISA method (Table 32 for kit information). This method uses a capture and a detection antibody, thus "sandwiching-in" the target antigen in-between. The detection antibody is bound to an HRP-label which is used for detection (using 3,3',5,5-tetramethylbenzidine; TMB) and quantification. The advantage of this technique is the high sensitivity and specificity for the target antigen (*Overview of ELISA - DE*, n.d.).

Supernatants collected from $2x10^6$ siRNA-treated (and further 8 hrs-restimulated) $CD4^+$ T-cells were used to determine their IFNγ secretion levels. Initially, frozen supernatant samples were diluted 1:50 in their cell culture medium (RPMI 10%).

Further steps were performed by Lena Krause, PhD student (group member in AG Bogeski). Briefly, a 96-well plate was coated with capture antibody at 4°C overnight. The next day, the plate was washed 3 times with 1xDPBS + 0,1% Tween for 30 sec, and then 3 times with 1xDPBS. The wells were blocked with ELISA/Elispot solution (provided by the kit) (200 µL per well) for 1 hr at RT. Afterwards, the plate was washed again as described, and 100 µL of diluted samples or standards (2-fold serial dilutions) were added per well (in triplicates). An incubation step of 2 hrs at RT followed. After sample incubation, a washing step was applied and then incubation with detection antibody (1:250 in ELISA/Elispot solution; provided by the kit) followed for 1 hr at RT. The plate was washed again and 100 µl/well of Streptavidin-HRP conjugate were added (provided by the kit). After an incubation step of 30 min at RT, the plate was washed and 100 µL/well of TMB solution (provided by the kit) were added. Incubation step of 15 min at RT followed. Finally, 100 µL/well of stop solution (H_2SO_4 2 N) were added quickly and absorbance was measured using the CLARIOstar microplate reader (excitations at 450 and 570 nm).

Values at 570 nm were subtracted from values at 450 nm for each well. Average values for replicate wells were calculated and the average zero-background control was subtracted from each standard. A standard curve was generated from the known standard concentrations and was used to calculate IFNγ concentration of unknown samples (concentration was

calculated based on the slope-intercept formula applied to the standard curve). Microsoft Excel 2019 and GraphPad Prism 9 were used for calculation and plotting purposes.

2.2.14 Trans-well human $CD4^+$ T-cell migration and invasion

$CD4^+$ T-cells (siRNA-treated) were kept in RPMI (w/o FCS) culture medium (starvation period) for 3 hrs in standard culture conditions (37ºC, 5% CO_2). In the meantime, conditioned media were prepared: 1) supernatant from the $CD4^+$ T-cells used for the assay – addition of 10% FCS and 2) collected medium from 70-90% confluent 1205Lu melanoma cells (provided by Wistar Institute; lung metastatic melanoma cell line) – addition of 10% FCS (prepared by Andrea Paluschkiwitz, technical assistant in AG Bogeski). Both media were filtered through 0.2 µm sterile filters (Sarstedt, Cat# 83.1826.001) and kept at RT until further use. After the starvation period, 750 µL of conditioned medium were pipetted per well (in triplicate) in 24-well cell culture plate. A working dilution of 50 ng/mL was added from both CXCL12 and CCL19 to establish a chemokine gradient (Table 31). Subsequently, $1x10^6$ $CD4^+$ T-cells were subjected to a trans-well assay by pipetting 200 µL per trans-well insert (5 µm pore, Costar Life Sciences) (Table 34). For invasion assays, the trans-well inserts were coated for 1 hr at 37°C with 40 µL of Matrigel (1:1 dilution in RPMI w/o FCS). Cells were allowed to migrate for 4 hrs. Quantification of total migrated cells in conditioned media was achieved by cell counting using the Countess™ 3 Automatic Cell Counter.

2.2.15 Determination of mitochondrial respiration and ATP production rate

Mitochondrial respiration rates were assessed using the Seahorse XF Mito Stress Test (Seahorse XFe by Agilent). This assay evaluates mitochondrial function by directly measuring the oxygen consumption rate (OCR) using well-established precise O_2 sensors (agilent.com).

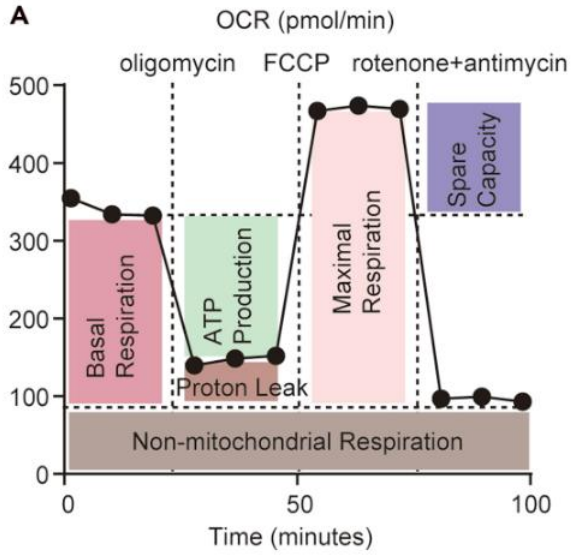

Figure 11. A scheme illustrating mitochondrial stress test according to drugs injected. (Image taken from Gotoh et al., *Star Protocols*, 2021).

Figure 11 shows the injection sequence of the drugs used throughout the assay and the parameters that can be obtained. Oligomycin is a Complex V (ATP synthase) inhibitor of the oxidative phosphorylation system in mitochondria. It causes a decrease in electron flow, resulting in a reduction in OCR which is linked to mitochondrial ATP production. Carbonyl cyanide-4-(trifluoromethoxy)-phenylhydrazone (FCCP; carbonylcyanide-3-chlorophenyl-hydrazone (CCCP) can also be used) is an uncoupler which causes disrupted mitochondrial membrane potential. As a result, electron flow is uninhibited and OCR reaches maximal values. The last drugs injected are rotenone, a Complex I inhibitor, and antimycin A, a Complex III inhibitor of the oxidative phosphorylation system. This combination completely shuts mitochondrial respiration down and enables the calculation of non-mitochondrial respiration (Gotoh et al., 2021).

In addition, the Seahorse XFe system has the possibility to simultaneously measure release of protons (H^+) via glycolysis and the Krebs cycle, thereby estimating mitochondrial ATP production rate in live cells. After addition of the inhibitors oligomycin and rotenone + antimycin A, pathway-specific mitochondrial ATP and glycolytic ATP production rates can be calculated. For this study, mitochondrial ATP production rates were of interest. Calculation was performed according to the formulas given below:

1) OCR_{ATP} (pmol O_2/min) = OCR (pmol O_2/min) – $OCR_{Oligomycin}$ (pmol O_2/min),

where $OCR_{Oligomycin}$ represents the OCR inhibited by addition of oligomycin, and

2) mitoATP (pmol ATP/min) = OCR_{ATP} (pmol O_2/min) x 2 x P/O (pmol ATP/pmol O),

where P/O is the number of ADP molecules to ATP per atom of O reduced by an electron pair (a value of P/O=2.75 has been validated to accurately represent the assay conditions and is taken as a standard) (agilent.com).

2.2.15.1 $CD4^+$ T-cells

One day prior to performing the assay, the wells of a 96-well Seahorse well plate (Table 34) were coated and maintained at 4°C with 50 µg/mL poly-D-lysine (20 µL per well) overnight. A sensor cartridge was hydrated with Seahorse XF calibrant solution (Agilent, Cat# 100840-000) and incubated in a non-CO_2 incubator (37°C) (Agilent) overnight (prepared by Tanja Gall, group member in the Department of Cellular Biochemistry, Göttingen).

On the day of the assay, a required number of $CD4^+$ T-cells (naive, effector or siRNA-treated) were harvested and resuspended in Seahorse XF medium (containing 4.5 g/L glucose, 1 mM Na-pyruvate and 2 mM L-glutamine). The poly-D-lysine was removed from the 96-well plate, the wells were washed once with sterile ddH_2O and the plate was allowed to dry for 3-4 min at RT. Afterwards, $2x10^5$ $CD4^+$ T-cells were seeded (180 µL per well) (several replicates; depending on number of conditions included) and allowed to settle and attach in a non-CO_2 incubator (37°C) for 1 hr. Corner wells were left blank (only XF medium). In the meantime, the drug cartridge was loaded with the respective drugs diluted in Seahorse XF medium according to the Table 45 below:

Table 45. Drugs used for Seahorse mitochondrial respiration assay.

Name of drug	Stock Concentration	Volume of Seahorse XF medium	Working concentration
Oligomycin	50 mM	5 mL	30 µM
CCCP	100 mM	5 mL	10 µM
Antimycin A	10 mM	5 mL	10 µM
Rotenone	10 mM		10 µM

The respective drug dilution was loaded in the cartridge by using an automatic multichannel pipette according to the following scheme:

Port A: 20 µL of oligomycin

Port B: 22 µL of CCCP

Port C: 25 µL of rotenone + antimycin A

System calibration was performed and the assay was run for approximately 2 hrs.

For quantification of mitochondrial ATP production rate in $CD4^+$ T-cells, the same protocol was used, without injecting CCCP.

Normalization according to viable cell number was performed by PhD student Angela Boshnakovska (group member in the Department of Cellular Biochemistry, Göttingen) using the CyQUANT™ Cell Proliferation Assay kit (Thermo Fisher, Cat# C7026), following manufacturer instructions.

Quantification was performed using the Seahorse Wave Desktop Software. Data were plotted and statistics were performed using GraphPad Prism 9.

2.2.15.2 HeLa cells

One day before measurement, siRNA-treated HeLa cells were digested by using Trypsin. $0.7x10^5$ cells were seeded (200 µL per well) (several replicates depending on number of conditions used) in DMEM 10% cell culture medium, in a 96-well Seahorse well plate. Corner wells were left blank. The sensor cartridge was hydrated as explained in the previous paragraph.

On the day of measurement, DMEM 10% was aspirated from the cells, and the cells were washed once with 1xDPBS. Afterwards, 180 µL of warm Seahorse XF medium (containing 4.5 g/L glucose, 1 mM Na-pyruvate and 2 mM L-glutamine) were added per well. The plate was incubated in a non-CO_2 incubator (37°C) for 45-60 min. The rest of the assay, the normalization and the quantification were performed in the same way as previously described for $CD4^+$ T-cells.

2.2.16 Cytosolic calcium and store-operated calcium entry measurements

Cytosolic Ca^{2+} and SOCE were measured at RT in naive and effector $CD4^+$ T-cells by using live-cell fluorescence imaging on a fluorescence microscope equipped with an Axiovert S100TV (Zeiss), pE340Fura (CoolLED) and a sCMOS camera pco edge. Data acquisition was performed with the VisiView 2.1.2 software, data processing and statistics with Microsoft Excel 2019, and plotting with GraphPad Prism 9.

2.2.16.1 Sample preparation

$CD4^+$ T-cells ($2x10^5$) (naive, effector, or siRNA-treated) were resuspended and stained with 1 µM of Fura2-AM (Table 27) for 30 min at RT under low-light conditions. Fura2-AM is a ratiometric $_cCa^{2+}$ indicator, characterized by a high affinity for Ca^{2+} ions and its relatively easy use compared with other fluorescence-based dyes. The excitation ratio of 340 nm/380 nm

(emission=510 nm) allows accurate measurements of $_c[Ca^{2+}]$ (*Fura-2, AM*, n.d.). After staining, the cells were pelleted down (5 min, 800 rpm) and washed once with working Ringer's solution (1 mM Ca^{2+}, refer to Table 15) to remove unbound dye. The cells were then left to attach for 20 min on a 25 mm coverslip previously coated with 100 µL of 1:10 diluted poly-L-ornithine (Table 1), under low-light conditions.

2.2.16.2 $_c[Ca^{2+}]$ measurements (short protocol)

A coverslip containing attached naive $CD4^+$ T-cells was assembled on an open custom-made microscopy chamber ring which allows for direct addition of stimulants throughout the measurement. The coverslip was washed twice gently and the cells were allowed to settle in 300 µL of working 1 mM Ca^{2+} Ringer's solution.

The measurement protocol according to cycle number (1 cycle = 5 sec) is given in Table 46:

Table 46. Short protocol used for $_c[Ca^{2+}]$ measurements upon $CD4^+$ T-cell activation.

Number of measurement cycle	Solution/Stimulant used
0-Start of protocol	1 mM Ca^{2+} Ringer's solution
24	CD3+CD28 beads or Antibody solution
120-Stop of protocol	-

Fura2-AM measurement settings used are given in Table 47:

Table 47. Fura2-AM measurements settings used for $_c[Ca^{2+}]$ measurements.

Excitation 1	340 nm (25% LED intensity, 30 msec exposure time)
Excitation 2	380 nm (5% LED intensity, 30 msec exposure time)
Dichroic mirror	T400 LP
Emission	510 nm
Objective used	40x (N. A 1.3) oil
Cycle interval	5 sec

Naive $CD4^+$ T-cell activation was performed by adding either 50 µL of CD3+CD28 antibody solution, or 50 µL of washed beads resuspended in working 1 mM Ca^{2+} Ringer's solution. Bead-activated T-cells were chosen for analysis by only selecting the cells that came into contact with a bead throughout the measurement. When antibody solution was used, all cells were selected. Background-corrected data were exported and analysed using Microsoft Excel 2019, and plotted as average ratio of F340/380 nm over time (min) using GraphPad Prism 9.

2.2.16.3 SOCE measurements (long protocol)

A coverslip containing attached $CD4^+$ T-cells was assembled on a closed custom-made microscopy chamber (Figure 12) which allows for cell perfusion with different solutions. A 2 mL syringe was loaded with the first measurement solution (0.5 mM Ca^{2+} Ringer's solution) and was connected to the tube leading to the fixed chamber. The cells were perfused twice with the first measurement solution and were left to settle for 2-3 min before starting the measurement.

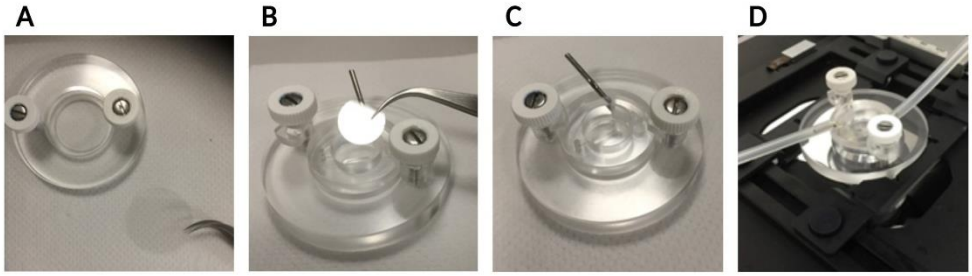

Figure 12. Closed microscopy chamber setup for long $_c[Ca^{2+}]$ measurements with a perfusion system. The chamber (**A**) is closed with a smaller ring covered by a 12 mm coverslip (**B**). This ring contains two tube openings (**C**) which connect to a perfusion system (**D**).

After obtaining a baseline, the chamber was perfused with Ca^{2+}-free Ringer's solution to deplete $_cCa^{2+}$. To achieve ER Ca^{2+} store depletion, the cells were perfused with Ca^{2+}-free Ringer's solution containing 1 µM of thapsigargin (Tg), followed by a small increase in intracellular $[Ca^{2+}]$, which quickly returns to baseline. SOCE was measured by re-addition of 1 mM Ca^{2+} Ringer's solution containing 1 µM Tg, which resulted in a sharp intracellular $[Ca^{2+}]$ increase. A detailed protocol according to cycle number (1 cycle = 5 sec) is given in Table 48:

Table 48. Long protocol used for SOCE measurements.

Number of measurement cycle	Solution/Stimulant used
0-Start of protocol	0.5 mM Ca^{2+} Ringer's solution
20	0 mM Ca^{2+} Ringer's solution
60	0 mM Ca^{2+} Ringer's solution + Tg
160	1 mM Ca^{2+} Ringer's solution + Tg
260-Stop of protocol	-

Fura2-AM protocol settings, data acquisition and analyses were performed the same as described in 2.2.16.2 (Table 47). Average F340/380 nm ratios were further normalized to T-cell volume (in μm^3) and plotted as normalized F340/380 over time (min).

2.2.17 Mitochondrial calcium measurements

2.2.17.1 Human $CD4^+$ T-cells and HeLa cells

Mitochondrial Ca^{2+} ($_mCa^{2+}$) measurements were performed at 37°C in both $CD4^+$ T-cells (naive, effector, siRNA-treated, inhibitor-treated) and HeLa cells by using live-cell fluorescence imaging on a fluorescence Zeiss D1 Cell Observer microscope equipped with a 40x oil Neofluar (N. A 1.3) objective, Axiocam 702 mono and LED system (Colibri, Zeiss). Data acquisition was performed with the Zen 2.6 software, data processing and statistics with Microsoft Excel 2019, and plotting with GraphPad Prism 9.

Transient transfection with plasmid DNA was performed as previously described in section 2.2.5 using the ratiometric $_mCa^{2+}$ biosensor Ratiometric MT3.1 Pericam (Nagai et al., 2001). This biosensor consists of yellow fluorescent protein (YFP) tagged with calmodulin-binding protein and a mitochondrial-targeting sequence. Upon an increase in $[Ca^{2+}]$, calmodulin binds to calmodulin-binding protein, leading to a conformational change in the biosensor which causes a shift in the excitation peak from 415 to 494 nm, while the emission spectrum remains the same (515 nm) (Figure 13).

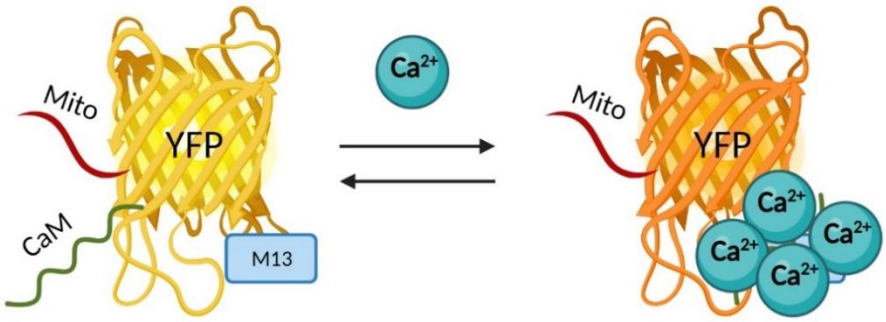

Figure 13. Structure of Ratiometric MT3.1 Pericam. Image created in BioRender (based on Nagai et al., 2001).

Sample preparation for $CD4^+$ T-cells was performed as previously mentioned in section 2.2.16.1. HeLa cells had already been seeded on coverslips and transfected for 48 hrs before measurements. The measurement protocols and settings used are given in Tables 49, 50 and 51 below:

Table 49. Short protocol used for $_m[Ca^{2+}]$ measurements in $CD4^+$ T-cells (using 1 mM Ca^{2+} Ringer's solution).

Number of measurement cycle	Solution/Stimulant used
0-Start of protocol	1 mM Ca^{2+} Ringer's solution
120	4 µM Ionomycin
180-Stop of protocol	-

Table 50. Short protocol used for $_m[Ca^{2+}]$ measurements in HeLa cells (using 0.5 mM Ca^{2+} Ringer's solution).

Number of measurement cycle	Solution/Stimulant used
0-Start of protocol	1 mM Ca^{2+} Ringer's solution
30	100 µM Histamine
130-Stop of protocol	-

Table 51. MT3.1 Pericam measurements settings used for $_m[Ca^{2+}]$ measurements.

	T-cells	HeLa
Excitation 1	420 nm (30% LED intensity, 50 msec exposure time)	420 nm (20% LED intensity, 10 msec exposure time)
Excitation 2	505 nm (30% LED intensity, 90 msec exposure time)	505 nm (20% LED intensity, 20 msec exposure time)
Filter	HyPer (BS: 515; Em: 539/25) *	HyPer (BS: 515; Em: 539/25)
Objective used	40x (N. A 1.3) oil	40x (N. A 1.3) oil
Cycle interval	2 sec	2 sec

BS=Beam splitter; Em=emission filter

Single cell measurement points were analysed and plotted as a MT3.1 Pericam 420/505 nm ratio (normalized to background fluorescence and T-cell volume when required) over time (min).

2.2.17.2 Rat $CD4^+$ T-cells

Rat $CD4^+$ effector T-cells were designed to express the Ca^{2+} biosensor GCaMP6s, containing a mitochondrial targeting sequence and a fluorescent tag Scarlet (see section 2.2.25 and Figure 14). The 4 different cell lines generated were used to measure basal $_m[Ca^{2+}]$ and $_mCa^{2+}$ uptake upon both physiological and non-physiological stimulation via live-cell fluorescence imaging on a fluorescent Zeiss D1 Cell Observer microscope. Data acquisition was performed with the Zen 2.6 software, data processing and statistics with Microsoft Excel 2019, and plotting with GraphPad Prism 9.

GCaMP biosensors, similarly to Ratiometric MT3.1 Pericam, consist of circularly permuted fluorescent proteins; in this case green fluorescent protein (GFP), a calcium-binding

protein calmodulin, and calmodulin-interacting M13 peptide (peak excitation = 480 nm; peak emission = 510 nm) (Chen et al., 2013). The fluorescent tag Scarlet (excitation peak = 569 nm; emission peak = 594 nm) was added to enable more accurate ratiometric calculations of $[_{m}Ca^{2+}]$.

T-cells (~$2x10^5$) were resuspended and a centrifugation step was applied (1000 rpm, 5 min, RT). The pellet was resuspended in 40 µL of TCGF medium and left to attach onto a poly-L-ornithine-coated 25 mm coverslip. The chamber was set up as described previously in section 2.2.16.2. The measurement protocols and settings used are given in Tables 52 and 53 below:

Table 52. Measurement protocol used for $_{m}[Ca^{2+}]$ measurements in rat $CD4^+$ T-cells (using 1 mM Ca^{2+} Ringer's solution).

Number of measurement cycle	Solution/Stimulant used
0-Start of protocol	1 mM Ca^{2+} Ringer's solution
50	α-rat CD3+CD28 + α-mouse cross-linker Ab (1:1000)
150	4 µM ionomycin
200-Stop of protocol	-

Table 51. GCaMP-Scarlet measurement settings used for $_{m}[Ca^{2+}]$ measurements.

Excitation 1	505 nm (100% LED intensity, 30 msec exposure time)
Excitation 2	555 nm (100% LED intensity, 5 msec exposure time)
Filters	HyPer (BS: 515; Em: 539/25); R-GECO (BS: 573; Em: 630/92)
Objective used	40x (N. A 1.3) oil
Cycle interval	5 sec

BS=Beam splitter; Em=emission filter

Data were analysed and plotted as a 505/555 nm ratio (normalized to background fluorescence) over time (min).

2.2.18 Mitochondrial membrane potential measurements

Mitochondrial membrane potential (ΔΨm) is dependent on the active transfer of positively charged protons across the inner mitochondrial membrane upon ATP production. This transfer results in a net negative charge maintained around -140 mV which can be detected by staining the cells with positively charged dyes, such as tetramethylrhodamine ethyl ester (TMRE) and 5,5,6,6'-tetrachloro-1,1',3,3' tetraethylbenzimi-dazoylcarbocyanine iodide (JC-1). ΔΨm is important for maintaining mitochondrial homeostasis through elimination of dysfunctional mitochondria. It is also a driving force for transport of ions and proteins necessary for healthy mitochondria (Zorova et al., 2018). Therefore, investigating the possible

role of MCU in regulating ΔΨm, and thereby proper mitochondrial function, is of great importance.

2.2.18.1 TMRE

TMRE emits red fluorescence (excitation = 548 nm; emission = 575 nm) which can be detected by fluorescence microscopy (Crowley et al., 2016). The fluorescence Zeiss D1 Cell Observer microscope was used to perform TMRE measurements. Data acquisition was performed with the Zen 2.6 software, data processing and statistics with Microsoft Excel 2019 and ImageJ/Fiji, and plotting with GraphPad Prism 9.

$2x10^5$ $CD4^+$ T-cells per donor (naive, effector or siRNA-treated) were stained with 100 nM TMRE (Table 27) for precisely 15 min at RT under low-light conditions. The cells were later washed once with working Ringer's solution (1 mM [Ca^{2+}]) to remove unbound dye, and left to attach on previously-coated coverslips with poly-L-ornithine. Table 53 below shows the protocol used for these measurements, and Table 54 shows the measurement settings.

In order to investigate changes in ΔΨm upon $CD4^+$ T-cell activation, cells were treated with either CD3+CD28 Ab solution, CD3+CD28 Ab solution + Orai inhibitor CM4620 (1 µM), CD3+CD28 Ab solution + MCU inhibitor Mitoxantrone (10 µM), or CD3+CD28 Ab solution + DMSO control. Measurements were performed from baseline until 150 min after cell treatment (measuring every 30 min in between).

Table 53. Protocol used for TMRE ΔΨm measurements (using 1 mM Ca^{2+} Ringer's solution).

Number of measurement cycle	Solution/Stimulant used
0-Start of protocol	1 mM Ca^{2+} Ringer's solution
60	2 µM CCCP
120-Stop of protocol	-

Table 54. TMRE measurements settings.

Excitation	555 nm (20% LED intensity, 3 msec exposure time)
Filter	R-GECO (BS: 573; Em: 630/92)
Objective used	40x (N. A 1.3) oil
Cycle interval	2 sec

BS=Beam splitter; Em=emission filter

Data were analysed, normalized to cell volume, and plotted as mean fluorescence intensity (normalized to background fluorescence) over time (min). ImageJ/Fiji was used to quantify pixel intensity and particle size, based on mean gray levels.

2.2.18.2 JC-1

JC-1 dye is a lipophilic, cationic dye able to stain mitochondria, where it accumulates and starts forming complexes called J-aggregates in a concentration-dependent manner. J-aggregates exhibit excitation and emission in the red spectrum (550 and 600 nm), whereas JC-1 itself exhibits excitation and emission in the green spectrum (485 and 585 nm). In healthy cells with a normal ΔΨm, the dye accumulates in negatively charged mitochondria and spontaneously forms red fluorescent J-aggregates, therefore it can be used as a ratiometric measurement of ΔΨm (Sivandzade et al., 2019).

$2x10^5$ $CD4^+$ T-cells per donor (naive or effector) were stained with 500 nM JC-1 (Table 27) for 20 min at RT under low-light conditions. The cells were washed once with working Ringer's solution (1 mM [Ca^{2+}]) to remove unbound dye, and left to attach on previously-coated coverslips. Table 55 below shows the protocol used for these measurements, and Table 56 shows the measurement settings.

Table 55. Protocol used for JC-1 ΔΨm measurements (using 1 mM Ca^{2+} Ringer's solution).

Number of measurement cycle	Solution/Stimulant used
0-Start of protocol	1 mM Ca^{2+} Ringer's solution
60	2 μM CCCP
100-Stop of protocol	-

Table 56. JC-1 measurements settings.

Excitation – red	550 nm (20% LED intensity, 2 msec exposure time)
Excitation – green	485 (20% LED intensity, 2 msec exposure time)
Filter 1	R-GECO (BS: 573; Em: 630/92)
Filter 2	HyPer (BS:5 15; Em: 539/25)
Objective used	40x (N. A 1.3) oil
Cycle interval	2 sec

BS=Beam splitter; Em=emission filter

Data were analysed and plotted as red/green ratio (normalized to background fluorescence) over time (min).

2.2.19 Glutathione redox potential measurements

To explore the role of redox processes in $CD4^+$ T-cells and their mitochondria, and to further investigate the influence of MCU influences on redox dynamics, glutathione redox potential (E_{GSH}) was measured in cell cytosol and locally in mitochondria by using live-cell

fluorescence imaging. Data acquisition and analyses were performed as mentioned in section 2.2.17.

Transient plasmid DNA transfection was performed in siRNA-treated $CD4^+$ T-cells as previously described in section 2.2.5, using the two plasmids Grx1-roGFP2 and mitoGrx1-roGFP2 (Table 26).

Glutathione (GSH) plays an important role in ROS scavenging, reduction of disulphide bonds, and protection from irreversible oxidation. It is synthesized in the cytosol and transported to other compartments of the cell, including mitochondria. In order to keep its surrounding environment reduced, GSH is oxidized to glutathione disulphide (GSSG). NADPH-dependent enzymes (GSH reductases) are required to maintain GSH in its reduced state (Kojer et al., 2012). Mitochondria harbour various redox pathways which influence GSH pools, therefore it is important to investigate whether MCU plays a role in this regard. Redox-sensitive green fluorescent proteins (roGFPs) (excitation at ~400 and ~490 nm; emission at ~510 nm) have been designed to sensitively report GSH and GSSG, allowing for dynamic live imaging of E_{GSH} in different cellular compartments (Gutscher et al., 2008). The Grx1-roGFP plasmids consist of human glutaredoxin-1 (Grx1) fused to the N-terminus of roGFP2 (with or without a mitochondrial-targeting sequence). To estimate E_{GSH} from fluorescence ratio measurements, the minimal and maximal fluorescence ratios (at excitation 490 nm) are determined, corresponding to 100% biosensor reduction and oxidation respectively. These can be used to approximate the degree of sensor oxidation (OxD_{roGFP2}), which is further used for E_{roGFP} estimation.

Sample preparation of $CD4^+$ T-cells was performed as previously mentioned in section 2.2.16.1. The measurement protocol and settings used are given in Tables 57 and 58 below:

Table 57. Protocol used for cytosolic and mitochondrial glutathione redox potential measurements in $CD4^+$ T-cells (using 1 mM Ca^{2+} Ringer's solution).

Number of measurement cycle	Solution/Stimulant used
0-Start of protocol	1 mM Ca^{2+} Ringer's solution
60	200 µM H_2O_2 - oxidation
150	100 µM DTT - reduction
250-Stop of protocol	-

Table 58. Grx1-roGFP2 measurements settings used.

Excitation 1	400 nm (50% LED intensity, 100 msec exposure time)
Excitation 2	505 nm (50% LED intensity, 20 msec exposure time)
Filter	YFP (BS: 520; Em: 542/27)
Objective used	40x (N. A 1.3) oil
Cycle interval	3 sec

BS=Beam splitter; Em=emission filter

Data were analysed and plotted as a 400/505 nm ratio (normalized to background fluorescence) over time (min).

2.2.20 Cytosolic and mitochondrial hydrogen peroxide measurements

To investigate whether MCU influences H_2O_2 production in $CD4^+$ T-cells, live-cell fluorescence imaging was performed on naive, effector and siRNA-treated cells. Measurements were performed as described in section 2.2.17.

Transient cell transfection with the biosensors HyPer3 and HyPer-dMito (Table 26) was performed as previously mentioned in section 2.2.5.

H_2O_2 is the most commonly produced ROS molecule as a product of incomplete O_2 reduction. It acts as an important second messenger in many signalling pathways, selectively oxidizing protein cysteine residues (Lambert & Brand, 2009). T-cell activation is known to cause significantly increased H_2O_2 production, in both mitochondria and cytosol (Siemoni & Bogeski, 2015). Therefore, it is of interest to investigate effects of MCU on H_2O_2 levels. HyPer biosensors consist of circularly permutated YFP (excitation 420 and 500 nm; emission 516 nm) integrated into a domain of H_2O_2-sensing protein Oxy-RD (Bilan et al., 2013) which contains two cysteine residues. Upon increase in H_2O_2, these cysteines form a disulphide bond, causing a shift in the excitation peak at 420 nm which decreases proportionally to the increase in the peak at 500 nm, such that ratiometric measurements of H_2O_2 levels can be achieved. The design of HyPers allows for measurements in different cell compartments, such as mitochondria, by including targeting sequences.

Sample preparation for $CD4^+$ T-cells was performed as previously mentioned in section 2.2.16.1. The measurement protocol and settings used are shown in Tables 59 and 60 below:

Table 59. Protocol used for cytosolic and mitochondrial H_2O_2 measurements (using 1 mM Ca^{2+} Ringer's solution).

Number of measurement cycle	Solution/Stimulant used
0-Start of protocol	1 mM Ca^{2+} Ringer's solution
100	100 µM H_2O_2
200-Stop of protocol	-

Table 60. HyPer measurements settings used.

Excitation 1	420 nm (30% LED intensity, 30 msec exposure time)
Excitation 2	505 nm (30% LED intensity, 90 msec exposure time)
Filter	HyPer (BS: 515; Em:5 39/25)
Objective used	40x (N. A 1.3) oil
Cycle interval	2 sec

BS=Beam splitter; Em=emission filter

Data were analysed and plotted as a 505/420 nm ratio (normalized to background fluorescence) over time (min).

2.2.21 Mitochondrial protein translation-^{35}S metabolic labelling

The mitochondrial genome contains 37 genes, out of which 13 encode for proteins part of the oxidative phosphorylation chain and the rest encode for ribosomal and transfer RNAs necessary for mitochondrial protein translation. Labelling of mitochondrial translation proteins is useful for the assessment of global rates of synthesis of the 13 proteins and can easily be visualized on a gel (Yousefi et al., 2021). Since alterations in the mitochondrial machinery can lead to changes in translation, labelling was performed on naive, effector and siRNA-treated T-cells.

Naive T-cells were activated with beads, according to the protocol outlined previously, for 24, 48 and 72 hrs, and the two MCU knockdown models were generated as described in section 2.2.5.2. To perform the assay, $2x10^6$ cells were used. The entire labelling procedure, gel preparation and visualization were performed by Dr. Sven Dennerlein (group member in the Department of Cellular Biochemistry, Göttingen).

Briefly, $2x10^6$ T-cells were pelleted and resuspended in 1 mL of serum- and methionine-free medium in a low-binding tube. Cells were then treated with emetine (inhibitor of cytoplasmic translation) for 10 min at 37°C, followed by labelling with 20 µL of ^{35}S methionine for 60 min. The labelled cells were then harvested, washed with cold 1xDPBS and protein concentration was determined using a Bradford assay. 40 µg of the total protein

(with loading dye) was loaded onto a Tris-Tricine gel and run overnight at 80 V, 25 mA. Protein transfer was performed the following day and the membrane was scanned on a radioactive plate.

The 13 mitochondrially synthesized proteins were visualized and normalized to the respective control for quantification. Quantification was performed using the Image Studio Lite Ver 5.2 software.

2.2.22 $CD4^+$ T-cell treatment with MCU inhibitor Ruthenium 265

Naive and effector $CD4^+$ T-cells were treated with a range of concentrations (50-200 µM) of the novel MCU inhibitor Ruthenium 265 (Ru265) (Woods et al., 2019), for 24 hrs before performing further experiments (mitochondrial calcium measurements, mitochondrial membrane potential measurements, and proliferation assays). Treatments were performed in 24-well plates (cells seeded in 1mL cell culture medium per well), or 96-well plates when assessing proliferation (cells were seeded in 100 µL cell culture medium per well).

2.2.23 $CD4^+$ T-cell treatment with H_2O_2-measurement of antioxidant properties

siRNA-treated $CD4^+$ T-cells were used to investigate the effect of MCU on antioxidant properties. Cells were seeded in 96-wells plates ($0{,}5x10^5$ cells/well) (in triplicates) and treated with different H_2O_2 concentrations: 0.1 µM; 1 µM, 10 µM, 25 µM, 50 µM, and 100 µM. Proliferation assays were performed using the Cell Titer Blue® Cell Viability Assay as described in section 2.2.7. Proliferation rates were plotted for each [H_2O_2] per time (hrs) of measurement.

2.2.24 Mitochondrial ATP measurements in HeLa cells using live-cell imaging

Mitochondrial ATP was measured in siRNA-treated HeLa cells using the BioTracker ATP-Red Live Cell Dye (Table 27) (Wang et al., 2016). Data acquisition and analyses were performed on the Zeiss D1 Cell Observer microscope as described in section 2.2.17.

HeLa cells (~$0{,}5x10^5$) were loaded with 5 µM working dye solution (stock 10 mM in DMSO) for 15 min at 37°C. Measurements were performed in 0.5 mM [Ca^{2+}] Ringer's solution. The coverslips were washed with the solution 4-5 times before the measurement to remove unbound dye. The measurement protocol and settings used are given in Tables 61 and 62 below:

Table 61. Protocol used for mitochondrial ATP measurements (using 0.5 mM Ca^{2+} Ringer's solution).

Number of measurement cycle	Solution/Stimulant used
0-Start of protocol	0.5 mM Ca^{2+} Ringer's solution
36	5 mM Mg-ATP
80	4 µM CCCP
100-Stop of protocol	-

Table 62. ATP-Red measurements settings used.

Excitation 1	555 nm (80% LED intensity, 4 msec exposure time)
Filter	R-GECO (BS: 573; Em: 630/92)
Objective used	40x (N. A 1.3) oil
Cycle interval	10 sec

BS=Beam splitter; Em=emission filter

Single cells were selected and analysed by calculating the mean fluorescence intensity normalized to background signal using Microsoft Excel 2019. The mean of all cells per group was plotted against the time (min) using GraphPad Prism 9.

2.2.25 Rat $CD4^+$ T-cell culture and retroviral transduction

2.2.25.1 Design and cloning of expression constructs for targeting *MCU* in rat effector T-cells

Design, cloning and testing of expression constructs for this project was performed in collaboration with Dr. Dmitri Lodygin (group member in the Molecular and Cellular Neuroimmunology group at the Institute of Neuroimmunology and Multiple Sclerosis Research, Göttingen). The aim was to generate stable T-cell lines with MCU downregulation. To this end, cultures were established from Lewis rats ubiquitously expressing transgenic Cas9 nuclease. Gene editing in this system can be achieved by T-cell transduction with retroviruses encoding short guide RNA (sgRNA) (e.g. Puro2A-TurqFP-U6 vector, Figure 14A). Three different sgRNAs were designed for targeting MCU (each one targeted to a different site of the *MCU* gene (refer to S Table 2 for sequence information). One sgRNA was designed as a control, targeting the ubiquitously-expressed non-coding locus Rosa26. Each sgRNA construct was cloned into the BbsI site downstream of the U6 RNA III polymerase promoter (Figure 14A). To enable mitochondrial Ca^{2+} detection, the retroviral expression vector was modified by replacing the Turquoise fluorescent protein with a fusion Scarlet-GCaMP6s protein targeted

to the mitochondrial inner membrane space (2mt) (Figure 14A).

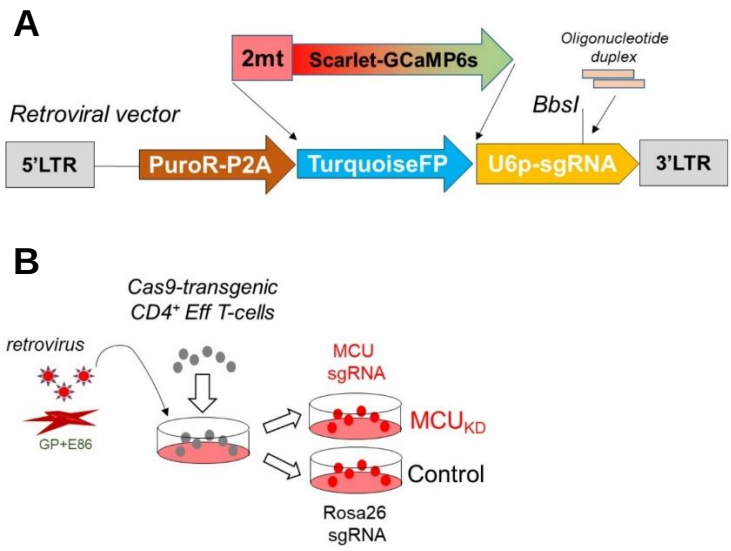

Figure 14. Expression constructs and experimental outline used for stable rat effector CD4$^+$ T-cell line generation. Design of expression vectors for T-cell transduction (**A**). 2mt=tandem mitochondrial localisation signal; LTR=retroviral long terminal repeats; PuroR=puromycin resistance gene; U6p=mouse U6 RNA III polymerase promoter; FP=fluorescent protein. Experimental procedure used to inactivate *MCU* expression in rat effector T-cells (**B**). Stable retroviral packaging cell lines (GP+E86) were generated to produce viruses encoded by the constructs indicated in (**A**) and used for co-culture with effector CD4+ T-cells derived from Cas9-transgenic Lewis rats. Eff=Effector.

2.2.25.2 Generation of retroviral packaging cell lines

After establishing the vectors and verifying them by sequencing (SeqLab, Microsynth AG), targeting efficiency was investigated in HEK293 cells utilising a co-transfection experiment. Accordingly, the cDNA of the rat *MCU* gene was amplified by PCR (5'-GGACTCAGATCTCGAGGAGAGATGGCGGCCGCCGCAGGTAGATCG-3'; 5'-CCATGGTGGCGACCGGTCCGGATCCTTCCTTTTCTCCGATCTGTCGGAGG-3'; deleting the STOP codon) and cloned as a fusion construct into a pCMV-mCherry plasmid. HEK293 cells were co-transfected with three constructs: 1) Cas9 plasmid, 2) Turquoise-MCU-sgRNA-encoding retroviral construct, and 3) MCU-Cherry fusion construct, by using Lipofectamine^{TM} 3000 (Thermo Fisher, Cat# L3000001), per manufacturer's instructions (Figure 15). The Cherry fluorescent signal was assessed by fluorescent microscopy (AxioVision setup, Zeiss) and flow cytometry (Cytoflex, Beckman Coulter) on the following day.

Figure 15. HEK293 co-transfection-experimental outline. Targeting efficiency of individual sgRNAs was tested using HEK293 cells. The cells were co-transfected with a Cas9 expression construct pCas9, a guide RNA-expression construct pTurq-MCUsgRNA, and a reporter construct expressing MCU-Cherry fusion protein.

After ensuring that each of the tested sgRNAs containing the three protospacers ps4, ps5 and ps6 substantially reduced MCU-Cherry expression, four stable packaging cell lines (sgMCUps4, 5, 6 and sgRosa26) were established using GP+E86 cells (Figure 14B) (Markowitz et al., 1988). Briefly, 1-2 µg of Puro2A-2mt-ScarletGCaMP6s-U6sgRNA plasmid was linearised by digestion with ScaI (FastDigest enzyme, Thermo Fisher, Cat# FD0434) and precipitated by 1:1 addition of isopropanol followed by centrifugation (13,000 rpm, 10 min). The DNA pellet was dried and resuspended in 50 µL of OptiMEM. In a separate Eppendorf tube, 2.5 µL of Lipofectamine^{TM} 3000 reagent (Thermo Fisher, Cat# L3000001) were mixed with 47.5 µL of OptiMEM and the resuspended DNA solution. After incubation at RT for 10 min, the transfection mixture was added dropwise to the GP+E86 cells, previously seeded in 12-well plates (40-60% confluency). Two days after transfection, the cell lines were seeded onto T75 cell culture flasks and selection using 1 µg/mL puromycin was started. After 7 days of selection with puromycin, the cells with the brightest Scarlet-GCaMP6s signal were enriched from the pool of puromycin-resistant GP+E86 by FACS sorting (FACS Aria II cytometer, Beckton Dickennson; refer to Lodygin et al., 2013).

2.2.25.3 Establishing $CD4^+$ rat T-cell lines

Prior to isolation of lymph node cells from Lewis rats, $1{,}5x10^4$ packaging cells were seeded per well (50 µL/well) in U-bottom 96-well plates (4 plates per cell line) in Re-stimulation medium. Cells were allowed to adhere for at least 2 hrs under standard culture conditions (37°C, 5% CO_2).

Popliteal, inguinal and para-aortal lymph nodes were aseptically dissected and placed in ice-cold Re-stimulation medium. The tissue was homogenised by pressing through a metal strainer. Cell suspension was collected and resuspended well with a 10 mL serological pipette. A small volume of cell suspension was diluted 1:10 with trypan blue and used for manual

counting using a Neubauer chamber. A suspension of $20x10^6$ cells per 96-well plate was prepared by adding a required volume of Re-stimulation medium and 20 µg/mL myelin basic protein (MBP)-antigen. $2x10^5$ lymph node cells were seeded per well (50 µL/well) on top of the previously-seeded packaging cell lines in the U-bottom 96-well plates. Cells were cultured under standard culture conditions (37°C, 5% CO_2).

On day 2 after start of culture, 50 µL of T-cell growth factor (TCGF- T-cell medium supplemented with 10% horse serum and 1:50 diluted supernatant from IL-2 producing cell lines) were added per well in all the prepared well plates. On day 4, the generated T-cells were transferred to flat-bottom 96-well plates (using a multichannel pipette) and supplemented with 50 µL of TCGF and 1 µg/mL puromycin for selection.

The first T-cell re-stimulation was performed on day 7 after start of culture, by removing 100 µL of supernatant and adding $1.4x10^6$ irradiated (30 Gy) Lewis thymocytes per well (resuspended in 100 µL of Re-stimulation medium and 12 µg/mL of MBP). Experiments were performed 4-5 days after 2nd and 3rd re-stimulation cycles. Cells were gradually frozen in 50% FCS+10% DMSO and kept at -80°C or in liquid nitrogen until further use. After each thawing cycle, the cells were re-stimulated with irradiated thymocytes.

2.2.25.4 *In vitro* $CD4^+$ rat T-cell re-stimulation for RNA isolation

Rat $CD4^+$ T-cells were re-stimulated by using 96-well culture plates coated with anti-rat CD3 (clone G4.18) and anti-rat CD28 (clone JJ316) antibodies (BD Pharmingen) (1 µg/mL in DPBS, overnight at 4°C). 70,000 cells were added per well in Re-stimulation medium. At specific time points (0, 3, 6, and 9 hrs after re-stimulation), the cells were collected for RNA isolation (RNAEasy isolation kit, Qiagen, Cat# 74004) and subsequent cDNA synthesis and RT-qPCR.

2.2.25.5 T7 endonuclease 1 (T7E1) mismatch detection assay

To confirm and characterise the intended edit of the MCU sequence in the generated lines, as well as to control for off-target effects after CRISPR Cas9 editing, the T7E1 assay was performed by Dr. Dmitri Lodygin.

T7 endonuclease1 is an enzyme that recognizes mismatches and extrahelical loops in double-stranded DNA (Guschin et al., 2010). Briefly, isolated genomic DNA from the generated cell lines (sgRosa26 control, sgMCUps4, sgMCUps5, and sgMCUps6) was amplified by PCR using primers specific for the edited regions (refer to Table 63). During PCR, the DNA sequences denature and reanneal, forming heteroduplexes containing a mismatch.

Following PCR amplification, the products were then incubated with T7 endonuclease1, which recognizes the mismatches and cleaves upstream of the mismatch, leaving the wildtype double-stranded DNA intact. The wildtype strands and resulting cleaved fragments were then resolved in an agarose gel through electrophoresis and visualised under UV light.

Table 63. Sequences of primers used for T7E1 assay.

Name	Forward	Reverse
Protospacer (ps) 4	CTTTTCCATGAAGAGTCCATCATTC	TACACCCCTCCTCTAATCGCCCCTTC
Protospacer (ps) 5	CAAATCGAACGTGCCATCCCTTACT	GTCCGGTGCTGCTGGTGCGGCCGCT
Protospacer (ps) 6	GTACGGATTGAAATTAGCAGGAAAGC	GAGCCTCAGAACTTTAAGAATAATA

2.2.26 Experimental autoimmune encephalomyelitis (EAE) induction in rats

In vivo EAE induction was performed by adoptive T-cell transfer in anesthetised rats using the generated control cell line (Rosa26 Ctrl) and the $MCUa_{KD}$ cell lines (MCUps4 and MCUps5) according to a protocol described in detail in Lodygin et al. (2013). Collected EAE scores and animal weight changes were analysed and plotted by using GraphPad Prism 9.

2.2.27 Confocal Microscopy

Naive and Effector $CD4^+$ T-cells were stained with CellMask Green (0.5x working dilution) and MitoTracker Deep red (100 nM working dilution) (Table 27) in order to visualise the plasma membrane and the mitochondria. Cells were stained for 10 min at RT under low-light conditions and loaded on glass coverslips immediately before imaging. Images were acquired using the LSM800/Duolink Confocal microscope (Zeiss). Settings used are given in Table 64 below.

Table 64. Settings used for confocal microscopy.

Excitation 1	EGFP-488 nm (2% laser intensity) (SP545)
Excitation 2	MT-633 nm (0,3% laser intensity) (LP655)
Beam splitter	550 nm
Averaging	2x for 3D images; 14x for 2D images
Z-stack interval	0.15 µm
Objective used	63x (N. A 1.3) glycerine

Image analysis was performed by using the Zen 3.5 software (Zeiss). Channel intensities were adjusted as 'best-fit' in order to best visualise the cell membrane and mitochondria.

2.2.28 Statistical analyses

Raw data analyses were performed using Microsoft Excel 2019 and GraphPad Prism 9. Results were plotted using GraphPad Prism 9 and are shown as mean ± SEM, unless otherwise specified in the figure legends. Statistical significance was determined by a two-tailed paired or unpaired Student's t-test, and by one-way-ANOVA for multiple group comparisons. The two-tailed Welch's test was used when unequal variance was assumed. Significance (p) values are marked with ***** for $p \leq 0.05$, ****** for $p \leq 0.01$, ******* for $p \leq 0.001$ and ******** for $p \leq 0.0001$.

3. Results

3.1 Generation of a human effector CD4$^+$ T-cell model

To address the objectives of this study, primarily the role of MCU in T-cell metabolism and function, a reliable and robust experimental system was required. To this end, naive CD4$^+$ T-cells were isolated from healthy human donors as described in the methods section (2.2.2). These cells were then activated with CD3+CD28-coated beads for 72 hrs in order to obtain an 'effector CD4$^+$ T-cell' model. The effectiveness of using CD3+CD28 antibody solution for T-cell activation was additionally investigated by measuring $_c$[Ca2$^+$] increase upon physiological stimulation (**Figure 16A** and **B**) and by assessing T-cell proliferation (**Figure 16C** and **D**). However, the beads were a better TCR-stimulating agent, therefore they were utilised for most of the experiments performed, unless specified otherwise in the methods section and in the figure legends.

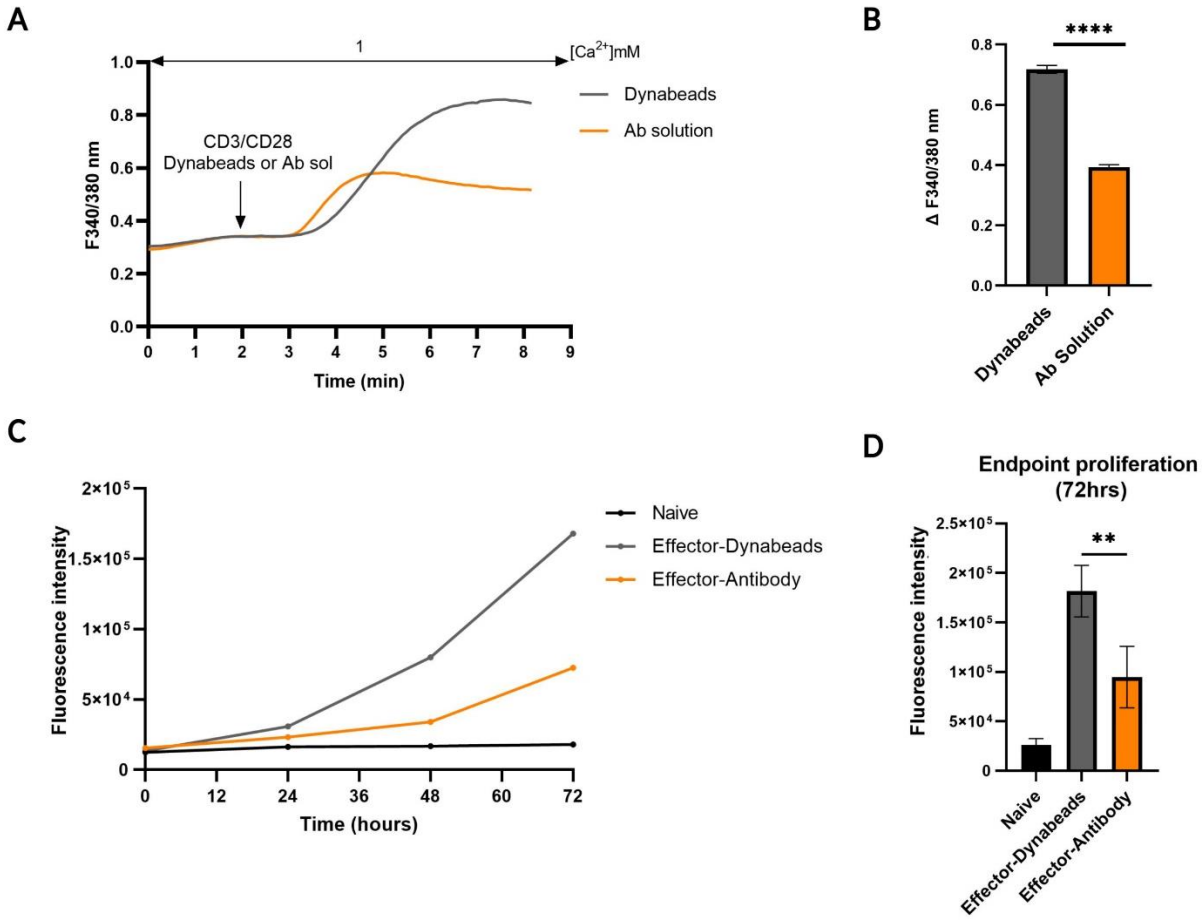

Figure 16. Efficient naive CD4$^+$ T-cell activation using CD3+CD28-coated magnetic beads and antibody solution. Cytosolic Ca^{2+} measurements indicated fast increases in $_c[Ca^{2+}]$ upon TCR stimulation. This effect was significantly greater when using beads, compared to antibody solution (**A**) and (**B**). Ca^{2+} traces (**A**) and quantifications (**B**) represent an average of 1,479 beads-activated and 1,656 antibody solution-activated T-cells (biological replicates) from 5 separate donors. T-cell proliferation was also significantly higher when naive cells were activated with beads compared to antibody solution (**C**) and (**D**). Traces (**C**) and quantification (**D**) represent an average of 8 separate donors/biological replicates (3 technical replicates per condition). Data are represented as mean ± standard error of means (SEM). ****-p <0.0001, **-p <0.01; assessed by two-tailed unpaired Student's t-test.

To validate the effector CD4$^+$ T-cell model, basic parameters known to be altered upon T-cell activation were investigated: $_c[Ca^{2+}]$ and SOCE, cell proliferation, cell volume, and IL-2 secretion (**Figures 17** and **18**). Part of these findings were obtained prior to the start of the Doctoral Thesis (Unpublished Master's Thesis; Shumanska, 2019). Cytosolic Ca^{2+} and SOCE are two important parameters known to increase considerably, shortly upon TCR stimulation. A significant difference was observed between the naive and effector T-cells used for this study (**Figure 17A, B** and **C**), even after normalisation to their respective cell volumes (quantified in **Figure 18C**). Furthermore, cell proliferation (**Figure 17D** and **E**) as well as IL-2 production (**Figure 17F**) were highly increased in the effector T-cells.

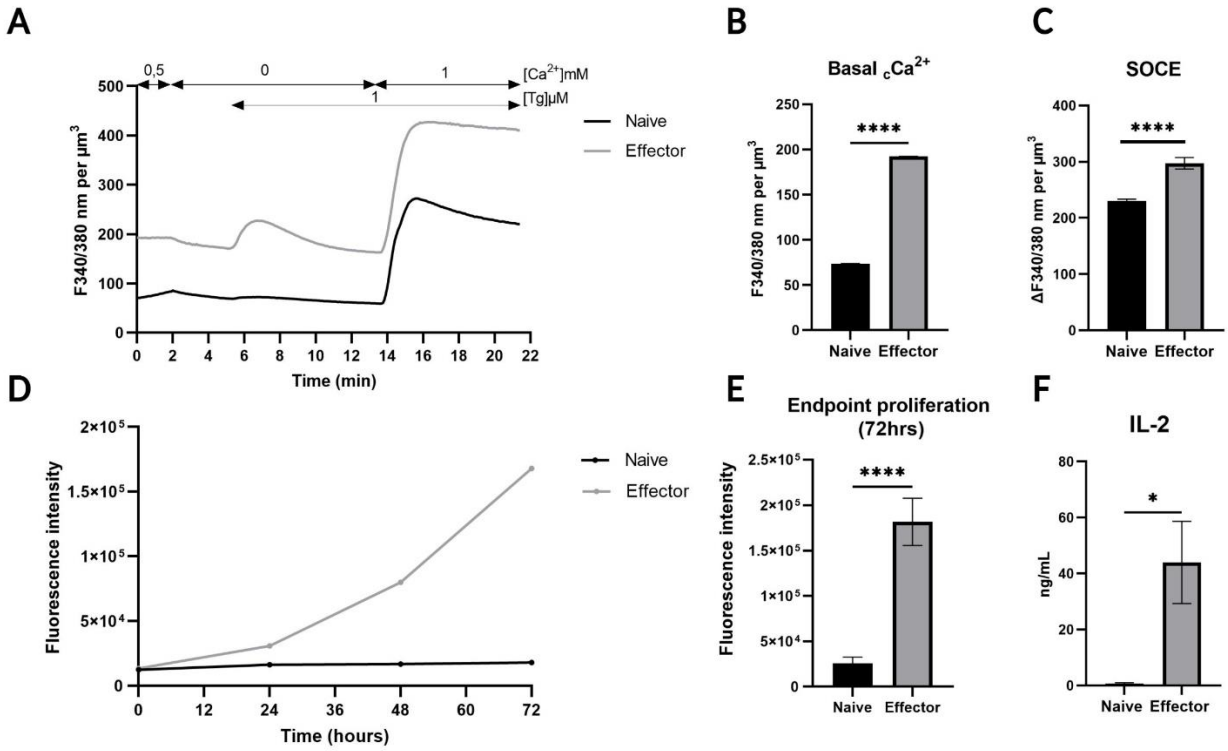

Figure 17. $CD4^+$ T-cell parameters measured for model validation: Naive and effector $CD4^+$ T-cells significantly differ in their Ca^{2+} signalling, proliferation and cytokine secretion profile. Upon activation, T-cells significantly increased the resting $_c[Ca^{2+}]$ and SOCE. Panel (**A**) shows the SOCE-measurement protocol based on addition of SERCA-blocker thapsigargin (Tg; 1 µM) and re-addition of Ca^{2+}. The traces represent an average of 768 naive T-cells and 577 effector T-cells (biological replicates from 3 different donors), normalized to their respective cell volume value (quantification given in **Figure 18C**). Panels (**B**) and (**C**) show the quantifications of average basal $_c[Ca^{2+}]$ and SOCE, respectively. Basal $_c[Ca^{2+}]$ was quantified as an average of the measurement points taken while cells remained in 0.5 mM Ca^{2+} Ringer's solution. SOCE was quantified as the difference between the minimal measurement points taken after ER store depletion and the maximal measurement points taken after re-introduction of Ca^{2+} in the working solution. The proliferation of effector T-cells (**D**) was also significantly increased compared to naive. The traces and quantification at 72 hrs (**E**) represent an average of 8 different donors/biological replicates. IL-2 secretion (**F**) was significantly higher upon T-cell activation (average of 3 donors/biological replicates). Data are represented as mean ± SEM. ****- $p < 0.0001$; *- $p \leq 0.05$, determined with two-tailed unpaired and paired Student's t-test. Naive $CD4^+$ T-cells are labelled with **black**, and effector $CD4^+$ T-cells with **grey** throughout all the figures.

T-cell volume, evaluated by confocal microscopy imaging and quantified using the Countess™ 3 Automatic Cell Counter and the formula for volume of a sphere, was also significantly increased in the effector T-cells (~568 μm^3), compared to naive (~194 μm^3) (**Figure 18, S Figure 1**). The quantified volumes were further used for normalisation purposes (indicated in the figure legends).

Expression of several other genes related to Ca^{2+} signalling in T-cells was also investigated (**S Figure 2**). Increased expression was observed in most of them, including *STIM1* and *NFAT4*, although statistically insignificant due to the small number of donors used and the high variability among those donors. Further analyses of gene expression should be performed in order to increase statistical power. Nevertheless, these results additionally supported the validation of the model.

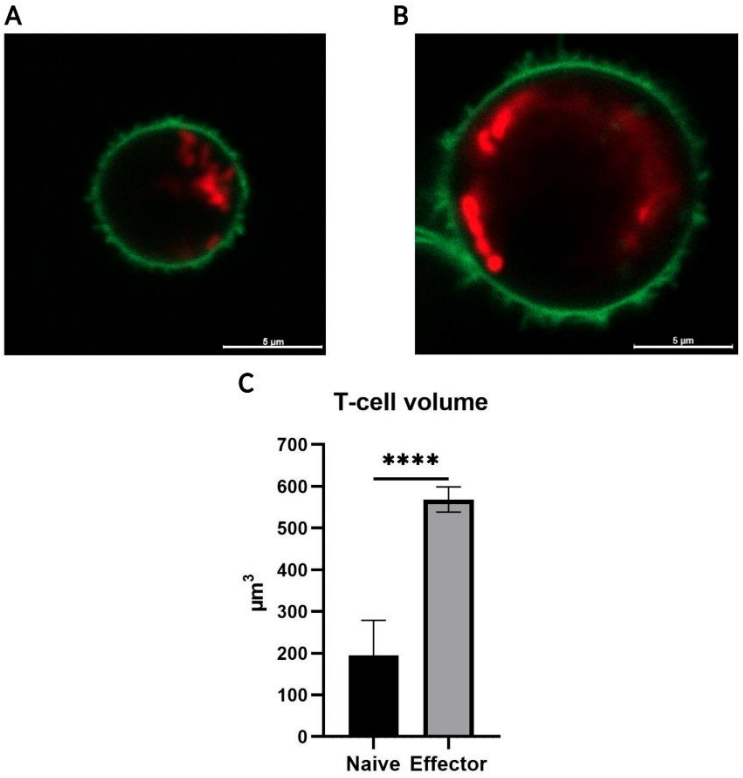

Figure 18. Significant increase in CD4$^+$ T-cell volume upon TCR stimulation. Representative confocal image of a (**A**) naive and an (**B**) effector T-cell. Plasma membrane was stained with CellMask Green and mitochondria with MitoTracker Deep red. Scale bar: 5 µm; magnification: 63x gly (N. A 1.3). Quantification of T-cell volume (**C**) representing an average of 199,400 naive and 702,500 effector T-cells from at least 3 separate donors/biological replicates. Cell volume was estimated by using the Countess™ 3 Automatic Cell Counter to determine cell diameter and the formula for volume of a sphere to calculate the volume. Data are represented as mean ± SEM. ****- p <0.0001, determined with two-tailed unpaired Student's t-test.

Moreover, cell purity check after naive CD4$^+$ T-cell isolation was performed using FACS analysis and indeed, a pure CD4$^+$ T-cell population of approximately 97% was achieved (**Figure 19**-example of two representative donors).

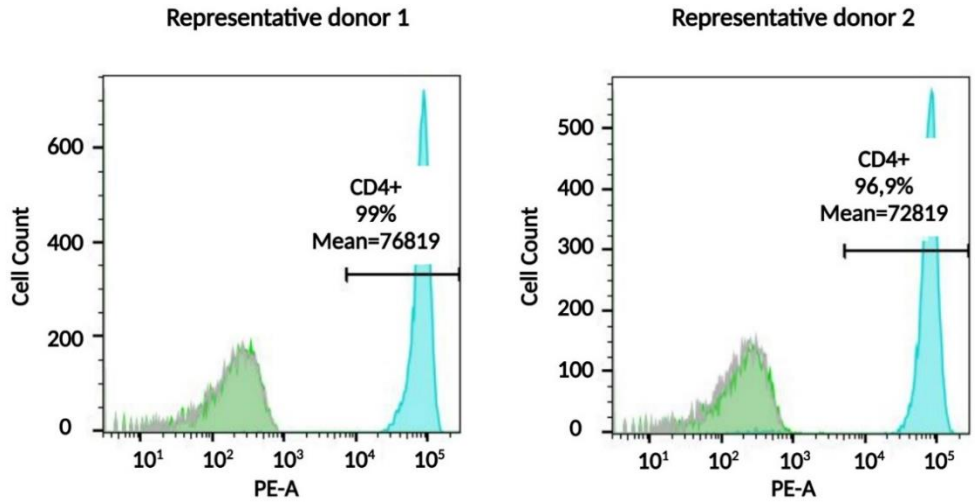

Figure 19. Pure $CD4^+$ naive T-cell population isolated from blood of healthy human donors. Naive T-cells mainly exhibited positive CD4 (PE-A) staining, and not CD8. 99% of screened cells from Donor 1 (left side) were CD4 +, whereas 96.9% of cells from Donor 2 (right side) were CD4 +. The histograms were generated from 10,000 events. Legend: Grey=unstained control; Green=CD8 staining; Blue=CD4 staining.

Taken together, these data confirmed that the generated T-cell model was reliable and could be used for further exploration. After validation, the two cell models (naive and effector) were used for investigation of the MCU complex and T-cell mitochondrial metabolism.

3.2 The MCU complex rearranges upon TCR stimulation, leading to higher $_mCa^{2+}$ uptake

Based on the initial $_cCa^{2+}$ measurements obtained, we hypothesised that upon increased $_cCa^{2+}$ concentrations, the mitochondrial Ca^{2+} buffering and uptake capacity would also be higher. To carefully investigate possible changes in the MCU complex itself, gene expression levels of every MCU complex component were determined (**Figure 20A**) in both naive and effector $CD4^+$ T-cells. At 72 hrs of TCR stimulation, the gene expression pattern of the MCU complex components rearranged in a way that genes encoding for proteins responsible for higher $_mCa^{2+}$ uptake (MCUa and Micu1) were upregulated. Furthermore, the gene encoding for MCUb, which mainly inhibits high $_mCa^{2+}$ uptake, was downregulated. *Micu2* and *EMRE* expression levels were not significantly different between naive and effector T-cells. *Micu3* was downregulated upon TCR stimulation; however, its relevance in T-cell function was not reported thus far. *MCUR1*, which also correlates with higher $_mCa^{2+}$ uptake, was upregulated in effector T-cells.

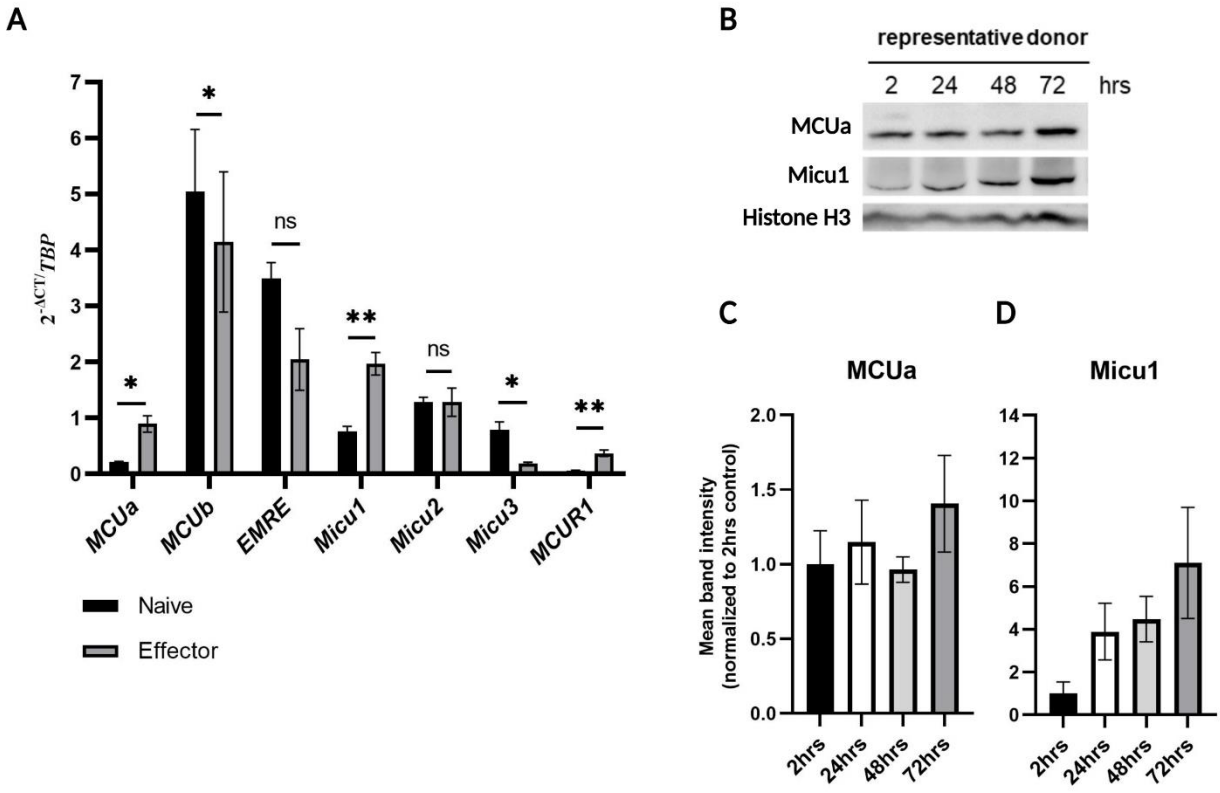

Figure 20. Rearrangement of the MCU complex in effector CD4$^+$ T-cells. Gene expression analyses (**A**) of MCU complex components showed a significant upregulation of *MCUa*, *Micu1* and *MCUR1*, and a significant downregulation of *MCUb* upon CD4$^+$ T-cell activation (data present the average of 7 donors/biological replicates for *MCUb* and 4 donors/biological replicates for all other given genes, using 2 technical replicates and a negative water control). Gene expression is normalised to the HK gene *TBP*. Protein expression levels of MCUa and Micu1 (**B**) were in line with mRNA expression data (image shows MCUa, Micu1, and Histone H3 protein expression levels of one representative donor; quantification bar charts (**C** and **D**) represent an average of 3 different donors/biological replicates normalized to 2 hrs control). Data are represented as mean ± SEM. **- p <0.01; *- p ≤0.05, assessed by two-tailed paired Student's t-test.

Protein expression of MCUa and Micu1 was additionally determined using Western blotting. Both proteins were upregulated shortly upon cell activation, with the highest expression 72 hrs after TCR stimulation (**Figure 20B, C** and **D**), validating the mRNA levels. Given the small number of donors used for determination of the steady-state protein expression of MCUa and Micu1, this experiment should be repeated. Nevertheless, it can be concluded that the MCU complex rearranges its molecular composition to accommodate for higher Ca^{2+} concentrations and higher $_mCa^{2+}$ uptake in effector T-cells.

To investigate functional differences in the MCU complex between naive and effector CD4$^+$ T-cells, $_m[Ca^{2+}]$ levels were measured by transiently overexpressing the $_mCa^{2+}$ biosensor MT3.1 Pericam (**Figure 21**). $_mCa^{2+}$ uptake was induced by external addition of ionomycin.

Naive T-cells had significantly lower resting levels of $_{m}Ca^{2+}$, compared to effector T-cells (**Figure 21B**), which was in accordance with the gene and protein expression (**Figure 20**). The $_{m}Ca^{2+}$ uptake in effector T-cells was present even when the cells were immerged in Ca^{2+}-free solution (**Figure 21C**). This indicated that active $_{m}Ca^{2+}$ uptake was still present and was not only due to increases in $_{c}[Ca^{2+}]$, but mainly due to higher MCU activity dependent on Ca^{2+} efflux from other organelles, such as the ER.

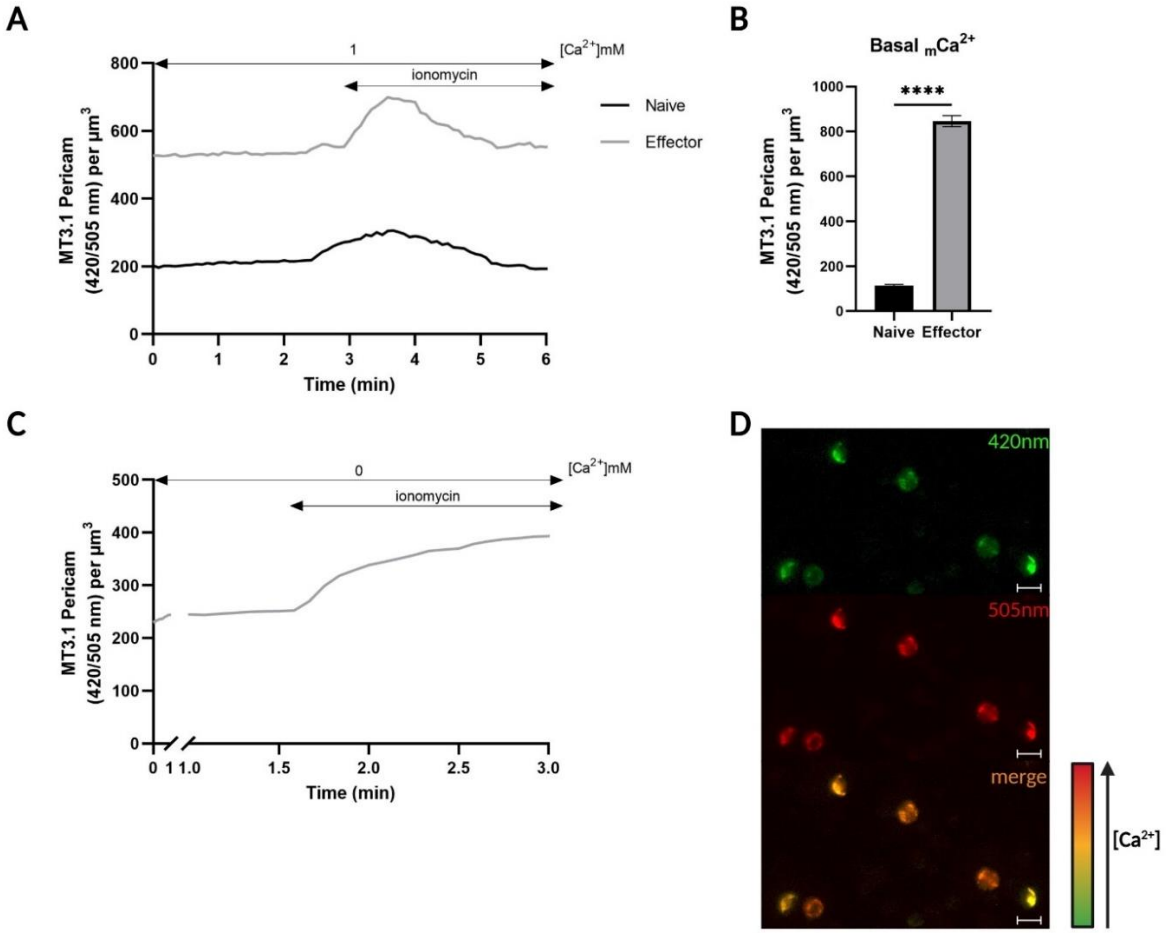

Figure 21. Higher $_{m}Ca^{2+}$ uptake upon $CD4^{+}$ T-cell activation. $_{m}[Ca^{2+}]$ levels were measured in naive and effector T-cells by overexpressing the $_{m}Ca^{2+}$ biosensor Ratiometric MT3.1 Pericam. Effector T-cells had significantly higher basal $_{m}[Ca^{2+}]$ compared to naive T-cells, even after normalisation with their respective cell volumes (**A**). Representative traces show an average of 19 naive and 27 effector T-cells (biological replicates) from 2 different donors. The quantification (**B**) represents the basal $_{m}[Ca^{2+}]$ and an average of 52 naive T-cells and 88 effector T-cells (biological replicates) from 6 different donors. Active $_{m}Ca^{2+}$ uptake after ionomycin addition (4 µM) was present even when measurements were performed in Ca^{2+}-free solution (**C**). The traces show an average of 34 effector T-cells (biological replicates) from 2 different donors. Panel **D** shows representative images of T-cells transfected with the biosensor Ratiometric MT3.1 Pericam (top to bottom: 420 nm, 505 nm, merged channels; magnification: 40x (N. A 1.3) oil; scale bar: 20 µm). An orange cell color in the merged image indicates higher $_{m}[Ca^{2+}]$ compared to a green cell color. Data are represented as mean ± SEM. ****- p <0.0001, assessed by two-tailed paired Student's t-test.

3.3 Increased mitochondrial metabolism and bioenergetics, shortly upon CD4$^+$ T-cell activation

It is well known that naive T-cells are rather quiescent and upon TCR stimulation, T-cell differentiation starts almost simultaneously with robust metabolic changes. Upon activation, T-cells boost their glycolytic metabolism via the mTOR pathway and through upregulation of glucose transporters. Furthermore, glutamine metabolism is also increased, which fuels the TCA cycle via conversion to α-ketoglutarate (Van der Windt & Pearce, 2012). A similar robust metabolic switch was observed in this study as well, initially by assessment of mitochondrial respiration, glycolytic rates, and ATP levels in both naive and effector T-cells (**Figure 22**). Effector T-cells had significant increases in both basal and maximal oxygen consumption rates (OCR) (**Figure 22B** and **C**). Furthermore, extracellular acidification rates (glycolytic rates; ECAR) (**Figure 22D**) and global ATP levels (**Figure 22E**) were significantly higher, compared with naive T-cells.

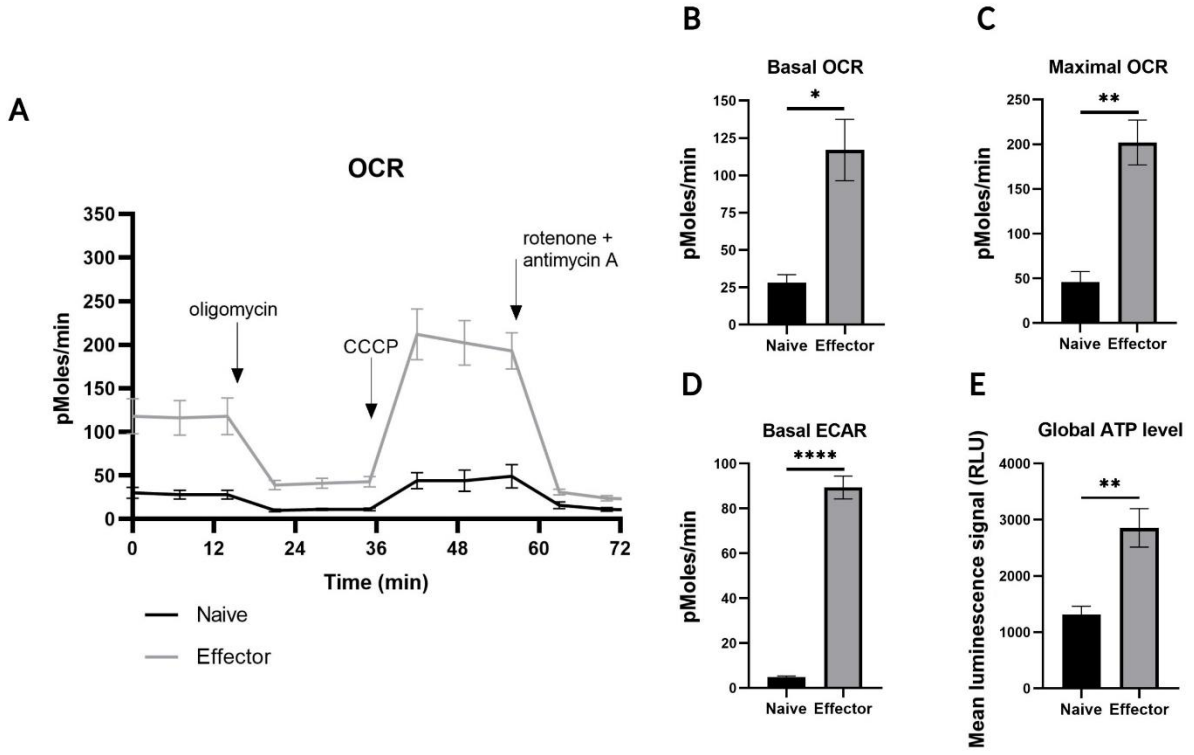

Figure 22. Higher mitochondrial respiration and ATP production in effector CD4$^+$ T-cells. Mitochondrial respiration measurements of naive and effector CD4$^+$ T-cells showed that naive cells were quiescent with low mitochondrial respiration capacity, compared to effector cells. Basal and maximal oxygen consumption rates (OCR) (**B**-**C**), extracellular acidification rates (ECAR) (**D**), and global ATP levels (assessed by Cell Titer Glo® Luminescence Assay) (**E**) were significantly increased upon T-cell activation. OCR traces (**A**) and quantifications (**B** and **C**) show an average of 3 different donors/biological replicates (using at least 6 technical replicates). ATP

quantification shows an average of 6 different donors/biological replicates. Data are represented as mean ± SEM. ****- p <0.0001; **- p <0.01; *- $p \leq 0.05$, assessed by two-tailed paired Student's t-test.

Another parameter important for proper mitochondrial function is the mitochondrial membrane potential (ΔΨm), dependent on proton (H^+) transfer. ΔΨm was measured in naive and effector $CD4^+$ T-cells stained with the dye TMRE. There was a significant increase of ΔΨm in effector T-cells compared to naive, indicating mitochondrial hyperpolarization (**Figure 23A**). These results were in accordance with the increase of mitochondrial respiration and ATP.

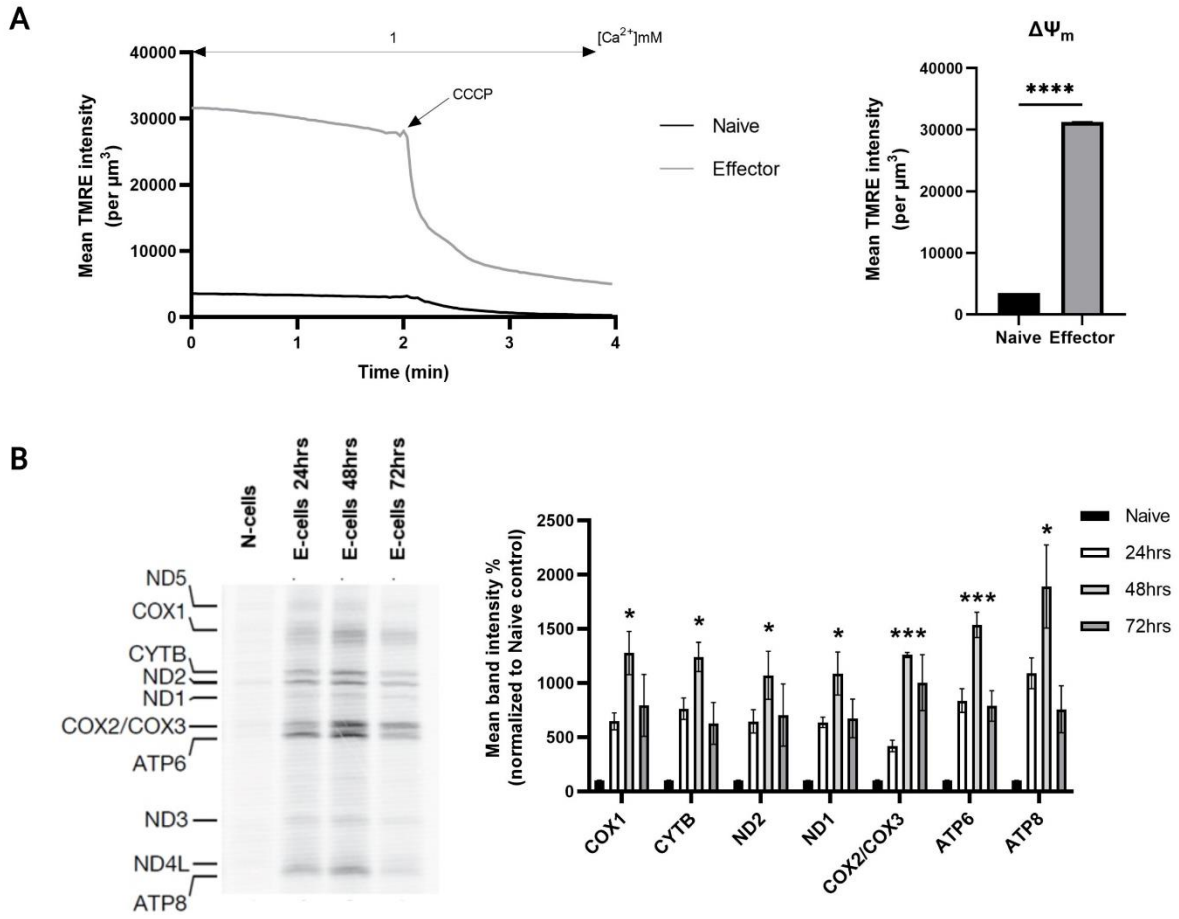

Figure 23. Increased mitochondrial membrane potential (ΔΨm) and mitochondrial protein translation upon T-cell activation. ΔΨm measured using TMRE was significantly increased in effector T-cells compared to naive (**A**). Traces show the average of 294 naive T-cells and 408 effector T-cells (biological replicates) from 4 different donors, normalised to their respective cell volumes. The quantification shows the average basal ΔΨm. Addition of CCCP (2 µM) depolarised the membrane, decreasing the TMRE fluorescence intensity. Panel **B** shows mitochondrial protein translation measured at 0, 24, 48, and 72 hrs after TCR activation, using ^{35}S Met labelling. The blot is representative of one donor and the quantification is an average of 3 different donors/biological replicates, as percentage of 'Naive control'. Mitochondrial protein translation was significantly increased, peaking 48 hrs after T-cell activation. Data are represented as mean ± SEM. ****- p <0.0001; ***- p <0.001; *- $p \leq 0.05$, assessed by two-tailed unpaired and paired Student's t-test. N=Naive; E=Effector.

For further confirmation, additional measurements using the ratiometric dye JC-1 were performed, which were in line with the increase in ΔΨm assessed by using TMRE (**Figure 24A** and **B**). Moreover, quantification of mean gray level per pixel area from representative images taken during the TMRE measurements (**Figure 24C**) affirmed the increase of TMRE intensity in the effector T-cells quantified during the single-cell measurements.

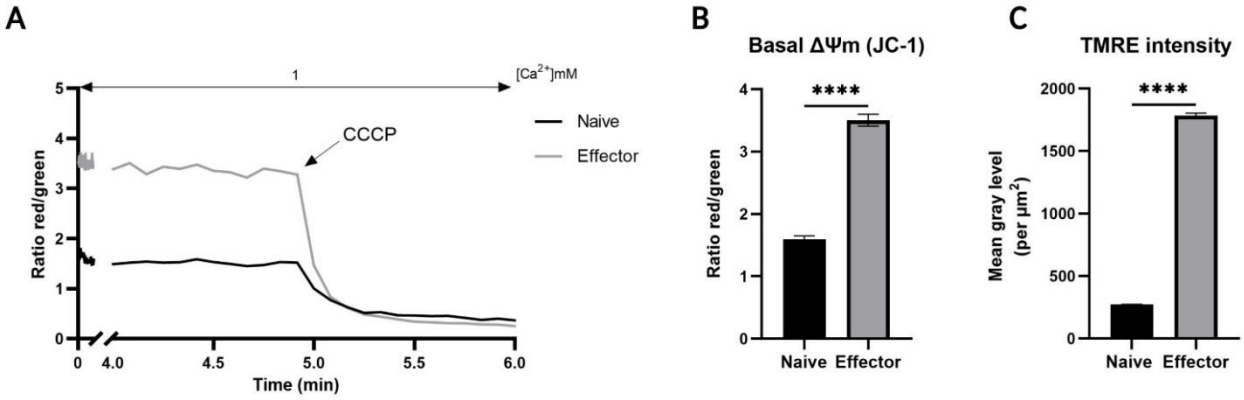

Figure 24. Significantly increased ΔΨm upon CD4⁺ T-cell activation, assessed by JC-1 and TMRE pixel intensity quantification. JC-1 traces (**A**) and quantification (**B**) represent an average of 121 naive and 164 effector T-cells (biological replicates) from 2 different donors. ImageJ/Fiji was used to process the images obtained from TMRE measurements and estimate average pixel area and mean gray levels (**C**). Normalisation of mean gray level to pixel area confirmed the higher TMRE intensity in effector T-cells, compared to naive. The quantification panel (**C**) is representative of an average of 602 naive and 435 effector CD4⁺ T-cells (biological replicates) from 3 separate donors. Data are represented as mean ± SEM. ****-p <0.0001, **-p <0.01; assessed by two-tailed unpaired Student's t-test. CCCP: 2 µM.

Since a constant ΔΨm value of ~-140 mV is common in a normal resting T-cell, it was interesting to see the extent of hyperpolarization which effector T-cells are able to achieve upon TCR stimulation. To further investigate this phenomenon and to determine the time when this ΔΨm switch occurs, measurements were performed in activated T-cells every 30 min after initial TCR stimulation. The ΔΨm switch occurred in the first 90 min, significantly increasing 150 min after TCR stimulation (orange line). This change was abolished when TCR activation was inhibited using the Orai inhibitor CM4620 (brown line), and furthermore when MCU was hindered using Mitoxantrone (dark green line) (**Figure 25**).

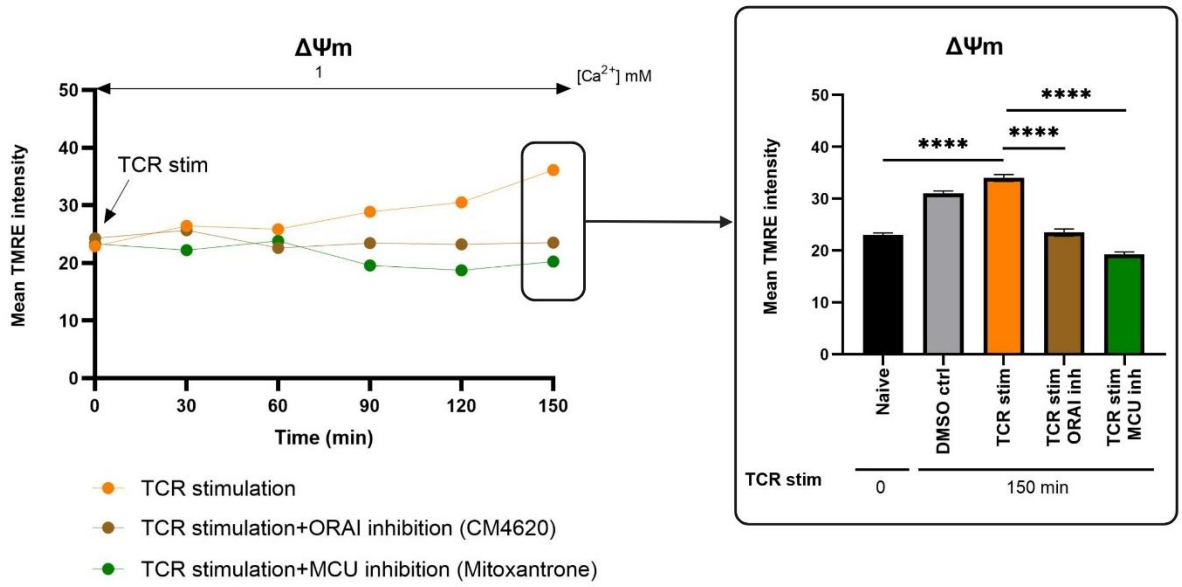

Figure 25. Mitochondrial membrane potential (ΔΨm) increase in activated CD4$^+$ T-cells occurs in the first 90 min, significantly at 150 min after TCR stimulation. These effects are abolished upon Orai and MCU inhibition. Quantification graph shows an average of 373 naive T-cells (5 donors), 399 activated DMSO control T-cells (4 donors), 399 activated T-cells (5 donors), 155 activated T-cells with Orai inhibition (2 donors), and 226 activated T-cells with MCU inhibition (2 donors). One cell=one biological replicate. Data are represented as mean ± SEM. ****- p <0.0001, assessed by two-tailed unpaired Student's t-test. CM4620: 1 µM; Mitoxantrone: 10 µM.

Mitochondria are unique organelles in the cell containing an independent genetic system encoding for 13 components of the mitochondrial respiratory chain. Mitochondrial protein translation is therefore highly regulated and important for cellular energy supply and mitochondrial function (Wang et al., 2021). Additionally, the ΔΨm contributes to proper respiratory chain complex assembly (Sato et al., 2019). Given the robust increase of ΔΨm in effector T-cells, mitochondrial protein translation was evaluated in naive and activated T-cells using a radioactive labelling assay. Translation of all assessed proteins was significantly increased in effector T-cells, peaking 48 hrs after TCR stimulation (**Figure 23B**). The complete experiment with illustrations from 3 different donors is given in **S Figure 3**. To exclude the possibility that the increase in protein translation occurred due to an upregulated expression of mitochondrial genes, mRNA levels of all 13 genes were evaluated in naive and effector CD4$^+$ T-cells. No significant differences in mitochondrial gene expression were observed (**Figure 26**). However, this experiment was performed using 3 biological donors which demonstrated high donor-to-donor variability. Therefore, these interpretations should be treated with caution.

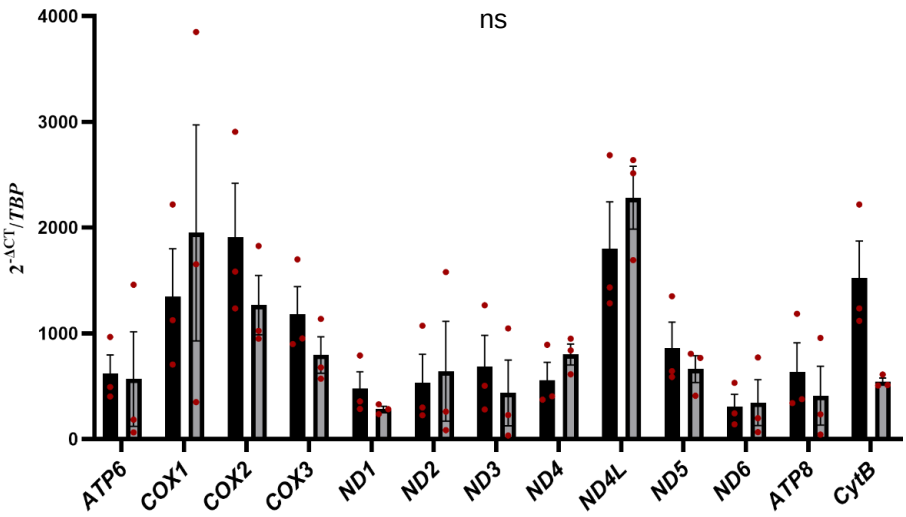

Figure 26. No differences in expression of mitochondria-encoded genes are observed between naive and effector CD4⁺ T-cells. Quantifications are representative of n=3 donors/biological replicates for all genes (2 technical replicates and a negative water control). Gene expression is normalised to HK gene *TBP*. Data are represented as mean ± SEM. Individual donor values are shown as red circles for each gene. ns-not statistically significant; assessed by two-tailed paired Student's t-test.

In accordance with the increase in mitochondrial respiration and protein translation, steady-state expression of few oxidative phosphorylation-related proteins, including TACO1, NDUFA9, SDHA and ATP5B, as well as m-AAA enzyme AFG3L2 were upregulated upon TCR stimulation (**Figure 27A** and **B**). This limited protein screening should be expanded to other respiratory chain complex components, such as COX1, COX6A (Complex IV), and UQCRC2 (Complex III) and performed using cells obtained from several donors to decrease high donor-to-donor variability.

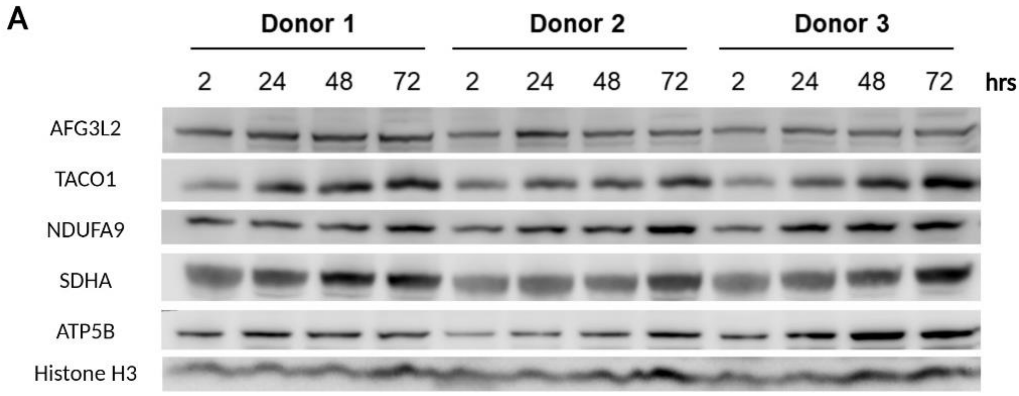

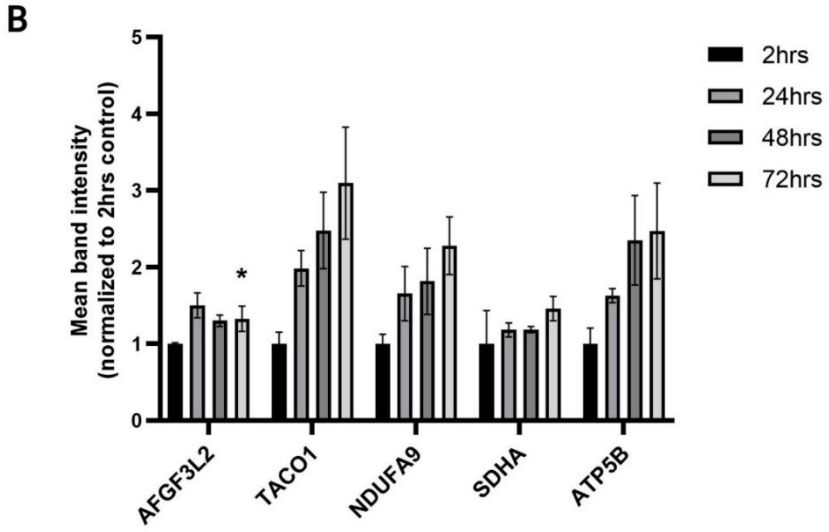

Figure 27. Activation of naive CD4$^+$ T-cells causes upregulation of multiple proteins related to oxidative phosphorylation.

The illustration (**A**) and quantification (**B**) show 3 different donors/biological replicates, activated for 2, 24, 48 and 72 hrs with CD3+CD28 beads. For quantification, data is normalised to the 2 hrs control samples, respectively for each donor. Data are represented as mean ± SEM. *-$p \leq 0.05$; assessed by two-tailed paired Student's t-test.

Taking these data together, it can be concluded that shortly after CD4$^+$ T-cell activation, the higher $_mCa^{2+}$ uptake correlates with an increase in mitochondrial respiration, metabolism, and bioenergetics. Accordingly, the MCU complex plays a key role in this metabolic transition of T-cells.

3.4 Increased cytosolic and mitochondrial ROS production in effector CD4$^+$ T-cells

Increased cytosolic ROS production after TCR stimulation has been investigated in previous studies, and also validated in this study. Naive and effector CD4$^+$ T-cells overexpressing cytosolic and mitochondria-targeted H_2O_2 biosensor HyPer were used to determine H_2O_2 levels. As expected, effector T-cells had significantly higher cytosolic H_2O_2 levels compared to naive cells (**Figure 28A** and **B**). In addition, effector T-cells had significantly increased mitochondrial H_2O_2 levels, in accordance with the higher mitochondrial respiration and ATP production (**Figure 28C** and **D**).

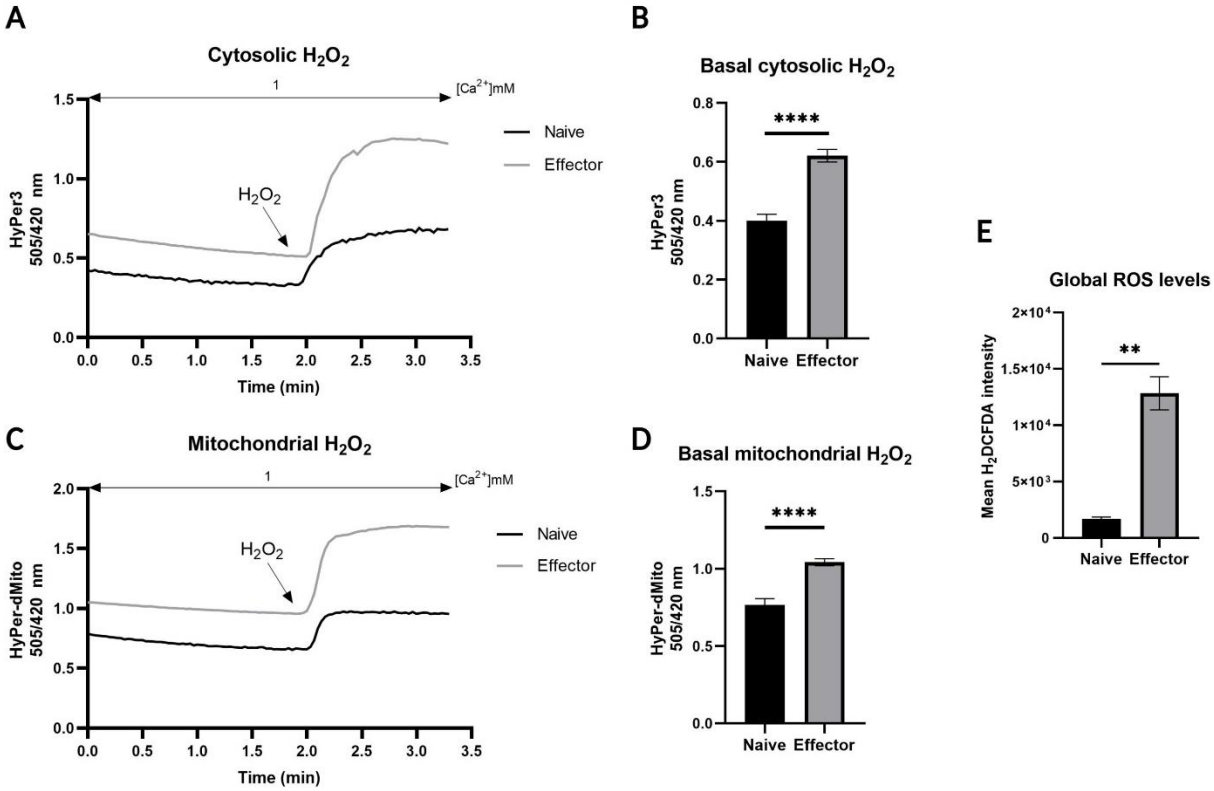

Figure 28. Increased cytosolic and mitochondrial H_2O_2 levels in effector T-cells. Cytosolic H_2O_2 traces (**A**) and quantifications (**B**) represent an average of 32 naive T-cells and 164 effector T-cells (biological replicates) from 3 different donors. Mitochondrial H_2O_2 traces (**C**) and quantifications (**D**) show an average of 43 naive and 71 effector T-cells (biological replicates) from 3 different donors. External H_2O_2 (100 µM) was used as a positive control to ensure proper biosensor response. An increase in global ROS levels in effector T-cells was confirmed by using the dye H_2DCFDA (**E**). Quantification shows an average of 3 different donors/biological replicates. Data are represented as mean ± SEM. ****- p <0.0001, **- p <0.01, assessed by two-tailed unpaired Student's t-test.

To further confirm the increase in total ROS levels in effector T-cells, the dye H_2DCFDA was used. Results were in agreement with the above-presented data; effector $CD4^+$ T-cells had significantly higher global ROS levels compared to naive cells (**Figure 28E**).

3.5 Significant differences in expression of genes related to mitochondrial metabolism among naive and effector CD4$^+$ T-cells revealed from RNA sequencing

To further investigate and confirm the differences among naive and effector CD4$^+$ T-cells, with respect to their mitochondrial metabolism, RNA sequencing was performed. Differentially-expressed gene (DEG) analysis showed multiple significantly up- or down-regulated genes upon T-cell activation. The volcano plot (**Figure 29A)** lists the DEGs, as well as the MCU complex components (marked with a blue frame). The expression changes of the MCU components were in accordance with mRNA levels assessed with RT-qPCR (**Figure 20A**).

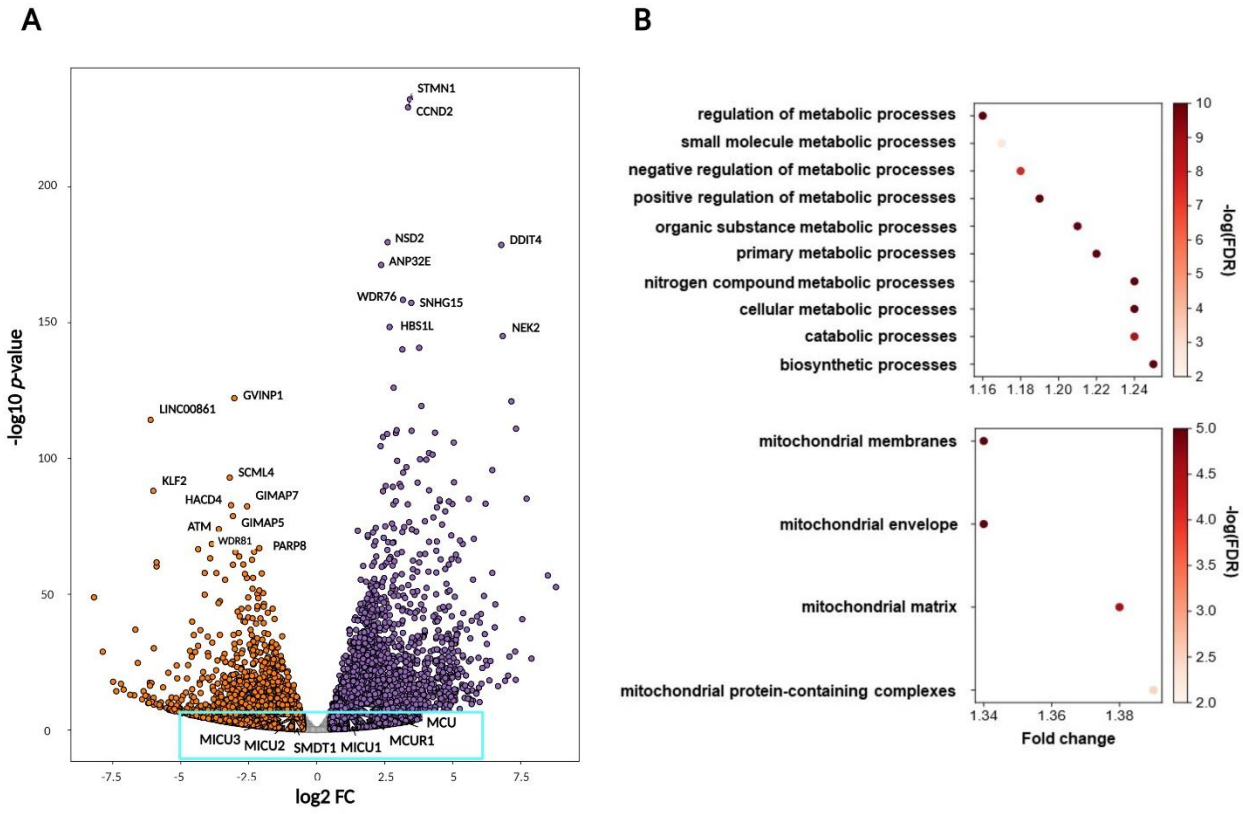

Figure 29. RNA sequencing data reveal significant changes in expression of genes related to mitochondrial metabolism upon CD4$^+$ T-cell activation. Panel (**A**) shows a volcano plot marking the DEGs after naive CD4$^+$ T-cell activation for 72 hrs. Candidates have been selected using an FDR cut-off of 0.05 and were further filtered by an absolute logarithmical fold change (log2 FC) of 0.5 and sorted as up- or down-regulated depending on the fold change (up - FC>0 (purple); down - FC<0 (orange)). MCU complex components are marked with a blue frame. Panel (**B**) shows the functional annotation and KEGG pathway analyses of all obtained DEGs. Annotated terms and pathways were filtered by an FDR cut-off of 0.05. In order to better interpret gene ontology terms, specific denominations were used, including Metabolic Processes (GO:0008152), and Mitochondria (GO:0005739).

Given the high number of DEGs revealed from this dataset after T-cell activation (**Figure 29A**), KEGG pathway analyses were utilized in order to link the obtained genomic information with functional information on cellular processes. To confirm the robust increase in T-cell metabolism, the link to metabolic and mitochondria-related pathways was investigated. It was evident that upon T-cell activation, multiple metabolic pathways were significantly altered to allow for the robust bioenergetic changes. Furthermore, specific mitochondrial pathways which were altered included changes in mitochondrial membranes, matrix, as well as protein complexes (**Figure 29B**). These data were in line with previous experiments performed on naive and effector T-cells in this study.

Additional pathway analyses with a focus on migration, adhesion and cell immune responses affirmed significant upregulation of immune response genes and cell adhesion genes upon T-cell activation, as expected (**Figure 30A**).

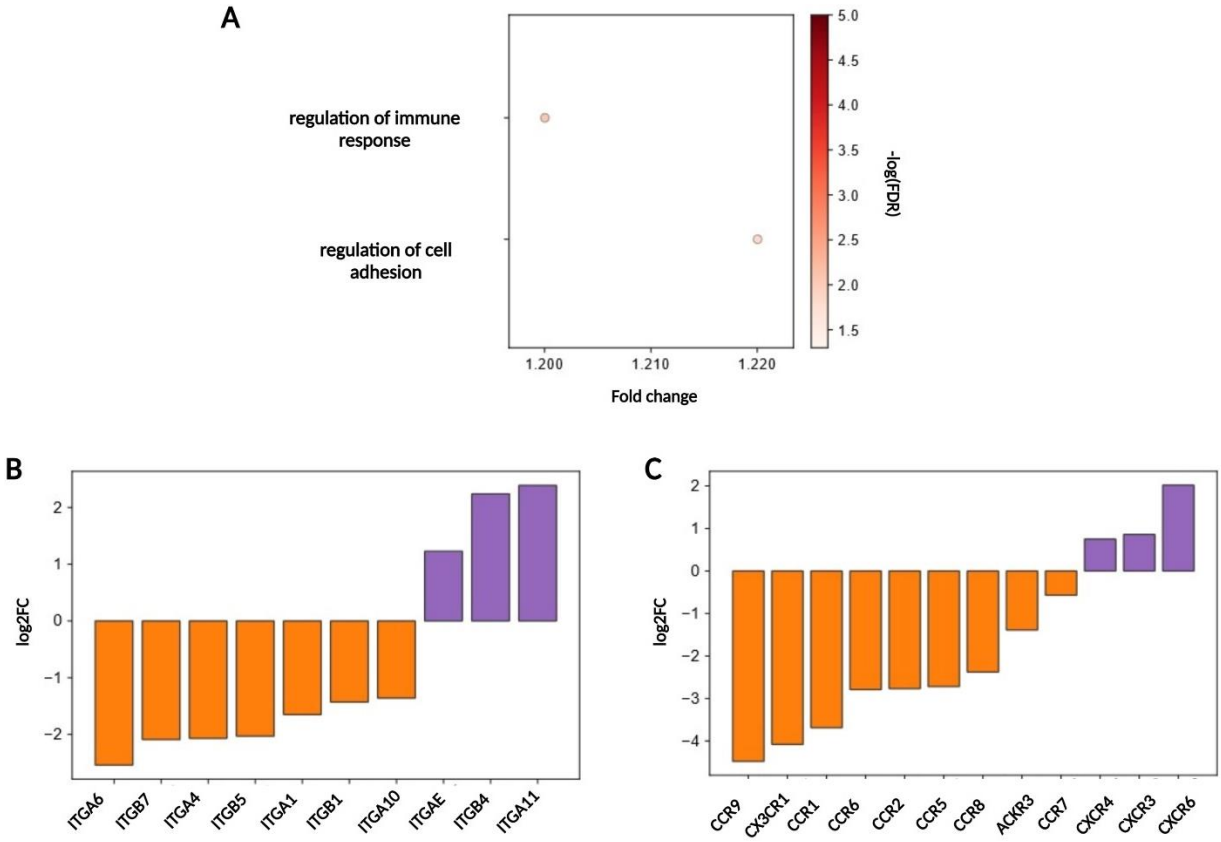

Figure 30. Significant changes in expression of genes related to immune responses, cell migration and adhesion upon CD4$^+$ T-cell activation. Panel (**A**) shows a functional annotation of significant DEGs relating to increased immune responses and cell adhesion upon naive CD4$^+$ T-cell activation. Annotated terms and pathways were filtered by an FDR cut-off of 0.05. Specific denominations used include Immune System Process (GO:0002376), Cell Migration (GO:0016477) and Cell Adhesion (GO:0007155). Panel (**B**) visualises differentially-expressed integrins, and panel (**C**) shows differentially-expressed chemokines upon cell activation.

Upregulated genes are shown in purple (FC>0) and downregulated in orange (FC<0). Families of integrins and chemokines were downloaded from the Pharmacology database.

Integrins act as adhesion molecules and are important for T-cell motility, proliferation and differentiation. They are expressed differently and have distinct roles in different $CD4^+$ T-cell subtypes, and in different T-cell developmental stages (Bertoni et al., 2018). This was also evident in the current dataset in this study (**Figure 30B**). Chemokines are a group of cytokines which regulate T-cell migration and homeostasis. T-cell subtypes express different chemokine receptors which determine their function and trafficking to tissues (Franciszkiewicz et al., 2012). T-cell differentiation from naive to effector was associated with changes in chemokine receptor expression (Colantonio et al., 2002), and also shown in this study (**Figure 30C**).

All in all, RNA sequencing data confirmed that upon activation, $CD4^+$ T-cells alter their expression profile of genes involved in T-cell function and metabolism.

3.6 Generation of a transient MCUa knockdown model in human $CD4^+$ effector T-cells

The substantial increase in mitochondrial metabolism and the compositional rearrangement of the MCU complex in effector T-cells prompted further investigation of the precise role of MCU and $_mCa^{2+}$ in $CD4^+$ T-cell metabolism and function. Transient MCUa knockdown in human effector $CD4^+$ T-cells was achieved using siRNA editing, as described in section 2.2.5.2. In order to validate the knockdown efficiency, three methods were applied. Firstly, *MCUa* mRNA levels were monitored in each donor separately after every transfection and were normalised to the housekeeping gene TATA-binding protein (*TBP*). *TBP* is a nuclear gene whose expression was not affected by T-cell editing. On average, there was a 60% *MCUa* mRNA knockdown efficiency (**Figure 31A**). Since primary T-cell transfection is a technically-challenging process (Gresch et al., 2004; Rahimmanesh et al., 2020; Zhang et al., 2018), this knockdown efficiency was considered successful. Gene expression changes of other MCU complex components, including *Micu1*, *MCUb*, and *EMRE*, as well as Ca^{2+} signalling-related genes (*Orai1*, *Orai3*, *STIM1*, *STIM2*, *NCLX*, *NFAT1*, and *NFAT4*) were evaluated to ensure absence of off-target effects which might have influenced the experimental outcome (**Figure 32**). No such changes were detected.

For simplicity, control-siRNA-treated $CD4^+$ T-cells are labelled as ‘siControl’, and MCUa-targeted siRNA-treated $CD4^+$ T-cells as ‘siMCU’ throughout the text.

Next, MCUa knockdown efficiency was examined on a protein level. An average of 50% MCUa protein level decrease (**Figure 31B** and **C**) was detected in $MCUa_{KD}$ cells, compared to control cells.

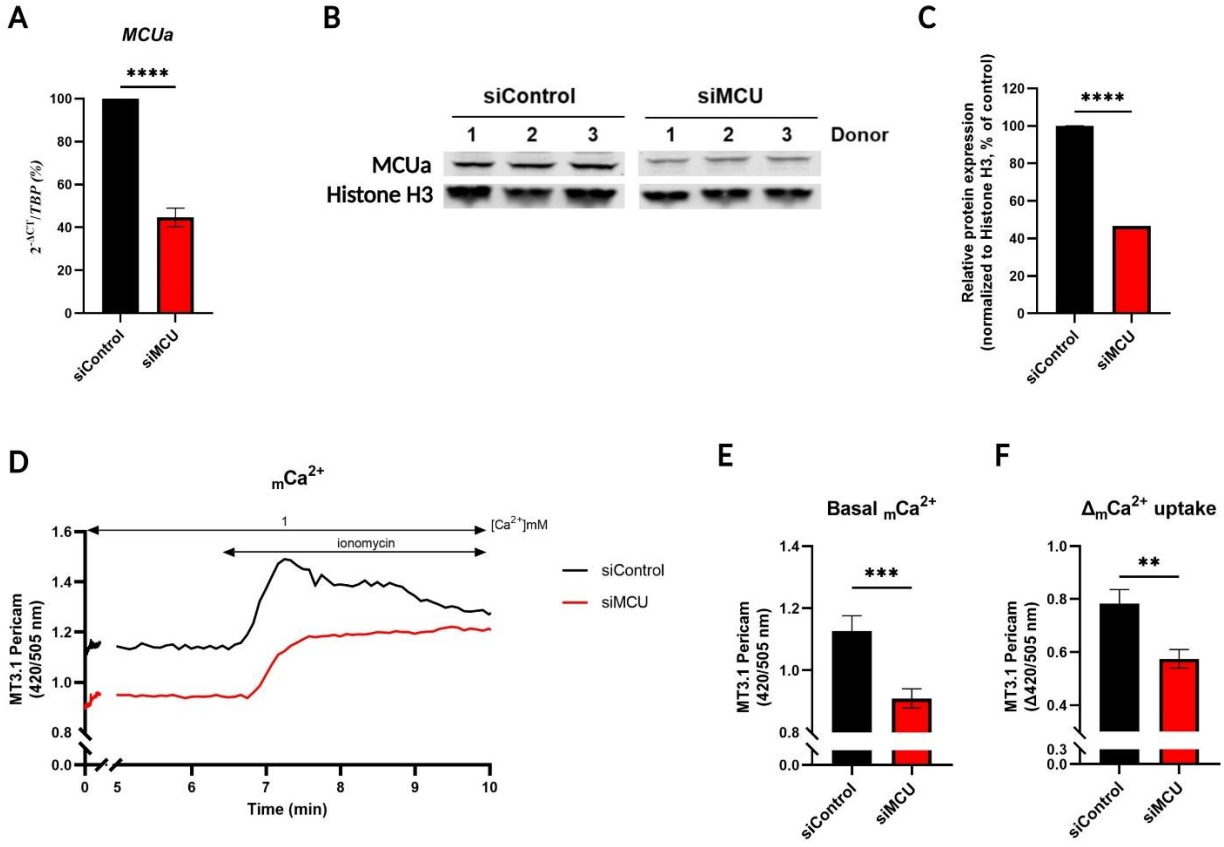

Figure 31. Transient MCUa knockdown model in human CD4⁺ effector T-cells. Knockdown efficiency was validated by interrogating MCUa mRNA and protein levels. There was an average mRNA knockdown of 60% (**A**). The quantified graph is representative of 9 different donors/biological replicates, as percentage of siControl (using 2 technical replicates and a negative water control). On protein level, MCUa expression was reduced to an average of 50% (**B**). The blot and quantification graph (**C**) show 3 separate donors/biological replicates as percentage of siControl, normalised to Histone H3. A decrease in MCU functionality was also observed (**D**) when measuring basal $_{m}[Ca^{2+}]$ and $_{m}Ca^{2+}$ uptake upon ionomycin stimulation (4 µM). The traces and graphs (**E** and **F**) show an average of 38 control effector T-cells and 48 MCU_{KD} effector T-cells (biological replicates) from 4 separate donors. For simplicity, control-siRNA-treated T-cells are labelled as "siControl", and MCUa-targeted siRNA-treated T-cells as "siMCU". Data are represented as mean ± SEM. ****- p <0.0001; ***-p <0.001; **-p <0.01, assessed by two-tailed unpaired and paired Student's t-test.

Lastly, the hindered function of the MCU complex was investigated by measuring resting $_{m}[Ca^{2+}]$ and $_{m}Ca^{2+}$ uptake. A significant reduction in basal $_{m}[Ca^{2+}]$ (**Figure 31E**), as well as in $_{m}Ca^{2+}$ uptake after ionomycin stimulation (**Figure 31F**) was observed upon MCUa downregulation.

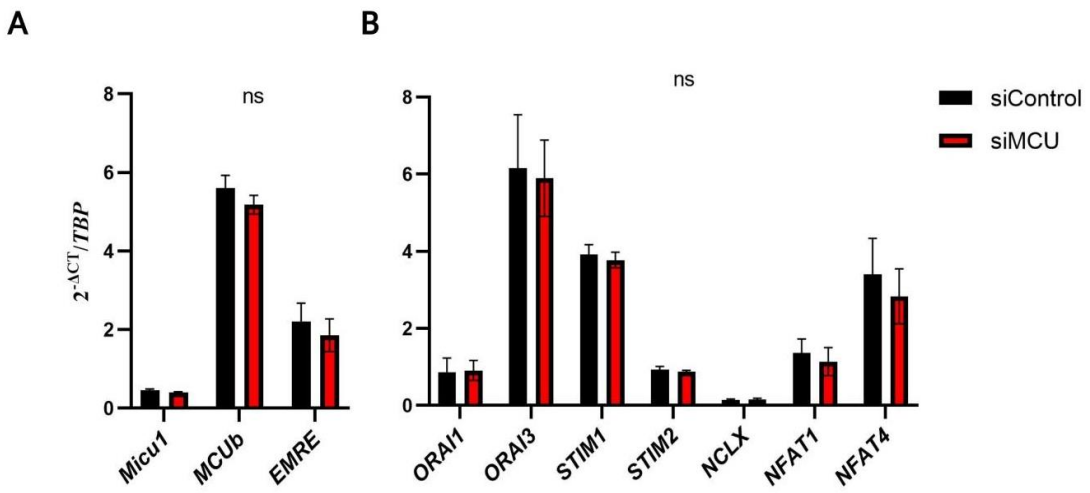

Figure 32. Expression of MCU complex components (A) and other Ca^{2+} signalling-related genes (B) is not affected by gene editing and transient knockdown of MCUa. Quantifications are representative of n=3 donors/biological replicates for all genes in both **A** and **B**. Experiments were performed using non-restimulated $CD4^+$ T-cells. Gene expression is normalised to HK gene *TBP*. Experiments were performed using 2 technical replicates per gene and a negative water control. Data are represented as mean ± SEM. ns-not statistically significant; assessed by two-tailed paired Student's t-test.

Taken together, these results confirmed that the generated MCUa knockdown model was successful and $_mCa^{2+}$ uptake was significantly impaired.

To further validate the experimental outcome, pharmacological MCU inhibition was applied by treatment of effector $CD4^+$ T-cells with the novel MCU inhibitor Ru265 (24 hour-treatment). Mitochondrial Ca^{2+} measurements indicated a significant decrease in both resting $_m[Ca^{2+}]$ and $_mCa^{2+}$ uptake (**Figure 33A, B** and **C**), in agreement with the differences seen among $MCUa_{KD}$ and control T-cells in this study and with findings obtained by Woods et al. (2019).

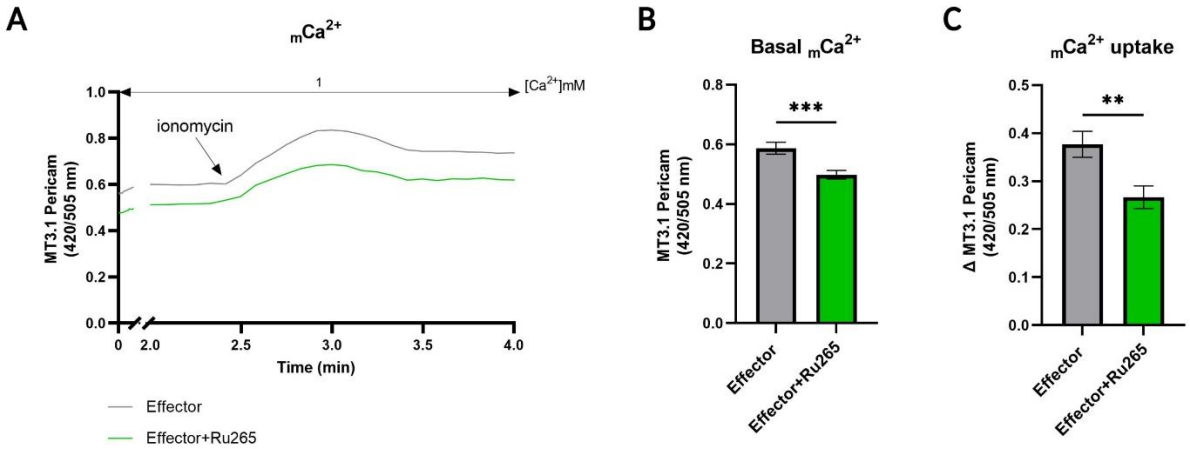

Figure 33. Treatment of CD4$^+$ T-cells with 100 µM of MCU inhibitor Ru265 causes a significant decrease in resting $_m$[Ca^{2+}] and $_m$Ca^{2+} uptake after stimulation with ionomycin (4 µM). Mitochondrial Ca^{2+} traces and quantifications (**B** and **C**) represent an average of 44 non-treated and 45 Ru265-treated effector CD4$^+$ T-cells (biological replicates) from 2 separate donors Data are represented as mean ± SEM. ***-*p* <0.001, **-*p* <0.01; assessed by two-tailed unpaired Student's t-test.

3.7 Impairment of $_m$Ca^{2+} uptake affects T-cell mitochondrial metabolism.

In order to investigate the role of MCU in the metabolism of CD4$^+$ T-cells, the generated MCUa$_{KD}$ and control cells were used to measure basic mitochondrial metabolic parameters, as previously performed for naive and effector CD4$^+$ T-cells.

Initially, mitochondrial respiration and mitochondrial ATP production rates were assessed. Additionally, a luminescent assay was applied to quantify global ATP levels in the cells. Both basal and maximal OCR were significantly reduced (**Figure 34**) in the MCUa$_{KD}$ T-cells. Furthermore, the rate of extracellular acidification was decreased, in line with lower ATP production which, although statistically insignificant, was observed in the MCUa$_{KD}$ cells. It has to be noted that the ATP production rate was highly donor-dependent (**S Figure 4**), therefore this experiment should be performed again to decrease sample variability.

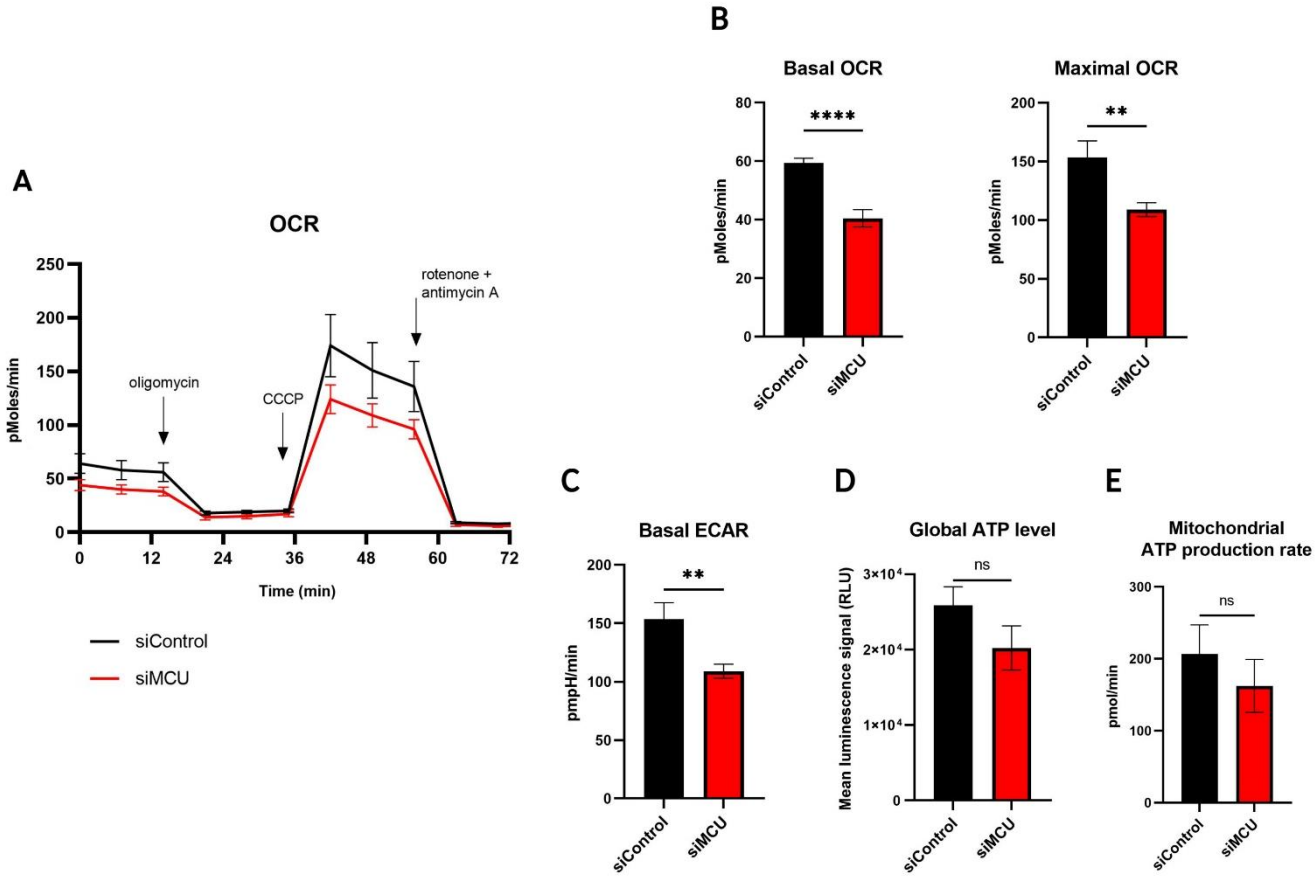

Figure 34. CD4$^+$ T-cell mitochondrial respiration and ATP production are hindered upon impaired $_mCa^{2+}$ uptake. Mitochondrial respiration measurements of siControl and siMCU CD4$^+$ T-cells showed that upon MCUa downregulation, T-cells appeared metabolically more similar to naive T-cells. Basal and maximal oxygen consumption rates (OCR) (**B**), extracellular acidification rates (ECAR) (**C**), and global ATP levels (measured with Cell Titer Glo® Luminescent Assay) (**D**) were reduced upon MCUa downregulation. Furthermore, mitochondrial ATP production rates were also decreased (**E**). OCR traces and quantifications, as well as assessment of mitochondrial ATP production rates, show an average of 3 different donors/biological replicates (assessed by using at least 6 technical replicates). Global ATP quantification shows an average of 4 different donors/biological replicates (assessed by using at least 3 technical replicates). Data are represented as mean ± SEM. ****- p <0.0001; **- p <0.01; ns-not statistically significant, assessed by two-tailed unpaired Student's t-test.

Considering the impotance of the ΔΨm in mitochondrial function, and the finding that MCU inhibition prevents mitochondrial hyperpolarisation after TCR stimulation (**Figure 25**), ΔΨm was additionally investigated in control and MCUa$_{KD}$ CD4$^+$ T-cells. In accordance with the decrease in OCR, ΔΨm was significantly reduced upon impairment of $_mCa^{2+}$ uptake via MCU (**Figure 35A**).

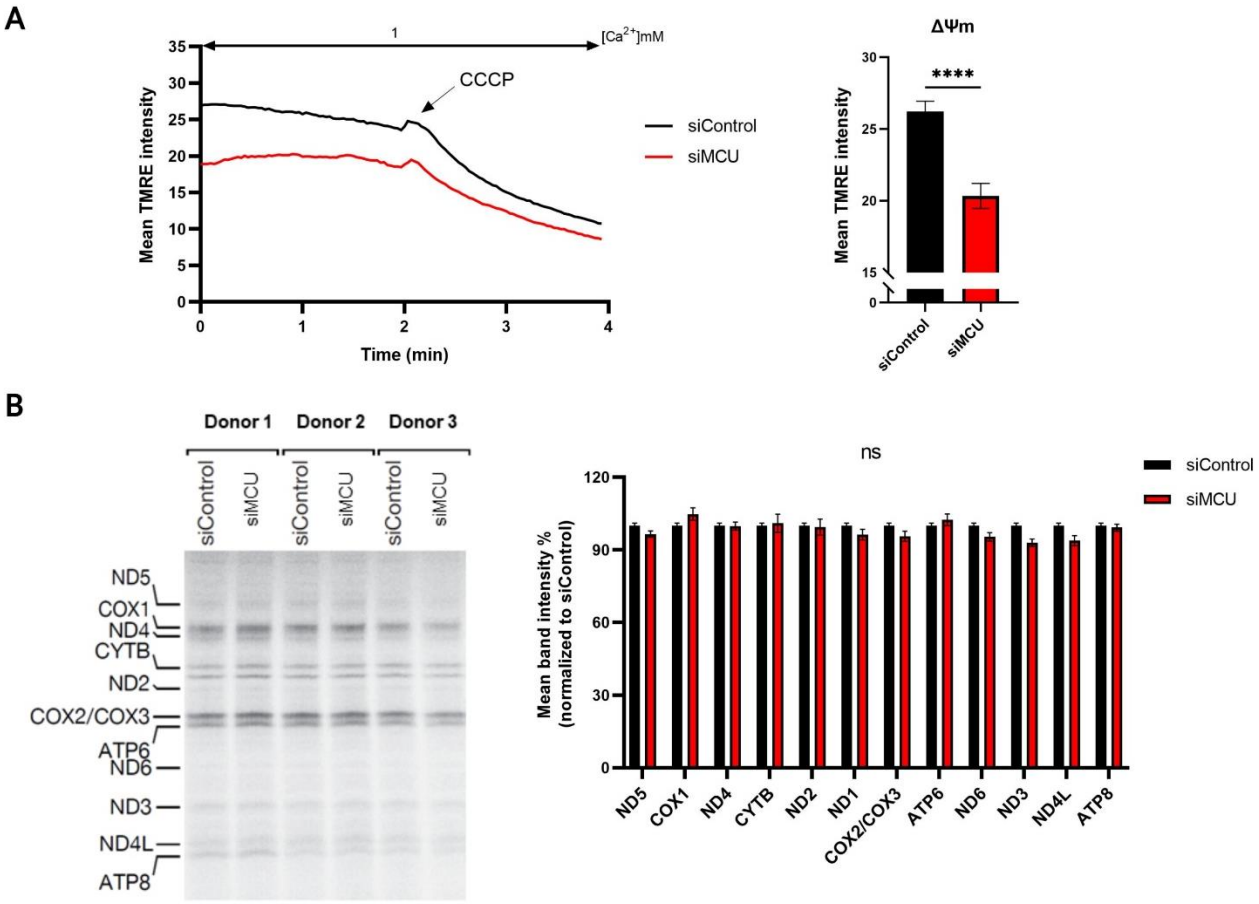

Figure 35. Effect of MCUa downregulation on mitochondrial membrane potential (ΔΨm) and mitochondrial protein translation. (**A**) A significant reduction in ΔΨm was observed upon MCUa downregulation. The traces and quantification show an average of 162 siControl and 125 siMCU T-cells (biological replicates) from 2 different donors. No differences were observed in mitochondrial protein translation (quantifications represent an average of the 3 different donors/biological replicates shown on the blot, as percentage of siControl). Data are represented as mean ± SEM. ****- p <0.0001; ns-not statistically significant, assessed by two-tailed unpaired and paired Student's t-test.

Treatment with the MCU inhibitor Ru265 on the other hand, did not affect ΔΨm (**Figure 36A**) or proliferation (**Figure 36B**) of effector T-cells. This was an unexpected finding; nevertheless, the absence of effects on ΔΨm was in accordance with the findings in the study by Woods et al. (2019). Cytosolic Ca^{2+} and SOCE should be evaluated in addition, to ensure the lack of non-specific Ru265 targets in T-cells.

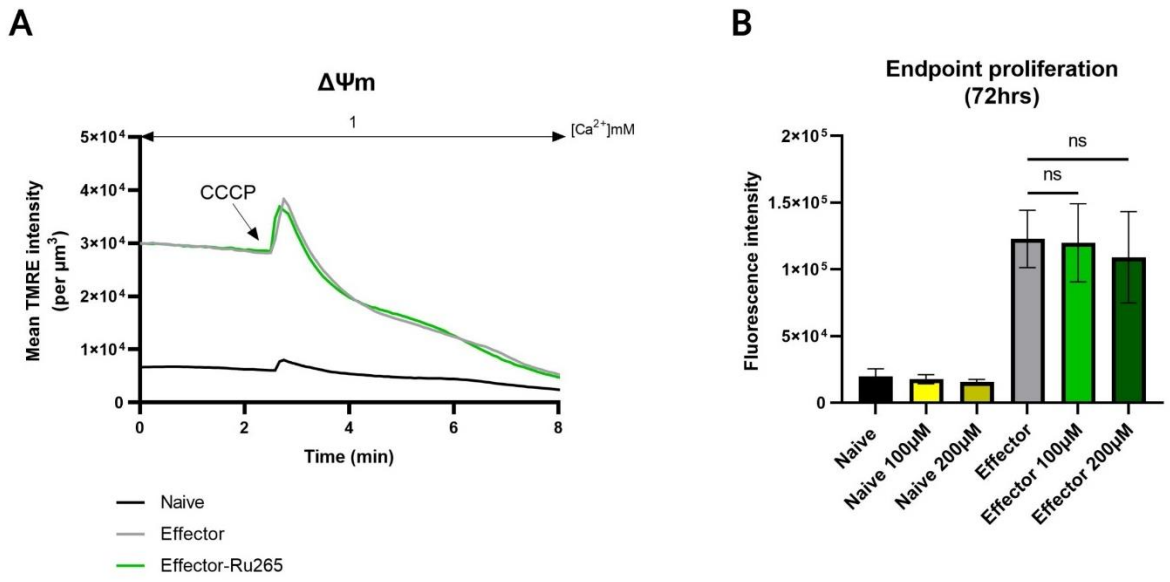

Figure 36. Treatment of CD4⁺ T-cells with 100 µM of MCU inhibitor Ru265 does not affect ΔΨm and effector T-cell proliferation. Mitochondrial membrane potential traces (**A**) represent an average of 84 non-treated naive, 98 non-treated effector, and 95 Ru265-treated effector T-cells (biological replicates) from 1 donor. [CCCP]=2 µM. Endpoint proliferation at 72 hrs (**B**) is shows 4 separate donors/biological replicates, non-treated or treated with 100 µM and 200 µM of Ru265 (3 technical replicates). Data are represented as mean ± SEM. ns-not statistically significant; assessed by two-tailed unpaired Student's t-test.

Unexpectedly, $MCUa_{KD}$ in effector $CD4^+$ T-cells did not significantly affect mitochondrial protein translation (**Figure 35B**). Since the increase in mitochondrial protein translation occurs very early in the T-cell activation process (already during the first 24 hrs after TCR stimulation, **Figure 23B**), it was important to assess whether MCUa downregulation

in naive T-cells has an impact on the translation process. Therefore, an "early-stage" $MCUa_{KD}$ model was generated (refer to section 2.2.5.2). The characterisation of this model (knockdown validation and the decreased MCU channel activity, shown in **Figure 37**) corresponded to the "late-stage" $MCUa_{KD}$ T-cell model. Both resting $_m[Ca^{2+}]$ and $_mCa^{2+}$ uptake were significantly reduced (**Figure 37B** and **C**). There was an average *MCUa* knockdown of 75% (**Figure 37D**). The two cell types are labelled as 'n-siControl-a' and 'n-siMCU-a', indicating that siRNA editing was performed on a naive T-cell-stage, followed by cell activation 24 hrs later.

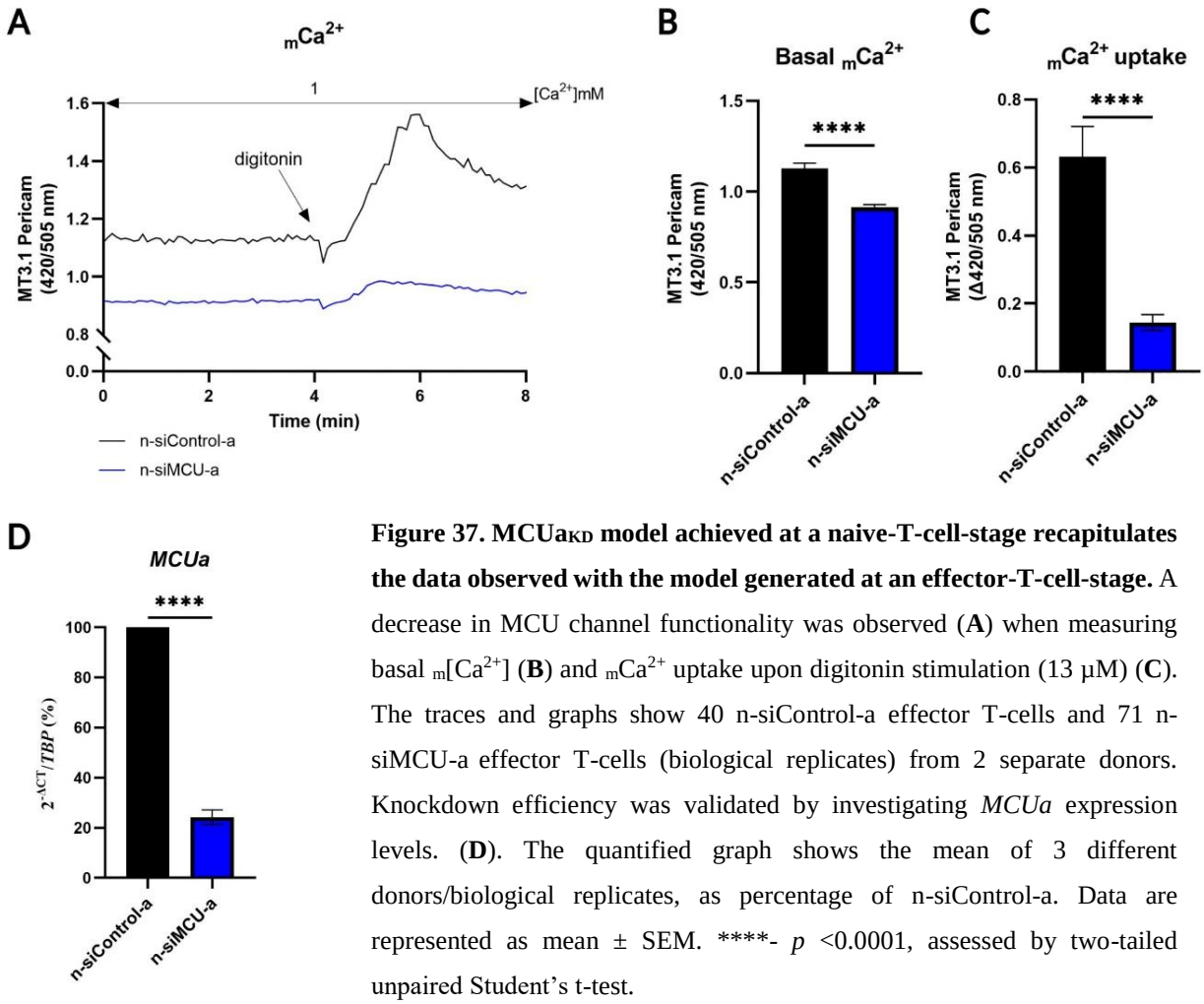

Figure 37. $MCUa_{KD}$ model achieved at a naive-T-cell-stage recapitulates the data observed with the model generated at an effector-T-cell-stage. A decrease in MCU channel functionality was observed (**A**) when measuring basal $_m[Ca^{2+}]$ (**B**) and $_mCa^{2+}$ uptake upon digitonin stimulation (13 µM) (**C**). The traces and graphs show 40 n-siControl-a effector T-cells and 71 n-siMCU-a effector T-cells (biological replicates) from 2 separate donors. Knockdown efficiency was validated by investigating *MCUa* expression levels. (**D**). The quantified graph shows the mean of 3 different donors/biological replicates, as percentage of n-siControl-a. Data are represented as mean ± SEM. ****- p <0.0001, assessed by two-tailed unpaired Student's t-test.

Nevertheless, no significant differences in mitochondrial protein translation were observed (**Figure 38**), independent of the timing of MCUa knockdown.

Treatment with 200 µM of Ru265 for 24 hrs showed a tendency to decrease mitochondrial protein translation in effector $CD4^+$ T-cells (**S Figure 3**); however, this effect was only mild, it was observed once and should be repeated and validated again.

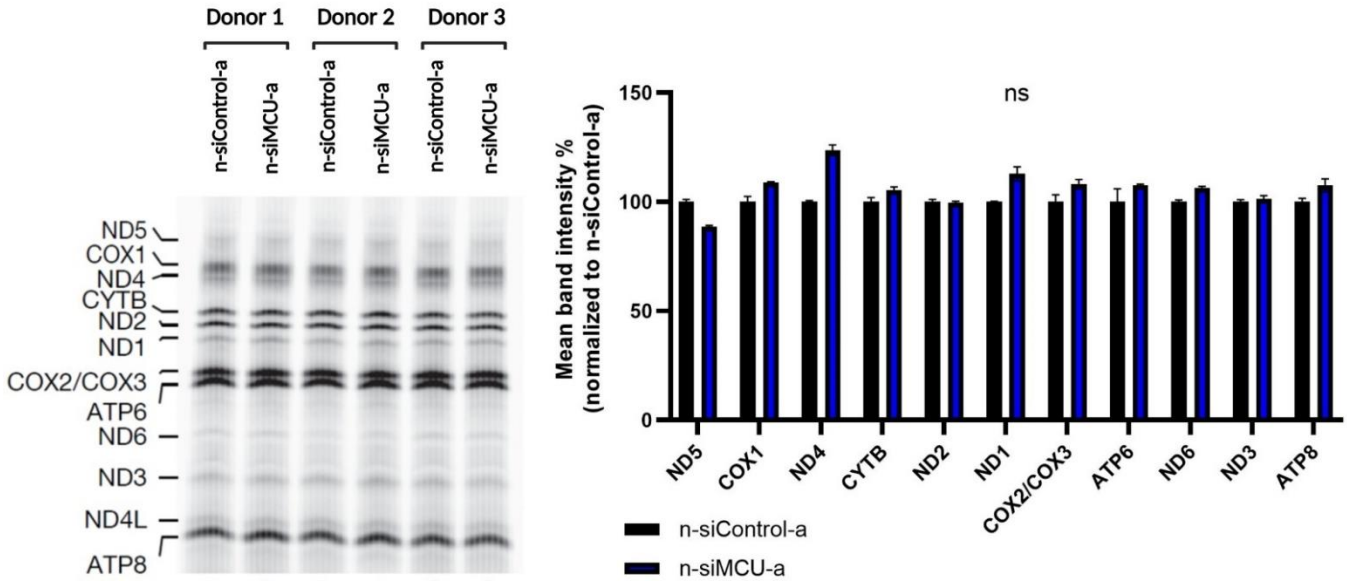

Figure 38. Mitochondrial protein translation ^{35}S labelling was performed on the "early-stage" $MCUa_{KD}$ model (naive T-cell stage). The stage of MCU downregulation does not affect mitochondrial protein translation. Data shows 3 different donors/biological replicates. For quantification, data is normalised to the 'n-siControl-a' sample, respectively for each donor. Data are represented as mean ± SEM. ns-not statistically significant; assessed by two-tailed paired Student's t-test.

3.8 Transient impairment of $_{m}Ca^{2+}$ uptake does not affect T-cell proliferation and ROS generation, but significantly affects $_{c}[Ca^{2+}]$ and SOCE.

T-cell proliferation is an important functional parameter indicating proper T-cell activation. Therefore, the effect of $MCUa_{KD}$ on effector $CD4^{+}$ T-cell proliferation was investigated. Interestingly, impaired MCU function did not significantly affect cell proliferation (**Figure 39A** and **B**). Similar results were observed when effector T-cells were treated with the MCU inhibitor Ru265 (**Figure 36B**).

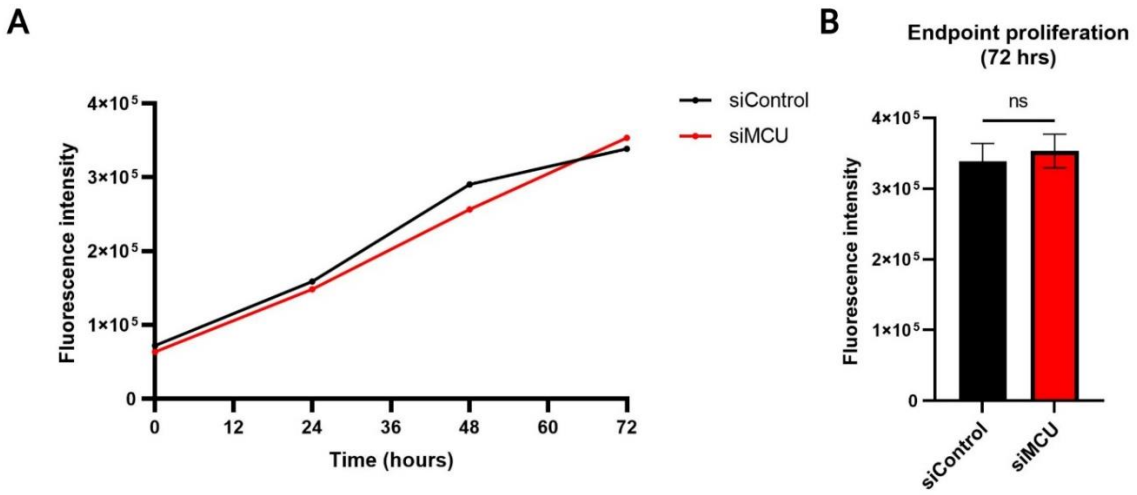

Figure 39. MCUa downregulation does not affect CD4⁺ T-cell proliferation rates. The traces (**A**) and quantification graph (72 hrs of proliferation) (**B**) show a mean of 4 different donors/biological replicates (using 3 technical replicates for each condition). Data are represented as mean ± SEM. ns-not statistically significant, assessed by two-tailed unpaired Student's t-test.

ROS production significantly increases upon T-cell activation (**Figure 28**). Therefore, it was important to investigate whether MCU has a role in ROS production and the regulation of the redox potential in T-cells. Both cytosolic and mitochondrial H_2O_2 levels were measured upon $MCUa_{KD}$, as well as both cytosolic and mitochondrial glutathione redox potential (E_{GSH}). Unexpectedly, no differences in both H_2O_2 levels (**Figure 40A-D**) and E_{GSH} (**Figure 40E-F**) were observed in $MCUa_{KD}$ cells compared to control cells, even upon maximal oxidation with external H_2O_2 addition and maximal reduction upon external DTT addition. This could indicate three possibilities: 1) transient partial MCU impairment does not affect ROS production, 2) an antioxidative mechanism exists which compensates as soon as lower $_m[Ca^{2+}]$ are detected, and/or 3) the biosensor HyPer is not sensitive enough to detect small changes in ROS levels.

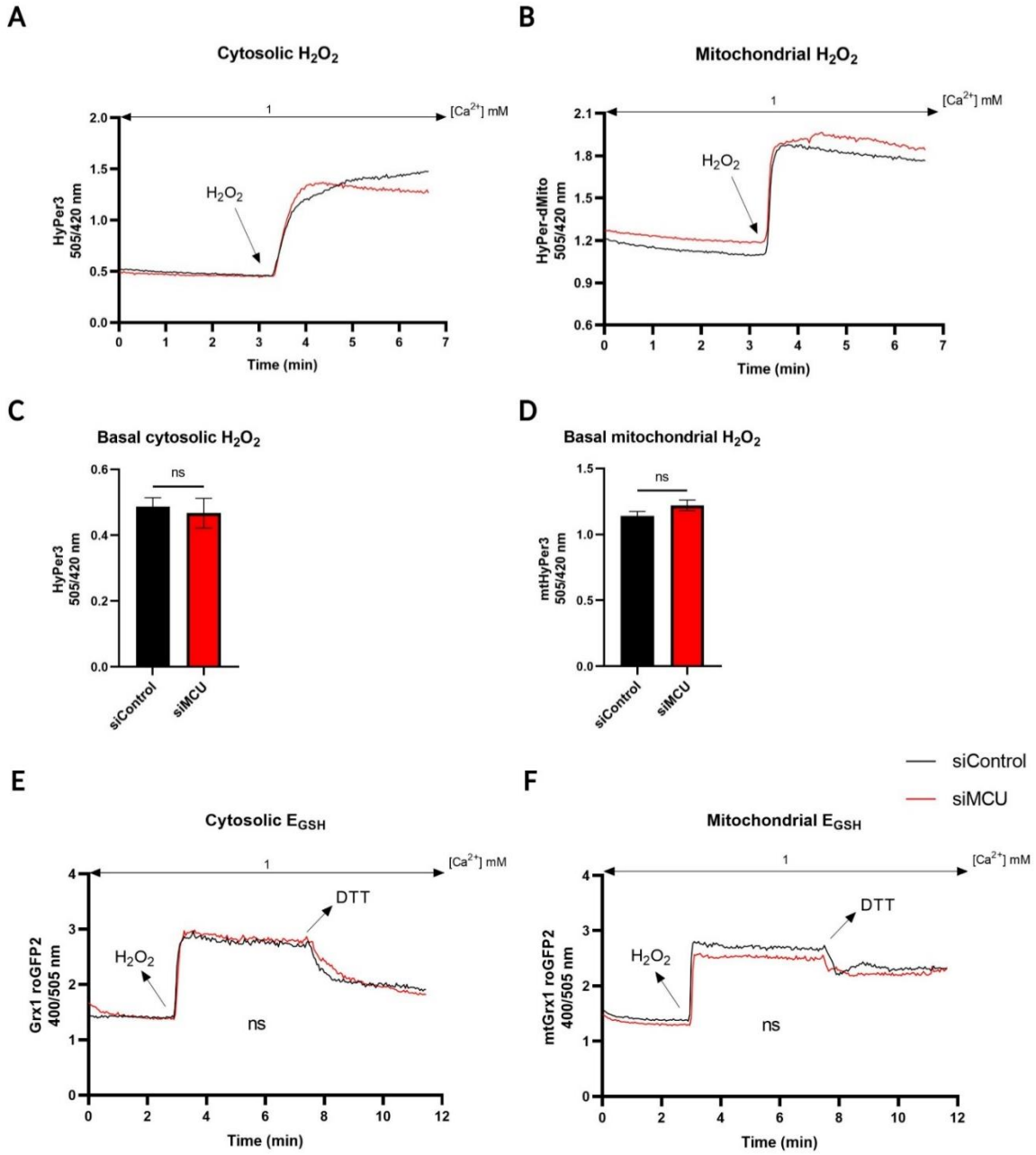

Figure 40. MCUa downregulation does not affect CD4$^+$ T-cell H_2O_2 levels and glutathione redox potential (E_{GSH}). Neither cytosolic nor mitochondrial H_2O_2 levels were significantly different among control and $MCUa_{KD}$ T-cells (**A-D**). Cytosolic H_2O_2 level traces (**A**) and quantification (**C**) show an average of 20 siControl and 36 siMCU T-cells (biological replicates) from 2 different donors. Mitochondrial H_2O_2 level traces (**B**) and quantification (**D**) show an average of 75 siControl and 79 siMCU T-cells (biological replicates) from 2 different donors. Additionally, both cytosolic and mitochondrial E_{GSH} were not affected by impairment of $_mCa^{2+}$ uptake (**E-F**). Cytosolic E_{GSH} traces (**E**) show an average of 9 siControl and 25 siMCU T-cells from (biological replicates) 1 donor. Mitochondrial E_{GSH} traces (**F**) represent an average of 48 siControl and 57 siMCU T-cells (biological replicates) from 3 different donors. Data are represented as mean ± SEM. ns-not statistically significant, assessed by two-tailed unpaired Student's t-test. [H_2O_2] =100 µM for (**A-B**), =200 µM for (**E-F**); [DTT] =100 µM.

To indirectly evaluate potential differences in antioxidant capacity upon MCUa downregulation, T-cells were treated with different concentrations of H_2O_2 and proliferation was assessed. No differences were observed among control and $MCUa_{KD}$ cells. Higher H_2O_2 concentrations led to an overall reduction in proliferation (**Figure 41**). However, these interpretations should be considered with caution, given that the experiment was performed only twice and high variability was observed. Furthermore, the enzymatic activity of antioxidant enzymes (superoxide dismutase, glutathione peroxidase and catalase) needs to be assessed in $MCUa_{KD}$ T-cells.

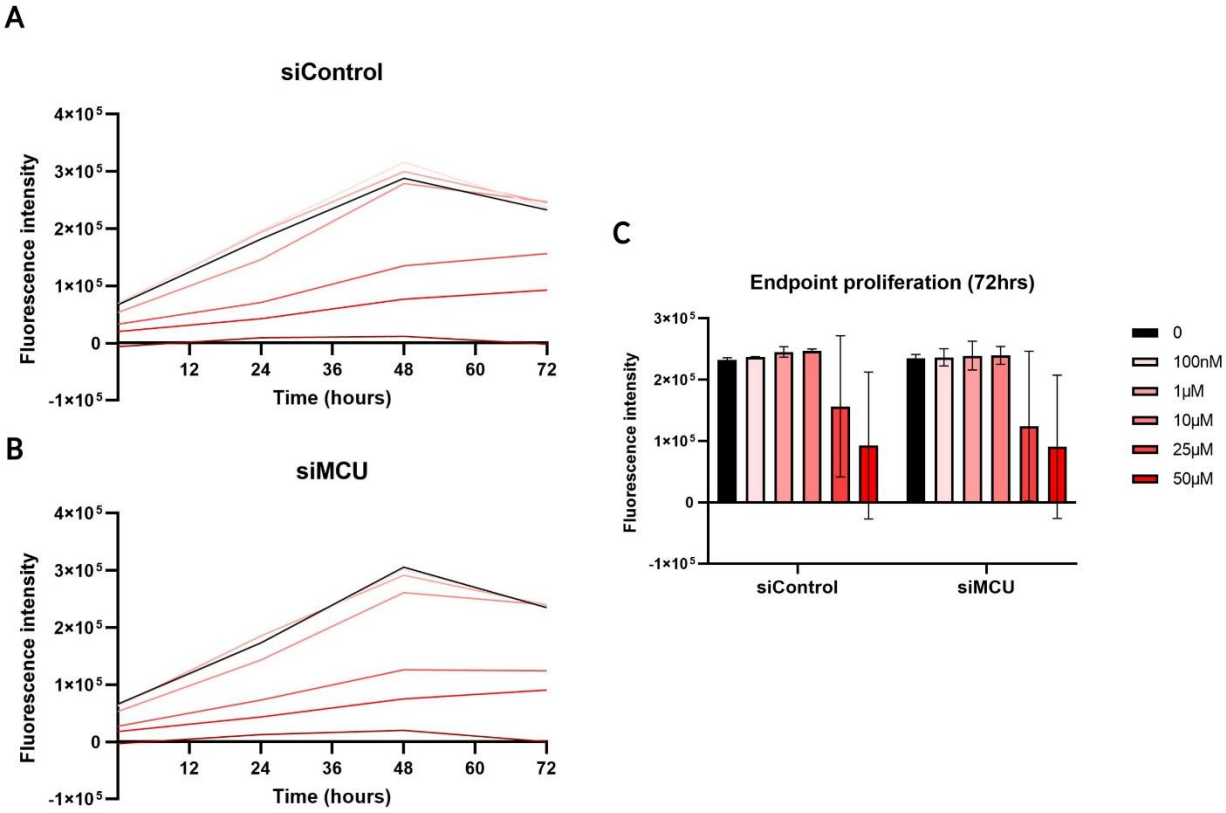

Figure 41. Impaired $_{m}Ca^{2+}$ uptake does not affect the antioxidant capacity of $CD4^+$ T-cells. Proliferation rates of T-cells were assessed after treatment with different concentrations of H_2O_2 (range from 0 to 50 µM). Lower H_2O_2 concentrations slightly increased T-cell proliferation, whereas higher concentrations were toxic. No significant differences in proliferation rates were observed between control and MCU_{KD} cells. The traces and quantifications represent an average of 2 different donors/biological replicates. Data show the mean ± SD.

To assess the effect of MCUa downregulation and thus, the relationship between the MCU complex and SOCE in T-cells, resting $_{c}[Ca^{2+}]$ and SOCE were assessed in $MCUa_{KD}$ and control T-cells. Interestingly, a significant decrease in basal $_{c}[Ca^{2+}]$ and SOCE was observed upon $MCUa_{KD}$ (**Figure 42**).

This indicated that the MCU complex has an effect on SOCE signalling in $CD4^+$ T-cells.

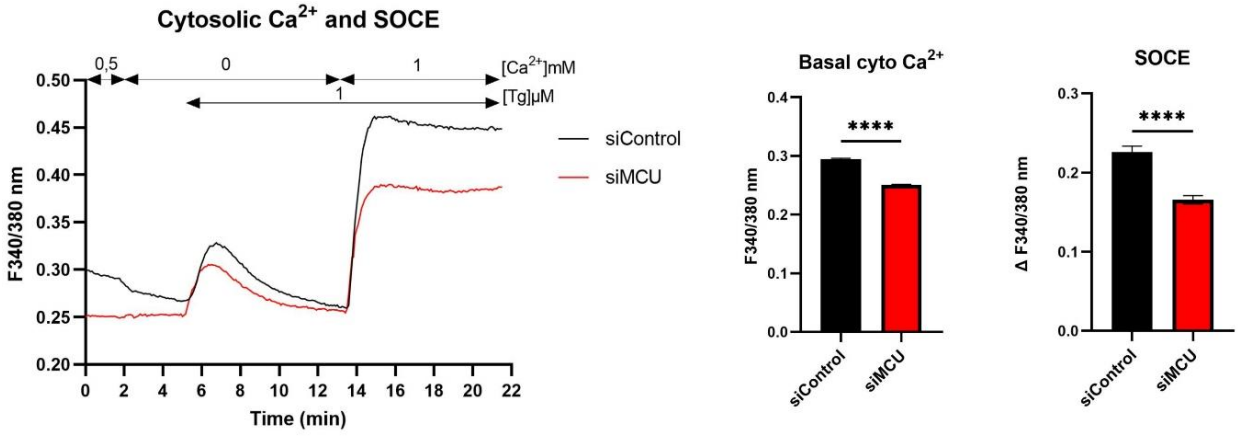

Figure 42. Significant decrease in cytosolic Ca^{2+} levels and SOCE upon MCUa downregulation. Traces and quantifications show an average of 648 siControl and 739 siMCU T-cells from (biological replicates) 3 different donors. Data are represented as mean ± SEM. ****- p <0.0001, assessed by two-tailed unpaired Student's t-test. Tg=thapsigargin (1 µM).

3.9 Transient impairment of $_mCa^{2+}$ uptake affects the proinflammatory function of $CD4^+$ T-cells.

$CD4^+$ T-cells carry out important functions, ranging from activation of other immune cells such as B-cells and cytotoxic T-cells, to suppression of immune system reactions. To be able to fulfil their functions, these cells carefully orchestrate their cytokine signals and migratory patterns. Since a decrease in $_mCa^{2+}$ uptake was shown to have profound effects on cell metabolism, it was of interest to investigate possible effects on $CD4^+$ T-cell function.

Initially, a small panel of gene expression of cytokines secreted by different $CD4^+$ T-cell subtypes was screened (**Figure 43A**).

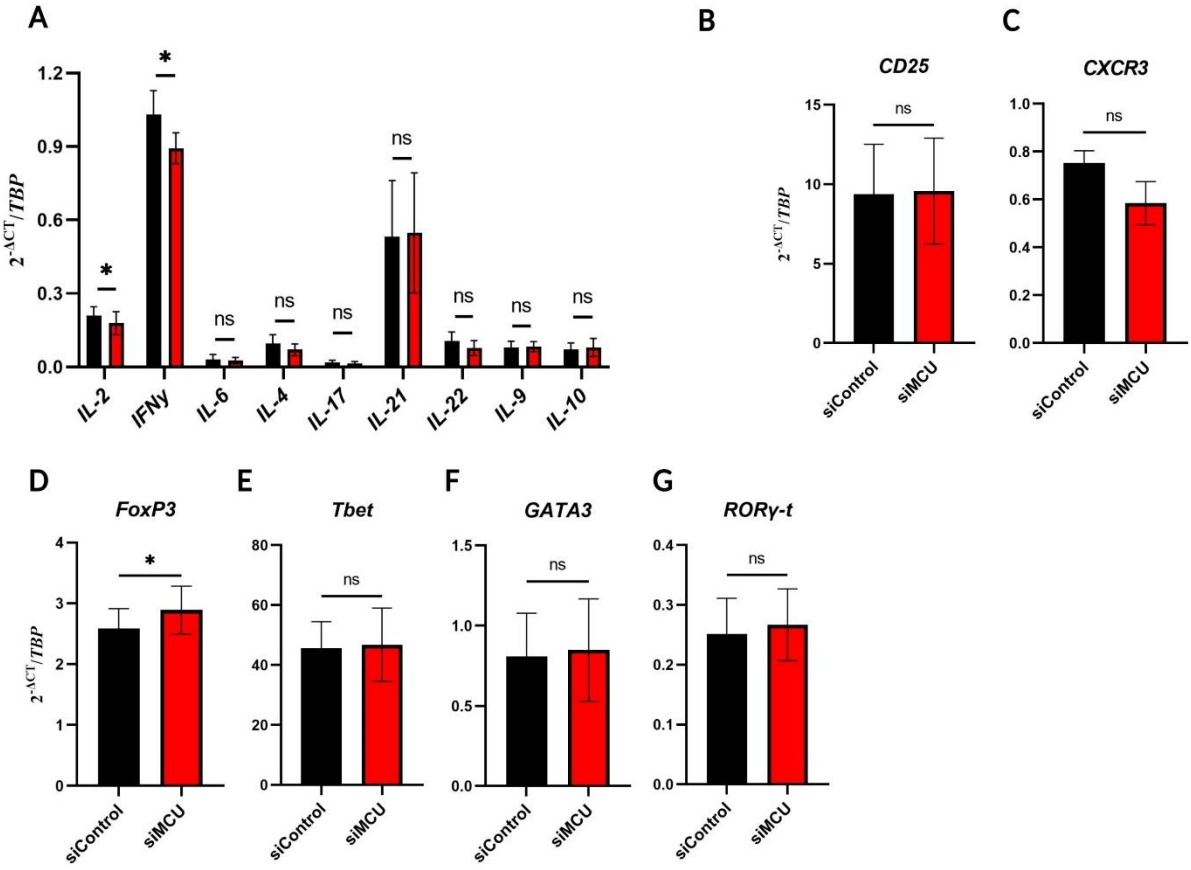

Figure 43. An mRNA panel of cytokines, transcription factors and surface markers performed to examine the role of MCU in T-cell function. A decreased expression of proinflammatory cytokines *IL-2* and *IFNγ*, and an increased expression of Treg transcription factor *FoxP3* are observed upon MCUa downregulation. No other significant changes are detected. Panel (**A**) shows gene expression analyses of common $CD4^+$ T-cell cytokines. Quantifications are representative of n=3 donors/biological replicates for *IL-2*, *IL-6* and *IL-4*, n=4 donors/biological replicates for *IL-17* and *IL-22*, n=5 donors/biological replicates for *IFNγ,* and n=6 donors/biological replicates for *IL-21*, *IL-9* and *IL-10*. Panels (**B**) and (**C**) show gene expression of common $CD4^+$ T-cell surface markers. Quantifications are representative of n=3 donors/biological replicates for both *CD25* and *CXCR3*. Panels (**D**)-(**G**) show gene expression of $CD4^+$ T-cell transcription factors. Quantifications are representative of n=6 donors/biological replicates for *FoxP3* and n=3 donors/biological replicates for *Tbet, GATA3* and *RORγ-t.* Experiments were performed using 8 hrs-restimulated $CD4^+$ T-cells. Gene expression is normalised to HK gene *TBP*. Experiments were performed using 2 technical replicates per gene and a negative water control. Data are represented as mean ± SEM. *-$p \leq 0.05$, ns-not statistically significant; assessed by two-tailed paired Student's t-test.

Upon MCUa downregulation, the gene expression of two crucial proinflammatory cytokines, IL-2 and IFNγ, was significantly decreased (**Figure 43A**). Additionally, upon cell re-stimulation with different concentrations of CD3+CD28 antibody cocktail, the same mRNA decrease trend was observed, although statistically insignificant (**Figure 44)**. It is of importance

to note that the re-stimulation kinetics experiment (**Figure 44**) was performed by using samples from 3 donors only. Increasing the number of donors would strengthen these findings and decrease sample variability.

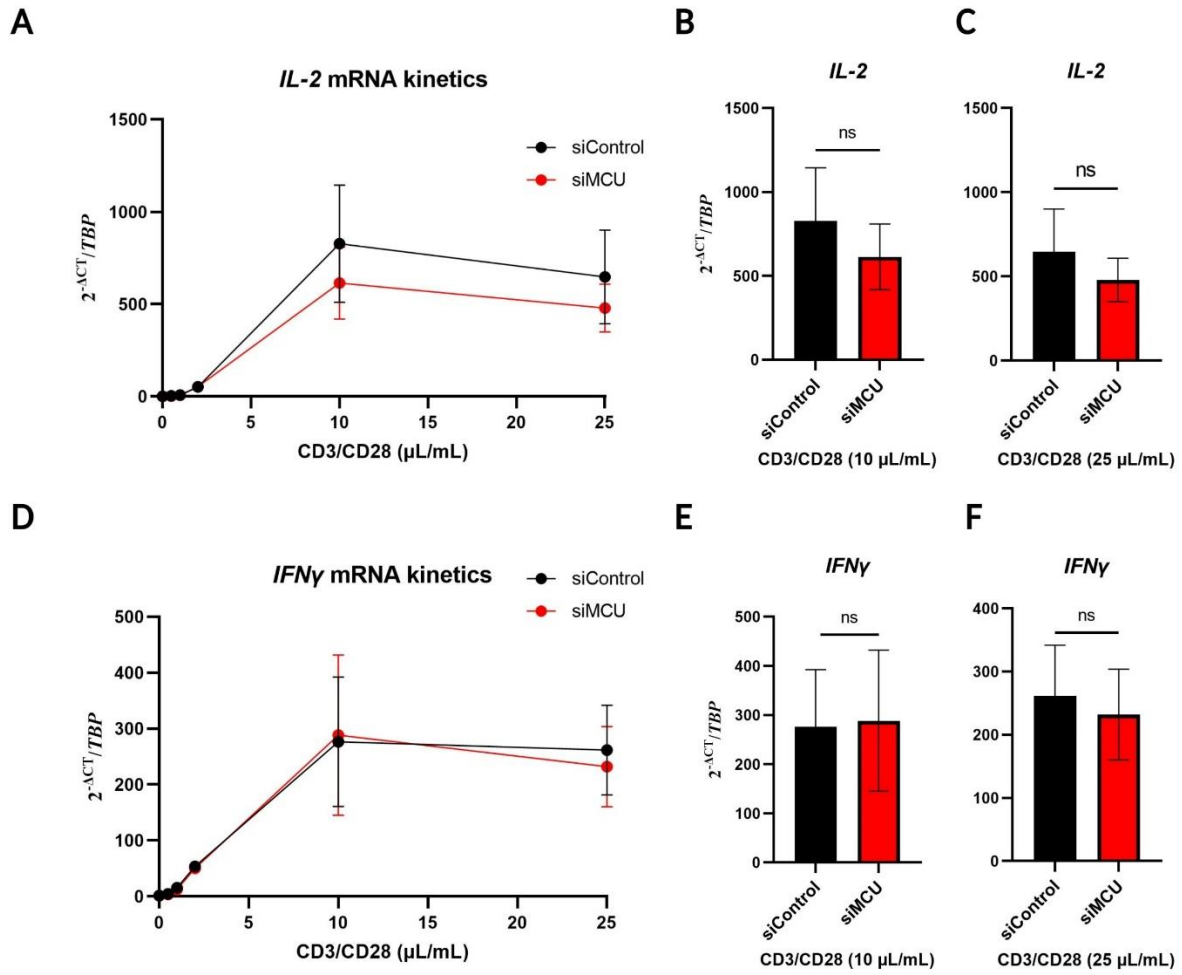

Figure 44. MCUa downregulation leads to reduced gene expression of crucial T-cell proinflammatory cytokines: IL-2 and IFNγ. mRNA expression data showed reduced levels of *IL-2* (**A-C**) and *IFNγ* (**D-F**) upon impairment of ${}_{m}Ca^{2+}$ uptake. Cell re-stimulation with different concentrations of CD3+CD28 antibody cocktail solution gave similar results. Both *IL-2* (**A**) and *IFNγ* (**D**) expression levels were lower in $MCUa_{KD}$ T-cells compared to control, even though statistically insignificant, when restimulated with both 10 µL/mL (**B** and **E**) and 25 µL/mL of CD3+CD28 solution (**C** and **F**). *IL-2* and *IFNγ* quantifications represent an average of 3 different donors/biological replicates. All experiments were performed by using 2 technical replicates and a negative water control. Expression data is normalised to HK gene *TBP*. Data are represented as mean ± SEM. ns- not statistically significant, assessed by two-tailed paired Student's t-test.

Furthermore, IL-2 and IFNγ secretion was reduced in $MCUa_{KD}$ T-cells upon CD3+CD28 antibody re-stimulation, statistically significant for IFNγ (**Figure 45A** and **B**). There was no difference in IL-6 secretion among control and $MCUa_{KD}$ cell lines (**Figure 45C**).

Nevertheless, strong conclusions cannot be made here due to the small number of experiments performed. Increasing the number of donors and further investigating IL-2 and IL-6 secretion would be beneficial for decreasing donor-to-donor variability in the study.

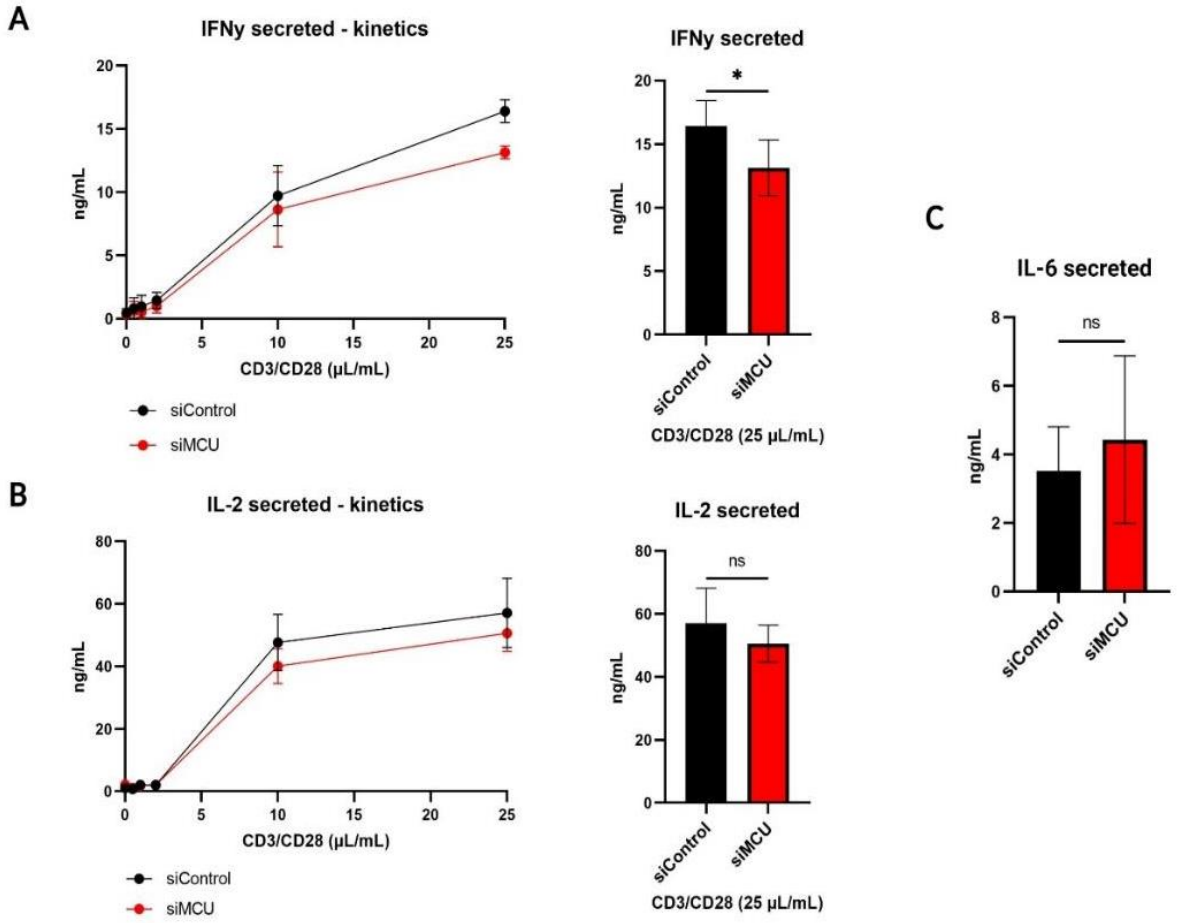

Figure 45. Changes in cytokine secretion upon downregulation of MCUa. Re-stimulation with CD3+CD28 antibody cocktail solution for 8 hrs led to significantly decreased IFNγ secretion in $MCUa_{KD}$ T-cells compared to control (**A**), the most evident difference detected when 25 µL/mL antibody solution were used. No significant differences were observed for IL-2 secretion (**B**) and IL-6 secretion (**C**). Traces and quantification graphs shown an average of 3 different donors/biological replicates for IL-2 and IL-6, and 5 different donors/biological replicates for IFNγ. Data are represented as mean ± SEM. *- $p \leq 0.05$; ns- not statistically significant, assessed by two-tailed paired Student's t-test.

Changes in transcription factors and surface markers expression levels were also investigated in control and $MCUa_{KD}$ $CD4^+$ T-cells (refer back to **Figure 43D-G**). A significant increase in Treg transcription factor *FoxP3* was observed upon MCUa downregulation (**Figure 43D**). No other significant changes were found.

Based on these findings, it can be concluded that impaired $_{m}Ca^{2+}$ uptake caused by MCUa downregulation leads to a moderately diminished proinflammatory action of $CD4^{+}$ T-cells, indicated by lower IFNγ and IL-2 levels.

T-cell migration and invasion are important functional parameters which were considered in this study. Migration was assessed in two different ways. Firstly, a chemokine gradient was established by using CXCL12 and CCL19 in T-cell conditioned medium, and the cells were allowed to migrate towards it, passing through a pore insert. No difference was observed between control and $MCUa_{KD}$ T-cells (**Figure 46A**). Additionally, T-cells were allowed to migrate towards a melanoma cell-conditioned medium. A study by Harlin et al. (2009) showed that metastatic melanoma cells are able to secrete chemokines which contribute to recruitment of cytotoxic T-cells. Based on this study, the lung-metastatic melanoma cell line 1205Lu was used to generate conditioned medium used for migration assays. $CD4^{+}$ T-cells were subjected to migration towards 1205Lu-conditioned medium alone, or 1205Lu-conditioned medium containing CXCL12 and CCL19. An external addition of the chemokine gradient led to an increased cell migration overall (**Figure 46B**); however, no significant difference was observed between control and $MCUa_{KD}$ T-cells.

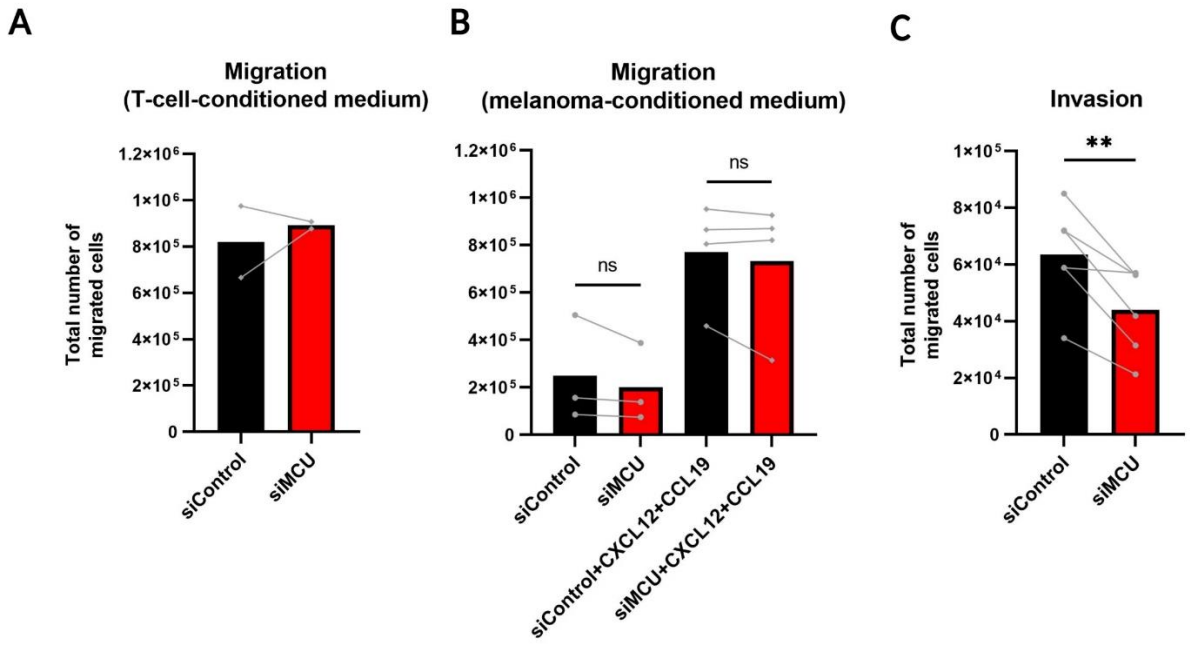

Figure 46. MCU influences $CD4^{+}$ T-cell invasion. $CD4^{+}$ T-cells ($1x10^{6}$) were subjected to two types of migration: (**A**)-towards a chemokine gradient in T-cell-conditioned medium and (**B**)-towards a chemokine gradient in 1205Lu melanoma-conditioned medium (with and without external addition of CXCL12 and CCL19). In both cases, no significant difference between control and $MCUa_{KD}$ cells was observed. Panel (**A**) represents an average of 2 different donors/biological replicates (using 3 technical replicates). Panel (**B**) represents an average of 3 different donors/biological replicates (using 3 technical replicates). When cells were subjected to a Matrigel-

invasion assay, a significantly reduced invasion was seen in $MCUa_{KD}$ cells compared with control (**C**). Panel (**C**) represents an average of 6 different donors/biological replicates (using 3 technical replicates). Data are represented as mean ± SEM (single donors are indicated as grey points). **- p <0.01, ns- not statistically significant, assessed by two-tailed paired Student's t-test.

T-cell invasion was quantified by allowing the $CD4^+$ T-cells to migrate towards a chemokine gradient through a Matrigel-coated pore insert, mimicking a tissue-invasive environment. Results showed that $MCUa_{KD}$ cells invaded significantly less compared to control cells (**Figure 46C**). Therefore, MCU was shown to have an important role in T-cell invasion *in vitro*.

3.10 Significant differences in expression of genes related to multiple crucial cell pathways upon $_mCa^{2+}$ inhibition in $CD4^+$ T-cells revealed from RNA sequencing data.

To further confirm differences among effector $CD4^+$ T-cells with and without impaired $_mCa^{2+}$ uptake via MCU, RNA sequencing was performed. DEG analysis showed multiple significantly up- or down-regulated genes upon $MCUa_{KD}$. The volcano plot (**Figure 47**) lists the top DEGs, as well as the two differentially-expressed transcription factors, MXI1 (Max-interacting protein 1) and SNAPC4 (snRNA-activating protein complex subunit 4) (labelled in **bold**). SNAPC4 is a transcription factor required for the transcription of both RNA polymerase II and III (Hinkley et al., 2003). MXI1 is a transcriptional repressor which antagonises the oncogene c-myc. It is a hypoxia-inducible factor (HIF)-target gene which has been shown to protect cells from c-myc-dependent apoptosis *in vitro* (Tsao et al., 2008).

The full list of significant DEGs is given in **S Table 1**.

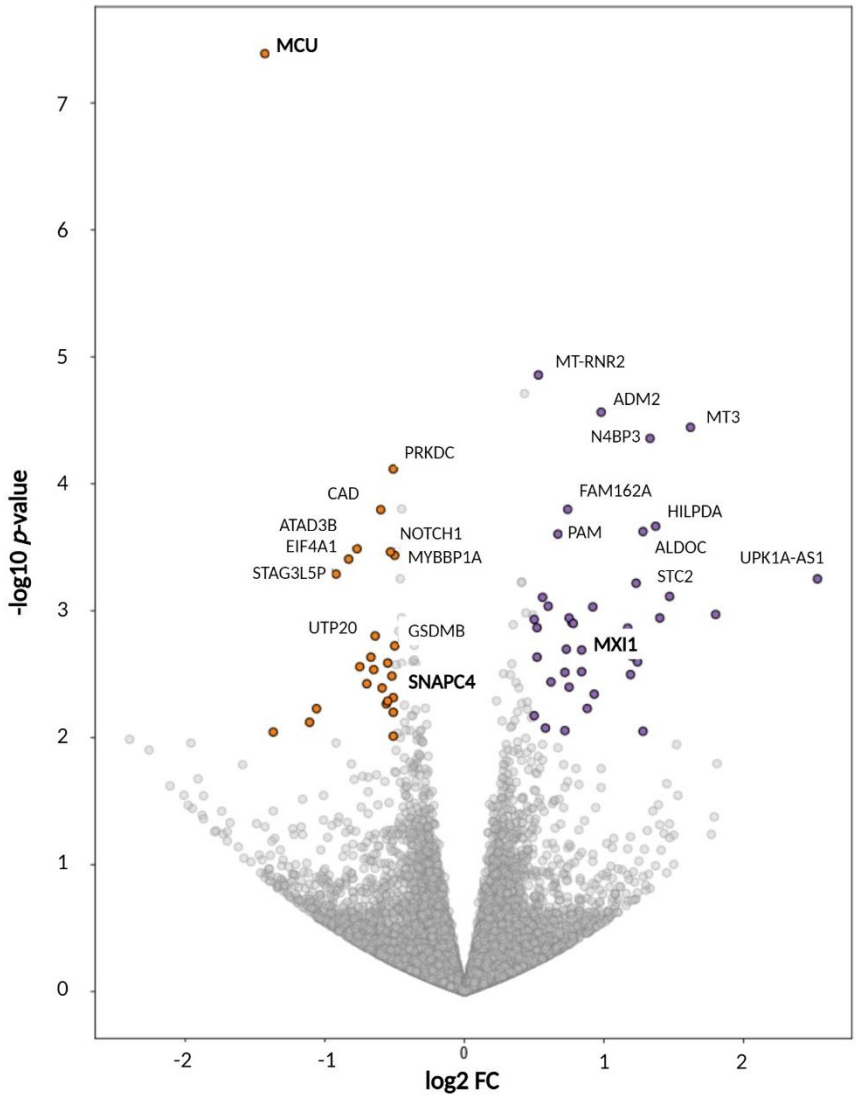

Figure 47. A volcano plot illustrating RNA sequencing data which revealed significant changes in expression of genes related to multiple cellular pathways upon MCUa downregulation. Candidates have been selected using a *p*-value cut-off of 0.05 and were further filtered by an absolute logarithmical fold change (log2 FC) of 0.5 and sorted as up- or down-regulated depending on the fold change (up - FC>0 (purple); down - FC<0 (orange)). Significant transcription factors are labelled in **bold**.

To associate the differences in gene expression affected by MCUa downregulation with functional cellular pathways, KEGG analyses were utilised. Upon impairment of $_{m}Ca^{2+}$ uptake through MCU, multiple cellular pathways were significantly altered, including rRNA metabolism and ribosome biogenesis, responses to hypoxia, transcriptional regulation by RNA polymerase II, and apoptosis (**Figure 48**). All these pathways are crucial for proper T-cell metabolism and function. These cellular pathway alterations indicated possible compensations of the T-cells which lack MCUa, in the context of preventing increase of cell stress and death.

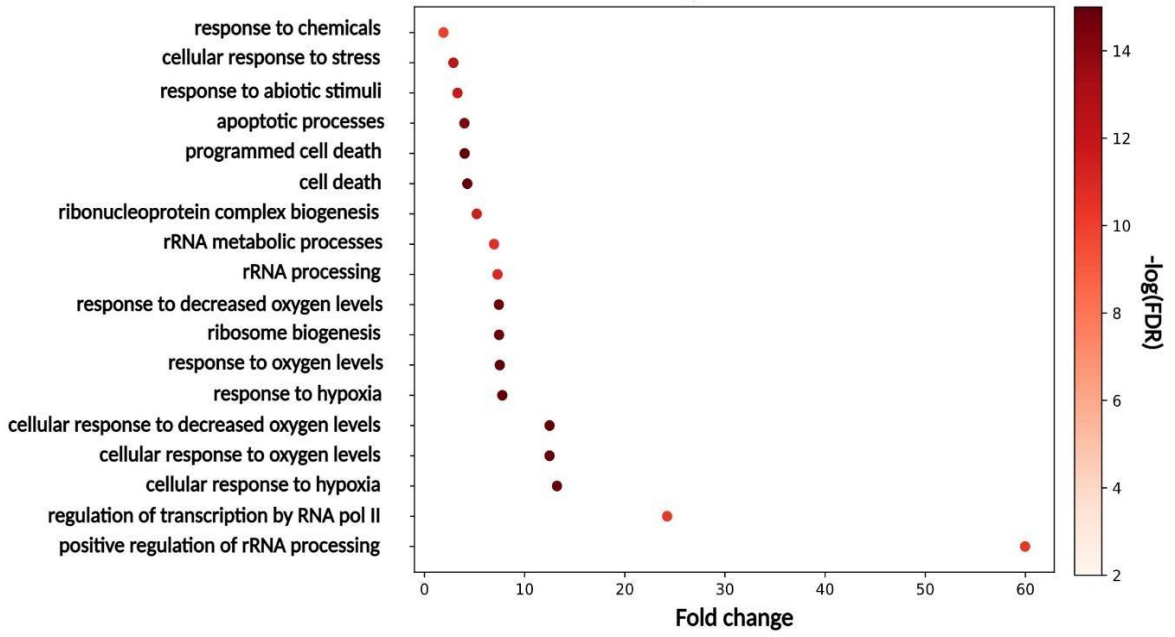

Figure 48. KEGG pathway analysis showing significantly affected cellular pathways after MCUa knockdown. Some of the most important pathways included: rRNA metabolism and ribosome biogenesis, responses to hypoxia, transcriptional regulation by RNA polymerase II, and apoptosis. Annotated terms and pathways were filtered by an FDR cut-off of 0.05.

To emphasise the role of the DEGs in T-cell signalling pathways which may be affected after MCUa downregulation and to better visalise and compare key differences between $MCUa_{KD}$ and control cells, proteomaps were generated. Upon $MCUa_{KD}$, signalling pathways including Notch signalling, apoptosis, and purine and pyrimidine metabolism were suppressed based on the downregulated DEGs. On the other hand, pathways including Wnt signalling, hypoxia signalling, PI3L-Akt signalling, glycolysis, and MAPK signalling were elevated based on the upregulated DEGs (**Figure 49**). This further confirmed possible compensatory pathways occurring upon acute MCUa downregulation. A proteomic screen would be beneficial to fully inspect changes in the proteome composition of $MCUa_{KD}$ T-cells.

All in all, these data indicated that MCUa downregulation and $_{m}Ca^{2+}$ uptake impairment significantly affect T-cell function and metabolism.

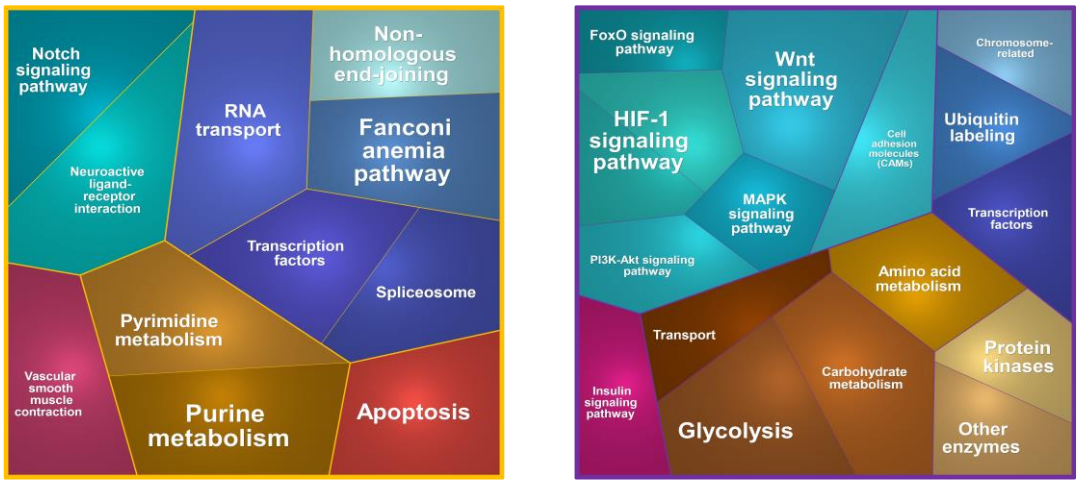

Figure 49. Proteomaps showing the quantitative composition of proteomes with a high probability to be suppressed (left panel-orange) and elevated (right panel-purple) upon MCUa knockdown. Proteomaps were generated based on the KEGG pathway analysis. Impaired $_{m}Ca^{2+}$ uptake plausibly affected several important signalling pathways, including Notch and Wnt signalling, glycolysis and amino acid metabolism, cell adhesion, and hypoxia-related pathways. Proteomaps were generated by Bionic Visualisations.

3.11 Upregulation of m-AAA protease AFG3L2 indirectly regulates MCU complex stability via EMRE proteolysis.

Mitochondrial metabolism and ribosomal biogenesis were two significantly affected T-cell pathways upon $MCUa_{KD}$ based on the current findings in this study indicated by the RNA sequencing analyses. To that end, a limited protein abundance screening was performed in $MCUa_{KD}$ and control $CD4^{+}$ T-cells. Accordingly, expression levels of several proteins, ribosomal subunits and proteases involved in mitochondrial and ribosomal metabolism were assessed. Out of the 11 screened proteins, only the mitochondrial-AAA protease, AFG3-like protein 2 (AFG3L2), was significantly upregulated upon $MCUa_{KD}$ (**Figure 50**, light-green frame).

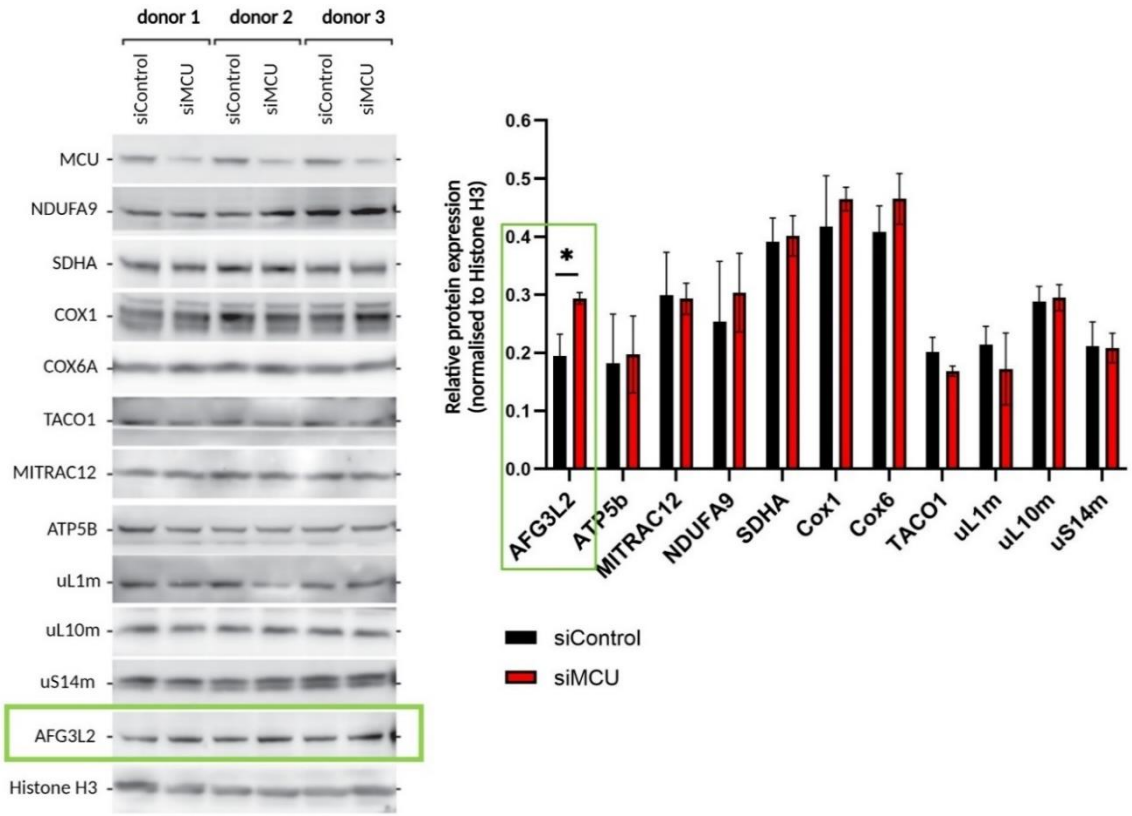

Figure 50. Upregulation of the mitochondrial-AAA protease, AFG3-like protein 2 (AFG3L2) upon MCUa downregulation. Protein screening performed in $CD4^+$ T-cells with downregulated MCUa and control $CD4^+$ T-cells from 3 different donors/biological replicates. Data are represented as mean ± SEM. *- $p \leq 0.05$, assessed by two-tailed paired Student's t-test. Protein expression data are normalised to Histone H3.

Notably, AFG3L2 upregulation was only observed on protein level, and not on mRNA level (**Figure 51**). Furthemore, RNA sequencing did not reveal *AFG3L2* as a DEG.

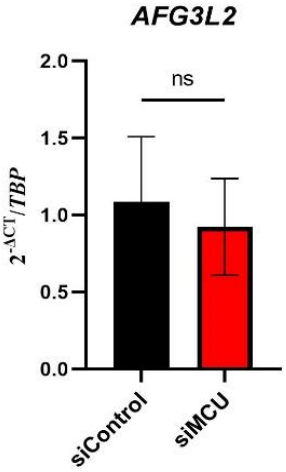

Figure 51. No difference in *AFG3L2* mRNA expression upon MCUa knockdown. The quantification represents an average of 3 different donors/biological replicates (using 2 technical replicates and a negative water control). Data are represented as mean ± SEM. ns-not statistically significant, assessed by two-tailed paired Student's t-test. Expression data are normalised to HK gene *TBP*.

It has been shown that AFG3L2 controls MCU assembly and $_{m}Ca^{2+}$ homeostasis by degrading non-assembled EMRE proteins and ensuring balanced MCU regulation. If EMRE degradation is impaired in the absence of the AFG3L2, excess EMRE can bind to MCU independently of Micu proteins, resulting in the accumulation of constitutively open MCU-EMRE complexes and $_{m}[Ca^{2+}]$ overload (Patron et al., 2018). Since MCUa has been downregulated in our model, the presence of excessive non-assembled EMRE is likely higher. Therefore, an upregulation of AFG3L2 as a compensatory mechanism was not unexpected. EMRE protein expression has not been evaluated in this study due to the current lack of a specific and working antibody.

To investigate the role of AFG3L2 in $CD4^{+}$ T-cells, $AFG3L2_{KD}$ was performed using siRNA editing. AFG3L2 downregulation of around 50% was observed on both mRNA (**Figure 52A**) and protein levels (**Figure 52B** and **C**). Mitochondrial Ca^{2+} measurements using MT3.1 Pericam demonstrated significantly higher resting $_{m}[Ca^{2+}]$ upon AFG3L2 downregulation (**Figure 52E**), indicating an increase of over-active MCU-EMRE complexes and prolonged MCU half-life.

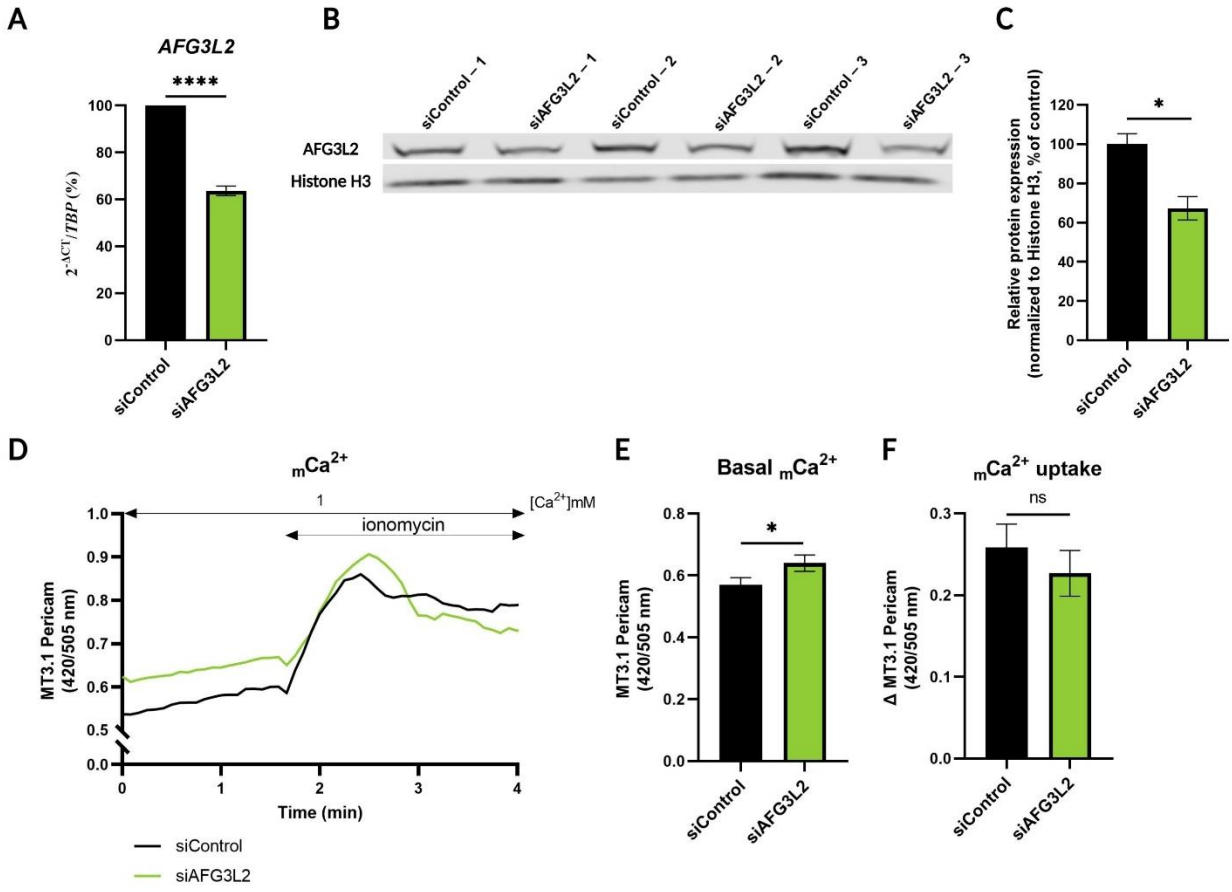

Figure 52. AFG3L2$_{KD}$ in CD4$^+$ T-cells which leads to an increase in resting $_m$[Ca^{2+}]. Successful knockdown was observed on both mRNA (**A**; quantification represents an average of 3 separate donors/biological replicates normalised to HK gene *TBP*) and protein levels (**B-C**; quantification represents an average of 3 separate donors/biological replicates given in the illustration normalised to Histone H3). Basal $_mCa^{2+}$ concentration was increased upon downregulation of AFG3L2 (**D-E**), with no changes in $_mCa^{2+}$ uptake upon ionomycin (4 µM) addition (**F**). Traces and quantifications represent an average of 36 siControl and 30 siAFG3L2 CD4$^+$ T-cells (biological replicates) from 2 separate donors. Data are represented as mean ± SEM. ****- p <0.0001, *-p ≤0.05, ns-not statistically significant; assessed by two-tailed unpaired and paired Student's t-test.

Mitochondrial respiration measurements and ATP production assessments interestingly showed no significant differences between AFG3L2$_{KD}$ and control CD4$^+$ T-cells (**Figure 53**).

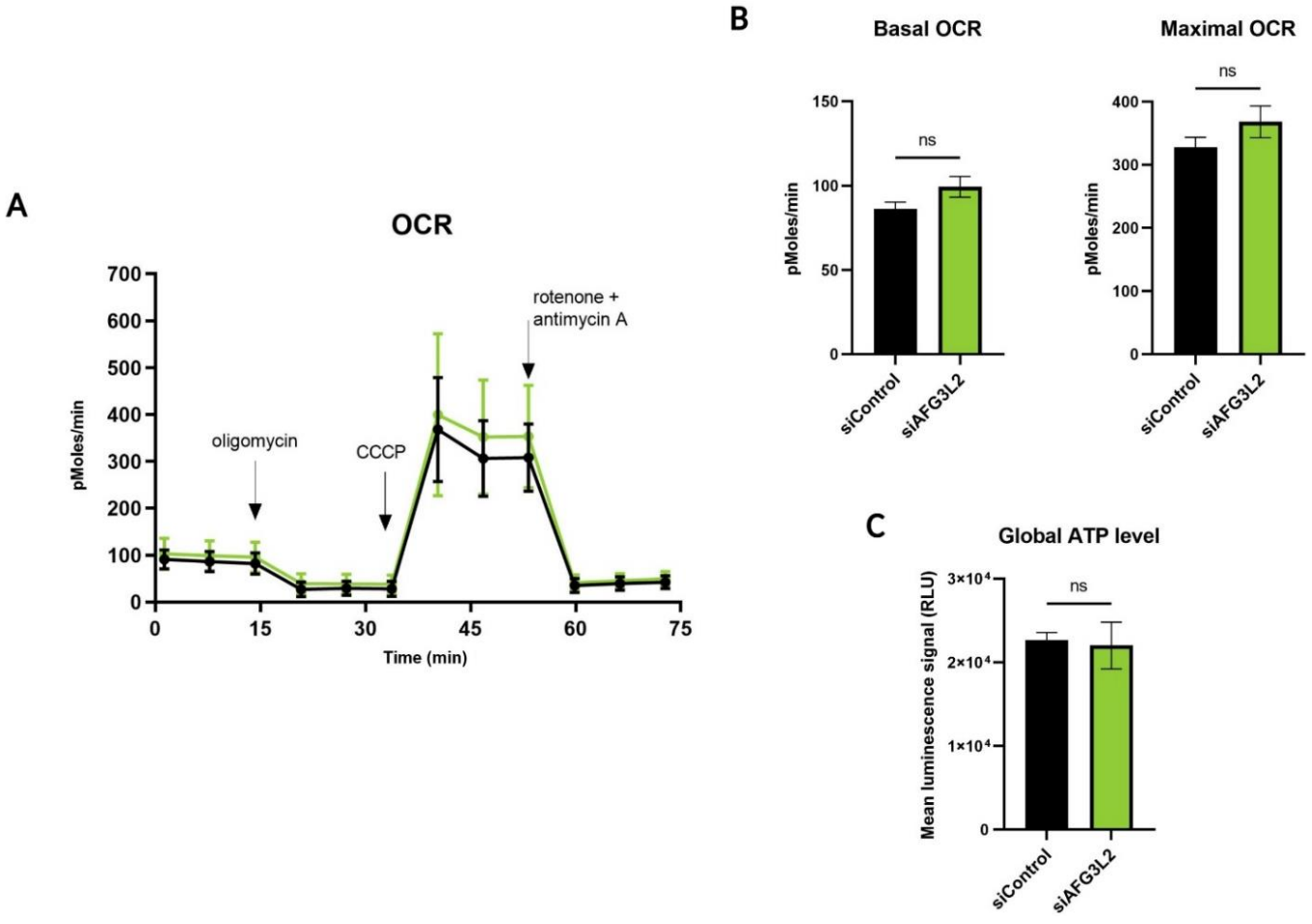

Figure 53. Partial AFG3L2 downregulation does not affect mitochondrial respiration and ATP production in CD4$^+$ T-cells. Mitochondrial respiration traces (**A**), basal and maximal OCR (**B**) represent an average of 3 different donors/biological replicates. Global ATP levels quantified using the luminescence assay Cell Titer Glo® represent an average of 3 separate donors/biological replicates. Data are represented as mean ± SEM. ns-not statistically significant, assessed by two-tailed unpaired Student's t-test.

These results were in line with the findings that the m-AAA protease AFG3L2 indirectly regulates MCU function via degradation of EMRE. Downregulation of AFG3L2 possibly led to over-accumulation of MCU-EMRE complexes and subsequent increase in resting $_{m}[Ca^{2+}]$. There was no effect observed with respect to the mitochondrial metabolism in $CD4^{+}$ T-cells, likely because of the presence of residual active AFG3L2 enzyme due to incomplete siRNA downregulation.

To further examine the relationship between MCU and AFG3L2 with an easier-to-handle *in vitro* approach, experiments were performed using the immortalized human HeLa cell line, by Bachelor's student Kira Pahl (unpublished Bachelor's Thesis, 2022). Mitochondrial Ca^{2+} uptake was evaluated following physiological stimulation with histamine, known to induce robust ER Ca^{2+} store depletion and thus $_{m}Ca^{2+}$ entry (Montero et al., 2003). AFG3L2 downregulation led to a significantly increased $_{m}Ca^{2+}$ uptake in HeLa cells compared to control (**Figure 54**), in accordance with the results obtained using $CD4^{+}$ T-cells.

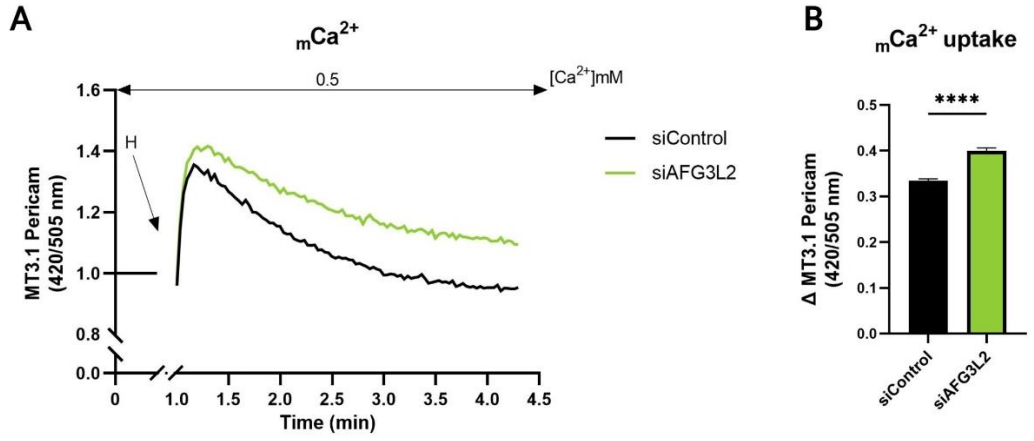

Figure 54. Changes in $_{m}Ca^{2+}$ uptake in HeLa cells upon downregulation of m-AAA protease AFG3L2. AFG3L2 downregulation led to an increase in $_{m}Ca^{2+}$ uptake. Measurement traces (**A**) and quantification (**B**) represent an average of 309 siControl and 183 siAFG3L2 single HeLa cells (biological replicates) from 3 separate experiments. Data is normalised to basal $_{m}Ca^{2+}$ levels measured prior to histamine addition. Data are represented as mean ± SEM. ****- $p<0.0001$; assessed by two-tailed unpaired Student's t-test. H=histamine (100 µM).

Knockdown efficiency of AFG3L2 in HeLa cells was observed on both mRNA (80%) and protein (50%) levels (**Figure 55A-C**).

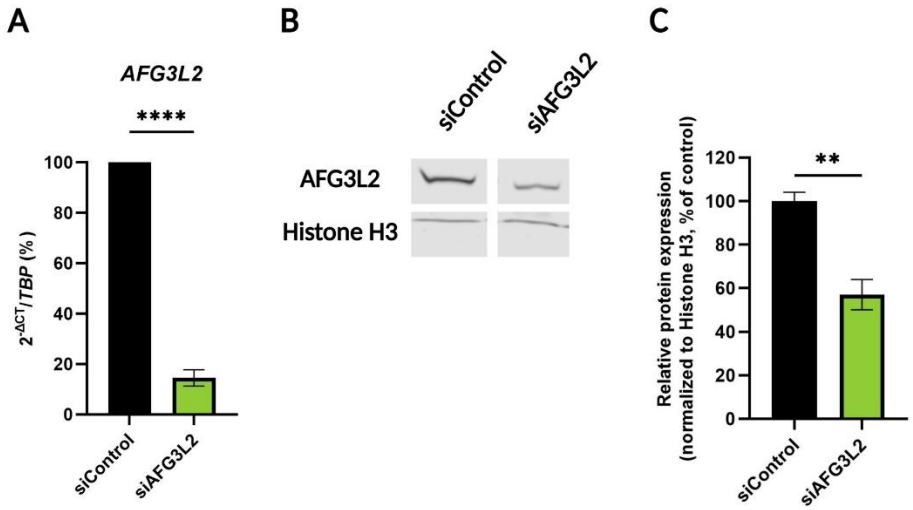

Figure 55. AFG3L2 knockdown on both mRNA (A) and protein (B) levels. mRNA quantification plot (**A**) is representative of 4 separate experiments/biological replicates (2 technical replicates and a negative water control). Protein quantification (**C**) is representative of 8 separate experiments/biological replicates. Data are represented as mean ± SEM. ****-*p* <0.0001, ***-*p* <0.001; assessed by two-tailed unpaired Student's t-test.

With respect to mitochondrial metabolism, mitochondrial respiration assessments showed no differences in AFG3L2$_{KD}$ HeLa cells compared to control (**Figure 56**).

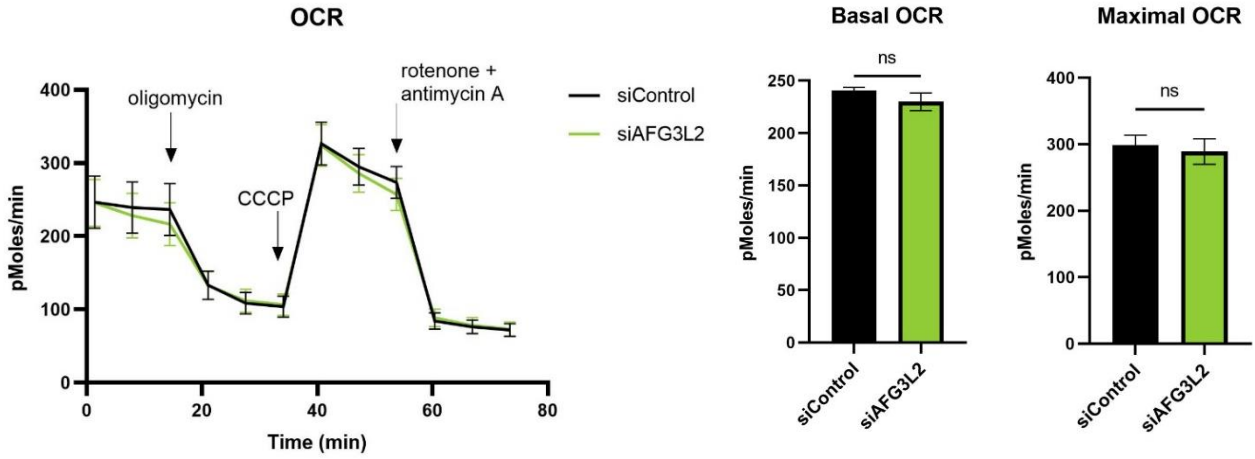

Figure 56. Assessment of mitochondrial respiration (oxygen consumption rates) upon downregulation of the protease AFG3L2 in HeLa cells. No significant differences in respiration were observed upon AFG3L2$_{KD}$. Maximal OCR was also not affected. Analysis shows an average of 3 experiments/biological replicates. Data are represented as mean ± SEM. ns-not statistically significant; assessed by two-tailed unpaired Student's t-test.

Mitochondrial ATP measured using the novel mitochondria-targeted ATP dye showed slightly higher, but not statistically significant, ATP levels in HeLa cells with downregulated AFG3L2 (**Figure 57A-B**). Nevertheless, the ΔΨm was significantly higher, as expected, considering the increase in $_m[Ca^{2+}]$ uptake (**Figure 57C-D**).

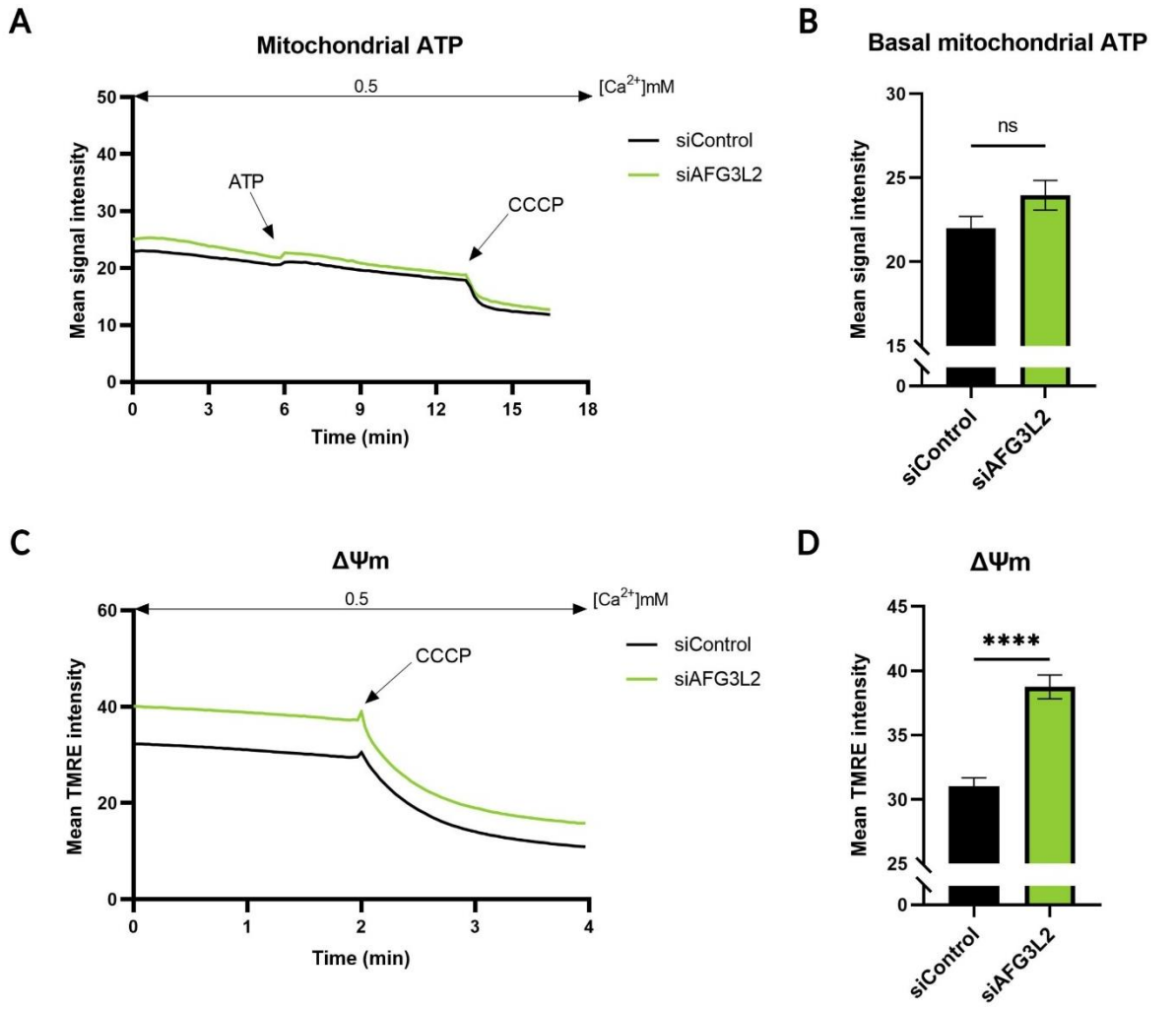

Figure 57. Downregulation of AFG3L2 in HeLa cells leads to a minor increase in mitochondrial ATP levels and a significant increase in ΔΨm. Mitochondrial ATP levels (**A-B**) were measured using the novel mito-ATP red dye. Resting mitochondrial ATP was slightly higher in cells with downregulated AFG3L2, although not statistically significant. Addition of external ATP (5 mM) to the cells increased the signal intensity, whereas depolarisation due to CCCP (4 μM) (positive control) reduced it. ΔΨm was significantly increased upon AFG3L2 downregulation, which was in accordance with the increased resting $_m[Ca^{2+}]$ (**C-D**). Traces and quantification in panel **B** represent an average of 216 siControl and 83 siAFG3L2 single HeLa cells (biological replicates). Traces and quantification in panel **D** represent an average of 437 siControl and 316 siAFG3L2 single HeLa cells (biological replicates). Data are represented as mean ± SEM. ****-*p* <0.0001, ns-not statistically significant; assessed by two-tailed unpaired Student's t-test.

Combining the results generated from both $CD4^+$ T-cells and HeLa cells, it can be concluded that AFG3L2 is an important protein quality control enzyme, mediating the function of the MCU complex by regulating its stability. Partial $AFG3L2_{KD}$ significantly increases the $_mCa^{2+}$ content and the ΔΨm; however, residual enzyme activity is sufficient to prevent further mitochondrial metabolic changes.

3.12 $MCUa_{KD}$ model in primary rat $CD4^+$ T-cells confirms the *in vitro* data generated in human $CD4^+$ T-cells.

To confirm the effect of inhibited $_mCa^{2+}$ uptake in a different T- cell model, primary rat $CD4^+$ T-cells with a stable $MCUa_{KD}$ were generated using the CRISPR Cas9 gene editing, as described in the Methods section (2.2.25). Primary rat $CD4^+$ T-cells reactive against MBP were retrovirally engineered to express a mitochondria-targeted Scarlet-GCaMP6s fusion protein. Three of the created cell lines featured a knockdown of MCUa. An additional cell line was used as a CRISPR control. MCUa knockdown was confirmed on protein level (**Figure 58A**) in all three cell lines, with lowest expression in cell lines MCUps4 (**Figure 58B**) and MCUps5.

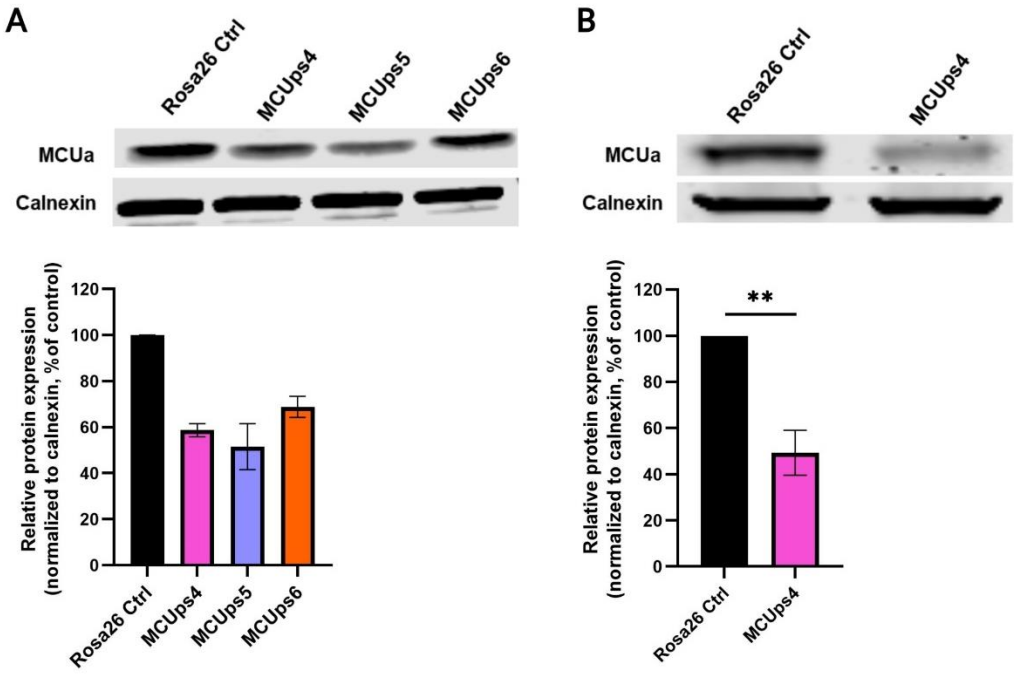

Figure 58. MCUa knockdown confirmed in all three generated rat $CD4^+$ T-cell lines, compared to CRISPR control cell line. An average of 60% $MCUa_{KD}$ was observed in all 3 cell lines (**A**). The quantification is representative of 2 different experiments/biological replicates. (**B**) An average of 50% $MCUa_{KD}$ was observed in the MCUps4 cell line. The quantification represents 3 different experiments/biological replicates. Protein

expression data are normalised to the loading control calnexin. Data are represented as mean ± SD in panel (**A**) and mean ± SEM in panel (**B**). **-*p*<0.01; assessed by two-tailed unpaired Student's t-test.

In vitro $_{m}[Ca^{2+}]$ measurements showed a decreased resting $_{m}Ca^{2+}$, as well as $_{m}Ca^{2+}$ uptake upon TCR stimulation with anti-rat CD3+CD28 antibodies (**Figure 59**).

Based on the MCU knockdown efficiency of 50% on protein level (**Figure 58B**) and the significant effect on impairment of $_{m}Ca^{2+}$ uptake after TCR stimulation (**Figure 59**), the primary cell line chosen for further experiments was MCUps4.

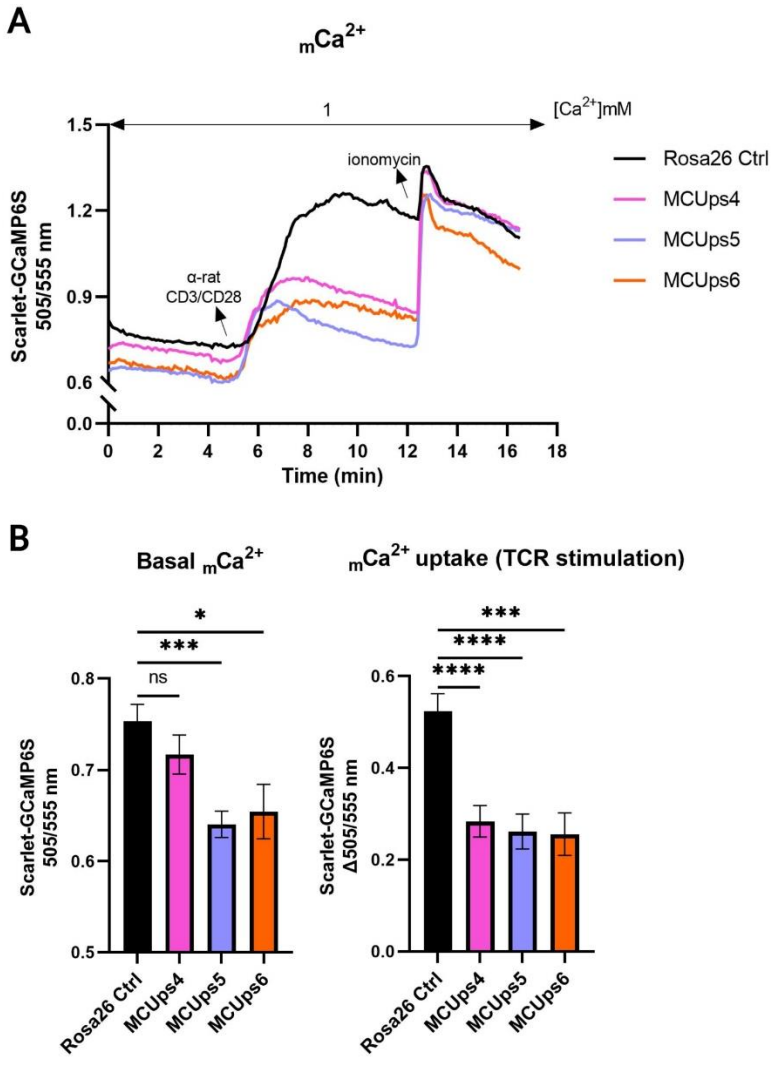

Figure 59. Significant impairment of resting $_{m}[Ca^{2+}]$ and $_{m}Ca^{2+}$ uptake upon TCR stimulation in stable MCUa$_{KD}$ primary rat CD4^{+} T-cell lines. Traces and quantifications represent an average of 72 Rosa26 control, 82 MCUps4, 51 MCUps5, and 32 MCUps6 single cells (biological replicates). Data are represented as mean ± SEM. ****- *p* <0.0001, ***-*p* <0.001, *-*p* ≤0.05, ns-not statistically significant; assessed by ordinary one-way ANOVA. Stimulation was achieved with 1:1000 antibody (anti-rat CD3+CD28) working dilution and 4 µM of ionomycin as a positive control.

To confirm proper editing of the MCUa sequence without off-target effects, a T7E1 assay was performed (**Figure 60**). Editing in the genome of the three established cell lines, introduced by the Cas9 enzyme (marked by stars), was detected accordingly. Efficient targeting

of the designed guide RNA used for generation of the MCUps4 cell line was further validated in HEK293 cells co-transfected with a pTurq-MCUsgRNA expression construct and an MCU-Cherry reporter construct. Reduction in mCherry fluorescence was evident (**S Figure 6B** and **C**). Proper biosensor localization in the mitochondrial inner membrane was confirmed after fluorescence microscopy imaging (**S Figure 7A**).

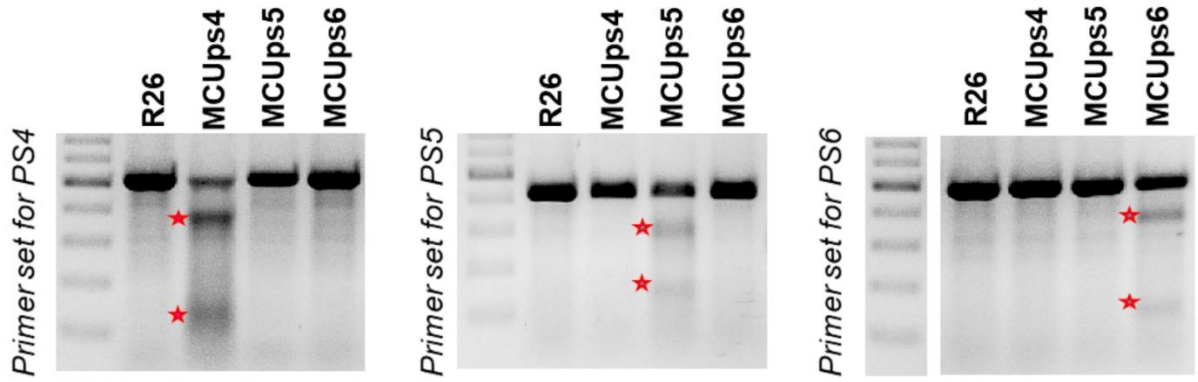

Figure 60. T7E1 assay performed to confirm and characterise the intended edit of the *MCUa* sequence in the generated lines. Indels introduced by Cas9 activity in the genome of established T-cell lines are detected. Genomic DNA isolated from the four T-cell lines 5 days after initial restimulation was analysed by PCR and T7 endonuclease digestion. T7 cleavage fragments, marked by a star, revealed sequence alterations introduced by Cas9 at a genomic level.

Mitochondrial respiration and ATP assessments in the rat MCUps4$_{KD}$ CD4^{+} T-cells validated the data obtained from human MCUa$_{KD}$ CD4^{+} T-cells (**Figure 61**). Accordingly, both basal and maximal OCR were decreased (**Figure 61B** and **C**). It is nevertheless important to mention here that this experiment was only performed twice and should be performed again to strengthen these findings. Furthermore, global ATP levels were significantly decreased in the MCUps4$_{KD}$ cells compared to control (**Figure 61D**).

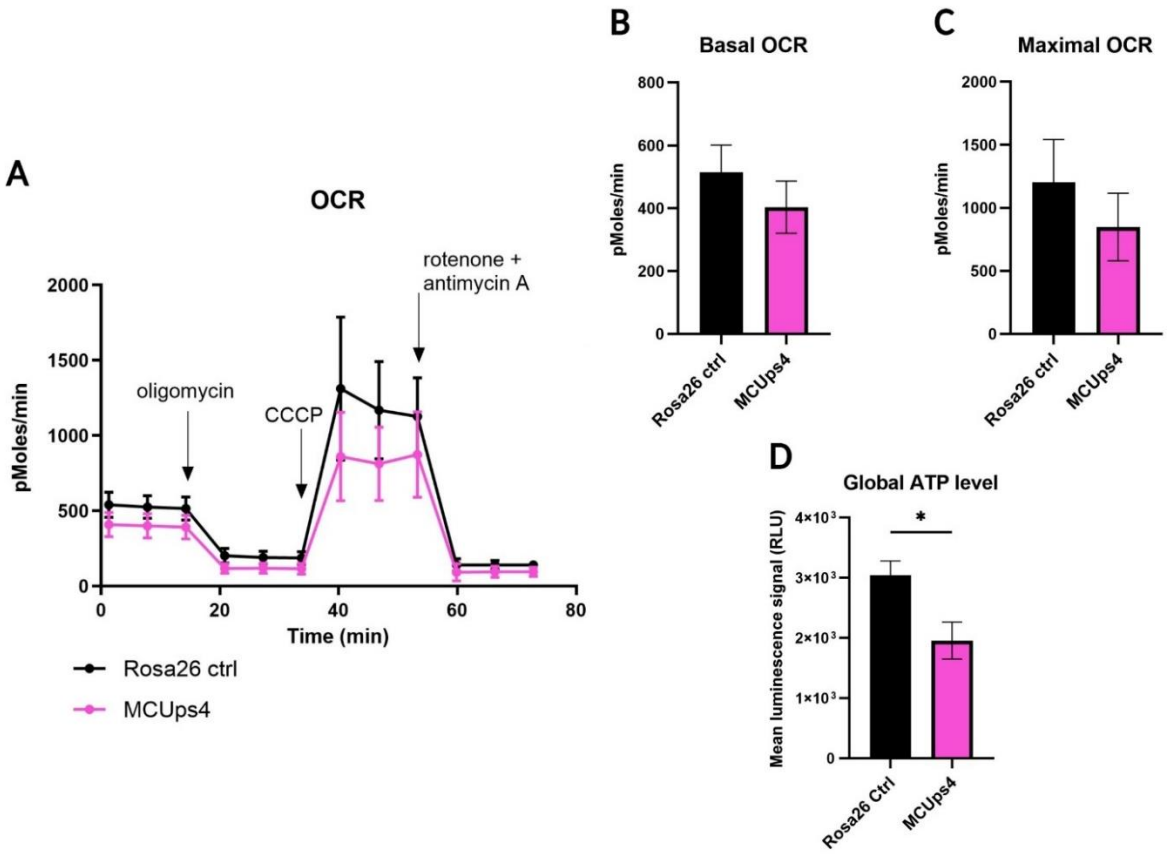

Figure 61. Decreased mitochondrial respiration and ATP levels in rat CD4$^+$ T-cells with MCUa$_{KD}$. Mitochondrial respiration measurements are representative of 2 separate experiments/biological replicates (using at least 10 technical replicates). Data are represented as mean ± SD. ATP luminescence assay and quantification shows the mean of 4 separate experiments/biological replicates (using at least 6 technical replicates). Data are represented as mean ± SEM. *-$p \leq 0.05$; assessed by two-tailed unpaired Student's t-test.

In contrast to the results obtained with the human CD4$^+$ T-cells, mRNA kinetic screening of control and MCUps4$_{KD}$ rat T-cells did not indicate significant differences in gene expression of cytokines IFNγ and IL-2 (**Figure 62A** and **B**) after stimulation with anti-rat CD3+ CD28 antibodies. However, this does not fully confirm that the cytokine secretion levels, and therefore the proinflammatory function of these cells, were not affected by MCUa$_{KD}$. Further assessments, including secretion of other cytokines (IL-17, IL-22, TNFα, IL-1, or IL-12) and *in vitro* invasion assays should be performed in addition.

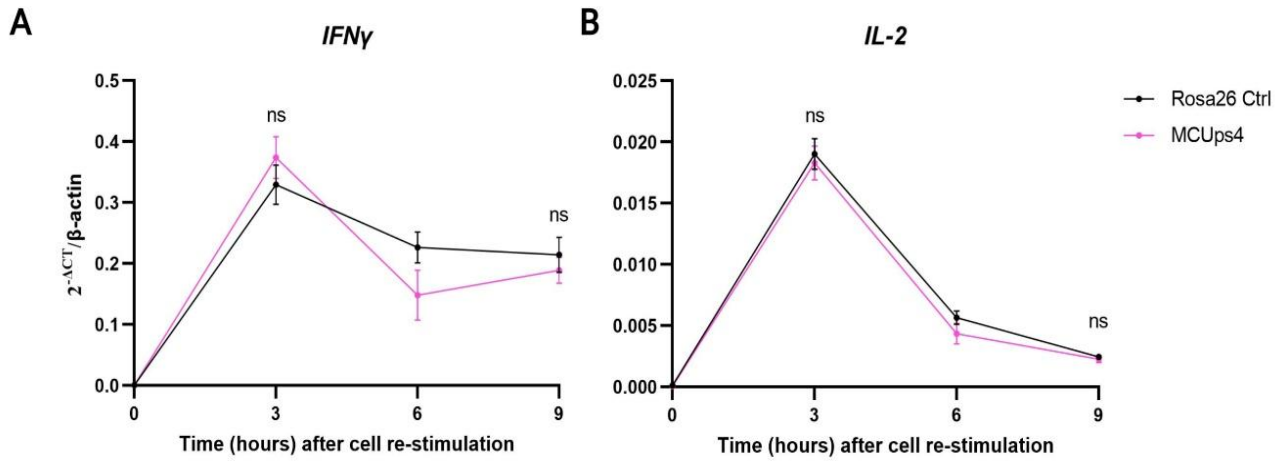

Figure 62. Gene expression of proinflammatory cytokines upon $_{m}Ca^{2+}$ inhibition in rat CD4^{+} T-cells. No significant differences were observed for (**A**) *IFNγ* and (**B**) *IL-2* expression. The traces and quantifications represent an average of 3 different experiments/biological replicates (using 2 technical replicates and a negative water control). Gene expression is normalised to the HK gene *β-actin*. Data are represented as mean ± SEM. ns-not statistically significant; assessed by two-tailed unpaired Student's t-test.

3.13 Delayed EAE onset in animals injected with MCUa$_{KD}$ CD4^{+} T-cells.

In order to better understand the role of MCU in T-cell function *in vivo*, a rat experimental model of multiple sclerosis (experimental autoimmune encephalomyelitis; EAE) was utilised (with the help of our collaboration partners at the Institute of Neuroimmunology and Multiple Sclerosis Research, UMG Göttingen). Adoptive T-cell transfer was performed in rats using three different cell amounts (ranging from 0.75 to 1.2 million cells), from both the Rosa26 control cell line and the MCUps4$_{KD}$ cell line. The animals were weighed and scored daily for clinical signs of disease. No significant weight changes were observed among the single animals (**S Figure 5**).

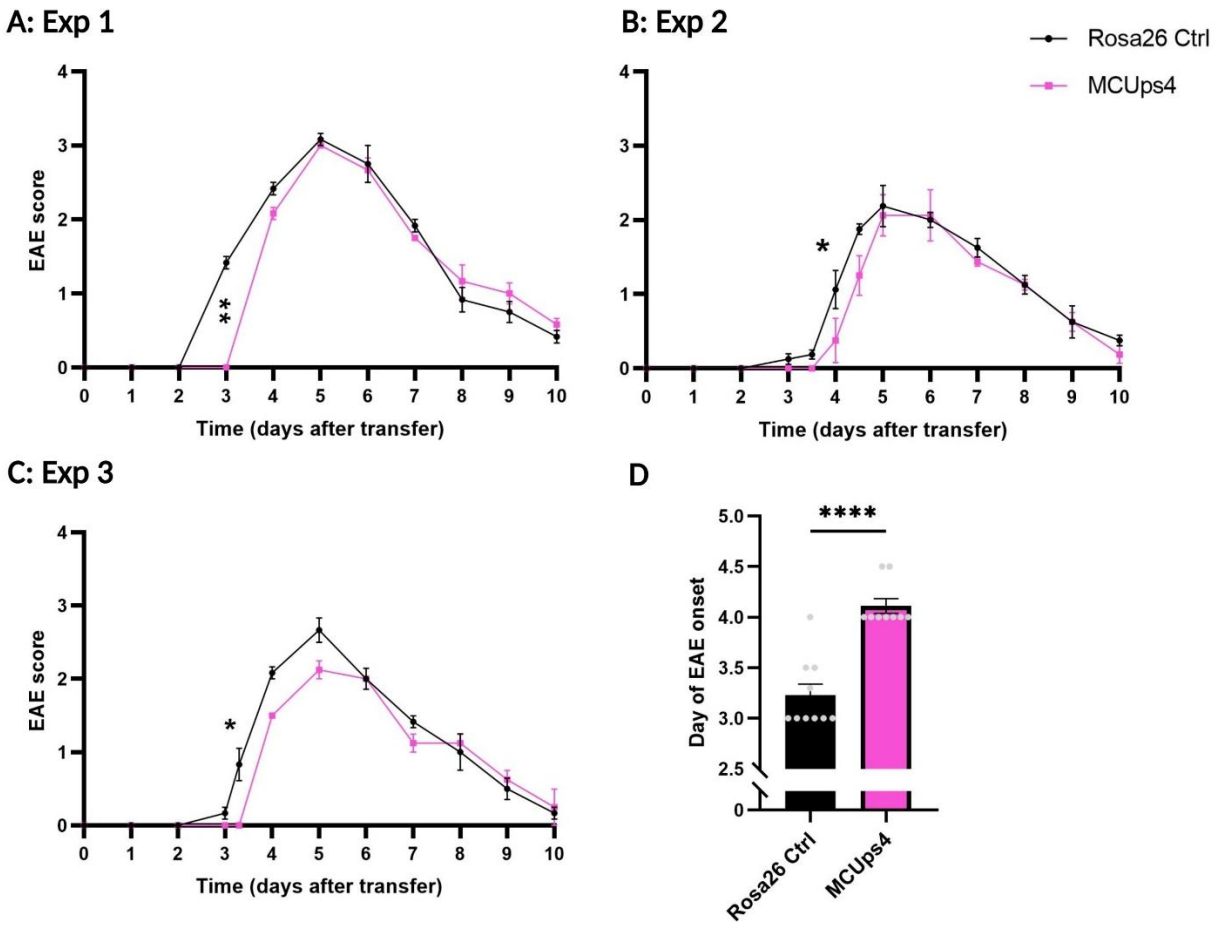

Figure 63. Significant delay in day of onset of experimental autoimmune encephalomyelitis (EAE) in rats injected with MCUa$_{KD}$ CD4^{+} T-cells. Panel (**A**) represents a single experiment where 1.2x10^{6} Rosa26 ctrl or MCUps4 KD cells were injected in rats to induce EAE. The traces are representative of 3 animals/biological replicates per condition. Panel (**B**) represents a single experiment where 1x10^{6} Rosa26 ctrl or MCUps4 KD cells were injected in rats to induce EAE. The traces are representative of 4 animals/biological replicates per condition. Panel (**C**) represents a single experiment where 0.75x10^{6} Rosa26 ctrl or MCUps4 KD cells were injected in rats to induce EAE. The traces are representative of 3 control animals/biological replicates and 2 MCUps4-injected animals/biological replicates. Panel (**D**) represents the plotted day of EAE onset for all 10 animals (**grey** points) investigated in the 3 experiments. Data are represented as mean ± SEM. ****-*p* <0.0001; assessed by two-tailed Welch's t-test.

It was evident that upon injection of MCUa$_{KD}$ CD4^{+} T-cells, the onset of EAE was delayed on average by one day (onset of disease on day 4 compared to day 3 when the control cell line was used) (**Figure 63A-D**). This difference was highly significant in all three individual experiments performed. These results suggested that the lower metabolic activity of the MCUa$_{KD}$ T-cells might be responsible for the lower proinflammatory action and invasion, depicted as a delayed onset of autoimmune disease *in vivo*.

To further validate this outcome using two different $MCUa_{KD}$ cell lines, the MCUps5 line was newly generated and utilised for evaluating EAE onset *in vivo*. The downregulation of MCU protein in the MCUps5 cell line was strikingly higher compared to previously (refer back to **Figure 58A**) (80% reduction of protein expression; **Figure 64**). However, protein expression was investigated only once due to limited sample availability, therefore conclusions should be interpreted with caution.

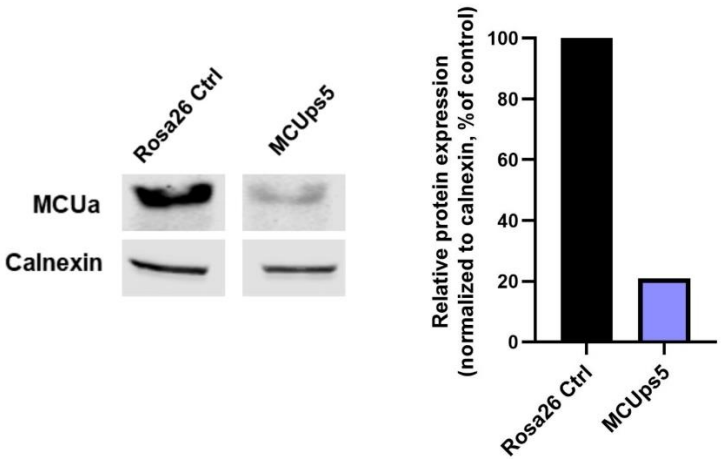

Figure 64. MCUa knockdown further confirmed in the $MCUps5_{KD}$ cell line.
An average of 80% knockdown was observed. The image and quantification are representative of a single experiment.

Onset of EAE upon injection of both MCUps4 and MCUps5 $CD4^+$ T-cells was delayed on average by one day (**Figure 65A** and **B**), similar to previous findings. Due to some variability among animals, the effects were statistically insignificant; however, this experiment was performed only once and needs further exploration. Strikingly, injection of MCUps5 cells not only caused delay of EAE onset but also led to a substantial reduction of chronic disease severity in the animals (**Figure 65C**), compared to control. No significant weight changes were observed among the single animals (**S Figure 5D**).

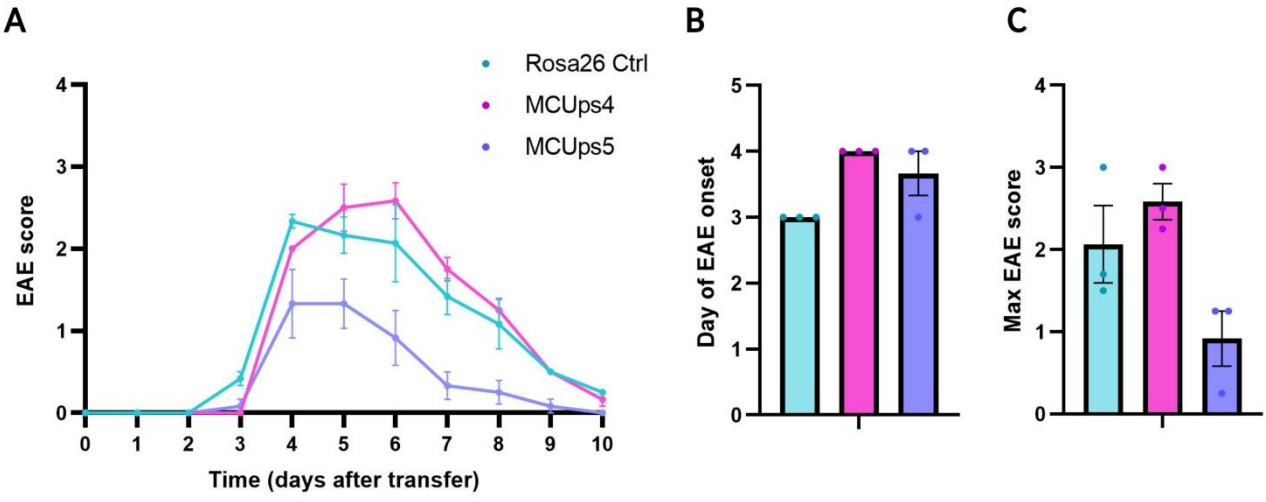

Figure 65. Reduction of chronic disease severity in animals injected with MCUps5$_{KD}$ CD4^{+} T-cells. Panel (**A**) represents a single experiment where Rosa26 control or MCUps4/5$_{KD}$ cells were injected in rats to induce EAE. The traces are representative of 3 animals/biological replicates per condition. Panel (**B**) represents the plotted day of EAE onset for all animals (showing single animals as points). Panel (**C**) shows the plotted maximal EAE score recorded throughout the experiment for each animal (showing single animals as points). Data are represented as mean ± SEM.

Considering the noteworthy effects observed upon MCUps5$_{KD}$ CD4^{+} T-cell injection, this cell line warrants additional exploration with respect to mitochondrial metabolism, as well as T-cell function, to further determine the role of MCU in autoimmunity.

4. Discussion

The dynamic nature of mitochondria and, in particular, their spatial distribution within cells, have an utmost importance in regulating a vast number of cellular functions. This has become clearly evident in the last six decades, when an unbalanced mitochondrial dynamic was related to a vast number of diseases which reach beyond just mitochondria-related pathologies (Yapa et al., 2021). Such diseases include, and are not limited to, cardiovascular pathologies (heart failure, stroke and diabetes), neurodegenerative pathologies (multiple sclerosis, Alzheimer's and Parkinson's), many types of cancer, inflammation, chronic kidney diseases, and chronic lung diseases. Clear causes of pathological cell dysfunction involve reduced ATP synthesis, increased apoptosis, and changes in mitochondrial quality control (Nunnari & Suomalainen, 2012). Nevertheless, further understanding of other molecular mechanisms which underlie the dysregulation of mitochondrial dynamics in specific tissues, cell types, and diseased states are necessary to clear a path for novel and better therapeutic approaches.

T-cell activation and differentiation are complex processes which require numerous environmental and intrinsic cellular signals, as well as highly engaged transcriptional machinery and epigenetic reprogramming. Different combinations of triggers can result in a different T-cell fate, which may be both physiological or pathological (Scharping et al., 2021). Therefore, it is of utmost importance to fully understand mitochondrial T-cell metabolism.

Store-operated calcium entry is essential for T-cell function. A sustained cytosolic Ca^{2+} increase, induced by the formation of an immune synapse, is required for activation of NFAT-mediated pathways, cytokine production, clonal expansion, differentiation, and function. The increased of Ca^{2+} microdomains in the surrounding of mitochondria cause mitochondrial Ca^{2+} uptake in T-cells, mainly mediated by the MCU complex in the IMM. Mitochondrial Ca^{2+} modulates mitochondrial metabolism and apoptotic pathways in T-cells (Feske, 2007; Trebak & Kinet, 2019; Wang et al., 2020). Accordingly, recognising the role of mitochondrial Ca^{2+} uptake by MCU in T-cell metabolism and function is of vital importance.

This project aimed to provide novel insights into the role of MCU-mediated mitochondrial Ca^{2+} uptake in human $CD4^+$ T-cell metabolism. This findings within this study contribute to unravelling the mechanism of MCU regulation in T-cell mitochondria *in vitro*. Moreover, using a rat EAE model of multiple sclerosis, the role of MCU in $CD4^+$ T-cell function was investigated *in vivo*. The outcomes point to a clear effect of impaired

mitochondrial Ca^{2+} uptake via MCU on $CD4^+$ T-cell mitochondrial metabolism and function, suggesting that targeting MCU in T-cells may be beneficial for autoimmune suppression and control of immune system dysregulation.

4.1 Naive and activated $CD4^+$ T-cells have distinct mitochondrial metabolic properties and MCU complex arrangement

Resting naive T-cells mainly use oxidative phosphorylation to provide for their low metabolic demand, whereas activated T-cells undergo rapid metabolic reprogramming that requires increased glycolysis, in addition to the upregulated oxidative phosphorylation. Furthermore, each $CD4^+$ T-cell subset utilises a distinct metabolic program (Beckermann et al., 2017). Therefore, it is important to precisely decipher the metabolic shift which occurs upon T-cell activation.

Findings obtained from the generated effector $CD4^+$ T-cells were in agreement with results from other studies regarding T-cell metabolism so far (Beier et al., 2015; Cham & Gajewski, 2005; Peng et al., 2016). We were able to show that activated T-cells immensely increase their mitochondrial metabolic capacity, evident by an increase in respiration, glycolytic rates, ATP production, and mitochondrial membrane potential (**Figures 22** and **23**). This metabolic rise is crucial for their rapid clonal expansion and immune function in the context of inflammation. Furthermore, the increase in mitochondrial protein translation is in line with the higher respiration. Pathway analyses of DEGs among naive and effector T-cells indicate several bioenergetic and mitochondria-related processes which are significantly upregulated upon cell activation (**Figure 29**). Since an increase in mitochondrial Ca^{2+} uptake correlates with a higher respiratory chain activity and ATP generation, it became evident that MCU controls the metabolic reprogramming which occurs in activated T-cells.

Interestingly, the rapid changes in gene and protein expression occur almost simultaneously with the increase in mitochondrial membrane potential (90-150 min after TCR stimulation). It has been shown that mitochondrial hyperpolarisation is associated with proper T-cell activation and function, by regulating ATP synthesis, ROS production, and release of apoptotic factors (Nagy et al., 2003). Since Ca^{2+} contributes to mitochondrial hyperpolarisation, as well as ROS production, uptake of Ca^{2+} through MCU undoubtably regulates T-cell activation. This is depicted by the decrease in mitochondrial membrane potential upon pharmacological MCU and Orai/SOCE inhibition (**Figure 25**). Increased mitochondrial ROS levels in activated T-cells also correlate with the higher respiration and

IMM hyperpolarisation.

Based on these observations, it was not surprising to observe higher resting mitochondrial Ca^{2+} and mitochondrial Ca^{2+} uptake upon T-cell activation. Since MCU complex components are differentially expressed in various cell types depending on their function (Fieni et al., 2012), it is important to investigate the MCU composition in $CD4^+$ T-cells. Our observations show a rearrangement of the MCU complex shortly upon $CD4^+$ T-cell activation which accommodates for the higher mitochondrial Ca^{2+} uptake and higher metabolic demands (**Figures 20** and **21**). These observations are in agreement with data obtained from models showing that MCU has a crucial role in conditions which require a high energetic demand (Kwong et al., 2015; Liu et al., 2016; Mammucari et al., 2015). An RNA sequencing immune cell dataset generated by Monaco et al. (2019) provided supporting evidence for our findings. mRNA expression levels of *MCUa* and *MCUb* extracted from their dataset were compared between naive and activated immune cells, specifically $CD4^+$ T-cells, and $CD8^+$ T-cells. These two cell types undergo a metabolic switch upon activation and require high inputs of energy to exert their function. An increase in *MCUa* and a decrease in *MCUb* expression was evident upon T-cell activation (**S Figure 8**).

Summing up, the metabolic reprogramming of T-cells upon activation, required for proper cell function, is dependent on controlled mitochondrial Ca^{2+} influx through the MCU complex.

4.2 Impaired mitochondrial calcium uptake via MCU suppresses mitochondrial metabolism in activated human and rat $CD4^+$ T-cells

Recent studies investigating the MCU function in T-cells have shown contradictory results. Indirectly targeting MCU function, for example via disruption of the mitochondrial membrane potential with FCCP, causes diminished IL-2 production and mitochondrial ROS (Sena et al., 2013). Furthermore, downregulating Ca^{2+} signalling proteins (Orai1 and STIM1) leads to compensatory downregulation of MCU, resistance to oxidative stress, and lower NADPH levels (Shanmughapriya et al., 2015). On the other hand, directly targeting MCU using animal models and MCU KO Jurkat T-cells suggests that MCU might be dispensable for T-cell function, which, given the importance of mitochondrial Ca^{2+}, was rather surprising. Notwithstanding, compensatory effects controlled by other proteins cannot be excluded in these studies and require further investigation.

In this current study, we decided to establish an MCUa knockdown model in primary human $CD4^+$ T-cells and examine the effects of diminished mitochondrial Ca^{2+} uptake on T-cell metabolism and function. Working with primary cells poses a technical challenge, especially when using naive, non-proliferating cells with low metabolic capabilities. Despite the difficulties, we were able to achieve a transient knockdown of around 50% on protein level which was sufficient to significantly decrease mitochondrial Ca^{2+} uptake (**Figure 31**). Importantly, no effects on other MCU complex components and other Ca^{2+} signalling-related components were observed upon $MCUa_{KD}$ (**Figure 32**).

Recently, a novel mitochondrial Ca^{2+} channel known as transmembrane Bax inhibitor-1 motif 5 (TMBIM5) was identified as a Ca^{2+}/H^+ exchanger located in the IMM, exporting Ca^{2+} out of the matrix (Patron et al., 2022). TMBIM5 ensures cell survival and respiration, allowing Ca^{2+} efflux and limiting Ca^{2+} overload. This channel is ubiquitously expressed in different tissues, with a quite low expression in the spleen (Lisak et al., 2015). Nevertheless, its expression and possible role in mitochondrial Ca^{2+} signalling in T-cells cannot be neglected. It is also important to mention that a study by Zhang et al. (2022) showed conflicting evidence that TMBIM5 can also uptake Ca^{2+} into the IMM in skeletal muscle mitochondria. Therefore, TMBIM5 is an essential part of the mitochondrial ion transport system and its contribution to mitochondrial Ca^{2+} homeostasis in T-cells requires further investigation. TMBIM5 was not detected as a DEG in our RNA sequencing analyses; however, this does not exclude that its protein expression levels have not been affected by $MCUa_{KD}$.

Despite the possible up- or downregulation of compensatory Ca^{2+} channels/transporters, we were able to detect significant alterations in mitochondrial metabolism and bioenergetics upon acute $MCUa_{KD}$ in human $CD4^+$ T-cells. Specifically, we postulate that impairment of mitochondrial Ca^{2+} uptake directly affects mechanisms involved in the regulation of the mitochondrial membrane potential, which in turn reduces mitochondrial respiration and ATP generation. In accordance with this hypothesis is the decrease in all mentioned parameters in the $MCUa_{KD}$ $CD4^+$ T-cells. Additionally, the data obtained on respiration and ATP levels from the $MCUa_{KD}$ rat effector $CD4^+$ T-cells were comparable to those obtained from the human $CD4^+$ T-cells (**Figure 61**).

Referring back to **Figures 35A** and **50**, neither changes in mitochondrial protein translation nor in the protein expression of multiple oxidative phosphorylation-related components and ribosomal subunits were detected upon transient $MCUa_{KD}$. It is likely that the activity of oxidative phosphorylation complexes is reduced, rather than their protein content. It has been shown that posttranslational modifications of these complexes acutely regulate their

activity to meet the increase in ATP demands. Such modifications include phosphorylation (commonly regulated by Ca^{2+}), acetylation, nitrosylation, and oxidation. In cells with low metabolic demands, oxidative phosphorylation complexes are operating at lower rates, whereas in cells with large dynamic ranges in energy, the complex activity is acutely modulated via posttranslational modifications (Phillips et al., 2012). Therefore, measuring complex activity in T-cells using colorimetric assays would be the next approach towards understanding the effects of Ca^{2+} on oxidative phosphorylation.

Additionally, no changes in H_2O_2 levels (both cytosolic and mitochondrial) and glutathione redox potential were observed upon $MCUa_{KD}$ (**Figure 40**). Accordingly, no differences in antioxidant capacity were detected (**Figure 41**). Based on these observations, it is possible that the remaining active MCU complex is sufficient to prevent a significant decrease in ROS production in the $MCUa_{KD}$ T-cells. In addition, the relatively low sensitivity of the utilised HyPer and Grx1-roGFP2 probes might also limit quantification of minor differences in mitochondrial ROS. Several of the DEGs identified by our RNA sequencing analysis are related to cellular responses to oxygen levels and hypoxia (such as transcription factors MXI1 and SNAPC4), hinting towards possible compensatory pathways that prevent alterations in ROS. Thus, a thorough proteomic screen could pinpoint specific proteins, complexes and/or posttranslational modifications which are altered upon $MCUa_{KD}$ in T-cells, correlating with the change in mRNA.

Downregulation of MCUa and impairment of mitochondrial Ca^{2+} uptake led to a significant reduction of resting cytosolic Ca^{2+} levels and SOCE in T-cells (**Figure 42**). These results were not in full agreement with studies performed by Yoast et al. (2021) and Wu et al. (2021), wherein pharmacological inhibition of MCU, MCU silencing, or a T-cell-specific MCU deletion *in vivo* associated with unaltered or even enhanced SOCE. Considering that MCU depletion alone is not sufficient to fully abolish mitochondrial Ca^{2+} uptake, and given the presence of multiple Ca^{2+} efflux pathways, adaptational changes, such as reduced efflux or even reversed Ca^{2+} transport direction, are likely to compensate for the total loss of MCU. In our model, partial MCU silencing presumably led to lower Ca^{2+} efflux into the cytosol in order to maintain mitochondrial Ca^{2+} homeostasis, which in turn decreased resting cytosolic Ca^{2+}.

All in all, our data show evidence that MCU-dependent Ca^{2+} influx has a vital effect on mitochondrial metabolism in $CD4^+$ T-cells, which in turn affects ATP production and SOCE.

4.3 Upregulation of m-AAA protease AFG3L2 is a compensatory mechanism that mediates MCU complex stability via EMRE proteolysis in $CD4^+$ T-cells and HeLa cells

Mitochondrial protein quality control is a vital mechanism for maintaining mitochondrial structure and function. Mitochondrial ATP-associated (m-AAA) proteases were first acknowledged as major quality control enzymes in yeast (Leonhard et al., 1999), and were later shown to be conserved in mammalian cells as well (Patron et al., 2022). AFG3L2, located in the IMM with its catalytic site towards the intermembrane space, is a major quality control enzyme responsible for degradation of aberrant proteins, and maintenance of ROS homeostasis and mitochondrial structure (Atorino et al., 2003; Ehses et al., 2009). Moreover, AFG3L2 ensures proper assembly of the MCU complex by degrading excess EMRE subunits and preventing over-active MCU-EMRE complexes (König et al., 2016; Tsai et al., 2017). Total loss of AFG3L2 results in the formation of MCU-EMRE complexes which lack gatekeeping activity (König et al., 2016). Such disturbed Ca^{2+} signalling has been linked to spinocerebellar ataxia and recessive hereditary spastic paraplegia (Pierson et al., 2011).

In the current study, out of 11 proteins screened after $MCUa_{KD}$, only AFG3L2 was significantly upregulated (**Figure 50**). This was observed on a protein, and not on mRNA level. Similar upregulation of AFG3L2 protein levels was evident in $MCUa_{KD}$ melanoma cells (Stejerean-Todoran et al., 2022). Based on existing data so far, we believe that AFG3L2 upregulation is a compensatory mechanism which allows for excess EMRE proteolysis (given the lack of available MCUa subunits). Considering that there is still a presence of residual MCUa, the increased EMRE proteolysis could lead to an overall lower MCU complex stability. AFG3L2 downregulation led to a significant increase in resting mitochondrial Ca^{2+} levels in effector $CD4^+$ T-cells, and a significant increase in mitochondrial Ca^{2+} uptake in HeLa cells (**Figures 52** and **54**). These results are in agreement with findings obtained in the study from König et al. (2016) and indicate that upon AFG3L2 downregulation, the presence of over-active MCU-EMRE complexes without gatekeepers is higher, as well as the overall half-life of the complex.

Mitochondrial respiration and ATP generation were not significantly affected upon downregulation of AFG3L2 neither in effector $CD4^+$ T-cells (**Figure 53**) nor in HeLa cells (**Figures 56** and **57A**). Considering the significant presence of leftover AFG3L2 enzyme (around 50%), it is likely that its enzymatic activity is high enough to prevent any changes in mitochondrial bioenergetics. It would be importat to perform these experiments using a full AFG3L2 knockout, or by simply inducing cellular stress by complex III inhibition with antimycin A (this has been shown to significantly decrease AFG3L2 levels; Patron et al., 2022).

Nevertheless, an increase in mitochondrial membrane potential was observed upon AFG3L2 KD in HeLa cells (**Figure 57C**). In accordance with our previous findings obtained after $MCUa_{KD}$ showing a decrease in mitochondrial membrane potential, we again postulate that mitochondrial Ca^{2+} levels directly influence the membrane potential; however, in this case, remaining enzymatic activity of AFG3L2 is sufficient to prevent alterations in respiration and ATP production.

The increased levels of AFG3L2 upon $MCUa_{KD}$ might also explain the unaltered ROS levels in T-cells. To this end, the Ca^{2+} transporter TMBIM5 was recently identified as a novel substrate and inhibitor of AFG3L2 in the IMM by Patron et al. (2022). At physiological conditions, TMBIM5 binds to the catalytic site of AFG3L2 and limits its activity. Upregulation of AFG3L2 upon $MCUa_{KD}$ would thus cause TMBIM5 degradation, which would then limit Ca^{2+} efflux from mitochondria. This AFG3L2-controlled modulation of mitochondrial Ca^{2+} efflux could prevent a more pronounced depletion of mitochondrial matrix Ca^{2+} levels following MCUa downregulation.

Taken together, our data on $CD4^+$ T-cells and HeLa cells show that AFG3L2 is a critical regulatory component ensuring proper mitochondrial function even when vital proteins, such as the MCU complex, have been altered. AFG3L2 regulates MCU complex stability via EMRE proteolysis and maintains a homeostatic oxidative environment in mitochondria.

4.4 Mitochondrial calcium uptake through MCU has a crucial role in $CD4^+$ T-cell function

Calcium signalling is essential for T-cell activation, differentiation and function. In this context, mitochondrial Ca^{2+} uptake via the MCU complex allows for proper oxidative metabolism and energy generation, as shown in this study. Despite the presence of studies tackling with the role of Ca^{2+} signalling in immune cells (Quintana et al., 2011; Quintana & Hoth, 2012; Samanta et al., 2014), studies with a focus on the role of MCU in T-cell function are lacking.

Here, we show that impairment of mitochondrial Ca^{2+} uptake by transient downregulation of MCUa in activated human $CD4^+$ T-cells affects their proinflammatory action. In particular, a reduction of IL-2 and IFNγ secretion and gene expression was observed upon $MCUa_{KD}$ (**Figure 43**). IL-2 production by $CD4^+$ T-cells is strongly induced upon cell antigen activation, influencing cell differentiation by acting on STAT5 and increasing the killing activity of $CD8^+$ T-cells and NK cells (Boyman & Sprent, 2012). IFNγ is mainly

secreted by Th1 cells and plays an important role in host defense against microbial infections and in development of autoimmune diseases, including multiple sclerosis (Ivashkiv, 2018). Furthermore, after a screening of main $CD4^+$ T-cell subtype transcription factors, we observed a higher mRNA expression of Treg transcription factor FoxP3. FoxP3 is expressed in Tregs which have a suppressive (anti-inflammatory) role in the immune system. FoxP3 suppresses NFAT and NFκB, which leads to a lower expression of proinflammatory cytokines, such as IL-2 and IFNγ (C. H. Kim, 2009). Based on these findings, we can deduce that the impaired mitochondrial Ca^{2+} uptake leads to higher expression of transcription factor FoxP3, which induces cell differentiation from a pro- to an anti-inflammatory cell type, with lower cytokine gene expression and lower IFNγ secretion. Since both cytokine and transcription factor mRNA expression levels are crucial for initial T-cell activation, it is important to analyse mRNA levels in the "early-stage" $MCUa_{KD}$ model as well. Additionally, STAT proteins are well known for their roles in $CD4^+$ T-cell differentiation and cytokine secretion (O'Shea et al., 2011). Thus, it is important to assess their expression levels in the current T-cell model as well.

An important parameter of T-cell function is the ability of the cell to migrate and invade tissues and sites of inflammation. In this study, we evaluated T-cell migration in two ways. Firstly, by subjecting the T-cells to a chemokine gradient and allowing them to migrate freely through a pore, and secondly, by allowing cells to migrate freely towards a chemokine "environment" generated by the metastatic melanoma cell line 1205Lu (based on a study done by Harlin et al., 2009). In general, there was no apparent difference in migration between $MCUa_{KD}$ and control $CD4^+$ T-cells. It would be important to further assess this observation by using different types of metastatic melanoma cells. T-cell invasion was evaluated by allowing the cells to migrate through a Matrigel-coated pore towards a chemokine gradient, mimicking a tissue-like environment. In this case, $MCUa_{KD}$ T-cells invaded significantly less compared to control (**Figure 46C**). Given that upon $MCUa_{KD}$, ATP generation is reduced in the T-cells, it is probable that a lowered cell migration is a direct consequence. Therefore, further investigation regarding migration and invasion is necessary, best by using 3D invasion models.

To evaluate the role of MCU in T-cell *in vivo*, we used an experimental model of multiple sclerosis (EAE) in rats, by injecting them with control cells and cells with a significant reduction of MCUa (refer to **Figures 63** and **65**). Evidently, an impairment of mitochondrial Ca^{2+} uptake leads to a significant delay of autoimmune disease onset (average delay of one day compared to control). Furthermore, a striking reduction of chronic disease severity was observed upon injection of one of the $MCUa_{KD}$ cell lines (MCUps5) (**Figure 65**), indicating a crucial role of MCU in progression of EAE. To our understanding, the suppressed

mitochondrial metabolism and ATP generation, likely affected the invasion of the T-cells to the brain of these animals, causing the delay of disease onset and the mild disease phenotype. It is important to mention that intravenously transferred T-cells initially reside in the lungs, before entering the blood and the central nervous system. A T-cell reprogramming process is initiated in the lungs where they upregulate their membrane receptors, chemokine receptors and adhesion proteins (Odoardi et al., 2012). Therefore, it is essential to explore the cells' activation status in different stages by isolating them at day 2 before disease onset, at days 3 and 4 when disease onset occurs, and at the day when the EAE score is highest. Additionally, isolating cells from different compartments (blood, lungs and spinal cord) could give indications of whether these cells are affected differently in different environments in the body.

4.5 An outlook on mitochondrial Ca^{2+} signalling in human T-cells

To our knowledge, the present study is among the first ones to acknowledge the role of MCU in mitochondrial metabolism and effector function of human $CD4^+$ T-cells and immune cells in general. Nevertheless, the vast complexity of the human immune system gives rise to many challenges in the scientific field which we have yet to explore.

One challenge that scientists face in all fields of research is biological sex differences in both physiological and pathological responses. In immunity, an effective immune response is highly influenced by genetics, the environment and the hormonal status, in a sex-dependant manner. Sex hormones (estrogens, progesterone and testosterone) can bind to specific PM and/or nuclear receptors of all immune cells and influence their gene expression. Studies have reported sex-dependent differences in autoimmune diseases (Di Florio et al., 2020). Additionally, mitochondria exhibit strong sex-specificity. Research has shown that mitochondrial genes related to localisation and metabolism are upregulated in biological females and downregulated in biological males (including for e.g. COX5a, PDK4, and PPARGC1) (Ventura-Clapier et al., 2017). A study by Chweih et al. (2015) showed that biological females display a lower mitochondrial content, but higher mitochondrial efficiency, respiration, and glycolysis, and lower mitochondrial Ca^{2+} uptake and ROS production. Based on these observations, it would be important to evaluate the role of mitochondrial Ca^{2+} uptake through MCU in a sex-dependent manner. Unfortunately, information regarding biological sex of the human blood donors was not available for this study due to patient confidentiality. Future research could focus on this aspect, as well as examining age-dependent differences of the donors, given that the immune system differs significantly with increasing age as well.

Pharmacological inhibition of MCU has been problematic due to the low specificity of some existing inhibitors, as well as the low cell permeability, leading to variable results among studies. The recently developed inhibitor Ruthenium 265 is a good candidate because it is non-toxic and has no known effects on other mitochondrial Ca^{2+} channels (Woods et al., 2019, 2020). Ru265 significantly decreased resting mitochondrial Ca^{2+} and mitochondrial Ca^{2+} uptake in human $CD4^{+}$ T-cells after pre-treatment of 24 hours (**Figure 33**). To ensure the potential therapeutic use of Ru265, additional mitochondrial metabolic parameters and T-cell parameters need to be assessed and compared to the results obtained with the generated knockdown model. These include respiration, ATP generation, IL-2 and IFNγ secretion, and in particular, changes in mitochondrial membrane potential upon activation (as observed when using Mitoxantrone).

Recently, our group was able to show that MCUa controls the aggressive behaviour and therapeutic sensitivity of melanoma cancer cells. Specifically, upregulation or activation of the MCU complex increases the therapeutic sensitivity of melanoma cells and has a positive effect on patient survival (Stejerean-Todoran et al., 2022). Therefore, it seems that a tissue- or even a cell-specific regulation of MCU is required for certain pathologies. In the case of T-cell-mediated immunity, MCU inhibition would be beneficial for delaying progressive autoimmune disease. Such targeted therapies are not easy to develop, but recent advances in drug delivery systems and cell-based targeted therapies are emerging (Zhao et al., 2020) and have a great potential in improving the quality of life of autoimmune disease patients.

5. Conclusions

Previous studies exploring the role of MCU have shown contradictory results. Given the importance of mitochondrial function in T-cell biology, understanding the exact role of the MCU complex, i.e. mitochondrial Ca^{2+}, was of utmost importance. Accordingly, this study aimed to expand the current knowledge as well as provide more detailed information regarding the role of the MCU complex in human $CD4^+$ T-cells.

Naive T-cell activation through TCR stimulation leads to a rapid cellular reprogramming required for proper T-cell function, involving a considerable increase in mitochondrial Ca^{2+} uptake, respiration, ATP production, mitochondrial membrane potential, and protein translation. Our findings indicate that in order to accommodate for the immense metabolic demand, the MCU complex in T-cells alters its molecular composition, allowing for higher Ca^{2+} uptake. Transient, acute impairment of mitochondrial Ca^{2+} uptake through MCUa downregulation in effector $CD4^+$ T-cells causes a susbtantial reduction of mitochondrial metabolism and bioenergetic output, in both human and rat $CD4^+$ T-cells, evident by the decrease in mitochondrial respiration, ATP generation, and mitochondrial membrane potential. Interestingly, MCUa downregulation causes a compensatory upregulation of the mitochondrial protease AFG3L2 on a protein level only. $AFG3L2_{KD}$ affects mitochondrial $[Ca^{2+}]$ and IMM potential, likely via EMRE proteolysis, a finding demonstrating the importance of this protease in the context of Ca^{2+} modulation in immune cells (**Figure 66**).

Functionally, we observed a number of alterations in the $MCUa_{KD}$ $CD4^+$ T-cells. These include reduction of essential T-cell parameters such as cytokine expression and secretion (IL-2 and IFNγ), cell mobility and invasion. *In vivo*, the impairment of mitochondrial Ca^{2+} uptake via MCU caused a delay in disease onset, as well as a milder clinical phenotype in an experimental rat model of multiple sclerosis (EAE).

Overall, the collective data from this study show that mitochondrial Ca^{2+} pathways and the MCU complex should be considered when treating patients with autoimmune diseases. Targeted $CD4^+$ T-cell pharmacological inhibition of MCU could potentially be beneficial for suppression of progressive autoimmune disease and control of dysregulated immunity.

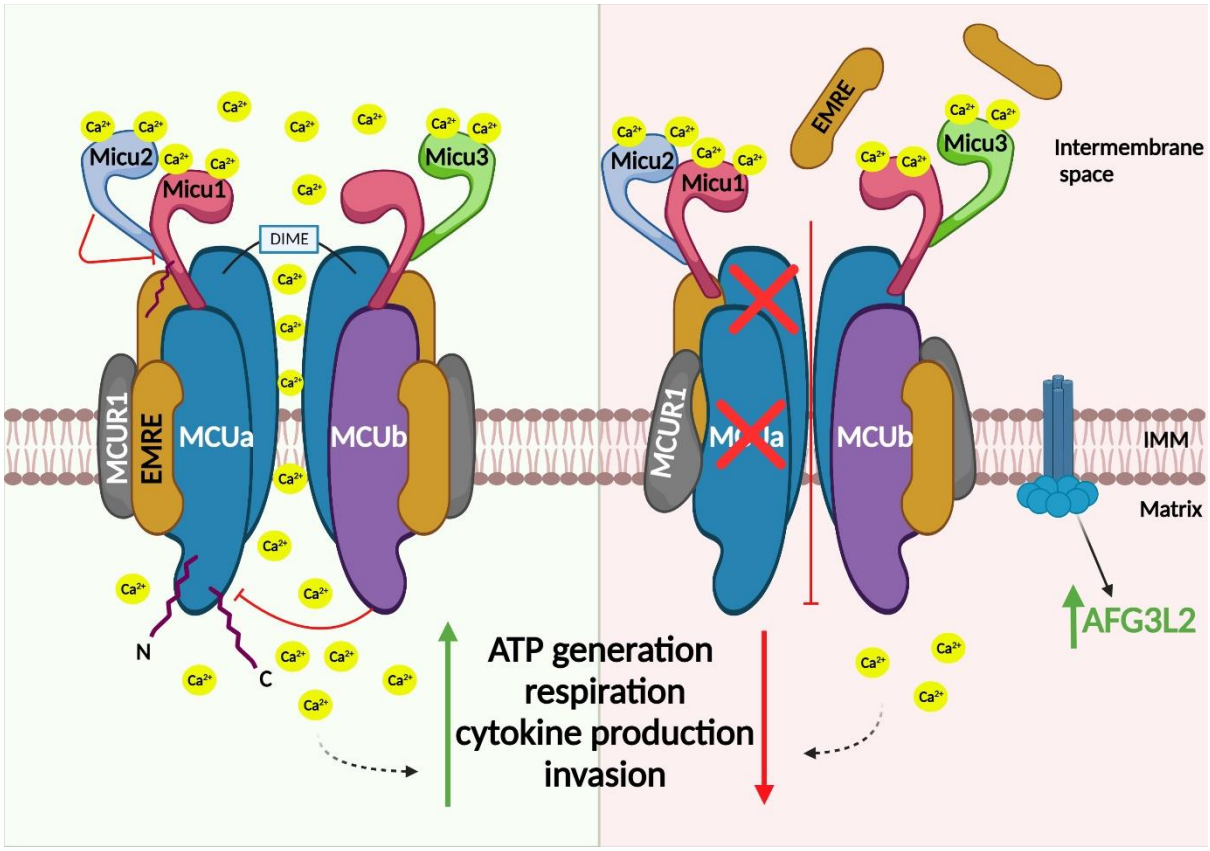

Figure 66. An overview of the main findings of this study. Normal MCU complex expression and physiological activity in the IMM of $CD4^+$ T-cells (left green panel) allows for controlled mitochondrial Ca^{2+} uptake and regulation of mitochondrial membrane potential, thereby normal respiration and ATP production. Moreover, proper T-cell effector function is achieved. Upon MCUa downregulation (right red panel), less Ca^{2+} is taken up in the matrix leading to a reduction in mitochondrial membrane potential, respiration, and ATP generation. Due to the lower metabolic rate, the effector function of $CD4^+$ T-cells is diminished, observed by a decrease in cytokine secretion and migration. MCUa downregulation induces a compensatory upregulation of m-AAA protease AFG3L2 which degrades excess EMRE accumulating in the intermembrane space and lowers the stability of the MCU complex. Image created in BioRender.

6. Bibliography

Ahmad, M., Wolberg, A., & Kahwaji, C. I. (2022). Biochemistry, Electron Transport Chain. In *StatPearls*. StatPearls Publishing. http://www.ncbi.nlm.nih.gov/books/NBK526105/.

Antony, A. N., Paillard, M., Moffat, C., Juskeviciute, E., Correnti, J., Bolon, B., Rubin, E., Csordás, G., Seifert, E. L., Hoek, J. B., & Hajnóczky, G. (2016). MICU1 Regulation of Mitochondrial Ca^{2+} Uptake Dictates Survival and Tissue Regeneration. *Nature Communications*, *7*(1), 10955. https://doi.org/10.1038/ncomms10955.

Arduino, D. M., Wettmarshausen, J., Vais, H., Navas-Navarro, P., Cheng, Y., Leimpek, A., Ma, Z., Delrio-Lorenzo, A., Giordano, A., Garcia-Perez, C., Médard, G., Kuster, B., García-Sancho, J., Mokranjac, D., Foskett, J. K., Alonso, M. T., & Perocchi, F. (2017). Systematic Identification of MCU Modulators by Orthogonal Interspecies Chemical Screening. *Molecular Cell*, *67*(4), 711-723.e7. https://doi.org/10.1016/j.molcel.2017.07.019.

Atorino, L., Silvestri, L., Koppen, M., Cassina, L., Ballabio, A., Marconi, R., Langer, T., & Casari, G. (2003). Loss of m-AAA Protease in Mitochondria Causes Complex I Deficiency and Increased Sensitivity to Oxidative Stress in Hereditary Spastic Paraplegia. *The Journal of Cell Biology*, *163*(4), 777–787. https://doi.org/10.1083/jcb.200304112.

Bachelerie, F., Ben-Baruch, A., Burkhardt, A. M., Charo, I. F., Combadiere, C., Förster, R., Farber, J. M., Graham, G. J., Hills, R., Horuk, R., Locati, M., Luster, A. D., Mantovani, A., Matsushima, K., Monaghan, A. E., Moschovakis, G. L., Murphy, P. M., Nibbs, R. J. B., Nomiyama, H., … Zlotnik, A. (2020). Chemokine Receptors. (Version 2020.5) in the IUPHAR/BPS Guide to Pharmacology Database. *IUPHAR/BPS Guide to Pharmacology* (5). https://doi.org/10.2218/gtopdb/F14/2020.5.

Badou, A., Jha, M. K., Matza, D., & Flavell, R. A. (2013). Emerging Roles of L-Type Voltage-Gated and Other Calcium Channels in T Lymphocytes. *Frontiers in Immunology*, *4*(243). https://doi.org/10.3389/fimmu.2013.00243.

Barlic, A., McDermott, D., Merrell, M., Gonzales, J., Via, L., & Murphy, P. (2004). Interleukin (IL)-15 and IL-2 Reciprocally Regulate Expression of the Chemokine Receptor CX3CR1 Through Selective NFAT1- and NFAT2-Dependent Mechanisms. *The Journal of Biological Chemistry*, *279*(47). https://doi.org/10.1074/jbc.M406978200.

Barnabei, L., Laplantine, E., Mbongo, W., Rieux-Laucat, F., & Weil, R. (2021). NF-κB: At the Borders of

Autoimmunity and Inflammation. *Frontiers in Immunology*, 12, 716469. https://doi.org/10.3389/fimmu.2021.716469.

Bartolák-Suki, E., Imsirovic, J., Nishibori, Y., Krishnan, R., & Suki, B. (2017). Regulation of Mitochondrial Structure and Dynamics by the Cytoskeleton and Mechanical Factors. *International Journal of Molecular Sciences*, *18*(8), 1812. https://doi.org/10.3390/ijms18081812.

Baughman, J. M., Perocchi, F., Girgis, H. S., Plovanich, M., Belcher-Timme, C. A., Sancak, Y., Bao, X. R., Strittmatter, L., Goldberger, O., Bogorad, R. L., Koteliansky, V., & Mootha, V. K. (2011). Integrative Genomics Identifies MCU as an Essential Component of the Mitochondrial Calcium Uniporter. *Nature*, *476*(7360), 341–345. https://doi.org/10.1038/nature10234.

Beckermann, K. E., Dudzinski, S. O., & Rathmell, J. C. (2017). Dysfunctional T Cell Metabolism in the Tumor Microenvironment. *Cytokine and Growth Factor Reviews*, *35*, 7–14. https://doi.org/10.1016/j.cytogfr.2017.04.003.

Beier, U. H., Angelin, A., Akimova, T., Wang, L., Liu, Y., Xiao, H., Koike, M. A., Hancock, S. A., Bhatti, T. R., Han, R., Jiao, J., Veasey, S. C., Sims, C. A., Baur, J. A., Wallace, D. C., & Hancock, W. W. (2015). Essential Role of Mitochondrial Energy Metabolism in Foxp3^{+} T-Regulatory Cell Function and Allograft Survival. *The Federation of American Societies for Experimental Biology Journal*, *29*(6), 2315–2326. https://doi.org/10.1096/fj.14-268409.

Benzing, C., Rossy, J., & Gaus, K. (2013). Do Signalling Endosomes Play a Role in T Cell Activation?. *The Federation of European Biochemical Societies Journal*, *280*(21), 5164–5176. https://doi.org/10.1111/febs.12427.

Bertin, S., Aoki-Nonaka, Y., Jong, P. R. de, Nohara, L. L., Xu, H., Stanwood, S. R., Srikanth, S., Lee, J., To, K., Abramson, L., Yu, T., Han, T., Touma, R., Li, X., González-Navajas, J. M., Herdman, S., Corr, M., Fu, G., Dong, H., … Raz, E. (2014). The Ion Channel TRPV1 Regulates the Activation and Proinflammatory Properties of CD4^{+} T Cells. *Nature Immunology*, *15*(11), 1055. https://doi.org/10.1038/ni.3009.

Bertoni, A., Alabiso, O., Galetto, A. S., & Baldanzi, G. (2018). Integrins in T Cell Physiology. *International Journal of Molecular Sciences*, *19*(2), 485. https://doi.org/10.3390/ijms19020485.

Bilan, D. S., Pase, L., Joosen, L., Gorokhovatsky, A. Yu., Ermakova, Y. G., Gadella, T. W. J., Grabher, C., Schultz, C., Lukyanov, S., & Belousov, V. V. (2013). HyPer-3: A Genetically Encoded H_2O_2 Probe with Improved Performance for Ratiometric and Fluorescence Lifetime Imaging. *American Chemical Society Chemical Biology*, *8*(3), 535–542. https://doi.org/10.1021/cb300625g.

Binns, D., Dimmer, E., Huntley, R., Barrel, D., O'Donovan, C., & Apweiler, R. (2009). QuickGO: A Web-Based Tool for Gene Ontology Searching. *Bioinformatics*, *25*(22), 3045–3046.

Bogeski, I., Kummerow, C., Al-Ansary, D., Schwarz, E., R, R., Kozai, D., Takahashi, N., Peinelt, C., Griesemer, D., Bozem, M., Mori, Y., Hoth, M., & Niemeyer, B. (2010). Differential Redox Regulation of ORAI Ion Channels: A Mechanism to Tune Cellular Calcium Signaling. *Science Signaling*, *3*(115). https://doi.org/10.1126/scisignal.2000672.

Boyman, L., Williams, G. S. B., Khananshvili, D., Sekler, I., & Lederer, W. J. (2013). NCLX: The Mitochondrial Sodium Calcium Exchanger. *Journal of Molecular and Cellular Cardiology*, *59*, 205–213. https://doi.org/10.1016/j.yjmcc.2013.03.012.

Boyman, O., & Sprent, J. (2012). The Role of Interleukin-2 During Homeostasis and Activation of the Immune System. *Nature Reviews Immunology*, *12*(3), 180–190. https://doi.org/10.1038/nri3156.

Bradford, M. M. (1976). A Rapid and Sensitive Method for the Quantitation of Microgram Quantities of Protein Utilizing the Principle of Protein-Dye Binding. *Analytical Biochemistry*, *72*, 248–254. https://doi.org/10.1006/abio.1976.9999.

Cahalan, M., & Chandy, G. (2009). The Functional Network of Ion Channels in T Lymphocytes. *Immunological Reviews*, *231*(1), 59–87. https://doi.org/10.1111/j.1600-065X.2009.00816.x.

Cahalan, M., & Lewis, R. (1988). Role of Potassium and Chloride Channels in Volume Regulation by T Lymphocytes. *Society of General Physiologists Series*, *43*, 281–301.

Calì, T., Brini, M., & Carafoli, E. (2017). Regulation of Cell Calcium and Role of Plasma Membrane Calcium ATPases. *International Review of Cell and Molecular Biology*, *332*, 259–296. https://doi.org/10.1016/bs.ircmb.2017.01.002.

Campbell, G. R., & Mahad, D. J. (2012). Mitochondrial Changes Associated with Demyelination: Consequences for Axonal Integrity. *Mitochondrion*, *12*(2), 173–179. https://doi.org/10.1016/j.mito.2011.03.007.

Cano, R. L. E., & Lopera, H. D. E. (2013). Introduction to T and B Lymphocytes. In *Autoimmunity: From Bench to Bedside*. El Rosario University Press. https://www.ncbi.nlm.nih.gov/books/NBK459471/.

Cham, C. M., & Gajewski, T. F. (2005). Glucose Availability Regulates IFN-Gamma Production and p70S6 Kinase Activation in $CD8^+$ Effector T Cells. *Journal of Immunology*, *174*(8), 4670–4677. https://doi.org/10.4049/jimmunol.174.8.4670.

Chemaly, E. R., Troncone, L., & Lebeche, D. (2018). SERCA Control of Cell Death and Survival. *Cell Calcium*, *69*, 46–61. https://doi.org/10.1016/j.ceca.2017.07.001.

Chen, J., Guan, L., Tang, L., Liu, S., Zhou, Y., Chen, C., He, Z., & Xu, L. (2019). T Helper 9 Cells: A New Player in Immune-Related Diseases. *DNA and Cell Biology*, *38*(10), 1040–1047. https://doi.org/10.1089/dna.2019.4729.

Chen, T.-W., Wardill, T. J., Sun, Y., Pulver, S. R., Renninger, S. L., Baohan, A., Schreiter, E. R., Kerr, R. A., Orger, M. B., Jayaraman, V., Looger, L. L., Svoboda, K., & Kim, D. S. (2013). Ultra-Sensitive Fluorescent Proteins for Imaging Neuronal Activity. *Nature*, *499*(7458), 295–300. https://doi.org/10.1038/nature12354.

Chinnery, P. F., & Hudson, G. (2013). Mitochondrial Genetics. *British Medical Bulletin*, *106*(1), 135–159. https://doi.org/10.1093/bmb/ldt017.

Chweih, H., Castilho, R. F., & Figueira, T. R. (2015). Tissue and Sex Specificities in Ca^{2+} Handling by Isolated Mitochondria in Conditions Avoiding the Permeability Transition. *Experimental Physiology*, *100*(9), 1073–1092. https://doi.org/10.1113/EP085248.

Clapham, D. (2007). Calcium Signalling. *Cell*, *131*(6), 1047–1058. https://doi.org/10.1016/j.cell.2007.11.028.

Coffman, R. L. (2006). Origins of the Th1-Th2 model: A Personal Perspective. *Nature Immunology*, *7*(6), 539–541. https://doi.org/10.1038/ni0606-539.

Cogliati, S., Enriquez, J. A., & Scorrano, L. (2016). Mitochondrial Cristae: Where Beauty Meets Functionality. *Trends in Biochemical Sciences*, *41*(3), 261–273. https://doi.org/10.1016/j.tibs.2016.01.001.

Colantonio, L., Recalde, H., Sinigaglia, F., & D'Ambrosio, D. (2002). Modulation of Chemokine Receptor Expression and Chemotactic Responsiveness During Differentiation of Human Naive T Cells into Th1 or Th2 cells. *European Journal of Immunology*, *32*(5), 1264–1273. https://doi.org/10.1002/1521-4141(200205)32:5<1264: AID-IMMU1264>3.0.CO;2-S.

Conforti, L. (2017). Potassium Channels of T Lymphocytes Take Center Stage in the Fight Against Cancer. *Journal for ImmunoTherapy of Cancer*, *5*(1), 1–3. https://doi.org/10.1186/s40425-016-0202-5.

Constantinescu, C. S., Farooqi, N., O'Brien, K., & Gran, B. (2011). Experimental Autoimmune Encephalomyelitis (EAE) as a Model for Multiple Sclerosis (MS). *British Journal of Pharmacology*, *164*(4), 1079–1106. https://doi.org/10.1111/j.1476-5381.2011.01302.x.

Coutinho-Silva, R., Knight, G., & Burnstock, G. (2005). Impairment of the Splenic Immune System in P2X(2)/P2X(3) Knockout Mice. *Immunobiology*, *209*(9), 661–668. https://doi.org/10.1016/j.imbio.2004.09.007.

Crotty, S. (2014). T Follicular Helper Cell Differentiation, Function, and Roles in Disease. *Immunity*, *41*(4), 529–

542. https://doi.org/10.1016/j.immuni.2014.10.004.

Crowley, L. C., Christensen, M. E., & Waterhouse, N. J. (2016). Measuring Mitochondrial Transmembrane Potential by TMRE Staining. *Cold Spring Harbor Protocols*, *2016*(12). https://doi.org/10.1101/pdb.prot087361.

Csordias, G., Golenar, T., Seifert, E., Kamer, K., Sancak, Y., Perocchi, F., Moffat, C., Weaver, D., De la Fuente Perez, S., Bogorad, R., Koteliansky, V., Adijanto, J., Mootha, V., & Hajnoczky, G. (2013). MICU1 Controls Both the Threshold and Cooperative Activation of the Mitochondrial Ca^{2+} Uniporter. *Cell Metabolism*, *17*(6). https://doi.org/10.1016/j.cmet.2013.04.020.

Dalby, B., Cates, S., Harris, A., Ohki, E. C., Tilkins, M. L., Price, P. J., & Ciccarone, V. C. (2004). Advanced Transfection with Lipofectamine 2000 Reagent: Primary Neurons, siRNA, and High-Throughput Applications. *Methods*, *33*(2), 95–103. https://doi.org/10.1016/j.ymeth.2003.11.023.

Davis, L. C., Morgan, A. J., Chen, J.-L., Snead, C. M., Bloor-Young, D., Shenderov, E., Stanton-Humphreys, M. N., Conway, S. J., Churchill, G. C., Parrington, J., Cerundolo, V., & Galione, A. (2012). NAADP Activates Two-Pore Channels on T Cell Cytolytic Granules to Stimulate Exocytosis and Killing. *Current Biology*, *22*(24), 2331. https://doi.org/10.1016/j.cub.2012.10.035.

De Jesús García-Rivas, G., Guerrero-Hernández, A., Guerrero-Serna, G., Rodríguez-Zavala, J. S., & Zazueta, C. (2005). Inhibition of the Mitochondrial Calcium Uniporter by the Oxo-Bridged Dinuclear Ruthenium Amine Complex (Ru360) Prevents from Irreversible Injury in Postischemic Rat Heart. *The Federation of European Biochemical Societies Journal*, *272*(13), 3477–3488. https://doi.org/10.1111/j.1742-4658.2005.04771.x.

De Mario, A., Tosatto, A., Hill, J. M., Kriston-Vizi, J., Ketteler, R., Vecellio Reane, D., Cortopassi, G., Szabadkai, G., Rizzuto, R., & Mammucari, C. (2021). Identification and Functional Validation of FDA-Approved Positive and Negative Modulators of the Mitochondrial Calcium Uniporter. *Cell Reports*, *35*(12), 109275. https://doi.org/10.1016/j.celrep.2021.109275.

De Stefani, D., Raffaello, A., Teardo, E., Szabò, I., & Rizzuto, R. (2011). A Forty-Kilodalton Protein of the Inner Membrane is the Mitochondrial Calcium Uniporter. *Nature*, *476*(7360), 336–340. https://doi.org/10.1038/nature10230.

Debattisti, V., Horn, A., Singh, R., Seifert, E. L., Hogarth, M. W., Mazala, D. A., Huang, K. T., Horvath, R., Jaiswal, J. K., & Hajnóczky, G. (2019). Dysregulation of Mitochondrial Ca^{2+} Uptake and Sarcolemma Repair Underlie Muscle Weakness and Wasting in Patients and Mice Lacking MICU1. *Cell Reports*,

29(5), 1274-1286.e6. https://doi.org/10.1016/j.celrep.2019.09.063.

Delves, P., Martin, S., Burton, D., & Roitt, I. (2011). *Roitt's Essential Immunology* (12th ed.). Wiley-Blackwell.

Dey, K., Bazala, M. A., & Kuznicki, J. (2020). Targeting Mitochondrial Calcium Pathways as a Potential Treatment Against Parkinson's Disease. *Cell Calcium*, *89*, 102216. https://doi.org/10.1016/j.ceca.2020.102216.

Di Florio, D. N., Sin, J., Coronado, M. J., Atwal, P. S., & Fairweather, D. (2020). Sex Differences in Inflammation, Redox Biology, Mitochondria and Autoimmunity. *Redox Biology*, *31*, 101482. https://doi.org/10.1016/j.redox.2020.101482.

Di Virgilio, F., Dal Ben, D., Sarti, A. C., Giuliani, A. L., & Falzoni, S. (2017). The P2X7 Receptor in Infection and Inflammation. *Immunity*, *47*(1), 15–31. https://doi.org/10.1016/j.immuni.2017.06.020.

Diaspro, A., Chirico, G., & Collini, M. (2006). Two-Photon Fluorescence Excitation and Related Techniques in Biological Microscopy. *Quarterly Reviews of Biophysics*, *38*(2), 97–166. https://doi.org/10.1017/S0033583505004129.

Drago, I., & Davis, R. L. (2016). Inhibiting the Mitochondrial Calcium Uniporter During Development Impairs Memory in Adult Drosophila. *Cell Reports*, *16*(10), 2763–2776. https://doi.org/10.1016/j.celrep.2016.08.017.

Ehses, S., Raschke, I., Mancuso, G., Bernacchia, A., Geimer, S., Tondera, D., Martinou, J.-C., Westermann, B., Rugarli, E. I., & Langer, T. (2009). Regulation of OPA1 Processing and Mitochondrial Fusion by m-AAA Protease Isoenzymes and OMA1. *The Journal of Cell Biology*, *187*(7), 1023–1036. https://doi.org/10.1083/jcb.200906084.

Eniafe, J., & Jiang, S. (2021). The Functional Roles of TCA Cycle Metabolites in Cancer. *Oncogene*, *40*(19), 3351–3363. https://doi.org/10.1038/s41388-020-01639-8.

Erdogmus, S., Concepcion, A. R., Yamashita, M., Sidhu, I., Tao, A. Y., Li, W., Rocha, P. P., Huang, B., Garippa, R., Lee, B., Lee, A., Hell, J. W., Lewis, R. S., Prakriya, M., & Feske, S. (2022). Cavβ1 Regulates T Cell Expansion and Apoptosis Independently of Voltage-Gated Ca^{2+} Channel Function. *Nature Communications*, *13*(1), 2033. https://doi.org/10.1038/s41467-022-29725-3.

Fahrner, M., Schindl, R., & Romanin, C. (2018). Studies of Structure-Function and Subunit Composition of Orai/STIM Channel. In *Calcium Entry Channels in Non-Excitable Cells*. CRC Press/Taylor & Francis. https://doi.org/10.1201/9781315152592-2.

Farndale, R. W., & Jarvis, G. E. (2019). Integrins (version 2019.4) in the IUPHAR/BPS Guide to Pharmacology

Database. *IUPHAR/BPS Guide to Pharmacology*, *2019*(4), Article 4. https://doi.org/10.2218/gtopdb/F760/2019.4.

Feno, S., Rizzuto, R., Raffaello, A., & Vecellio Reane, D. (2021). The Molecular Complexity of the Mitochondrial Calcium Uniporter. *Cell Calcium*, *93*, 102322. https://doi.org/10.1016/j.ceca.2020.102322.

Feske, S. (2007). Calcium Signalling in Lymphocyte Activation and Disease. *Nature Reviews Immunology*, *7*(9), 690–702. https://doi.org/10.1038/nri2152.

Feske, S., Giltnane, J., Dolmetsch, R., Staudt, L. M., & Rao, A. (2001). Gene Regulation Mediated by Calcium Signals in T Lymphocytes. *Nature Immunology*, *2*(4), 316–324. https://doi.org/10.1038/86318.

Feske, S., Gwack, Y., Prakriya, M., Srikanth, S., Puppel, S.-H., Tanasa, B., Hogan, P. G., Lewis, R. S., Daly, M., & Rao, A. (2006). A Mutation in Orai1 Causes Immune Deficiency by Abrogating CRAC Channel Function. *Nature*, *441*(7090), 179–185. https://doi.org/10.1038/nature04702.

Franciszkiewicz, K., Boissonnas, A., Boutet, M., Combadière, C., & Mami-Chouaib, F. (2012). Role of Chemokines and Chemokine Receptors in Shaping the Effector Phase of the Antitumor Immune Response. *Cancer Research*, *72*(24), 6325–6332. https://doi.org/10.1158/0008-5472.CAN-12-2027.

Fura-2, AM. (n.d.). Retrieved July 13, 2022, from https://www.thermofisher.com/order/catalog/product/F1221.

Garbincius, J. F., & Elrod, J. W. (2022). Mitochondrial Calcium Exchange in Physiology and Disease. *Physiological Reviews*, *102*(2), 893–992. https://doi.org/10.1152/physrev.00041.2020.

Germain, R. N. (2002). T-Cell Development and the CD4–CD8 Lineage Decision. *Nature Reviews Immunology*, *2*(5), 309–322. https://doi.org/10.1038/nri798.

Ghasemi, N., Razavi, S., & Nikzad, E. (2017). Multiple Sclerosis: Pathogenesis, Symptoms, Diagnoses and Cell-Based Therapy. *Cell Journal*, *19*(1), 1–10. https://doi.org/10.22074/cellj.2016.4867.

Gordon, S. (2008). *Elie Metchnikoff: Father of natural immunity*. *38*(12), 3257–3624. https://doi.org/10.1002/eji.200838855.

Gotoh, K., Takata, Y., Nakashima, Y., Mizuguchi, S., Komori, K., & Kang, D. (2021). Metabolic Analysis of Mouse Bone-Marrow-Derived Dendritic Cells Using an Extracellular Flux Analyzer: STAR Protocols. *Star Protocols*, *3*(1). https://doi.org/10.1016/j.xpro.2021.100401.

Gray, M. W. (2012). Mitochondrial Evolution. *Cold Spring Harbor Perspectives in Biology*, *4*(9), a011403.

Gresch, O., Engel, F. B., Nesic, D., Tran, T. T., England, H. M., Hickman, E. S., Körner, I., Gan, L., Chen, S., Castro-Obregon, S., Hammermann, R., Wolf, J., Müller-Hartmann, H., Nix, M., Siebenkotten, G., Kraus, G., & Lun, K. (2004). New Non-Viral Method for Gene Transfer into Primary Cells. *Methods*, *33*(2),

151–163. https://doi.org/10.1016/j.ymeth.2003.11.009.

Guschin, D. Y., Waite, A. J., Katibah, G. E., Miller, J. C., Holmes, M. C., & Rebar, E. J. (2010). A Rapid and General Assay for Monitoring Endogenous Gene Modification. *Methods in Molecular Biology*, *649*, 247–256. https://doi.org/10.1007/978-1-60761-753-2_15.

Guse, A. H., da Silva, C. P., Berg, I., Skapenko, A. L., Weber, K., Heyer, P., Hohenegger, M., Ashamu, G. A., Schulze-Koops, H., Potter, B. V. L., & Mayr, G. W. (1999). Regulation of Calcium Signalling in T Lymphocytes by the Second Messenger Cyclic ADP-Ribose. *Nature*, *398*(6722), 70–73. https://doi.org/10.1038/18024.

Gutscher, M., Pauleau, A.-L., Marty, L., Brach, T., Wabnitz, G. H., Samstag, Y., Meyer, A. J., & Dick, T. P. (2008). Real-Time Imaging of the Intracellular Glutathione Redox Potential. *Nature Methods*, *5*(6), 553–559. https://doi.org/10.1038/nmeth.1212.

Hinkley, C. S., Hirsch, H. A., Gu, L., LaMere, B., & Henry, R. W. (2003). The Small Nuclear RNA-Activating Protein 190 Myb DNA Binding Domain Stimulates TATA Box-binding Protein-TATA Box Recognition. *Journal of Biological Chemistry*, *278*(20), 18649–18657. https://doi.org/10.1074/jbc.M204247200.

Holman, S. P., Lobo, A. S., Novorolsky, R. J., Nichols, M., Fiander, M., Konda, P., Kennedy, B. E., Gujar, S., & Robertson, G. S. (2020). Neuronal Mitochondrial Calcium Uniporter Deficiency Exacerbates Axonal Injury and Suppresses Remyelination in Mice Subjected to Experimental Autoimmune Encephalomyelitis. *Experimental Neurology*, 333, 113430. https://doi.org/10.1016/j.expneurol.2020.113430.

Hughes, A., & Putney, J. W. (1990). Inositol Phosphate Formation and its Relationship to Calcium Signaling. *Environmental Health Perspectives*, *84*, 141–147.

Huo, J., Lu, S., Kwong, J. Q., Bround, M. J., Grimes, K. M., Sargent, M. A., Brown, M. E., Davis, M. E., Bers, D. M., & Molkentin, J. D. (2020). MCUb Induction Protects the Heart from Post Ischemic Remodeling. *Circulation Research*, *127*(3), 379–390. https://doi.org/10.1161/CIRCRESAHA.119.316369.

Ivashkiv, L. B. (2018). IFNγ: Signalling, Epigenetics and Roles in Immunity, Metabolism, Disease and Cancer Immunotherapy. *Nature Reviews Immunology*, *18*(9), 545–558. https://doi.org/10.1038/s41577-018-0029-z.

Jares-Erijman, E. A., & Jovin, T. M. (2003). FRET Imaging. *Nature Biotechnology*, *21*(11), 1387–1395. https://doi.org/10.1038/nbt896.

Jensen, E. C. (2012). Use of Fluorescent Probes: Their Effect on Cell Biology and Limitations. *The Anatomical Record*, *295*(12), 2031–2036. https://doi.org/10.1002/ar.22602.

Jiang, Q., Yang, G., Xiao, F., Xie, J., Wang, S., Lu, L., & Cui, D. (2021). Role of Th22 Cells in the Pathogenesis of Autoimmune Diseases. *Frontiers in Immunology*, *12*. https://www.frontiersin.org/articles/10.3389/fimmu.2021.688066.

Kamiński, M. M., Röth, D., Sass, S., Sauer, S. W., Krammer, P. H., & Gülow, K. (2012). Manganese Superoxide Dismutase: A Regulator of T cell Activation-Induced Oxidative Signaling and Cell Death. *Biochimica Et Biophysica Acta*, *1823*(5), 1041–1052. https://doi.org/10.1016/j.bbamcr.2012.03.003.

Kim, C. H. (2009). FOXP3 and its Role in the Immune System. *Advances in Experimental Medicine and Biology*, *665*, 17–29. https://doi.org/10.1007/978-1-4419-1599-3_2.

Kim, K.-H., Kim, S.-H., Jung, H.-H., Moon, J.-H., Jeong, S.-U., Yu, K., & Lee, C.-K. (2018). Thapsigargin Increases IL-2 Production in T Cells at Nanomolar Concentrations. *Immune Network*, *18*(4), e26. https://doi.org/10.4110/in.2018.18.e26.

Kircher, S., Merino-Wong, M., Niemeyer, B. A., & Alansary, D. (2018). Profiling Calcium Signals of *in vitro* Polarized Human Effector $CD4^+$ T Cells. *Biochimica et Biophysica Acta (BBA) - Molecular Cell Research*, *1865*(6), 932–943. https://doi.org/10.1016/j.bbamcr.2018.04.001.

Kojer, K., Bien, M., Gangel, H., Morgan, B., Dick, T., & Riemer, J. (2012). Glutathione Redox Potential in the Mitochondrial Intermembrane Space is Linked to the Cytosol and Impacts the Mia40 Redox State. *The European Molecular Biology Organization Journal*, *31*(14), 3169–3182. https://doi.org/10.1038/emboj.2012.165.

Kon, N., Murakoshi, M., Isobe, A., Kagechika, K., Miyoshi, N., & Nagayama, T. (2017). DS16570511 is a Small-Molecule Inhibitor of the Mitochondrial Calcium Uniporter. *Cell Death Discovery*, *3*(1), 1–7. https://doi.org/10.1038/cddiscovery.2017.45.

König, T., Tröder, S. E., Bakka, K., Korwitz, A., Richter-Dennerlein, R., Lampe, P. A., Patron, M., Mühlmeister, M., Guerrero-Castillo, S., Brandt, U., Decker, T., Lauria, I., Paggio, A., Rizzuto, R., Rugarli, E. I., De Stefani, D., & Langer, T. (2016). The m-AAA Protease Associated with Neurodegeneration Limits MCU Activity in Mitochondria. *Molecular Cell*, *64*(1), 148–162. https://doi.org/10.1016/j.molcel.2016.08.020.

Kosmach, A., Roman, B., Sun, J., Femnou, A., Zhang, F., Liu, C., Combs, C. A., Balaban, R. S., & Murphy, E. (2021). Monitoring Mitochondrial Calcium and Metabolism in the Beating MCU-KO Heart. *Cell*

Reports, *37*(3), 109846. https://doi.org/10.1016/j.celrep.2021.109846.

Krishnamoorthy, M., Wasim, L., Buhari, F., Zhao, T., Mahtani, T., Ho, J., Kang, V., Deason-Towne, F., Perraud, A., Schmitz, C., & Treanor, B. (2018). The Channel-Kinase TRPM7 Regulates Antigen Gathering and Internalization in B Cells. *Science Signaling*, *11*(533). https://doi.org/10.1126/scisignal.aah6692.

Kühlbrandt, W. (2015). Structure and Function of Mitochondrial Membrane Protein Complexes. *BioMed Central Biology*, *13*, 89. https://doi.org/10.1186/s12915-015-0201-x.

Kumar, B. V., Connors, T., & Farber, D. L. (2018). Human T Cell Development, Localization, and Function Throughout Life. *Immunity*, *48*(2), 202–213. https://doi.org/10.1016/j.immuni.2018.01.007.

Kwong, J. Q., Huo, J., Bround, M. J., Boyer, J. G., Schwanekamp, J. A., Ghazal, N., Maxwell, J. T., Jang, Y. C., Khuchua, Z., Shi, K., Bers, D. M., Davis, J., & Molkentin, J. D. (2018). The Mitochondrial Calcium Uniporter Underlies Metabolic Fuel Preference in Skeletal Muscle. *Journal of Clinical Investigation Insight*, *3*(22), e121689. https://doi.org/10.1172/jci.insight.121689.

Kwong, J. Q., Lu, X., Correll, R. N., Schwanekamp, J. A., Vagnozzi, R. J., Sargent, M. A., York, A. J., Zhang, J., Bers, D. M., & Molkentin, J. D. (2015). The Mitochondrial Calcium Uniporter Selectively Matches Metabolic Output to Acute Contractile Stress in the Heart. *Cell Reports*, *12*(1), 15–22. https://doi.org/10.1016/j.celrep.2015.06.002.

Lambert, A. J., & Brand, M. D. (2009). Reactive Oxygen Species Production by Mitochondria. *Methods in Molecular Biology*, *554*, 165–181. https://doi.org/10.1007/978-1-59745-521-3_11.

Lambert, S. A., Jolma, A., Campitelli, L. F., Das, P. K., Yin, Y., Albu, M., Chen, X., Taipale, J., Hughes, T. R., & Weirauch, M. T. (2018). The Human Transcription Factors. *Cell*, *172*(4), 650–665. https://doi.org/10.1016/j.cell.2018.01.029.

Launay, P., Fleig, A., Perraud, A.-L., Scharenberg, A., Penner, R., & Kinet, J.-P. (2002). TRPM4 Is a Ca^{2+}-Activated Nonselective Cation Channel Mediating Cell Membrane Depolarization. *Cell*, *109*(3), 397–407. https://doi.org/10.1016/S0092-8674(02)00719-5.

Lax, N. Z., Turnbull, D. M., & Reeve, A. K. (2011). Mitochondrial Mutations. *The Neuroscientist*, *17*(6), 645–658. https://doi.org/10.1177/1073858411385469.

Leonhard, K., Stiegler, A., Neupert, W., & Langer, T. (1999). Chaperone-Like Activity of the AAA Domain of the Yeast Yme1 AAA Protease. *Nature*, *398*(6725), 348–351. https://doi.org/10.1038/18704.

Lewis, R. S. (2003). Calcium Signaling Mechanisms in T Lymphocytes. *Annual Review of Immunology*, *19*, 497-521. doi.org/10.1146/Annurev.Immunol.19.1.497.

Li, J., Wang, L., Chen, Y., Yang, Y., Liu, J., Liu, K., Lee, Y. T., He, N., Zhou, Y., & Wang, Y. (2020). Visible Light Excited Ratiometric-GECIs for Long-Term *in cellulo* Monitoring of Calcium Signals. *Cell Calcium*, 87, 102165. https://doi.org/10.1016/j.ceca.2020.102165.

Liberti, M. V., & Locasale, J. W. (2016). The Warburg Effect: How Does it Benefit Cancer Cells? *Trends in Biochemical Sciences*, *41*(3), 211–218. https://doi.org/10.1016/j.tibs.2015.12.001.

Licht-Mayer, S., Campbell, G. R., Canizares, M., Mehta, A. R., Gane, A. B., McGill, K., Ghosh, A., Fullerton, A., Menezes, N., Dean, J., Dunham, J., Al-Azki, S., Pryce, G., Zandee, S., Zhao, C., Kipp, M., Smith, K. J., Baker, D., Altmann, D., Anderton, S. M., … Mahad, D. J. (2020). Enhanced Axonal Response of Mitochondria to Demyelination Offers Neuroprotection: Implications for Multiple Sclerosis. *Acta Neuropathologica*, *140*(2), 143–167. https://doi.org/10.1007/s00401-020-02179-x.

Lis, A., Zierler, S., Peinelt, C., Fleig, A., & Penner, R. (2010). A Single Lysine in the N-Terminal Region of Store-Operated Channels is Critical for STIM1-Mediated Gating. *The Journal of General Physiology*, *136*(6), 673. https://doi.org/10.1085/jgp.201010484.

Lisak, D. A., Schacht, T., Enders, V., Habicht, J., Kiviluoto, S., Schneider, J., Henke, N., Bultynck, G., & Methner, A. (2015). The Transmembrane Bax Inhibitor Motif (TMBIM) Containing Protein Family: Tissue Expression, Intracellular Localization and Effects on the ER Ca^{2+}-Filling State. *Biochimica et Biophysica Acta (BBA) - Molecular Cell Research*, *1853*(9), 2104–2114. https://doi.org/10.1016/j.bbamcr.2015.03.002.

Liu, J. C., Liu, J., Holmström, K. M., Menazza, S., Parks, R. J., Fergusson, M. M., Yu, Z.-X., Springer, D. A., Halsey, C., Liu, C., Murphy, E., & Finkel, T. (2016). MICU1 Serves as a Molecular Gatekeeper to Prevent *in vivo* Mitochondrial Calcium Overload. *Cell Reports*, *16*(6), 1561–1573. https://doi.org/10.1016/j.celrep.2016.07.011.

Liu, T., Yang, N., Sidor, A., & O'Rourke, B. (2021). MCU Overexpression Rescues Inotropy and Reverses Heart Failure by Reducing SR Ca^{2+} Leak. *Circulation Research*, *128*(8), 1191–1204. https://doi.org/10.1161/CIRCRESAHA.120.318562.

Liu, T., Zhang, L., Joo, D., & Sun, S. C. (2017). NF-κB Signaling in Inflammation. *Signal Transduction and Targeted Therapy*, 2, 17023–. https://doi.org/10.1038/sigtrans.2017.23.

Liu, Y., Jin, M., Wang, Y., Zhu, J., Tan, R., Zhao, J., Ji, X., Jin, C., Jia, Y., Ren, T., & Xing, J. (2020). MCU-Induced Mitochondrial Calcium Uptake Promotes Mitochondrial Biogenesis and Colorectal Cancer Growth. *Signal Transduction and Targeted Therapy*, *5*, 59. https://doi.org/10.1038/s41392-020-0155-5.

Lodygin, D., & Flügel, A. (2017). Intravital Real-Time Analysis of T Cell Activation in Health and Disease. *Cell Calcium*, *64*, 118–129. https://doi.org/10.1016/j.ceca.2016.12.007.

Lodygin, D., Hermann, M., Schweingruber, N., Flügel-Koch, C., Watanabe, T., Schlosser, C., Merlini, A., Körner, H., Chang, H.-F., Fischer, H. J., Reichardt, H. M., Zagrebelsky, M., Mollenhauer, B., Kügler, S., Fitzner, D., Frahm, J., Stadelmann, C., Haberl, M., Odoardi, F., & Flügel, A. (2019). β-Synuclein-Reactive T Cells Induce Autoimmune CNS Grey Matter Degeneration. *Nature*, *566*(7745), 503–508. https://doi.org/10.1038/s41586-019-0964-2.

Lodygin, D., Odoardi, F., Schläger, C., Körner, H., Kitz, A., Nosov, M., van den Brandt, J., Reichardt, H. M., Haberl, M., & Flügel, A. (2013). A Combination of Fluorescent NFAT and H2B Sensors Uncovers Dynamics of T Cell Activation in Real Time During CNS Autoimmunity. *Nature Medicine*, *19*(6), 784–790. https://doi.org/10.1038/nm.3182.

Loma, I., & Heyman, R. (2011). Multiple Sclerosis: Pathogenesis and Treatment. *Current Neuropharmacology*, *9*(3), 409–416. https://doi.org/10.2174/157015911796557911.

Luckheeram, R. V., Zhou, R., Verma, A. D., & Xia, B. (2012). $CD4^+$T Cells: Differentiation and Functions. *Clinical and Developmental Immunology*, *2012*, 925135. https://doi.org/10.1155/2012/925135.

Macian, F. (2005). NFAT Proteins: Key Regulators of T-Cell Development and Function. *Nature Reviews Immunology*, *5*(6), 472–484. https://doi.org/10.1038/nri1632.

Macián, F., López-Rodríguez, C., & Rao, A. (2001). Partners in Transcription: NFAT and AP-1. *Oncogene*, *20*(19), 2476–2489. https://doi.org/10.1038/sj.onc.1204386.

Mahmood, T., & Yang, P.-C. (2012). Western Blot: Technique, Theory, and Trouble Shooting. *North American Journal of Medical Sciences*, *4*(9), 429–434. https://doi.org/10.4103/1947-2714.100998.

Mallilankaraman, K., Cárdenas, C., Doonan, P. J., Chandramoorthy, H. C., Irrinki, K. M., Golenár, T., Csordás, G., Madireddi, P., Yang, J., Müller, M., Miller, R., Kolesar, J. E., Molgó, J., Kaufman, B., Hajnóczky, G., Foskett, J. K., & Madesh, M. (2012). MCUR1 is an Essential Component of Mitochondrial Ca^{2+} Uptake that Regulates Cellular Aetabolism. *Nature Cell Biology*, *14*(12), 1336–1343. https://doi.org/10.1038/ncb2622.

Mammucari, C., Gherardi, G., Zamparo, I., Raffaello, A., Boncompagni, S., Chemello, F., Cagnin, S., Braga, A., Zanin, S., Pallafacchina, G., Zentilin, L., Sandri, M., De Stefani, D., Protasi, F., Lanfranchi, G., & Rizzuto, R. (2015). The Mitochondrial Calcium Uniporter Controls Skeletal Muscle Trophism *in vivo*. *Cell Reports*, *10*(8), 1269–1279. https://doi.org/10.1016/j.celrep.2015.01.056.

Marchi, S., Corricelli, M., Branchini, A., Vitto, V. A. M., Missiroli, S., Morciano, G., Perrone, M., Ferrarese, M., Giorgi, C., Pinotti, M., Galluzzi, L., Kroemer, G., & Pinton, P. (2019). Akt-Mediated Phosphorylation of MICU1 Regulates Mitochondrial Ca^{2+} Levels and Tumor Growth. *The European Molecular Biology Organization Journal*, *38*(2), e99435. https://doi.org/10.15252/embj.201899435.

Markowitz, D., Goff, S., & Bank, A. (1988). A Safe Packaging Line for Gene Transfer: Separating Viral Genes on Two Different Plasmids. *Journal of Virology*, *62*(4), 1120–1124. https://doi.org/10.1128/JVI.62.4.1120-1124.1988.

Matlib, M. A., Zhou, Z., Knight, S., Ahmed, S., Choi, K. M., Krause-Bauer, J., Phillips, R., Altschuld, R., Katsube, Y., Sperelakis, N., & Bers, D. M. (1998). Oxygen-bridged Dinuclear Ruthenium Amine Complex Specifically Inhibits Ca^{2+} Uptake into Mitochondria in Vitroand in Situ in Single Cardiac Myocytes. *Journal of Biological Chemistry*, *273*(17), 10223–10231. https://doi.org/10.1074/jbc.273.17.10223.

Matsumoto, H., Haniu, H., & Komori, N. (2019). Determination of Protein Molecular Weights on SDS-PAGE. *Methods in Molecular Biology*, 1855, 101–105. https://doi.org/10.1007/978-1-4939-8793-1_10.

Matza, D., Badou, A., Klemic, K. G., Stein, J., Govindarajulu, U., Nadler, M. J., Kinet, J.-P., Peled, A., Shapira, O. M., Kaczmarek, L. K., & Flavell, R. A. (2016). T Cell Receptor Mediated Calcium Entry Requires Alternatively Spliced Cav1.1 Channels. *Public Library of Science One*, *11*(1). https://doi.org/10.1371/journal.pone.0147379.

McComb, S. (2019). Introduction to the Immune System. In *Immunoproteomics: Methods in Molecular Biology*, *2024*. Springer. https://link.springer.com/protocol/10.1007/978-1-4939-9597-4_1.

Mercer, J. C., Dehaven, W. I., Smyth, J. T., Wedel, B., Boyles, R. R., Bird, G. S., & Putney, J. W., Jr (2006). Large Store-Operated Calcium Selective Currents due to Co-Expression of Orai1 or Orai2 with the Intracellular Calcium Sensor, Stim1. *The Journal of Biological Chemistry*, *281*(34), 24979–24990. https://doi.org/10.1074/jbc.M604589200.

Mergulis, L. (1970). *Origin of Eukaryotic Cells: Evidence and Research Implications for a Theory of the Origin and Evolution of Microbial, Plant and Animal Cells on the Precambrian Earth*. Yale University Press.

Mi, H., Muruganujan, A., Ebert, D., Huang, X., & Thomas, P. D. (2019). PANTHER version 14: More Genomes, a New PANTHER GO-slim and Improvements in Enrichment Analysis Tools. *Nucleic Acids Research*, *47*(D1), 419–426. https://doi.org/10.1093/nar/gky1038.

Mohtashami, M., Zarin, P., & Zúñiga-Pflücker, J. C. (2016). Induction of T Cell Development *in vitro* by Delta-Like (Dll)-Expressing Stromal Cells. *Methods in Molecular Biology*, *1323*, 159–167.

https://doi.org/10.1007/978-1-4939-2809-5_14.

Monaco, G., Lee, B., Xu, W., Mustafah, S., Hwang, Y. Y., Carré, C., Burdin, N., Visan, L., Ceccarelli, M., Poidinger, M., Zippelius, A., Pedro de Magalhães, J., & Larbi, A. (2019). RNA-Seq Signatures Normalized by mRNA Abundance Allow Absolute Deconvolution of Human Immune Cell Types. *Cell Reports*, *26*(6), 1627-1640.e7. https://doi.org/10.1016/j.celrep.2019.01.041.

Montero, M., Lobatón, C. D., Gutierrez-Fernández, S., Moreno, A., & Alvarez, J. (2003). Modulation of Histamine-Induced Ca^{2+} Release by Protein Kinase C. Effects on Cytosolic and Mitochondrial [Ca^{2+}] Peaks. *The Journal of Biological Chemistry*, *278*(50), 49972–49979. https://doi.org/10.1074/jbc.M308378200.

Murphy, M. P. (2009). How Mitochondria Produce Reactive Oxygen Species. *Biochemical Journal*, *417*(1), 1–13. https://doi.org/10.1042/BJ20081386.

Nagai, T., Sawano, A., Park, E. S., & Miyawaki, A. (2001). Circularly Permuted Green Fluorescent Proteins Engineered to Sense Ca^{2+}. *Proceedings of the National Academy of Sciences of the United States of America*, *98*(6), 3197–3202. https://doi.org/10.1073/pnas.051636098.

Nagy, G., Koncz, A., & Perl, A. (2003). T Cell Activation-Induced Mitochondrial Hyperpolarization Is Mediated by Ca^{2+}- and Redox-Dependent Production of Nitric Oxide. *Journal of Immunology*, *171*(10), 5188–5197.

Nakai, J., Ohkura, M., & Imoto, K. (2001). A High Signal-to-Noise Ca^{2+} Probe Composed of a Single Green Fluorescent Protein. *Nature Biotechnology*, *19*(2), 137–141. https://doi.org/10.1038/84397.

Nakayama, S., & Kretsinger, R. (1994). *Evolution of the EF-Hand Family of Proteins*. https://doi.org/10.1146/annurev.bb.23.060194.002353.

Nissim, T. B.-K., Zhang, X., Elazar, A., Roy, S., Stolwijk, J. A., Zhou, Y., Motiani, R. K., Gueguinou, M., Hempel, N., Hershfinkel, M., Gill, D. L., Trebak, M., & Sekler, I. (2017). Mitochondria Control Store-Operated Ca^{2+} Entry Through Na^{+} and Redox Signals. *The European Molecular Biology Organization Journal*, *36*(6), 797. https://doi.org/10.15252/embj.201592481.

Nunnari, J., & Suomalainen, A. (2012). Mitochondria: In Sickness and in Health. *Cell*, *148*(6), 1145–1159. https://doi.org/10.1016/j.cell.2012.02.035.

Odoardi, F., Sie, C., Streyl, K., Ulaganathan, V. K., Schläger, C., Lodygin, D., Heckelsmiller, K., Nietfeld, W., Ellwart, J., Klinkert, W. E., Lottaz, C., Nosov, M., Brinkmann, V., Spang, R., Lehrach, H., Vingron, M., Wekerle, H., Flügel-Koch, C., & Flügel, A. (2012). T Cells Become Licensed in the Lung to Enter the

Central Nervous System. *Nature*, *488*(7413), 675–679. https://doi.org/10.1038/nature11337.

O'Shea, J. J., Lahesmaa, R., Vahedi, G., Laurence, A., & Kanno, Y. (2011). Genomic Views of STAT Function in $CD4^+$ T Helper Cell Differentiation. *Nature Reviews Immunology*, *11*(4), 239–250. https://doi.org/10.1038/nri2958.

O-Uchi, J., Jhun, B. S., Xu, S., Hurst, S., Raffaello, A., Liu, X., Yi, B., Zhang, H., Gross, P., Mishra, J., Ainbinder, A., Kettlewell, S., Smith, G. L., Dirksen, R. T., Wang, W., Rizzuto, R., & Sheu, S.-S. (2014). Adrenergic Signaling Regulates Mitochondrial Ca^{2+} Uptake Through Pyk2-Dependent Tyrosine Phosphorylation of the Mitochondrial Ca^{2+} Uniporter. *Antioxidants and Redox Signaling*, *21*(6), 863–879. https://doi.org/10.1089/ars.2013.5394.

Overview of ELISA - DE. (n.d.). Retrieved July 13, 2022, from https://www.thermofisher.com/de/de/home/life-science/protein-biology/protein-biology-learning-center/protein-biology-resource-library/pierce-protein-methods/overview-elisa.html.

Pahl, K. (2022). Exploring the role of mitochondrial proteases in the metabolism of HeLa and $CD4^+$ T-cells. Unpublished Bachelor's Thesis.

Pan, X., Liu, J., Nguyen, T., Liu, C., Sun, J., Teng, Y., Fergusson, M. M., Rovira, I. I., Allen, M., Springer, D. A., Aponte, A. M., Gucek, M., Balaban, R. S., Murphy, E., & Finkel, T. (2013). The Physiological Role of Mitochondrial Calcium Revealed by Mice Lacking the Mitochondrial Calcium Uniporter (MCU). *Nature Cell Biology*, *15*(12), 1464–1472. https://doi.org/10.1038/ncb2868.

Park, J., Lee, Y., Park, T., Kang, J. Y., Mun, S., Jin, M., Yang, J., & Eom, S. H. (2020). Structure of the MICU1–MICU2 Heterodimer Provides Insights into the Gatekeeping Threshold Shift. *The International Union of Crystallography Journal*, *7*(2), 355–365. https://doi.org/10.1107/S2052252520001840.

Parker, I., & Smith, I. (2010). Recording Single-Channel Activity of Inositol Trisphosphate Receptors in Intact Cells with a Microscope, not a Patch Clamp. *Journal of General Physiology*, *136*(2), 119–127. https://doi.org/10.1085/jgp.200910390.

Parkin, J., & Cohen, B. (2001). *An Overview of the Immune System*. *357*(9270), 1777–1789. https://doi.org/10.1016/S0140-6736(00)04904-7.

Patron, M., Granatiero, V., Espino, J., Rizzuto, R., & De Stefani, D. (2019). MICU3 is a Tissue-Specific Enhancer of Mitochondrial Calcium Uptake. *Cell Death and Differentiation*, *26*(1), 179–195. https://doi.org/10.1038/s41418-018-0113-8.

Patron, M., Sprenger, H.-G., & Langer, T. (2018). m-AAA Proteases, Mitochondrial Calcium Homeostasis and

Neurodegeneration. *Cell Research*, *28*(3), 296–306. https://doi.org/10.1038/cr.2018.17.

Patron, M., Tarasenko, D., Nolte, H., Kroczek, L., Ghosh, M., Ohba, Y., Lasarzewski, Y., Ahmadi, Z. A., Cabrera-Orefice, A., Eyiama, A., Kellermann, T., Rugarli, E. I., Brandt, U., Meinecke, M., & Langer, T. (2022). Regulation of Mitochondrial Proteostasis by the Proton Gradient. *The European Molecular Biology Organization Journal*, *41*(16), e110476. https://doi.org/10.15252/embj.2021110476.

Paupe, V., Prudent, J., Dassa, E. P., Rendon, O. Z., & Shoubridge, E. A. (2015). CCDC90A (MCUR1) Is a Cytochrome c Oxidase Assembly Factor and Not a Regulator of the Mitochondrial Calcium Uniporter. *Cell Metabolism*, *21*(1), 109–116. https://doi.org/10.1016/j.cmet.2014.12.004.

Payne, R., Li, C., Fernandez-Garcia, E., Vais, H., & Foskett, K. (2019). The MCU Inhibitor Ds16570511 has Off-Target Effects on Mitochondrial Membrane Potential. *Biophysical Journal*, *116*(3, Supplement 1), 270a. https://doi.org/10.1016/j.bpj.2018.11.1461.

Peng, M., Yin, N., Chhangawala, S., Xu, K., Leslie, C. S., & Li, M. O. (2016). Aerobic Glycolysis Promotes T Helper 1 Cell Differentiation Through an Epigenetic Mechanism. *Science*, *354*(6311), 481–484. https://doi.org/10.1126/science.aaf6284.

Perocci, F., Gohil, V., Girgis, H., Bao, R., McCombs, J., Palmer, A., & Mootha, V. (2010). MICU1 Encodes a Mitochondrial EF Hand Protein Required for Ca^{2+} Uptake. *Nature*, *467*, 291–296. https://doi.org/10.1038/nature09358.

Persechini, A., Lynch, J. A., & Romoser, V. A. (1997). Novel Fluorescent Indicator Proteins for Monitoring Free Intracellular Ca^{2+}. *Cell Calcium*, *22*(3), 209–216. https://doi.org/10.1016/s0143-4160(97)90014-2.

Petrungaro, C., Zimmermann, K. M., Küttner, V., Fischer, M., Dengjel, J., Bogeski, I., & Riemer, J. (2015). The $Ca^{(2+)}$-Dependent Release of the Mia40-Induced MICU1-MICU2 Dimer from MCU Regulates Mitochondrial $Ca^{(2+)}$ Uptake. *Cell Metabolism*, *22*(4), 721–733. https://doi.org/10.1016/j.cmet.2015.08.019.

Phillips, D., Covian, R., Aponte, A. M., Glancy, B., Taylor, J. F., Chess, D., & Balaban, R. S. (2012). Regulation of Oxidative Phosphorylation Complex Activity: Effects of Tissue-Specific Metabolic Stress Within an Allometric Series and Acute Changes in Workload. *American Journal of Physiology-Regulatory, Integrative and Comparative Physiology*, *302*(9), 1034–1048. https://doi.org/10.1152/ajpregu.00596.2011.

Pierson, T. M., Adams, D., Bonn, F., Martinelli, P., Cherukuri, P. F., Teer, J. K., Hansen, N. F., Cruz, P., Mullikin For The Nisc Comparative Sequencing Program, J. C., Blakesley, R. W., Golas, G., Kwan, J., Sandler,

A., Fuentes Fajardo, K., Markello, T., Tifft, C., Blackstone, C., Rugarli, E. I., Langer, T., … Toro, C. (2011). Whole-Exome Sequencing Identifies Homozygous AFG3L2 Mutations in a Spastic Ataxia-Neuropathy Syndrome Linked to Mitochondrial m-AAA Proteases. *Public Library of Science Genetics*, *7*(10), e1002325. https://doi.org/10.1371/journal.pgen.1002325.

Pizzino, G., Irrera, N., Cucinotta, M., Pallio, G., Mannino, F., Arcoraci, V., Squadrito, F., Altavilla, D., & Bitto, A. (2017). Oxidative Stress: Harms and Benefits for Human Health. *Oxidative Medicine and Cellular Longevity*, *2017*, 8416763. https://doi.org/10.1155/2017/8416763.

Pozzan, T., & Rizzuto, R. (2000). The Renaissance of Mitochondrial Calcium Transport. *European Journal of Biochemistry*, *267*(17), 5269–5273. https://doi.org/10.1046/j.1432-1327.2000.01567.x.

Pozzan, T., & Rudolf, R. (2009). Measurements of Mitochondrial Calcium *in vivo*. *Biochimica et Biophysica Acta (BBA) - Bioenergetics*, *1787*(11), 1317–1323. https://doi.org/10.1016/j.bbabio.2008.11.012.

Prakriya, M., Feske, S., Gwack, Y., Srikanth, S., Rao, A., & Hogan, P. G. (2006). Orai1 is an Essential Pore Subunit of the CRAC Channel. *Nature*, *443*(7108), 230–233. https://doi.org/10.1038/nature05122.

Protasoni, M., & Zeviani, M. (2021). Mitochondrial Structure and Bioenergetics in Normal and Disease Conditions. *International Journal of Molecular Sciences*, *22*(2), 586. https://doi.org/10.3390/ijms22020586.

Putney, J. W. (1986). A model for Receptor-Regulated Calcium Entry. *Cell Calcium*, *7*(1), 1-12. https://doi.org/10.1016/0143-4160(86)90026-6.

Quintana, A., & Hoth, M. (2012). Mitochondrial Dynamics and Their Impact on T Cell Function. *Cell Calcium*, *52*(1), 57–63. https://doi.org/10.1016/j.ceca.2012.02.005.

Quintana, A., Griesmer, D., Schwarz, E., & Hoth, M. (2005). Calcium-Dependent Activation of T-Lymphocytes. *European Journal of Physiology*, *450*, 1–12. https://doi.org/10.1007/s00424-004-1364-4.

Quintana, A., Pasche, M., Junker, C., Al-Ansary, D., Rieger, H., Kummerow, C., Nuñez, L., Villalobos, C., Meraner, P., Becherer, U., Rettig, J., Niemeyer, B. A., & Hoth, M. (2011). Calcium Microdomains at the Immunological Synapse: How ORAI Channels, Mitochondria and Calcium pumps Generate Local Calcium Signals for Efficient T-Cell Activation. *The European Molecular Biology Organisation Journal*, *30*(19), 3895–3912. https://doi.org/10.1038/emboj.2011.289.

Quintana, A., Schwindling, C., Wenning, A. S., Becherer, U., Rettig, J., Schwarz, E. C., & Hoth, M. (2007). T Cell Activation Requires Mitochondrial Translocation to the Immunological Synapse. *Proceedings of the National Academy of Sciences of the United States of America*, *104*(36), 14418–14423.

https://doi.org/10.1073/pnas.0703126104.

Raffaello, A., De Stefani, D., Sabbadin, D., Teardo, E., Merli, G., Picard, A., Checchetto, V., Moro, S., Szabò, I., & Rizzuto, R. (2013). The Mitochondrial Calcium Uniporter is a Multimer that Can Include a Dominant-Negative Pore-Forming Subunit. *The European Molecular Biology Organisation Journal*, *32*(17), 2362–2376. https://doi.org/10.1038/emboj.2013.157.

Rahimmanesh, I., Totonchi, M., & Khanahmad, H. (2020). The Challenging Nature of Primary T Lymphocytes for Transfection: Effect of Protamine Sulfate on the Transfection Efficiency of Chemical Transfection Reagents. *Research in Pharmaceutical Sciences*, *15*(5), 437–446. https://doi.org/10.4103/1735-5362.297846.

Rasmussen, T. P., Wu, Y., Joiner, M. A., Koval, O. M., Wilson, N. R., Luczak, E. D., Wang, Q., Chen, B., Gao, Z., Zhu, Z., Wagner, B. A., Soto, J., McCormick, M. L., Kutschke, W., Weiss, R. M., Yu, L., Boudreau, R. L., Abel, E. D., Zhan, F., … Anderson, M. E. (2015). Inhibition of MCU Forces Extramitochondrial Adaptations Governing Physiological and Pathological Stress Responses in Heart. *Proceedings of the National Academy of Sciences of the United States of America*, *112*(29), 9129–9134. https://doi.org/10.1073/pnas.1504705112.

Rudolf, R., Mongillo, M., Magalhães, P. J., & Pozzan, T. (2004). *In vivo* Monitoring of Ca^{2+} Uptake into Mitochondria of Mouse Skeletal Muscle During Contraction. *The Journal of Cell Biology*, *166*(4), 527–536. https://doi.org/10.1083/jcb.200403102.

Salam, N., Rane, S., Das, R., Faulkner, M., Gund, R., Kandpal, U., Lewis, V., Mattoo, H., Prabhu, S., Ranganathan, V., Durdik, J., George, A., Rath, S., & Bal, V. (2013). T Cell Ageing: Effects of Age on Development, Survival & Function. *The Indian Journal of Medical Research*, *138*(5), 595–608.

Samanta, K., Douglas, S., & Parekh, A. B. (2014). Mitochondrial Calcium Uniporter MCU Supports Cytoplasmic Ca^{2+} Oscillations, Store-Operated Ca^{2+} Entry and Ca^{2+}-Dependent Gene Expression in Response to Receptor Stimulation. *Public Libraary of Science One*, *9*(7), e101188. https://doi.org/10.1371/journal.pone.0101188.

Samet, J. M., & Wages, P. A. (2018). Oxidative Stress from Environmental Exposures. *Current Opinion in Toxicology*, *7*, 60–66.

Sancak, Y., Markhard, A. L., Kitami, T., Kovács-Bogdán, E., Kamer, K. J., Udeshi, N. D., Carr, S. A., Chaudhuri, D., Clapham, D. E., Li, A. A., Calvo, S. E., Goldberger, O., & Mootha, V. K. (2013). EMRE is an Essential Component of the Mitochondrial Calcium Uniporter Complex. *Science*, *342*(6164), 1379–

1382. https://doi.org/10.1126/science.1242993.

Sanchez-Collado, J., Jardin, I., López, J. J., Ronco, V., Salido, G. M., Dubois, C., Prevarskaya, N., & Rosado, J. A. (2021). Role of Orai3 in the Pathophysiology of Cancer. *International Journal of Molecular Sciences*, *22*(21). https://doi.org/10.3390/ijms222111426.

Sato, T.K., Kawano, S. & Endo, T. Role of the Membrane Potential in Mitochondrial Protein Unfolding and Import. *Scientific Reports*, 9, 7637 (2019). https://doi.org/10.1038/s41598-019-44152-z.

Saul, S., Gibhardt, C. S., Schmidt, B., Lis, A., Pasieka, B., Conrad, D., Jung, P., Gaupp, R., Wonnenberg, B., Diler, E., Stanisz, H., Vogt, T., Schwarz, E. C., Bischoff, M., Herrmann, M., Tschernig, T., Kappl, R., Rieger, H., Niemeyer, B. A., & Bogeski, I. (2016). A Calcium-Redox Feedback Loop Controls Human Monocyte Immune Responses: The Role of ORAI Ca^{2+} Channels. *Science Signaling*, *9*(418), 26. https://doi.org/10.1126/scisignal.aaf1639.

Scharping, N. E., Rivadeneira, D. B., Menk, A. V., Vignali, P. D. A., Ford, B. R., Rittenhouse, N. L., Peralta, R., Wang, Y., Wang, Y., DePeaux, K., Poholek, A. C., & Delgoffe, G. M. (2021). Mitochondrial Stress Induced by Continuous Stimulation Under Hypoxia Rapidly Drives T Cell Exhaustion. *Nature Immunology*, *22*(2), 205–215. https://doi.org/10.1038/s41590-020-00834-9.

Selwyn, M., Dawson, A., & Dunnet, S. (1970). Calcium Transport in Mitochondria. *Federation of European Biochemical Societies Letters*, *10*(1), 1–5.

Sena, L. A., Li, S., Jairaman, A., Prakriya, M., Ezponda, T., Hildeman, D. A., Wang, C.-R., Schumacker, P. T., Licht, J. D., Perlman, H., Bryce, P. J., & Chandel, N. S. (2013). Mitochondria are Required for Antigen-Specific T Cell Activation Through Reactive Oxygen Species Signaling. *Immunity*, *38*(2), 225–236. https://doi.org/10.1016/j.immuni.2012.10.020.

Shah, K., Al-Haidari, A., Sun, J., & Kazi, J. U. (2021). T Cell Receptor (TCR) Signaling in Health and Disease. *Signal Transduction and Targeted Therapy*, *6*(1), 1–26. https://doi.org/10.1038/s41392-021-00823-w.

Shanmughapriya, S., Rajan, S., Hoffman, N. E., Zhang, X., Guo, S., Kolesar, J. E., Hines, K. J., Ragheb, J., Jog, N. R., Caricchio, R., Baba, Y., Zhou, Y., Kaufman, B., Cheung, J. Y., Kurosaki, T., Gill, D. L., & Madesh, M. (2015). Ca^{2+} Signals Regulate Mitochondrial Metabolism by Stimulating CREB-Mediated Expression of the Mitochondrial Ca^{2+} Uniporter Gene *mcu*. *Science Signaling*, *8*(366), 23. https://doi.org/10.1126/scisignal.2005673.

Shaw, J., Utz, P., Durand, D., Toole, J., Emmel, E., & Crabtree, G. (1988). Identification of a Putative Regulator of Early T Cell Activation Genes. *Science*, *241*(4862). https://doi.org/10.1126/science.3260404.

Sherman, B. T., Hao, M., Qiu, J., Jiao, X., Baseler, M. W., Lane, H. C., Imamichi, T., & Chang, W. (2022). DAVID: A Web Server for Functional Enrichment Analysis and Functional Annotation of Gene Lists (2021 update). *Nucleic Acids Research*, *50*(1), 216–221. https://doi.org/10.1093/nar/gkac194.

Shumanska, M. (2019). Differentiation-Induced Reorganization of the Mitochondrial Calcium Uniporter Complex in $CD4^+$ T-Cells. Unpublished Master's Thesis.

Siemoni, L., & Bogeski, I. (2015). Redox Regulation of T-Cell Receptor Signaling. *Biological Chemistry*, *396*(5), 555–569. https://doi.org/10.1515/hsz-2014-0312.

Sies, H. (2015). Oxidative Stress: A Concept in Redox Biology and Medicine. *Redox Biology*, *4*, 180–183. https://doi.org/10.1016/j.redox.2015.01.002.

Silverstein, A. (2009). *A History of Immunology* (2nd ed.). Academic Press.

Silverthorn, D. U. (2016). *Human Physiology* (7th ed.). Pearson Education.

Sivandzade, F., Bhalerao, A., & Cucullo, L. (2019). Analysis of the Mitochondrial Membrane Potential Using the Cationic JC-1 Dyeas a Sensitive Fluorescent Probe. *Bio-Protocol*, *9*(1), e3128. https://doi.org/10.21769/BioProtoc.3128.

Soboloff, J., Rothberg, B. S., Madesh, M., & Gill, D. L. (2012). STIM Proteins: Dynamic Calcium Signal Transducers. *Nature Reviews. Molecular Cell Biology*, *13*(9), 549. https://doi.org/10.1038/nrm3414.

Soman, S. K., Bazała, M., Keatinge, M., Bandmann, O., & Kuznicki, J. (2019). Restriction of Mitochondrial Calcium Overload by *mcu* Inactivation Renders a Neuroprotective Effect in Zebrafish Models of Parkinson's Disease. *Biology Open*, *8*(10), bio044347. https://doi.org/10.1242/bio.044347.

Soria Lopez, J. A., González, H. M., & Léger, G. C. (2019). Alzheimer's Disease. *Handbook of Clinical Neurology*, 167, 231–255. https://doi.org/10.1016/B978-0-12-804766-8.00013-3.

Stathopulos, P., Zheng, L., Li, G.-Y., Plevin, M., & Ikura, M. (2008). Structural and Mechanistic Insights into STIM1-Mediated Initiation of Store-Operated Calcium Entry. *Cell*, *135*(1), 110–122. https://doi.org/10.1016/j.cell.2008.08.006.

Stejerean-Todoran, I., Zimmermann, K., Gibhardt, C., Vultur, A., Ickes, C., Shannan, B., Bonilla del Rio, Z., Wölling, A., Cappello, S., Sung, H.-M., Shumanska, M., Zhang, X., Nanadikar, M., Latif, M., Wittek, A., Lange, F., Waters, A., Brafford, P., Wilting, J., … Bogeski, I. (2022). MCU Controls Melanoma Progression Through a Redox-Controlled Phenotype Switch. *European Molecular Biology Organisation Reports*. http://doi.org/10.15252/embr.202254746.

Suzuki, J., Kanemaru, K., & Iino, M. (2016). Genetically Encoded Fluorescent Indicators for Organellar Calcium

Imaging. *Biophysical Journal*, *111*(6), 1119–1131. https://doi.org/10.1016/j.bpj.2016.04.054.

Takahashi, A., Camacho, P., Lechleiter, J. D., & Herman, B. (1999). Measurement of Intracellular Calcium. *Physiological Reviews*, *79*(4), 1089–1125. https://doi.org/10.1152/physrev.1999.79.4.1089.

Taylor, R. W., & Turnbull, D. M. (2005). Mitochondrial DNA Mutations in Human Disease. *Nature Reviews Genetics*, *6*(5), 389–402. https://doi.org/10.1038/nrg1606.

Thestrup, T., Litzlbauer, J., Bartholomäus, I., Mues, M., Russo, L., Dana, H., Kovalchuk, Y., Liang, Y., Kalamakis, G., Laukat, Y., Becker, S., Witte, G., Geiger, A., Allen, T., Rome, L. C., Chen, T.-W., Kim, D. S., Garaschuk, O., Griesinger, C., & Griesbeck, O. (2014). Optimized Ratiometric Calcium Sensors for Functional *in vivo* Imaging of Neurons and T Lymphocytes. *Nature Methods*, *11*(2), 175–182. https://doi.org/10.1038/nmeth.2773.

Thompson, J. L., Mignen, O., & Shuttleworth, T. J. (2010). The N-Terminal Domain of Orai3 Determines Selectivity for Activation of the Store-Independent ARC Channel by Arachidonic Acid. *Channels*, *4*(5), 398. https://doi.org/10.4161/chan.4.5.13226.

Tilokani, L., Nagashima, S., Paupe, V., & Prudent, J. (2018). Mitochondrial Dynamics: Overview of Molecular Mechanisms. *Essays in Biochemistry*, *62*(3), 341–360. https://doi.org/10.1042/EBC20170104.

Trebak, M., & Kinet, J. P. (2019). Calcium Signalling in T Cells. *Nature Reviews Immunology*, *19*(3), 154. https://doi.org/10.1038/s41577-018-0110-7.

Tsai, C.-W., Wu, Y., Pao, P.-C., Phillips, C. B., Williams, C., Miller, C., Ranaghan, M., & Tsai, M.-F. (2017). Proteolytic Control of the Mitochondrial Calcium Uniporter Complex. *Proceedings of the National Academy of Sciences of the United States of America*, *114*(17), 4388–4393. https://doi.org/10.1073/pnas.1702938114.

Tsao, C. C., Teh, B. T., Jonasch, E., Shreiber-Agus, N., Efstathiou, E., Hoang, A., Czerniak, P. B., Logothetis, C., & Corn, P. G. (2008). Inhibition of Mxi1 Suppresses HIF-2α-Dependent Renal Cancer Tumorigenesis. *Cancer Biology and Therapy*, *7*(10), 1619–1627. https://doi.org/10.4161/cbt.7.10.6583.

Tsien, R. Y., Pozzan, T., & Rink, T. J. (1982). Calcium Homeostasis in Intact Lymphocytes: Cytoplasmic Free Calcium Monitored with a New, Intracellularly Trapped Fluorescent Indicator. *Journal of Cell Biology*, *94*(2), 325–334. https://doi.org/10.1083/jcb.94.2.325.

Uhlén, M., Fagerberg, L., Hallström, B. M., Lindskog, C., Oksvold, P., Mardinoglu, A., Sivertsson, Å., Kampf, C., Sjöstedt, E., Asplund, A., Olsson, I., Edlund, K., Lundberg, E., Navani, S., Szigyarto, C. A., Odeberg, J., Djureinovic, D., Takanen, J. O., Hober, S., Alm, T., … Pontén, F. (2015). Proteomics. Tissue-Based

Map of the Human Proteome. *Science*, *347*(6220), 1260419. https://doi.org/10.1126/science.1260419.

Uzhachenko, R., Shanker, A., & Dupont, G. (2016). Computational Properties of Mitochondria in T Cell Activation and Fate. *Open Biology*, *6*(11), 160192. https://doi.org/10.1098/rsob.160192.

Vaeth, M., Yang, J., Yamashita, M., Zee, I., Eckstein, M., Knosp, C., Kaufmann, U., Jani, P. K., Lacruz, R. S., Flockerzi, V., Kacskovics, I., Prakriya, M., & Feske, S. (2017). ORAI2 Modulates Store-Operated Calcium Entry and T Cell-Mediated Immunity. *Nature Communications*, *8*. https://doi.org/10.1038/ncomms14714.

Van der Windt, G. J. W., & Pearce, E. L. (2012). Metabolic Switching and Fuel Choice During T-Cell Differentiation and Memory Development. *Immunological Reviews*, *249*(1), 27–42. https://doi.org/10.1111/j.1600-065X.2012.01150.x.

Van Rossum, G. (1995). Python tutorial, Technical Report CS-R9526. *Centrum Voor Wiskunde En Informatica (CWI), Amsterdam*.

Ventura-Clapier, R., Moulin, M., Piquereau, J., Lemaire, C., Mericskay, M., Veksler, V., & Garnier, A. (2017). Mitochondria: A Central Target for Sex Differences in Pathologies. *Clinical Science*, *131*(9), 803–822. https://doi.org/10.1042/CS20160485.

Venugopal, A., Iyer, M., Balasubramanian, V., & Vellingiri, B. (2020). Mitochondrial Calcium Uniporter as a Potential Therapeutic Strategy for Alzheimer's Disease. *Acta Neuropsychiatrica*, *32*(2), 65–71. https://doi.org/10.1017/neu.2019.39.

Vig, M., Peinelt, C., Beck, A., Koomoa, D. L., Rabah, D., Koblan-Huberson, M., Kraft, S., Turner, H., Fleig, A., Penner, R., & Kinet, J.-P. (2006). CRACM1 Is a Plasma Membrane Protein Essential for Store-Operated Ca^{2+} Entry. *Science*, *312*(5777). https://doi.org/10.1126/science.1127883.

Vultur, A., Gibhardt, C. S., Stanisz, H., & Bogeski, I. (2018). The Role of the Mitochondrial Calcium Uniporter (MCU) Complex in Cancer. *European Journal of Physiology*, *470*(8), 1149–1163. https://doi.org/10.1007/s00424-018-2162-8.

Wang, F., Zhang, D., Zhang, D., Li, P., & Gao, Y. (2021). Mitochondrial Protein Translation: Emerging Roles and Clinical Significance in Disease. *Frontiers in Cell and Developmental Biology*, 9, 675465. https://doi.org/10.3389/fcell.2021.675465.

Wang, G., Zhao, L., Jiang, M., Tian, T., Mei, Y., Fu, G., & Zhou, N. (2022). Effects of MCU Mediated Ca^{2+} Homeostasis on Ovarian Cancer Cell SKOV3 Proliferation, Migration and Transforming. *Current Molecular Medicine*. https://doi.org/10.2174/1566524022666220617143754.

Wang, H., Zhang, X., Xue, L., Xing, J., Jouvin, M.-H., Putney, J. W., Anderson, M. P., Trebak, M., & Kinet, J.-P. (2016). Low Voltage-Activated CaV3.1 Calcium Channels in T Cells: A Role in Shaping the Immune Response. *Immunity*, *44*(4), 782. https://doi.org/10.1016/j.immuni.2016.01.015.

Wang, L., Yuan, L., Zeng, X., Peng, J., Ni, Y., Er, J. C., Xu, W., Agrawalla, B. K., Su, D., Kim, B., & Chang, Y.-T. (2016). A Multisite-Binding Switchable Fluorescent Probe for Monitoring Mitochondrial ATP Level Fluctuation in Live Cells. *Angewandte Chemie*, *55*(5), 1773–1776. https://doi.org/10.1002/anie.201510003.

Wang, Y., Tao, A., Vaeth, M., & Feske, S. (2020). Calcium Regulation of T-cell Metabolism. *Current Opinion in Physiology*, *17*, 207–223. https://doi.org/10.1016/j.cophys.2020.07.016.

Weiss, A., Imboden, J., Shoback, D., & Stobo, J. (1984). Role of T3 Surface Molecules in Human T-Cell Activation: T3-Dependent Activation Results in an Increase in Cytoplasmic Free Calcium. *Proceedings of the National Academy of Sciences of the United States of America*, *81*(13), 4169. https://doi.org/10.1073/pnas.81.13.4169.

Whitaker, M. (2010). Genetically-Encoded Probes for Measurement of Intracellular Calcium. *Methods in Cell Biology*, *99*, 153–182. https://doi.org/10.1016/B978-0-12-374841-6.00006-2.

Woods, J. J., & Wilson, J. J. (2020). Inhibitors of the mitochondrial calcium uniporter for the treatment of disease. *Current Opinion in Chemical Biology*, *55*, 9–18. https://doi.org/10.1016/j.cbpa.2019.11.006.

Woods, J. J., Lovett, J., Lai, B., Harris, H. H., & Wilson, J. J. (2020). Redox Stability Controls the Cellular Uptake and Activity of Ruthenium-Based Inhibitors of the Mitochondrial Calcium Uniporter (MCU). *Angewandte Chemie International Edition*, *59*(16), 6482–6491. https://doi.org/10.1002/anie.202000247.

Wu, H., Brand, B., Eckstein, M., Hochrein, S. M., Shumanska, M., Dudek, J., Nickel, A., Maack, C., Bogeski, I., & Vaeth, M. (2021). Genetic Ablation of the Mitochondrial Calcium Uniporter (MCU) Does not Impair T Cell-Mediated Immunity *In Vivo*. *Frontiers in Pharmacology*, *12*. https://www.frontiersin.org/articles/10.3389/fphar.2021.734078.

Xing, Y., Wang, M., Wang, J., Nie, Z., Wu, G., Yang, X., & Shen, Y. (2019). Dimerization of MICU Proteins Controls Ca^{2+} Influx through the Mitochondrial Ca^{2+} Uniporter. *Cell Reports*, *26*(5), 1203-1212.e4. https://doi.org/10.1016/j.celrep.2019.01.022.

Xue, Q., Pei, H., Liu, Q., Zhao, M., Sun, J., Gao, E., Ma, X., & Tao, L. (2017). MICU1 Protects Against Myocardial Ischemia/Reperfusion Injury and its Control by the Importer Receptor Tom70. *Cell Death and Disease*, *8*(7), e2923. https://doi.org/10.1038/cddis.2017.280.

Yapa, N. M. B., Lisnyak, V., Reljic, B., & Ryan, M. T. (2021). Mitochondrial Dynamics in Health and Disease. *Federation of European Biochemical Societies Letters*, *595*(8), 1184–1204. https://doi.org/10.1002/1873-3468.14077.

Yoast, R. E., Emrich, S. M., Zhang, X., Xin, P., Arige, V., Pathak, T., Benson, J. C., Johnson, M. T., Abdelnaby, A. E., Lakomski, N., Hempel, N., Han, J. M., Dupont, G., Yule, D. I., Sneyd, J., & Trebak, M. (2021). The Mitochondrial Ca^{2+} Uniporter is a Central Regulator of Interorganellar Ca^{2+} Transfer and NFAT Activation. *The Journal of Biological Chemistry*, *297*(4), 101174. https://doi.org/10.1016/j.jbc.2021.101174.

Yousefi, R., Fornasiero, E., Cyganek, L., Montoya, J., Jakobs, S., Rizzoli, S., Rehling, P., & Pacheu-Grau, D. (2021). Monitoring Mitochondrial Translation in Living Cells. *European Molecular Biology Organisation Reports*, *22*(4), e51635. https://doi.org/10.15252/embr.202051635.

Zhang, D., Redington, E., & Gong, Y. (2021). Rational Engineering of Ratiometric Calcium Sensors with Bright Green and Red Fluorescent Proteins. *Communications Biology*, *4*(1), 1–12. https://doi.org/10.1038/s42003-021-02452-z.

Zhang, K., Yan, J., Wang, L., Tian, X., Zhang, T., Guo, L., Li, B., Wang, W., & Liu, X. (2018). The Pyk2/MCU Pathway in the Rat Middle Cerebral Artery Occlusion Model of Ischemic Stroke. *Neuroscience Research*, *131*, 52–62. https://doi.org/10.1016/j.neures.2017.09.002.

Zhang, L., Dietsche, F., Seitaj, B., Rojas-Charry, L., Latchman, N., Tomar, D., Wüst, R. C., Nickel, A., Frauenknecht, K. B., Schoser, B., Schumann, S., Schmeisser, M. J., Vom Berg, J., Buch, T., Finger, S., Wenzel, P., Maack, C., Elrod, J. W., Parys, J. B., Bultynck, G., … Methner, A. (2022). TMBIM5 Loss of Function Alters Mitochondrial Matrix Ion Homeostasis and Causes a Skeletal Myopathy. *Life Science Alliance*, *5*(10), e202201478. https://doi.org/10.26508/lsa.202201478.

Zhang, S. L., Yeromin, A. V., Hu, J., Amcheslavsky, A., Zheng, H., & Cahalan, M. D. (2011). Mutations in Orai1 Transmembrane Segment 1 Cause STIM1-Independent Activation of Orai1 Channels at Glycine 98 and Channel Closure at Arginine 91. *Proceedings of the National Academy of Sciences of the United States of America*, *108*(43), 17838–17843. https://doi.org/10.1073/pnas.1114821108.

Zhang, Z., Qiu, S., Zhang, X., & Chen, W. (2018). Optimized DNA Electroporation for Primary Human T Cell Engineering. *BMC biotechnology*, *18*(1), 4. https://doi.org/10.1186/s12896-018-0419-0.

Zhao, Z., Ukidve, A., Kim, J., & Mitragotri, S. (2020). Targeting Strategies for Tissue-Specific Drug Delivery. *Cell*, *181*(1), 151–167. https://doi.org/10.1016/j.cell.2020.02.001.

Zhou, B., & Tian, R. (2018). Mitochondrial Dysfunction in Pathophysiology of Heart Failure. *The Journal of Clinical Investigation*, *128*(9), 3716–3726. https://doi.org/10.1172/JCI120849.

Zhu, J., & Paul, W. E. (2008). CD4 T Cells: Fates, Functions, and Faults. *Blood*, *112*(5), 1557–1569. https://doi.org/10.1182/blood-2008-05-078154.

Zitt, C., Strauss, B., Schwarz, E., Spaeth, N., Rast, G., Hatzelmann, A., & Hoth, M. (2004). Potent Inhibition of Ca^{2+} Release-activated Ca^{2+} Channels and T-lymphocyte Activation by the Pyrazole Derivative BTP2. *Journal of Biological Chemistry*, *279*(13), 12427–12437. https://doi.org/10.1074/jbc.M309297200.

Zorova, L. D., Popkov, V. A., Plotnikov, E. Y., Silachev, D. N., Pevzner, I. B., Jankauskas, S. S., Babenko, V. A., Zorov, S. D., Balakireva, A. V., Juhaszova, M., Sollott, S. J., & Zorov, D. B. (2018). Mitochondrial Membrane Potential. *Analytical Biochemistry*, *552*, 50–59. https://doi.org/10.1016/j.ab.2017.07.009.

Zúñiga-Pflücker, J. C. (2004). T-cell Development Made Simple. *Nature Reviews Immunology*, *4*(1), 67–72. https://doi.org/10.1038/nri1257.

7. Appendix

7.1 Supplementary Figures

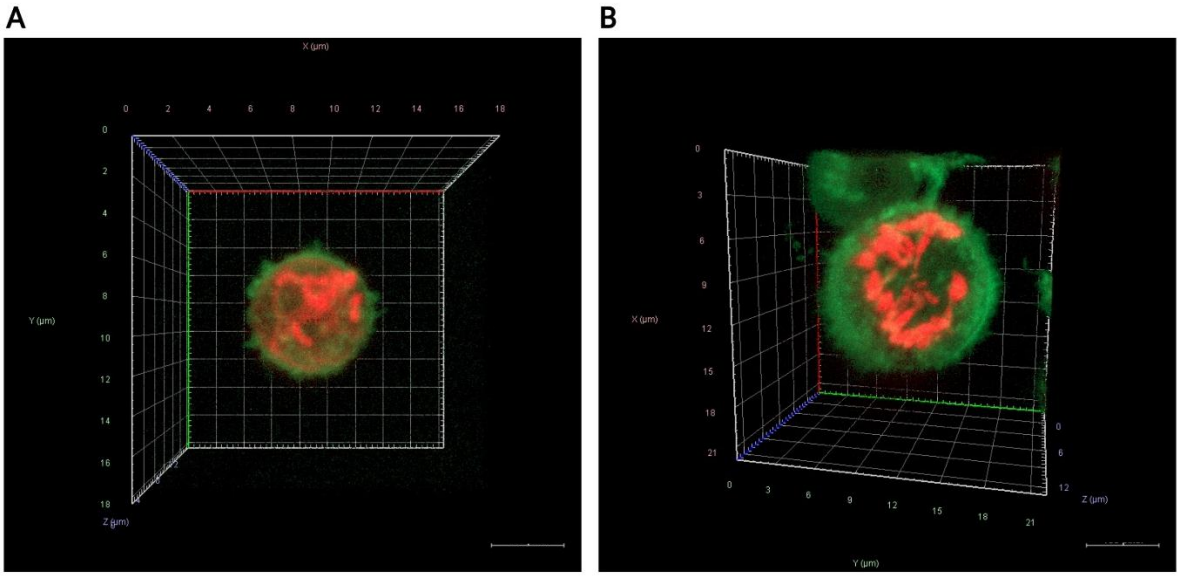

S Figure 1. 3D structure of a naive (A) and an effector (B) CD4$^+$ T-cell. Plasma membrane was stained with CellMask Green and mitochondria with MitoTracker Deep red. Scale bar: 100 pixels; magnification: 63x gly (N. A 1.73). Grid: brown line = x-axis (µm); green line = y-axis (µm); purple line = z-axis (µm). Images were obtained and processed with Zen 3.5 software (Zeiss).

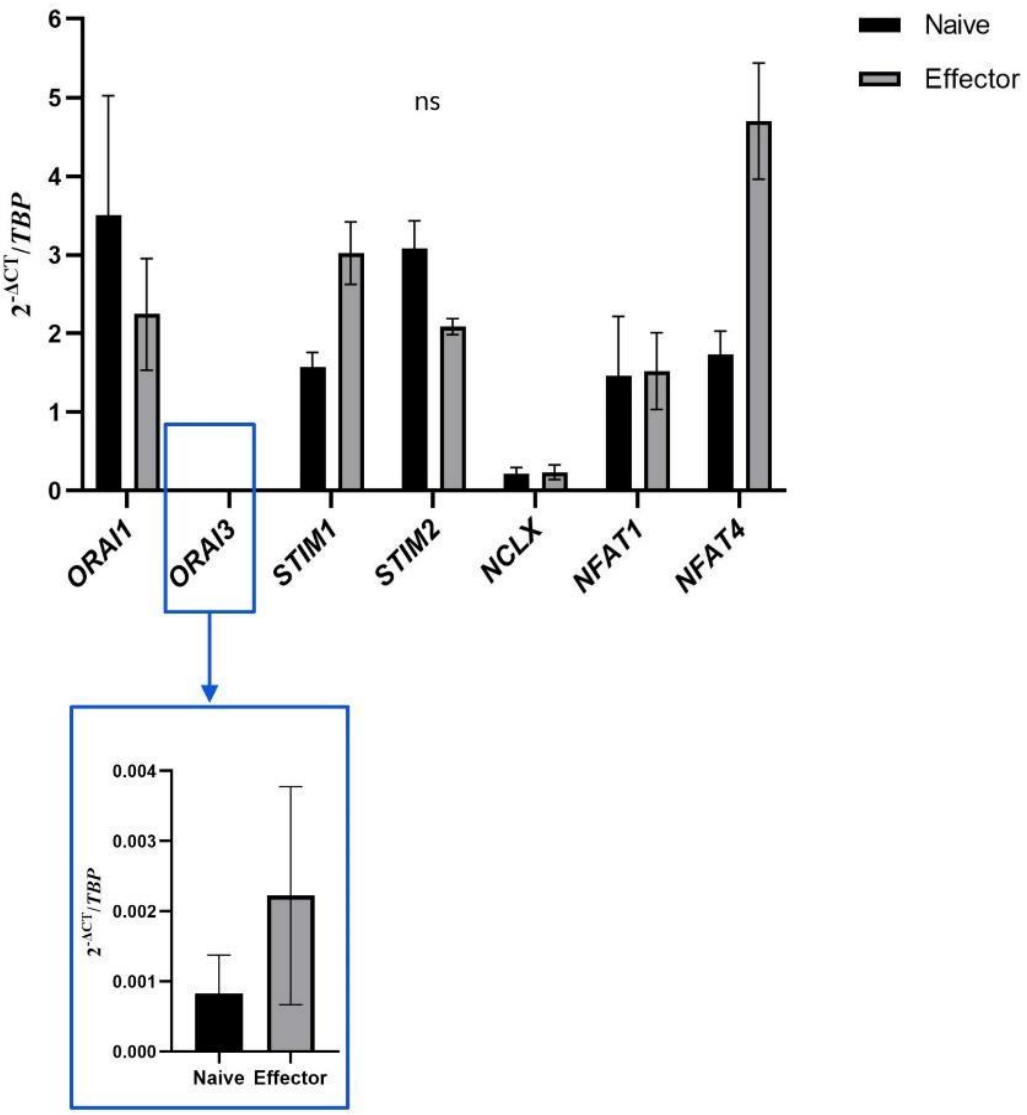

S Figure 2. TCR stimulation induces an increase in expression of multiple genes related to Ca^{2+} signalling, especially NFAT proteins. Quantification is representative of naive and effector cells from 3 different donors/biological replicates (2 technical replicates and a negative water control). Gene expression is normalised to HK gene *TBP*. Data are represented as mean ± SEM. ns-not statistically significant; assessed by two-tailed paired Student's t-test.

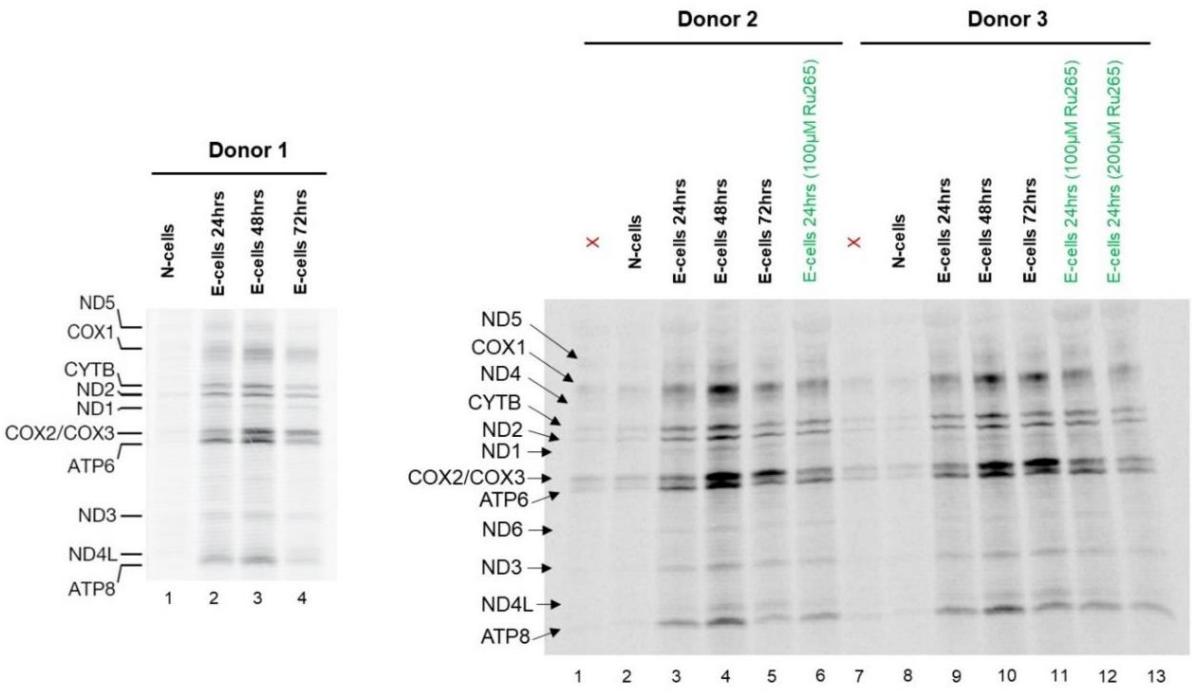

S Figure 3. Mitochondrial protein translation ^{35}S labelling showed significantly increased translation peaking 48 hrs after TCR stimulation. Effector cells treated with Ru265 for 24 hrs are labelled with green. Pharmacological MCU inhibition mildly reduced mitochondrial protein translation, visible after treatment with 200 µM of Ru265 (lane 13, donor 3). X=empty lane; N=Naive; E=Effector. Labelling experiment and gel visualisation was performed by Dr. Sven Dennerlein.

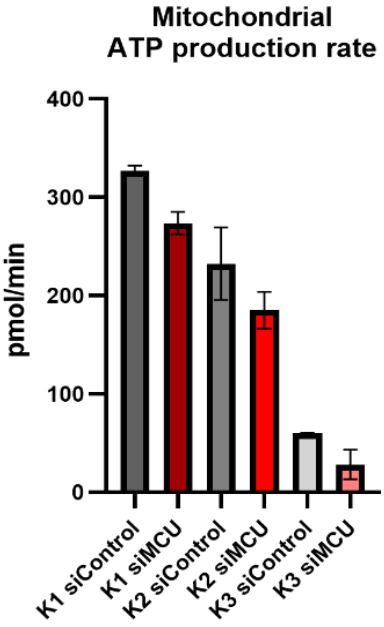

S Figure 4. Reduced mitochondrial ATP production rates assessed in 3 separate donors (K1, K2, K3) upon MCUa downregulation. Variability between the donors was visible. The experiment included 3 technical replicates. Data are represented as mean ± SEM.

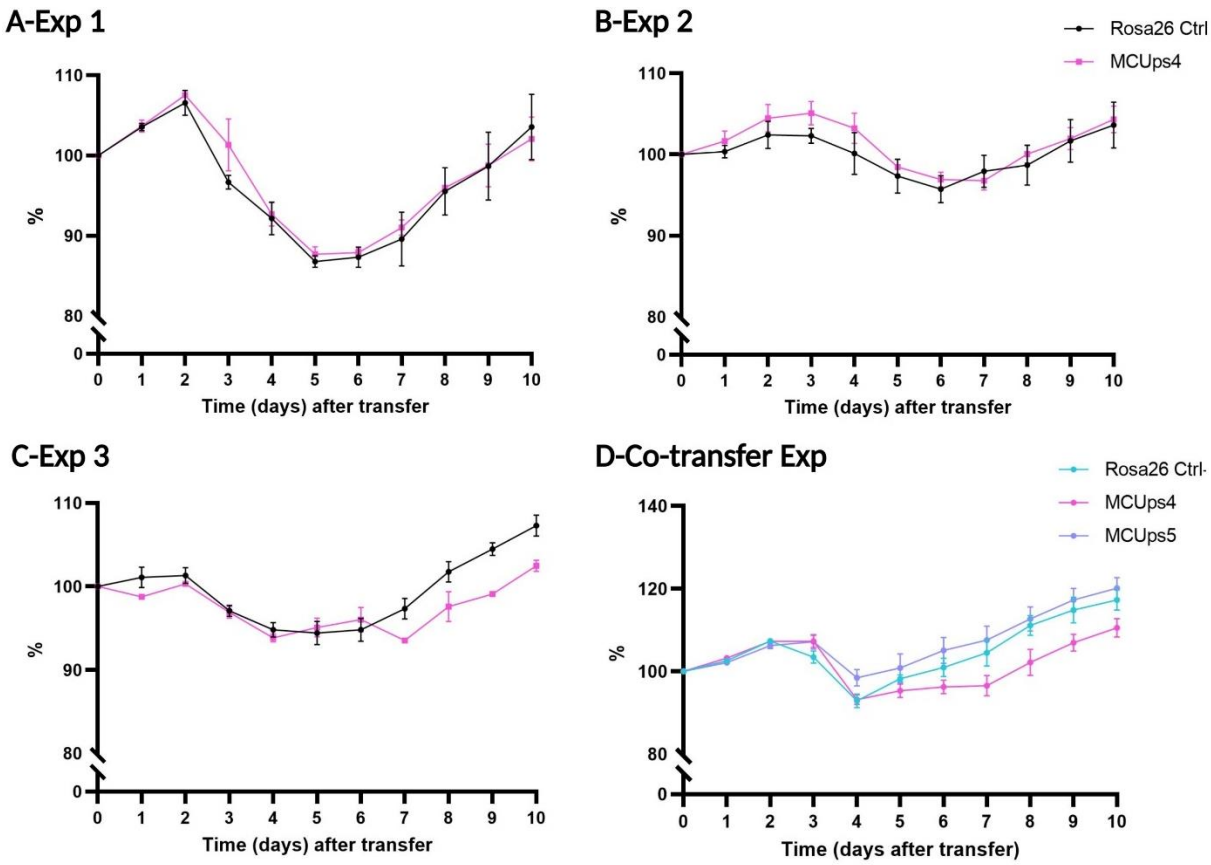

S Figure 5. EAE onset can cause small weight changes in animals; this can be observed at days 5 and 6 in (A) and is less obvious in (B), (C) and (D). Nevertheless, no significant difference was observed between animals injected with control cells and animals injected with MCUa$_{KD}$ cells. Measurements in panel (**A**) show an average of 3 rats/biological replicates per group, in panel (**B**) of 4 rats/biological replicates per group, in panel (**C**) of 3 Rosa 26 control and 2 MCUps4 rats/biological replicates, and in panel (**D-Co-transfer**) of 3 rats/biological replicates per group. Data are represented as mean ± SEM. Exp=Experiment.

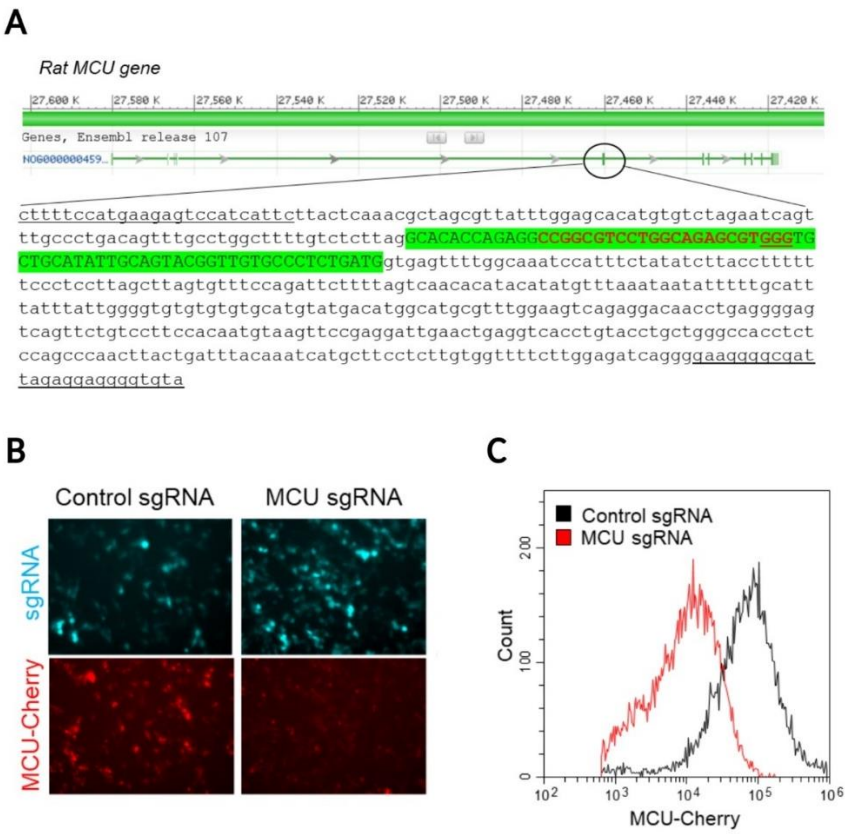

S Figure 6. Targeted editing of the rat *MCUa* gene (CRISPR Cas9). A schematic view (**A**) of the rat *MCUa* genomic structure (sequence extracted from the NCBI Gene database). Vertical bars indicate exons. A sequence around the coding exon 2 (capital letters shaded in green) and flanking intronic regions (small letters) are indicated, as an example for guide RNA design for MCUps4. PS4 and its protospacer adjacent motif (PAM) are given in red. Primers used for the T7E assay are underlined. Targeting efficiency of the designed sgRNAs was tested in HEK293 cells with a co-transfection experiment (**B-C**). Reduction of mCherry fluorescence confirmed gene editing, determined by fluorescent microscopy (**B**) and flow cytometry (**C**). Experiments shown in (**B**) and (**C**) were performed and analysed by Dr. Dmitri Lodygin.

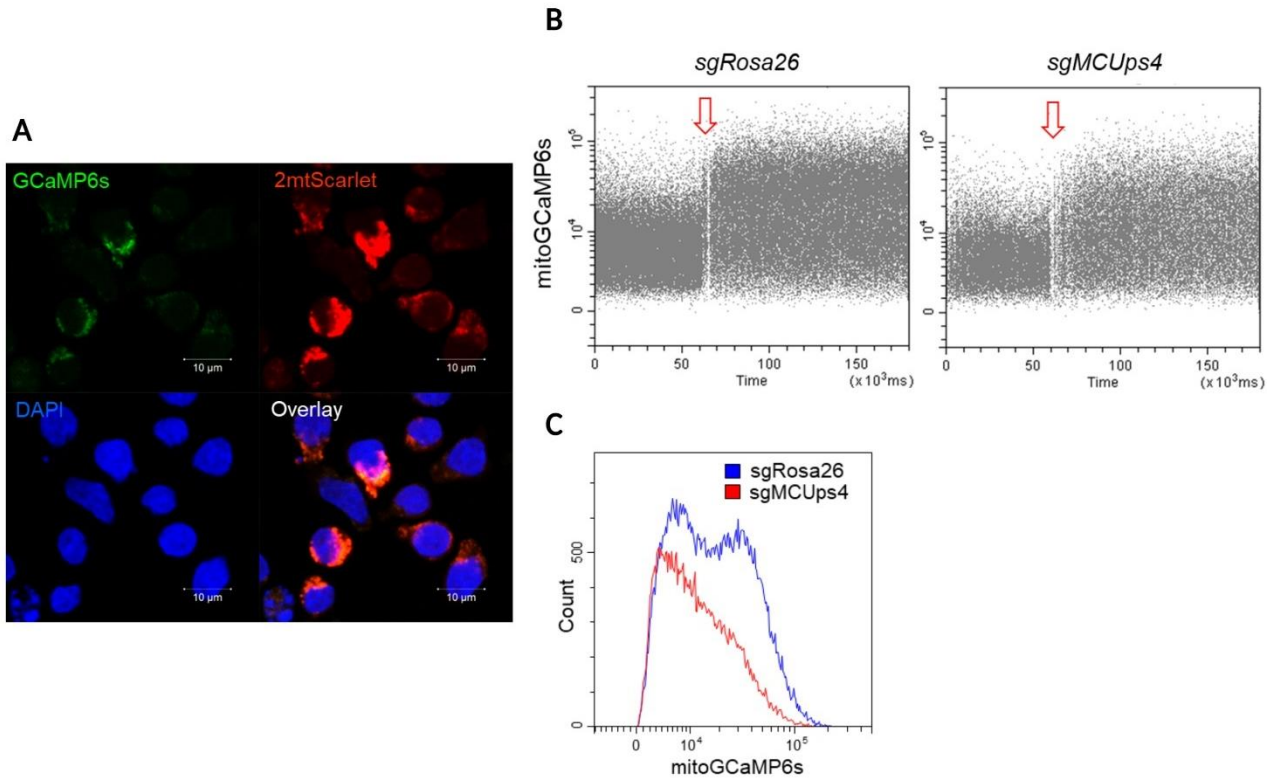

S Figure 7. Biosensor localisation and responses to stimulation examined in Control (sgRosa26) and MCUa$_{KD}$ (sgMCUps4) rat effector T-cells. (**A**) Confocal images of DAPI-stained MCUps4 T-cell line transduced by Puro2A-2mtScarletGCaMP6s virus. Proper mitochondrial localisation of 2mtScarlet-GCaMP6s is observed. Magnification: 40x. Scale bar: 10 µm. (**B-C**) Rosa26 and MCUps4 T-cells analyzed by flow cytometry. Resting T-cells were measured for 1 min, then treated with 4 µM of ionomycin (red arrows) and measured for additional 2 min. Dot plots (**B**) and overlay histogram (**C**) show the mitochondrial GCaMP6s signal. MCUps4 cells responded overall less to ionomycin stimulation compared to Rosa26 control cells. Experiments shown were performed and analysed by Dr. Dmitri Lodygin.

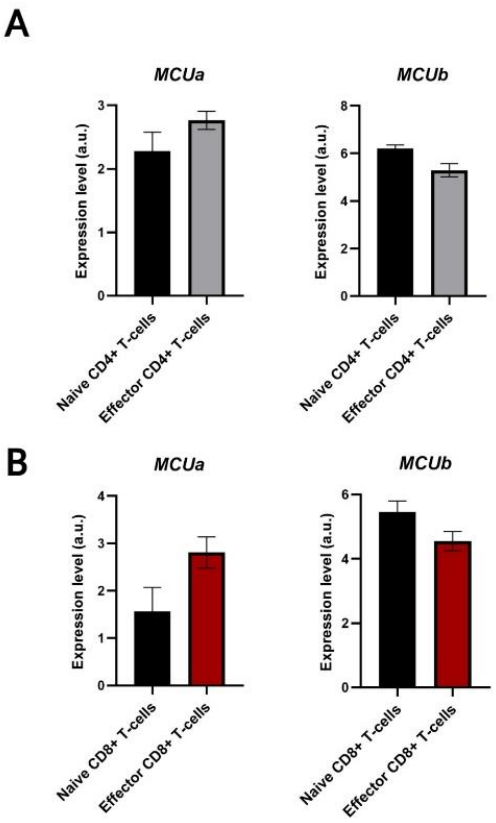

S Figure 8. MCU complex rearrangement is necessary for T-cell transition from a 'naive' to an 'activated' cell type. *MCUa* expression increases, whereas *MCUb* expression decreases upon immune cell activation. Such cells included here are $CD4^+$ T-cells (**A**) and $CD8^+$ cytotoxic T-cells (**B**). Data processed directly from a dataset generated by Monaco et al. (2019). Data show a mean ± SEM of 4 naive T-cell donors and 3 effector T-cell donors.

7.2 Supplementary Tables

S Table 1. A list of significant DEGs upon MCUa downregulation and impairment of $_{m}Ca^{2+}$ uptake in primary human $CD4^{+}$ T-cells. Log2FoldChange indicates up- or downregulated gene expression (continues on next page).

Gene ID	Gene Name	log2FoldChange	*p*-value
ENSG00000024862	*CCDC28A*	0.52	0.00136
ENSG00000026036	*RTEL1-TNFRSF6B*	-1.06	0.00591
ENSG00000059804	*SLC2A3*	0.75	0.004
ENSG00000073605	*GSDMB*	-0.5	0.00189
ENSG00000084774	*CAD*	-0.6	0.00016
ENSG00000087250	*MT3*	1.62	$3.59E^{-05}$
ENSG00000099875	*MKNK2*	0.6	0.000921
ENSG00000104765	*BNIP3L*	0.77	0.00124
ENSG00000109107	*ALDOC*	1.28	0.000238
ENSG00000112159	*MDN1*	-0.51	0.00972
ENSG00000113739	*STC2*	1.23	0.000607
ENSG00000114023	*FAM162A*	0.74	0.000159
ENSG00000114268	*PFKFB4*	1.24	0.00253
ENSG00000115457	*IGFBP2*	1.4	0.00114
ENSG00000116761	*CTH*	0.88	0.00589
ENSG00000117305	*HMGCL*	0.5	0.00671
ENSG00000119801	*YPEL5*	0.5	0.00117
ENSG00000119950	*MXI1*	0.84	0.00204
ENSG00000120800	*UTP20*	-0.64	0.00158
ENSG00000121716	*PILRB*	-0.7	0.00376
ENSG00000123360	*PDE1B*	-0.67	0.00232
ENSG00000124785	*NRN1*	1.28	0.0089
ENSG00000127663	*KDM4B*	0.52	0.00232
ENSG00000128165	*ADM2*	0.98	$2.73E^{-05}$
ENSG00000129521	*EGLN3*	0.73	0.00201
ENSG00000132382	*MYBBP1A*	-0.5	0.000366
ENSG00000135245	*HILPDA*	1.37	0.000216
ENSG00000135925	*WNT10A*	1.47	0.000772
ENSG00000138764	*CCNG2*	0.58	0.0084
ENSG00000145730	*PAM*	0.67	0.000249
ENSG00000145911	*N4BP3*	1.33	$4.39E^{-05}$
ENSG00000147852	*VLDLR*	0.92	0.000933
ENSG00000148400	*NOTCH1*	-0.53	0.000344
ENSG00000148840	*PPRC1*	-0.56	0.00541
ENSG00000151640	*DPYSL4*	0.72	0.00879
ENSG00000156026	***MCU***	**-1.43**	**$4.09E^{-08}$**
ENSG00000160072	*ATAD3B*	-0.77	0.000325
ENSG00000161960	*EIF4A1*	-0.83	0.000392
ENSG00000162373	*BEND5*	1.2	0.00228

Gene ID	Gene Name	Log2FoldChange	*p*-value
ENSG00000164096	*C4orf3*	0.56	0.000784
ENSG00000164638	*SLC29A4*	1.19	0.00318
ENSG00000165271	*NOL6*	-0.55	0.00258
ENSG00000165684	*SNAPC4*	-0.52	0.00327
ENSG00000166086	*JAM3*	0.93	0.00454
ENSG00000167971	*CASKIN1*	1.8	0.00107
ENSG00000167978	*SRRM2*	-0.51	0.00631
ENSG00000168209	*DDIT4*	0.75	0.00114
ENSG00000173281	*PPP1R3B*	0.84	0.00302
ENSG00000177181	*RIMKLA*	1.17	0.00137
ENSG00000186352	*ANKRD37*	0.72	0.00306
ENSG00000188566	*NDOR1*	-0.51	0.00483
ENSG00000196756	*SNHG17*	-0.55	0.00515
ENSG00000197774	*EME2*	-0.59	0.00406
ENSG00000198711	*SSBP3-AS1*	-1.37	0.00903
ENSG00000203761	*MSTO2P*	-1.11	0.00756
ENSG00000204681	*GABBR1*	-0.65	0.00291
ENSG00000210082	*MT-RNR2*	0.53	$1.39E^{-05}$
ENSG00000225855	*RUSC1-AS1*	-0.75	0.00276
ENSG00000226510	*UPK1A-AS1*	2.53	0.000561
ENSG00000242294	*STAG3L5P*	-0.92	0.000514
ENSG00000253729	*PRKDC*	-0.51	$7.65E^{-05}$
ENSG00000260231	*KDM7A-DT*	0.78	0.00126
ENSG00000152256	*PDK1*	0.62	0.00364

Log2FoldChange of upregulated genes is labelled with purple and of downregulated genes with orange. Downregulated MCU is shown in **bold**.

S Table 2. Short guide RNA sequences used for CRISPR Cas9 editing of MCU gene in $CD4^+$ rat T-cells. Protospacer adjacent motif, PAM, is underlined.

Name	Sequence
Protospacer (ps) 4	CCGGCGTCCTGGCAGAGCGTGGG
Protospacer (ps) 5	CCGCAGGTAGATCGCTCCTGCTG
Protospacer (ps) 6	CCTGGGACATCATGGAACCGGTC

8. List of Main Figures

Figure 35. Effect of MCUa downregulation on mitochondrial membrane potential (ΔΨm) and mitochondrial protein translation.

Figure 36. Treatment of $CD4^+$ T-cells with 100μM of MCU inhibitor Ru265 does not affect ΔΨm and effector T-cell proliferation.

Figure 37. $MCUa_{KD}$ model achieved at a naive-T-cell-stage recapitulates the data observed with the model generated at an effector-T-cell-stage.

Figure 38. Mitochondrial protein translation ^{35}S labelling was performed on the "early-stage" $MCUa_{KD}$ model (naive T-cell stage). The stage of MCU downregulation does not affect mitochondrial protein translation.

Figure 39. MCUa downregulation does not affect $CD4^+$ T-cell proliferation rates.

Figure 40. MCUa downregulation does not affect $CD4^+$ T-cell H_2O_2 levels and glutathione redox potential (E_{GSH}).

Figure 41. Impaired $_mCa^{2+}$ uptake does not affect the antioxidative capacity of $CD4^+$ T-cells.

Figure 42. Significant decrease in cytosolic Ca^{2+} levels and SOCE upon MCUa downregulation.

Figure 43. An mRNA panel of cytokines, transcription factors and surface markers performed to examine the role of MCU in T-cell function. A decreased expression of proinflammatory cytokines *IL-2* and *IFNγ*, and an increased expression of Treg transcription factor *FoxP3* are observed upon MCUa downregulation. No other significant changes are detected.

Figure 44. MCUa downregulation leads to reduced gene expression of crucial T-cell proinflammatory cytokines: IL-2 and IFNγ.

Figure 45. Changes in cytokine secretion upon downregulation of MCUa.

Figure 46. MCU influences $CD4^+$ T-cell invasion.

Figure 47. A volcano plot illustrating RNA sequencing data which revealed significant changes in expression of genes related to multiple cellular pathways upon MCUa downregulation.

Figure 48. KEGG pathway analysis showing significantly affected cellular pathways after MCUa knockdown.

Figure 49. Proteomaps showing the quantitative composition of proteomes with a high probability to be suppressed (left panel-orange) and elevated (right panel-purple) upon MCUa knockdown.

Figure 50. Upregulation of the mitochondrial-AAA protease, AFG3-like protein 2 (AFG3L2) upon MCUa downregulation.

Figure 51. No difference in *AFG3L2* mRNA expression upon MCUa knockdown.

Figure 52. $AFG3L2_{KD}$ in $CD4^+$ T-cells which leads to an increase in resting $_m[Ca^{2+}]$ levels.

Figure 53. Partial AFG3L2 downregulation does not affect mitochondrial respiration and ATP production in $CD4^+$ T-cells.

Figure 54. Changes in $_mCa^{2+}$ uptake in HeLa cells upon downregulation of m-AAA protease AFG3L2.

Figure 55. AFG3L2 knockdown on both mRNA (A) and protein (B) levels.

Figure 56. Assessment of mitochondrial respiration (oxygen consumption rates) upon downregulation of the protease AFG3L2 in HeLa cells.

Figure 57. Downregulation of AFG3L2 in HeLa cells leads to a minor increase in mitochondrial ATP levels and a significant increase in $\Delta\Psi m$.

Figure 58. MCUa knockdown confirmed in all three generated rat $CD4^+$ T-cell lines, compared to CRISPR control cell line.

Figure 59. Significant impairment of resting $_m[Ca^{2+}]$ and $_mCa^{2+}$ uptake upon TCR stimulation in stable $MCUa_{KD}$ primary rat $CD4^+$ T-cell lines.

Figure 60. T7E1 assay performed to confirm and characterise the intended edit of the *MCUa* sequence in the generated lines.

Figure 61. Decreased mitochondrial respiration and ATP levels in rat $CD4^+$ T-cells with $MCUa_{KD}$.

Figure 62. Gene expression of proinflammatory cytokines upon $_mCa^{2+}$ inhibition in rat $CD4^+$ T-cells.

Figure 63. Significant delay in day of onset of experimental autoimmune encephalomyelitis (EAE) in rats injected with $MCUa_{KD}$ $CD4^+$ T-cells.

Figure 64. MCUa knockdown further confirmed in the $MCUps5_{KD}$ cell line.

Figure 65. Reduction of chronic disease severity in animals injected with $MCUps5_{KD}$ $CD4^+$ T-cells.

Figure 66. An overview of the main findings of this study.

S Figure 1. 3D structure of a naive (A) and an effector (B) $CD4^+$ T-cell.

S Figure 2. TCR stimulation induces an increase in expression of multiple genes related to Ca^{2+} signalling, especially NFAT proteins.

S Figure 3. Mitochondrial protein translation ^{35}S labelling showed significantly increased translation peaking 48 hrs after TCR stimulation.

S Figure 4. Reduced mitochondrial ATP production rates assessed in 3 separate donors (K1, K2, K3) upon MCUa downregulation.

S Figure 5. EAE onset can cause small weight changes in animals; this can be observed at days 5 and 6 in (A) and is less obvious in (B), (C) and (D). Nevertheless, no significant difference was observed between animals injected with control cells and animals injected with $MCUa_{KD}$ cells.

S Figure 6. Targeted editing of the rat *MCUa* gene (CRISPR Cas9).

S Figure 7. Biosensor localisation and responses to stimulation examined in Control (sgRosa26) and $MCUa_{KD}$ (sgMCUps4) rat effector T-cells.

S Figure 8. MCU complex rearrangement is necessary for T-cell transition from a 'naive' to an 'activated' cell type.

9. Acknowledgements

Words cannot express the gratitude I have for all who have been a part of my PhD journey.

First and foremost, I would like to thank my supervisor, Prof. Dr. Ivan Bogeski, who gave me the opportunity to be a part of a great team, who patiently supported and guided me throughout the last four years. This endeavor would not have been possible without your involvement in our project and your decision to accept 'yet another' Macedonian in the group. Ви благодарам за сè!

I am extremely grateful to my thesis committee members Prof. Dr. mult. Thomas Meyer and Prof. Dr. Jürgen Wienands, for their constant support, enthusiasm, and scientific advice during this period. Many thanks to the members of my extended examination committee, Prof. Dr. Ralf Kehlenbach, Prof. Dr. Alexander Flügel, and Prof. Dr. Stefan Jakobs for agreeing and taking the time to read and review my dissertation.

I would also like to express my deepest appreciation to all the members of my working group (current and otherwise), for their friendship and encouragement. Thank you for helping me and sharing your knowledge with me! Big thanks to Dr. Christine Gibhardt, Dr. Sabrina Cappello, and Dr. Hsu-Min Sung for their invaluable scientific support and assistance with experiments, to Dr. Zurine Bonilla Del Rio and Dr. Ioana Stejerean-Todoran for their constant help and motivation, especially towards the end of my PhD time, to Andrea Paluschkiwitz for her technical assistance and guidance in the lab. An even bigger thanks to Lena Krause for her friendship, for all the laughs, and for all the help with my project, to Kira Pahl for being a great hardworking student, to Christian Ickes for his (bioinformatic) wisdom and for always cheering me up, to Nanouk Kirpal and Julian Wojtachnia for their friendship and for making work more enjoyable.

Special thanks to Dr. Dmitri Lodygin for his involvement in the project and for his scientific guidance, and to all the members of the Molecular and Cellular Neuroimmunology group at the Institute of Neuroimmunology and Multiple Sclerosis Research. Their collaboration has been invaluable for the success of this project! Furthermore, many thanks to Dr. Sven Dennerlein for his help with the project, without which we would not have managed to achieve what we did. Big thanks to Prof. Dr. Peter Rehling and all members of the Department of Cellular Biochemistry for allowing me to use their lab resources, and to Angela Boshnakovska for always being there to plan and help with a Seahorse experiment, or to drink

a glass of wine with me.

I had the pleasure of receiving funding for my project and being part of the International Research Training Group 1816. To all the IRTG-members: Thank you for the support!

Getting through this PhD required much more than academic support and I have many people to thank for that. To my wonderful friends: Ana Maria, Marisol and Alisa, your friendship has shaped me into a better person, motivated me to go after my dreams and made me feel like a part of a family in Germany. Thank you for always being there! To all my other friends and colleagues which I met and still often run into around Göttingen, thank you for making me a part of your life here!

Last, but not least, I am deeply indebted to my parents and my sister, without whom I would not be where I am today. I am a proud daughter and an even prouder sister. I am grateful to have had such loving and supportive grandparents, especially my late grandfather who, even though I denied it, always knew that I would become a doctor one way or another. Finally, to my soulmate Stefan, thank you for being my rock all these years and for simply making my life happier. Ве сакам најмногу!

Selected Publications and Abstracts

Stejerean-Todoran, I., Zimmermann, K., Gibhardt, C. S., Vultur, A., Ickes, C., Shannan, B., Bonilla Del Rio, Z., Wölling, A., Cappello, S., Sung, H. M., **Shumanska, M**., Zhang, X., Nanadikar, M., Latif, M. U., Wittek, A., Lange, F., Waters, A., Brafford, P., Wilting, J., Urlaub, H., … Bogeski, I. (2022). MCU Controls Melanoma Progression Through a Redox-Controlled Phenotype Switch. *European Molecular Biology Organisation Reports*, e54746. https://doi.org/10.15252/embr.202254746.

Shumanska, M., Lodygin, D., Krause, L., Ickes, C., Rehling, P., Dennerlein, S., Flügel, A., and Bogeski, I. (2022). Differentiation-Induced Rearrangement of the Mitochondrial Calcium Uniporter Complex Regulates T-Cell-Mediated Immunity. *Biochimica et Biophysica Acta (BBA)-Bioenergetics*, 1863, 148721. (Abstract).

Shumanska, M., & Bogeski, I. (2022). Redoxing PTPN22 Activity. *eLife*, 11, e79125. https://doi.org/10.7554/eLife.79125.

Wu H, Brand B, Eckstein M, Hochrein SM, **Shumanska M**, Dudek J, Nickel A, Maack C, Bogeski I and Vaeth M. (2021) Genetic Ablation of the Mitochondrial Calcium Uniporter (MCU) Does not Impair T Cell-Mediated Immunity In Vivo. *Frontiers of Pharmacology*, 12:734078 doi: 10.3389/fphar.2021.734078.

Gibhardt, D.S., Cappello, S., Bhardwaj, R., Schober, R., Kirsch, S.A., Bonilla del Rio, Z., Gahbauer, S., Bochiccio, A., **Shumanska, M.**, Ickes, C., Stejerean-Todoran, I., Mitkovski, M., Alansary, D., Zhang, X., Revazian, A., Fahrner, M., Lunz, V., Frischauf, I., Luo, T., Ezerina, D., Messens, J., Belousov, V.V., Hoth, M., Böckmann, R.A., Hediger, M.A., Schindl, R., Bogeski, I. (2020) Oxidative Stress-Induced STIM2 Cysteine Modifications Suppress Store-Operated Calcium Entry. *Cell Reports 33*(3):108292. doi: 10.1016/j.celrep.2020.108292.

Shumanska, M. (2017). Seasonal Changes in Cancer Mortality Rates among Cancer and Cardiovascular Patients in the Netherlands. *Student Undergraduate Research E-Journal*, 3: 198-201.